UNIVERSITÀ
DI SIENA
1240

Università degli Studi di Siena

FACOLTÀ DI SCIENZE MATEMATICHE FISICHE E NATURALI

Tesi di dottorato in Fisica Sperimentale
PhD Thesis in Experimental Physics

Measurements of charmless b-hadron decays at CDF; first evidence for the annihilation $B_s^0 \to \pi^+\pi^-$ decay mode.

Candidate:
Dott. Fabrizio Ruffini

Advisors:
Prof. Giovanni Punzi

Dott. Michael Joseph Morello

Tutor:
Dott. Paolo Maestro

XXV Entrance, 2010-2012

A Paola,
a tutti gli angeli custodi
che abbiamo incontrato.

Contents

Introduction

The theory of fundamental particles, called Standard Model (SM), has proven to be successfully able to describe the way particles interact, over more than 40 years of attempting to invalidate its structure. Nevertheless, it is well known that the SM is far from being a "theory of everything": for instance, it is not able to incorporate the full gravitation theory and it does not explain the size of the matter-antimatter asymmetry of the universe. Thus it is necessary to move from the SM to look for new physics (NP) effects beyond it, representing the missing pieces of a large puzzle. In the past decades, key players in this quest were the collision machines, able to perform more and more precise measurements with the increase of energy and apparatus complexities. The Large Hadron Collider (LHC) at CERN, the latest and more powerful operating collider today, is able to study processes at the unexplored region of 7 TeV centre-of-mass energies (14 TeV are expected in the next run period). It recently reported fundamental results for the comprehension of how particles interact: amongst others, the observation of the Higgs boson by the Atlas and the CMS collaborations [1, 2], and the heavy-flavour counterpart measurement, the first evidence of the $B_s^0 \to \mu^+\mu^-$ decay at the LHCb collaboration [3]. So far, the measurements substantially confirmed the SM predictions, suggesting that direct searches of unexpected processes could be not straightforward at the present achievable energies. Therefore, in the current panorama the crucial ingredient to increase our knowledge is to provide several, different and as precise as possible physics measurements. This not only reduces the uncertainties of the theoretical framework but, as a critical consequence, makes possible to increase the predictive power of the model, over-constraining it from different sides.

The hadronic decays of particles containing b-quark is a very promising field of research. They show a rich set of topologies: tree, penguin, annihilation-type diagrams are typically involved, thus providing a powerful probe in searching effects from new higher mass particles, that may enter through high-order internal loops. Quantitative SM predictions are affected by significant uncertainties because a perturbative approach cannot be used to calculate hadronic decays amplitudes. However, combining several measurements of similar processes allows the cancellation of unknown parameters and consequently the reduction of the uncertainties, providing a powerful tool to compare experimental results and the theoretical framework. A large amount of important results involving the B^0 and the B^+ mesons

has been obtained at the b-factories during the past decade. The upgraded Collider Detector at Fermilab TeVatron (CDF II), operating until 2011, was able to study B^0, B^+, but also the much less accessible B_s^0 and Λ_b^0 decay modes in a different experimental environment. The topic of this thesis is the study of charmless two-body neutral b-hadrons decay modes at CDF, collectively called $B \to h^+h'^-$. We refer to $B \to h^+h'^-$ as the decays of a B_d^0 or a B_s^0 meson into charged pions or kaons, and the decays of a Λ_b^0 baryon into a proton and a charged pion or kaon. The $B \to h^+h'^-$ decays offer a rich set of important measurements: not yet observed branching ratios, such as the $\mathcal{B}(B_s^0 \to \pi^+\pi^-)$ and $\mathcal{B}(B^0 \to K^+K^-)$, and charge conjugation and parity inversion ($\mathcal{C}P$) violating effects in the $B^0 \to K^+\pi^-$, $B_s^0 \to K^-\pi^+$, $\Lambda_b^0 \to p\pi^-$, and $\Lambda_b^0 \to pK^-$ decays.

The measurements of charmless annihilation b-mesons decay modes $B_s^0 \to \pi^+\pi^-$ and $B^0 \to K^+K^-$ is one of the subjects of this work: in spite of a general progress of the field, this specific class of decay amplitudes has resisted attempts at quantitative predictions up to the present, and it is often simply neglected in calculations. Indeed, these decays proceed only via hard to predict processes, such as penguin-annihilation and W-exchange topologies. Predictions for their branching ratios typically lead to values of order $\sim 10^{-7}$, but calculations vary greatly between different theoretical approaches, and even within the same approach. The lack of knowledge of the size of annihilation-type amplitudes introduces irreducible uncertainties in predictions for several decays of great interest, such as $B^0 \to \pi^+\pi^-$ and $B_s^0 \to K^+K^-$. However, the annihilation $B_s^0 \to \pi^+\pi^-$ and $B^0 \to K^+K^-$ modes were still unobserved at the time of the analysis: the experimental investigation of both decay modes was therefore very desirable, and had the potential to provoke a significant advancement of this theoretical field: precise measurements allow a better understanding of the b-mesons system, and can be used as a check of the different theoretical approaches.

The second subject of this thesis are $\mathcal{C}P$ violating effect measurements in the B_s^0 and Λ_b^0 unexplored systems and in the well-studied B^0 decays. At the time of this analysis, no observations of $\mathcal{C}P$ violation in the B_s^0 system were performed. The only existing measurement of $\mathcal{A}_{\mathcal{C}P}(B_s^0 \to K^-\pi^+)$ was achieved in the previous version of this analysis at CDF, with a significance of more than 2σ. With the statistics available at the time of the analysis, we would expect to perform an $\mathcal{A}_{\mathcal{C}P}(B_s^0 \to K^-\pi^+)$ measurement with resolution less than 10%: assuming the SM prediction of the central value of about 30% to be correct, it should be possible to obtain the first evidence of this observable. It would also be the first precise measurement of a direct $\mathcal{C}P$ violation in the B_s^0 system. In addition, this measurement has been proposed as a nearly model-independent test for the presence of non-SM physics [4, 5]. The relationships between charged-current quark couplings in the SM predict a well-defined hierarchy between direct $\mathcal{C}P$ violation in $B^0 \to K^+\pi^-$ and $B_s^0 \to K^-\pi^+$ decays, yielding a significant asymmetry for the latter, of about 30%, as mentioned above. This large effect allows easier experimental investigation

and any discrepancy may indicate contributions from non-SM amplitudes. Thus simultaneous measurements of $\mathcal{A}_{\mathcal{C}P}(B^0 \to K^+\pi^-)$ and $\mathcal{A}_{\mathcal{C}P}(B_s^0 \to K^-\pi^+)$ are very desirable. In this thesis we were also able to perform a precise measurement of $\mathcal{A}_{\mathcal{C}P}(B^0 \to K^+\pi^-)$. This effect has already been studied at the b-factories for a long time, and the first observation was obtained back in 2007. The $\mathcal{C}P$ asymmetry in the $B^0 \to K^+\pi^-$ decay was protagonist of intense experimental and theoretical activity, together with the same effect in the $B^+ \to K^+\pi^0$ decays. Under standard assumptions of isospin symmetry and smallness of contributions from higher-order processes, similar $\mathcal{C}P$ asymmetries are predicted for $B^0 \to K^+\pi^-$ and $B^+ \to K^+\pi^0$ decays [6, 7]. However, experimental data show a significant discrepancy, referred to as the $K\pi$ puzzle. Even if the discrepancy can be accommodate within the SM or using simple extensions of the standard model, uncertainty on the contribution of higher-order SM amplitudes prevented a firm conclusion. Nevertheless, high accuracy measurements of the direct $\mathcal{C}P$ asymmetry $\mathcal{A}_{\mathcal{C}P}(B^0 \to K^+\pi^-)$ remain a very interesting subject of study.

To complete the picture, we also performed $\mathcal{C}P$ asymmetry measurements of $\Lambda_b^0 \to pK^-$ and $\Lambda_b^0 \to p\pi^-$ decays. While over the past two decades the b-meson $\mathcal{C}P$ asymmetries have been deeply and methodically investigated at the b-factories, the b-baryon system represents a new window to look at: the present predictions for $\mathcal{C}P$ violation in charmless b–baryon decays within the Standard Model (SM) lack of accuracy, and their branching fractions are observed being larger than expected. Precise measurements of $\mathcal{C}P$ asymmetries in $\Lambda_b^0 \to p\pi^-$ and $\Lambda_b^0 \to pK^-$ decays will increase our understanding of the underlying scenario.

Using the full sample of non leptonic two-body charmless decays of neutral b-hadrons $B \to h^+h'^-$ collected at the CDF II experiment, we report:

- the first evidence of the annihilation $B_s^0 \to \pi^+\pi^-$ decay modes;
- the first two-sided limit of the branching ratio $\mathcal{B}(B^0 \to K^+K^-)$;
- an evidence of $\mathcal{A}_{\mathcal{C}P}(B_s^0 \to K^-\pi^+)$, confirming the first evidence and then the first observation reported at LHCb [8, 9];
- the world's unique measurements of $\mathcal{A}_{\mathcal{C}P}(\Lambda_b^0 \to p\pi^-)$ and $\mathcal{A}_{\mathcal{C}P}(\Lambda_b^0 \to pK^-)$.

The search for the rare modes $B_s^0 \to \pi^+\pi^-$ and $B^0 \to K^+K^-$ was performed in 2011, when only a subsample of the total CDF data sample was available for the analysis. On the other hand, the $\mathcal{C}P$ measurements have been performed in 2012 using the final CDF data sample. The thesis is organized as follows. In chap. 1 we outline the motivation of the measurements and the dynamics of b-hadron decays, describing the $\mathcal{C}P$ violation phenomenon in detail. In chap. 2 we describe the experimental apparatus, while chap. 3 contains the description of the data sample used in the analysis and we show for the first time the sample mass distribution. Chapter 4 hosts a detailed description of the Monte Carlo samples

used. The accurate reproduction of the data distributions is one of the key point of this analysis, because it will be used in the fit of composition to obtain the desired measurements. In chap. 5 we discuss the fundamental point of the analysis: how it is possible to obtain statistical separation among the different $B \to h^+h'^-$ decay modes combining kinematics and particle identification information. We also report the structure of the Likelihood fit used to disentangle the different $B \to h^+h'^-$ decay modes. In chap. 6 we describe the kinematics templates while in chapter chap. 7 we report the templates containing the Particle Identification information, used in the fit of composition. Chapter 8 reports the results and the checks of the fit of composition. To obtain the physics measurements of branching fractions from the parameters returned from the fit we need to apply the corrections for different efficiency of the selection for the various decay modes. These efficiency corrections are reported in chap. 9. To obtain the physical $\mathcal{C}P$ observables desired, the raw results of the fit must be corrected for the charge asymmetry corrections between the positively and negatively charged kaons, pions and protons. These corrections are reported in chap. 10. Chapter 11 discusses the systematics effects and their uncertainties, and reports the method used to evaluate the significance of the annihilation decay modes results. Finally, chap. 12 contains a discussion about the obtained results and their interpretation.

Chapter 1

Two-body charmless $b-$hadron decays

This chapter briefly introduces the general aspects of the SM and describes in details only the most relevant theoretical points for this work. Our treatment will follow very closely the one presented in Ref. [10].

1.1 The Standard Model: a general introduction

The Standard Model (SM) of particle physics is the theory used to describe the fundamental nature's laws. It is the result of the human desire to understand the surrounding universe, and how does it works. The SM is a quantum field theory predicting three kind of interactions between elementary particles: the weak, the strong and the electromagnetic interaction. While the electromagnetic interaction is responsible for almost all the phenomena encountered in daily life (except gravity), the weak and strong forces are effective only over a very short range and dominate only at the level of subatomic particles. The weak force is responsible for phenomena like radioactive decays; the strong interaction holds together quarks to form proton and neutrons, and also proton and neutron themselves to form atom's nucleus, thus is strictly connected with nuclear fission phenomenon we use to obtain nuclear energy. The SM describes the interactions between elementary particles using the concept of mediation: the particles exchange between themselves the gauge bosons, that "mediate" the interaction. The gauge bosons introduced are the photon γ, mediating the electromagnetic interaction, the $W^{\pm}$ and Z^0, mediating the weak interaction, and the gluons, for the strong force. The elementary particles are divided into 6 leptons (electron e, muon μ, tau τ, and the corresponding neutrinos ν_e, ν_μ, ν_τ) and 6 quarks (up u, down d, charm c, strange s, top t and beauty b), with the corresponding antiparticles. Both leptons and quarks are effected by electroweak interaction (electromagnetic and weak unification), while only the quarks are affected by strong interaction. They are organized into three families (three

generations), according to the charge, as follow: As far as today, the SM resisted

	1st	2st	3rd	charge
Leptons	e^-	μ^-	τ^-	-1
	ν_e	ν_μ	ν_τ	0
Quarks	u	c	t	+2/3
	d	s	b	-1/3

Table 1.1: Quarks and leptons families.

over the years many tests of the accuracy of its predictions, proving to be able to describe with sufficient accuracy the subatomic world. However the model misses some important pieces: for example, it is not able to incorporate the most familiar force in our everyday lives, the gravity. So, even though the SM is currently the best description we have of the particles' and forces' behavior, it does not explain the complete picture. There are also other important questions it cannot answer: why our universe in composed mostly of matter, and where is the missing antimatter, why there are so many elementary particles, why their masses have exactly that values and many others.

This work of thesis will investigate the heavy flavor sector, involving decays of particles containing the most massive quarks. In particular, we will study the b-hadrons, that means particles containing b-quarks. The topic of this work is the measurements of $\mathcal{B}$ and $\mathcal{C}P$ asymmetries of two-body charmless decays of neutral b-hadrons, ($B^0_{(s)} \to h^+h'^-$ and $\Lambda^0_b \to ph^-$, where the h can be a pion or a kaon) collectively called $B \to h^+h'^-$. Next sections describe the theoretical framework in which the b-hadrons are included. Firstly, it is necessary to introduce the CKM matrix describing the electroweak interactions between quarks and how the phenomenon of the $\mathcal{C}P$ violation manifests itself.

1.2 The CKM Matrix

In the framework of the Standard Model of electroweak interactions [11], $\mathcal{C}P$-violating effects may originate from the charged-current interactions of quarks, having the structure

$$D \to UW^-. \tag{1.1}$$

Here $D \in \{d, s, b\}$ and $U \in \{u, c, t\}$ denote down- and up-type quark flavours, respectively, whereas the W^- is the weak boson. From a phenomenological point of view, it is convenient to collect the generic "coupling strengths" V_{UD} of the

charged-current processes in (1.1) in the form of the following matrix:

$$\hat{V}_{\rm CKM} = \begin{pmatrix} V_{ud} & V_{us} & V_{ub} \\ V_{cd} & V_{cs} & V_{cb} \\ V_{td} & V_{ts} & V_{tb} \end{pmatrix}, \tag{1.2}$$

which is referred to as the Cabibbo–Kobayashi–Maskawa (CKM) matrix [12, 13]. From a theoretical point of view, this matrix connects the electroweak states (d', s', b') of the down, strange and bottom quarks with their mass eigenstates (d, s, b) through the following unitary transformation:

$$\begin{pmatrix} d' \\ s' \\ b' \end{pmatrix} = \begin{pmatrix} V_{ud} & V_{us} & V_{ub} \\ V_{cd} & V_{cs} & V_{cb} \\ V_{td} & V_{ts} & V_{tb} \end{pmatrix} \cdot \begin{pmatrix} d \\ s \\ b \end{pmatrix}. \tag{1.3}$$

Consequently, $\hat{V}_{\rm CKM}$ is actually a unitary matrix. This feature ensures the absence of flavour-changing neutral-current (FCNC) processes at the tree level in the SM, and is hence at the basis of the famous Glashow–Iliopoulos–Maiani (GIM) mechanism [14]. If we express the non-leptonic charged-current interaction Lagrangian in terms of the mass eigenstates appearing in (1.3), we arrive at:

$$\mathcal{L}^{\rm CC}_{\rm int} = -\frac{g_2}{\sqrt{2}} \begin{pmatrix} \bar{u}_{\rm L}, & \bar{c}_{\rm L}, & \bar{t}_{\rm L} \end{pmatrix} \gamma^\mu \hat{V}_{\rm CKM} \begin{pmatrix} d_{\rm L} \\ s_{\rm L} \\ b_{\rm L} \end{pmatrix} W^\dagger_\mu \; + \; \text{h.c.}, \tag{1.4}$$

where the gauge coupling g_2 is related to the gauge group $SU(2)_{\rm L}$, and the $W^{(\dagger)}_\mu$ field corresponds to the charged W bosons. Looking at the interaction vertices following from (1.4), we observe that the elements of the CKM matrix describe in fact the generic strengths of the associated charged-current processes, as noted above. In fig. 1.1, we show the $D \to UW^-$ vertex and its $\mathcal{C}P$ conjugate. Since the corresponding $\mathcal{C}P$ transformation involves the replacement

$$V_{UD} \xrightarrow{\mathcal{C}P} V^*_{UD}, \tag{1.5}$$

$\mathcal{C}P$ violation could, in principle, be accommodated in the SM through complex phases in the CKM matrix. The question is whether there actually are physical complex phases in that matrix. In can be shown that the constraint of unitarity of the CKM matrix reduces the matrix observables to three Euler angles and a complex phase. This phase is the only source of $\mathcal{C}P$ violation in the quark sector allowed by the SM. A commonly used parameterization is due to Wolfenstein[15].

$$V_{CKM} = \begin{pmatrix} 1 - \frac{\lambda^2}{2} & \lambda & A\lambda^3(\bar{\rho} - i\bar{\eta}) \\ -\lambda & 1 - \frac{\lambda^2}{2} & A\lambda^2 \\ A\lambda^3(1 - \bar{\rho} - i\bar{\eta}) & -A\lambda^2 & 1 \end{pmatrix} + O(\lambda^4), \tag{1.6}$$

where $\lambda = |V_{us}|$ is the sine of the Cabibbo angle, and A, ρ, η are the other three observables. In particular, η is the phase responsible for the $\mathcal{C}P$ violation within the SM.

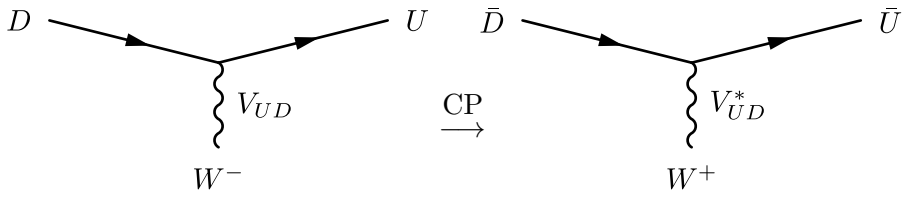

Figure 1.1: CP-conjugate charged-current quark-level interaction processes in the SM.

1.2.1 Further requirements for $\mathcal{C}P$ violation

In order to be able to accommodate $\mathcal{C}P$ violation within the framework of the SM through a complex phase in the CKM matrix, at least three generations are required. However, this feature is not sufficient for observable $\mathcal{C}P$ violating effects. Further conditions have to be satisfied, which can be summarized as follows [16, 17]:

$$(m_t^2 - m_c^2)(m_t^2 - m_u^2)(m_c^2 - m_u^2)(m_b^2 - m_s^2)(m_b^2 - m_d^2)(m_s^2 - m_d^2) \times J_{\rm CP} \neq 0, \quad (1.7)$$

where

$$J_{\rm CP} = |{\rm Im}(V_{i\alpha} V_{j\beta} V_{i\beta}^* V_{j\alpha}^*)| \quad (i \neq j,\, \alpha \neq \beta)\,. \quad (1.8)$$

The mass factors in (1.7) are related to the fact that the $\mathcal{C}P$-violating phase of the CKM matrix could be eliminated through an appropriate unitary transformation of the quark fields if any two quarks with the same charge had the same mass. Consequently, the origin of $\mathcal{C}P$ violation is closely related to the "flavour problem" in elementary particle physics. The second element of (1.7), the "Jarlskog parameter" $J_{\rm CP}$ [16], can be interpreted as a measure of the strength of $\mathcal{C}P$ violation in the SM. The experimental information on the CKM parameters implies $J_{\rm CP} = \mathcal{O}(10^{-5})$, so that $\mathcal{C}P$-violating phenomena are hard to observe. However, new complex couplings are typically present in scenarios for NP.

The Wolfenstein representation of the CKM matrix 1.6, up to the third order expansion of λ, shows that the complex terms are present in the elements connecting the first and the third generation of quarks, in the elements representing the $t \to d$ and $b \to u$ transitions. Thus, b-hadron decays are particularly suited for the experimental study of $\mathcal{C}P$ violation effects.

Mode	Topology contribution	Mode	Topology contribution
$B^0 \to \pi^+\pi^-$	$T + P + \frac{2}{3}P^C_{EW} + PA + E$	$B^0_s \to \pi^+\pi^-$	PA, E
$B^0 \to K^+\pi^-$	$T + P + \frac{2}{3}P^C_{EW}$	$B^0_s \to K^-\pi^+$	$T + P + \frac{2}{3}P^C_{EW}$
$B^0 \to K^+K^-$	PA, E	$B^0_s \to K^+K^-$	$T + P + \frac{2}{3}P^C_{EW} + PA + E$

Table 1.2: Diagrams contributing to the amplitudes of each charmless $B^0_{(s)}$ decay into to two charged mesons. See text for the definitions.

1.3 Decays of b–mesons

The b-meson system consists of charged and neutral B mesons, which are characterized by the following valence-quark contents:

$$\begin{array}{llll} B^+ \sim u\bar{b}, & B^+_c \sim c\bar{b}, & B^0_d \sim d\bar{b}, & B^0_s \sim s\bar{b}, \\ B^- \sim \bar{u}b, & B^-_c \sim \bar{c}b, & \bar{B}^0_d \sim \bar{d}b, & \bar{B}^0_s \sim \bar{s}b. \end{array} \tag{1.9}$$

As far as the weak decays of b–mesons are concerned, we distinguish between leptonic, semileptonic and non-leptonic transitions. The most complicated B decays are the non-leptonic transitions, which are mediated by $b \to q_1\,\bar{q}_2\,d\,(s)$ quark-level processes, with $q_1, q_2 \in \{u, d, c, s\}$. Non-leptonic two-body charmless decays are very interesting processes to study flavor physics in the b-meson sector. The large mass of the b-meson allows for several different channels, which provide multiple ways for testing the consistency of the Standard Model interpretation of $\mathcal{C}P$ violation. For each channel, observables include the $\mathcal{C}P$-averaged branching fractions, the direct $\mathcal{C}P$-violating asymmetries and, for certain decays of neutral mesons, the mixing-induced $\mathcal{C}P$-violating asymmetry.

1.3.1 $B^0_{(s)} \to h^+h'^-$ decay modes

Among all the non-leptonic two-body charmless decays, we now focus on the topic of this work of thesis, that are the $B^0 \to \pi^+\pi^-$, $B^0 \to K^+\pi^-$, $B^0 \to K^+K^-$, $B^0_s \to \pi^+\pi^-$, $B^0_s \to K^-\pi^+$, and $B^0_s \to K^+K^-$ decay modes, collectively called $B^0_{(s)} \to h^+h'^-$ decay modes.

Amplitudes of $B^0_{(s)} \to h^+h'^-$ decays are dominated by $\bar{b} \to \bar{u}$ (tree-type) and $\bar{b} \to \bar{s}(\bar{d})$ (penguin-type) quark transitions (see figs. 1.2–1.5). The different $B^0_{(s)} \to h^+h'^-$ decay modes receive contributions from different transitions, summarized in tab. 1.2. The observed decay-rates are $\mathcal{O}(10^{-5})$ and smaller because the former processes involve leading-order diagrams that are CKM suppressed ($|V_{ub}| \ll |V_{cb}|$), while the latter involves higher-order diagrams.

In general, in order to analyse non-leptonic B decays theoretically, one uses low-energy effective Hamiltonians. The problem of calculating hadronic amplitudes is simplified by considering that there are two different scales involved: the scale

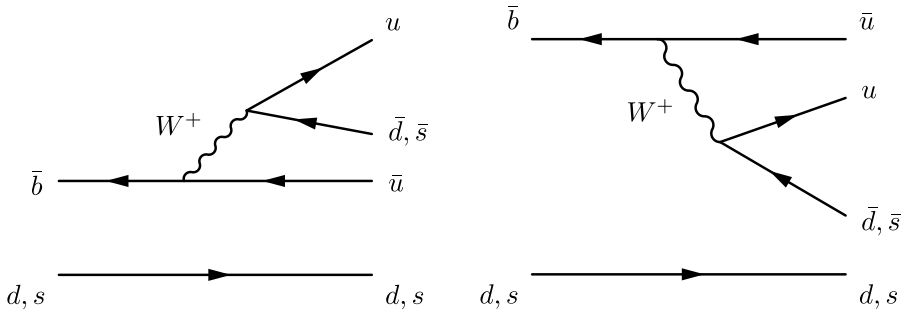

Figure 1.2: Color-allowed (left panel) and color suppressed (right panel) tree (T) diagrams contributing to $B \to h^+h^{'-}$ decays.

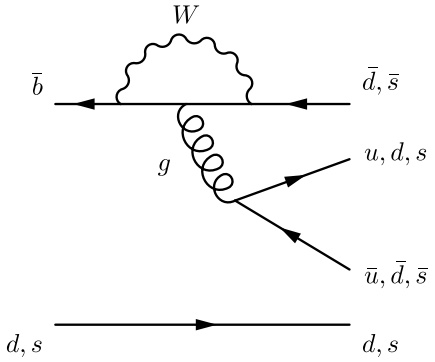

Figure 1.3: QCD penguin (P) diagram contributing to $B \to h^+h^{'-}$ decays.

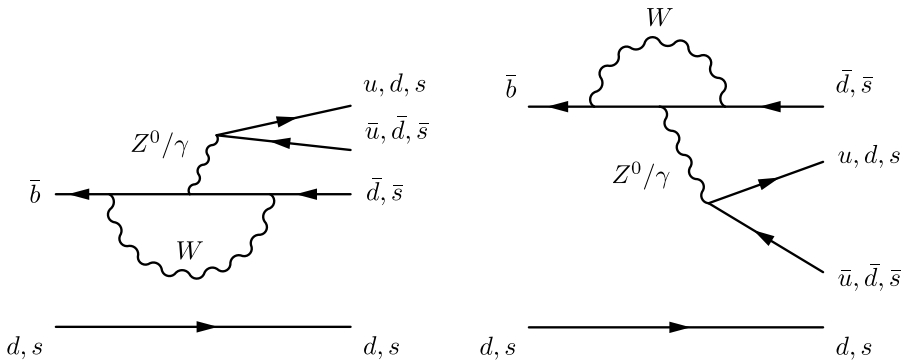

Figure 1.4: Color-allowed P_{EW} (left panel) and color suppressed P^C_{EW} (right panel) electroweak penguin diagrams contributing to $B \to h^+h^{'-}$ decays.

characterizing the electroweak interactions is $\mathcal{O}(100$ GeV), while the scale characterizing the hadronizations of quarks into hadrons is $\mathcal{O}(m_b)$. Given this difference, it is possible to factorize the problem using an "effective" hamiltonian approach. This effective theory is based on point-like interaction in analogy with the early

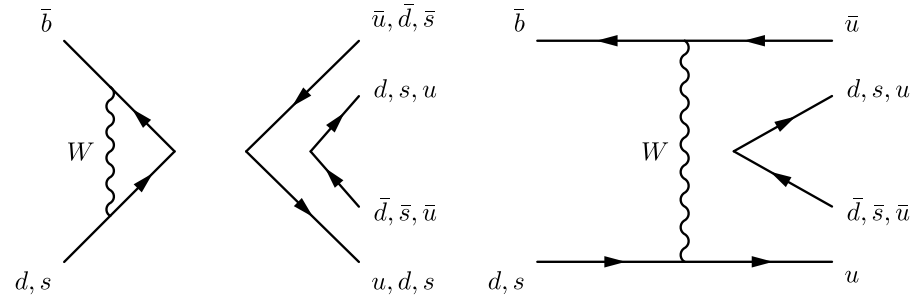

Figure 1.5: Penguin annihilation PA (left panel) and W − −exchange E (right panel) diagrams contributing to $B \to h^+ h'^-$ decays.

Fermi theory. Effective hamiltonians are calculated by making use of the OPE [18], "operator product expansion", yielding transition matrix elements of the following structure:

$$\langle f|\mathcal{H}_{\rm eff}|i\rangle = \frac{G_{\rm F}}{\sqrt{2}}\lambda_{\rm CKM}\sum_k C_k(\mu)\langle f|Q_k(\mu)|i\rangle. \tag{1.10}$$

Using this technique it is possible to separate the short-distance contributions, which are described by perturbative quantities $C_k(\mu)$ ("Wilson coefficient functions"), from the long-distance ones, described by non-perturbative quantities $\langle f|Q_k(\mu)|i\rangle$ ("hadronic matrix elements"). $G_{\rm F}$ is the Fermi constant, whereas $\lambda_{\rm CKM}$ is a CKM factor and μ denotes an appropriate renormalization scale appropriately chosen for the process of interest. $i\rangle$ and $\langle f|$ are the initial and final states. The Q_k are local operators, which are generated by electroweak interactions and QCD, and govern "effectively" the decay in question. The Wilson coefficients $C_k(\mu)$ can be considered as scale-dependent couplings related to the vertices described by the Q_k.

For the exploration of $\mathcal{C}P$ violation, the class of non-leptonic B decays that receives contributions both from tree and from penguin topologies plays a key rôle. If we apply the relation

$$V_{ur}^* V_{ub} + V_{cr}^* V_{cb} + V_{tr}^* V_{tb} = 0 \quad (r \in \{d, s\}), \tag{1.11}$$

which follows from the unitarity of the CKM matrix, and "integrate out" the top quark (which enters through the penguin loop processes) and the W boson, we may write

$$\mathcal{H}_{\rm eff} = \frac{G_{\rm F}}{\sqrt{2}}\left[\sum_{j=u,c} V_{jr}^* V_{jb}\left\{\sum_{k=1}^{2} C_k(\mu)\, Q_k^{jr} + \sum_{k=3}^{10} C_k(\mu)\, Q_k^{r}\right\}\right]. \tag{1.12}$$

Here we have introduced another quark-flavour label $j \in \{u, c\}$, and the Q_k^{jr} can be divided as follows:

- Current–current operators:

$$\begin{array}{rcl} Q_1^{jr} & = & (\bar{r}_\alpha j_\beta)_{\rm V-A}(\bar{j}_\beta b_\alpha)_{\rm V-A} \\ Q_2^{jr} & = & (\bar{r}_\alpha j_\alpha)_{\rm V-A}(\bar{j}_\beta b_\beta)_{\rm V-A}. \end{array} \tag{1.13}$$

- QCD penguin operators:

$$\begin{aligned} Q_3^r &= (\bar{r}_\alpha b_\alpha)_{\mathrm{V-A}} \sum_{q'} (\bar{q}'_\beta q'_\beta)_{\mathrm{V-A}} \\ Q_4^r &= (\bar{r}_\alpha b_\beta)_{\mathrm{V-A}} \sum_{q'} (\bar{q}'_\beta q'_\alpha)_{\mathrm{V-A}} \\ Q_5^r &= (\bar{r}_\alpha b_\alpha)_{\mathrm{V-A}} \sum_{q'} (\bar{q}'_\beta q'_\beta)_{\mathrm{V+A}} \\ Q_6^r &= (\bar{r}_\alpha b_\beta)_{\mathrm{V-A}} \sum_{q'} (\bar{q}'_\beta q'_\alpha)_{\mathrm{V+A}}. \end{aligned} \tag{1.14}$$

- EW penguin operators (the $e_{q'}$ denote the electrical quark charges):

$$\begin{aligned} Q_7^r &= \tfrac{3}{2}(\bar{r}_\alpha b_\alpha)_{\mathrm{V-A}} \sum_{q'} e_{q'} (\bar{q}'_\beta q'_\beta)_{\mathrm{V+A}} \\ Q_8^r &= \tfrac{3}{2}(\bar{r}_\alpha b_\beta)_{\mathrm{V-A}} \sum_{q'} e_{q'} (\bar{q}'_\beta q'_\alpha)_{\mathrm{V+A}} \\ Q_9^r &= \tfrac{3}{2}(\bar{r}_\alpha b_\alpha)_{\mathrm{V-A}} \sum_{q'} e_{q'} (\bar{q}'_\beta q'_\beta)_{\mathrm{V-A}} \\ Q_{10}^r &= \tfrac{3}{2}(\bar{r}_\alpha b_\beta)_{\mathrm{V-A}} \sum_{q'} e_{q'} (\bar{q}'_\beta q'_\alpha)_{\mathrm{V-A}}. \end{aligned} \tag{1.15}$$

The current–current, QCD and EW penguin operators are related to the tree, QCD and EW penguin processes with the same structure shown for the $B^0_{(s)} \to h^+ h'^-$ decays in figs. 1.2–1.5. At a renormalization scale $\mu = \mathcal{O}(m_b)$, the Wilson coefficients of the current–current operators are $C_1(\mu) = \mathcal{O}(10^{-1})$ and $C_2(\mu) = \mathcal{O}(1)$, whereas those of the penguin operators are $\mathcal{O}(10^{-2})$ [19, 20]. Note that penguin topologies with internal charm- and up-quark exchanges [21] are described in this framework by penguin-like matrix elements of the corresponding current–current operators [22], and may also have important phenomenological consequences [23, 24].

Since the ratio $\alpha/\alpha_s = \mathcal{O}(10^{-2})$ of the QED and QCD couplings is very small, we would expect naïvely that EW penguins should play a minor rôle in comparison with QCD penguins. This would actually be the case if the top quark was not "heavy". However, since the Wilson coefficient C_9 increases strongly with m_t, we obtain interesting EW penguin effects in several B decays: $B \to K\phi$ modes are affected significantly by EW penguins, whereas $B \to \pi\phi$ and $B_s \to \pi^0\phi$ transitions are even dominated by such topologies [25, 26]. EW penguins also have an important impact on the $B \to \pi K$ system [27].

The low-energy effective Hamiltonians discussed above apply to all B decays that are caused by the same quark-level transition, i.e. they are "universal". Consequently, the differences between the various exclusive modes of a given decay class arise within this formalism only through the hadronic matrix elements of the relevant four-quark operators. Unfortunately, the evaluation of such matrix elements is associated with large uncertainties and is a very challenging task. In this context, "factorization" is a widely used concept and has a long history [28]: during the time, several different approaches have been developed. The most commonly used are briefly described in the following.

1.4 Factorization approaches

1.4.1 QCD factorization

"QCD factorization" [29] is an approach developed in accordance with the old picture that factorization should hold for certain decays in the limit of $m_b \gg \Lambda_{\rm QCD}$ [30], provides a formalism to calculate the relevant amplitudes at the leading order of a $\Lambda_{\rm QCD}/m_b$ expansion. The resulting expression for the transition amplitudes incorporates elements both of the naive factorization approach sketched above and of the hard-scattering picture. Let us consider a decay $\bar{B} \to M_1 M_2$, where M_1 picks up the spectator quark. If M_1 is either a heavy (D) or a light (π, K) meson, and M_2 a light (π, K) meson, QCD factorization gives a transition amplitude of the following structure:

$$A(\bar{B} \to M_1 M_2) = [\text{"naive factorization"}] \times [1 + \mathcal{O}(\alpha_s) + \mathcal{O}(\Lambda_{\rm QCD}/m_b)]\,. \quad (1.16)$$

Several input parameters are needed, including quark masses, heavy-to-light form factors, light-cone distributions amplitudes etc. While the $\mathcal{O}(\alpha_s)$ terms, i.e. the radiative non-factorizable corrections, can be calculated systematically, the main limitation of the theoretical accuracy originates from the $\mathcal{O}(\Lambda_{\rm QCD}/m_b)$ terms. Infrared end-point logarithmic and linear divergences arise when calculating certain distributions, for example the penguin annihilation diagrams that are one of the topic of this thesis. In literature, this kind of linear divergences are typically treated extracting the divergence by introducing a parameter X_A:

$$\int_0^1 \frac{dy}{y} \Phi(y) \equiv X_A + c_1, \quad (1.17)$$

where Φ is a function of the amplitudes, X_A is an unknown parameter representing the soft gluon interaction with the quarks, c_1 is typically vanishing. Since the divergence is regulated by a physical scale of order $\mathcal{O}(\Lambda_{\rm QCD})$, X_A is treated as a complex number of order $\sim \ln(m_b/\Lambda_{\rm QCD})$. Logarithmic divergences are typically treated as follows:

$$\int_0^1 dy \frac{\ln y}{y} \to -\frac{1}{2}(X_A)^2. \quad (1.18)$$

These divergences usually need to be regularized parameterizing X_A from experimental results, thus introducing large uncertainties in the predictions. In the final chapter chap. 12 will see how thanks to our results several revisitations of the QCDF predictions have been performed in the last year. The benefits of the QCDF approach are that some of the hadronic parameters, namely ratios of tree-to-penguin amplitudes, strong phases, and corrections to form factors, are obtained from first principles and independently of models. However, the form factors evaluated at a point need to be determined from QCD sum-rules [31] or from data. QCDF predicts that most strong phases, being expansions in α_s, are suppressed. As a consequence, factorization small direct $\mathcal{C}P$ asymmetries, possibly in contrast with experimental data.

1.4.2 Perturbative QCD factorization

Another QCD approach to deal with non-leptonic B-meson decays, the "perturbative hard-scattering approach" (pQCD), was developed independently in [32], and differs from the QCD factorization formalism in some technical aspects. Form factors are assumed to have a perturbative expansion and the meson wave functions depend on transverse momenta. Non-perturbative parts are organized as universal hadron light-cone wave functions, which can be extracted from experimental data, constrained by lattice calculations or QCD sum-rules. It allows more stable treatment of end-point singularities arising when calculating non-factorizable and annihilation amplitudes with respect of the QCDF approach.

1.4.3 Other approaches

An interesting technique for "factorization proofs" is provided by the framework of the "soft collinear effective theory" (SCET) [33], which has received a lot of attention in the literature and led to various applications. It improves and generalizes QCDF approach allowing each of the scales m_b^2, Λ_{QCD}^2 etc. to be treated independently and factorization to be generalized to all orders of α_s.
Non-leptonic B decays can also be studied within QCD light-cone sum-rule approach [34].

1.5 $\mathcal{C}P$ violation in b-mesons

There are three kinds of $\mathcal{C}P$ violations:

- the direct $\mathcal{C}P$ violation: it occurs when the amplitude $A(i \to f)$ of a decay and the amplitude $A(\bar{i} \to \bar{f})$ of the $\mathcal{C}P$–conjugate eigenstate are different.

- the $\mathcal{C}P$ violation in the mixing: it occurs when the mass eigenstates and the $\mathcal{C}P$ eigenstates of a neutral meson are different.

- the $\mathcal{C}P$ violation in the interference between a decay without mixing, $B^0 \to f$ and a decay with mixing, $B^0 \to \bar{B}^0 \to f$.

The last two effects are usually referred to as "indirect" $\mathcal{C}P$ violation effects. Since the topics of this thesis are only the direct $\mathcal{C}P$ violation effects, we will report here a detailed description of this phenomenon.

Let us consider a non-leptonic decay $\bar{B} \to \bar{f}$ that is described by the low-energy effective Hamiltonian in (1.12). The corresponding decay amplitude is then given

as follows:

$$A(\bar{B}\to\bar{f}) = \langle\bar{f}|\mathcal{H}_{\rm eff}|\bar{B}\rangle$$
$$= \frac{G_{\rm F}}{\sqrt{2}}\left[\sum_{j=u,c} V_{jr}^* V_{jb}\left\{\sum_{k=1}^{2} C_k(\mu)\langle\bar{f}|Q_k^{jr}(\mu)|\bar{B}\rangle + \sum_{k=3}^{10} C_k(\mu)\langle\bar{f}|Q_k^{r}(\mu)|\bar{B}\rangle\right\}\right]. \quad (1.19)$$

Concerning the $\mathcal{CP}$-conjugate process $B\to f$, we have

$$A(B\to f) = \langle f|\mathcal{H}_{\rm eff}^{\dagger}|B\rangle$$
$$= \frac{G_{\rm F}}{\sqrt{2}}\left[\sum_{j=u,c} V_{jr} V_{jb}^*\left\{\sum_{k=1}^{2} C_k(\mu)\langle f|Q_k^{jr\dagger}(\mu)|B\rangle + \sum_{k=3}^{10} C_k(\mu)\langle f|Q_k^{r\dagger}(\mu)|B\rangle\right\}\right] \quad (1.20)$$

If we use now that strong interactions are invariant under $\mathcal{CP}$ transformations, insert $(\mathcal{CP})^\dagger(\mathcal{CP}) = \hat{1}$ both after the $\langle f|$ and in front of the $|B\rangle$, and take the relation

$$(\mathcal{CP})Q_k^{jr\dagger}(\mathcal{CP})^\dagger = Q_k^{jr} \quad (1.21)$$

into account, we arrive at

$$A(B\to f) = e^{i[\phi_{\rm CP}(B)-\phi_{\rm CP}(f)]}$$
$$\times\frac{G_{\rm F}}{\sqrt{2}}\left[\sum_{j=u,c} V_{jr} V_{jb}^*\left\{\sum_{k=1}^{2} C_k(\mu)\langle\bar{f}|Q_k^{jr}(\mu)|\bar{B}\rangle + \sum_{k=3}^{10} C_k(\mu)\langle\bar{f}|Q_k^{r}(\mu)|\bar{B}\rangle\right\}\right], \quad (1.22)$$

where the convention-dependent phases $\phi_{\rm CP}(B)$ and $\phi_{\rm CP}(f)$ are defined through

$$(\mathcal{CP})|B\rangle = e^{i\phi_{\rm CP}(B)}|\bar{B}\rangle, \quad (\mathcal{CP})|f\rangle = e^{i\phi_{\rm CP}(f)}|\bar{f}\rangle. \quad (1.23)$$

Consequently, we may write

$$A(\bar{B}\to\bar{f}) = e^{+i\varphi_1}|A_1|e^{i\delta_1} + e^{+i\varphi_2}|A_2|e^{i\delta_2} \quad (1.24)$$
$$A(B\to f) = e^{i[\phi_{\rm CP}(B)-\phi_{\rm CP}(f)]}\left[e^{-i\varphi_1}|A_1|e^{i\delta_1} + e^{-i\varphi_2}|A_2|e^{i\delta_2}\right]. \quad (1.25)$$

Here the $\mathcal{CP}$-violating phases $\varphi_{1,2}$ originate from the CKM factors $V_{jr}^* V_{jb}$, and the $\mathcal{CP}$-conserving "strong" amplitudes $|A_{1,2}|e^{i\delta_{1,2}}$ involve the hadronic matrix elements of the four-quark operators. In fact, these expressions are the most general forms of any non-leptonic B-decay amplitude in the SM, i.e. they do not only refer to the $\Delta C = \Delta U = 0$ case described by (1.12). Using (1.24) and (1.25), we obtain the following $\mathcal{CP}$ asymmetry:

$$\mathcal{A}_{\rm CP} \equiv \frac{\Gamma(B\to f)-\Gamma(\bar{B}\to\bar{f})}{\Gamma(B\to f)+\Gamma(\bar{B}\to\bar{f})} = \frac{|A(B\to f)|^2-|A(\bar{B}\to\bar{f})|^2}{|A(B\to f)|^2+|A(\bar{B}\to\bar{f})|^2}$$
$$= \frac{2|A_1||A_2|\sin(\delta_1-\delta_2)\sin(\varphi_1-\varphi_2)}{|A_1|^2+2|A_1||A_2|\cos(\delta_1-\delta_2)\cos(\varphi_1-\varphi_2)+|A_2|^2}. \quad (1.26)$$

We observe that a non-vanishing value can be generated through the interference between the two weak amplitudes, provided both a non-trivial weak phase difference

$\mathcal{A}_{\mathcal{C}P}$	BABAR	Belle	CDF
$B^0 \to K^+\pi^-$	$-10.7 \pm 1.6^{+0.6}_{-0.4}$	$-9.4 \pm 1.8 \pm 0.8$	$-8.6 \pm 2.3 \pm 0.9$
$B^0_s \to K^-\pi^+$	–	–	$39 \pm 15 \pm 8$
$\Lambda^0_b \to pK^-$	–	–	$3 \pm 15 \pm 8$
$\Lambda^0_b \to p\pi^-$	–	–	$37 \pm 17 \pm 3$

Table 1.3: Summary of $\mathcal{A}_{\mathcal{C}P}$ of $B \to h^+h'^-$ decays in unit of % at the time of the analysis from Babar [35], Belle [36], CDF[37].

Mode	BABAR	Belle	CDF
$B^0 \to \pi^+\pi^-$	$5.5 \pm 0.4 \pm 0.3$	$5.1 \pm 0.2 \pm 0.2$	$5.10 \pm 0.33 \pm 0.36$†
$B^0 \to K^+\pi^-$	$19.1 \pm 0.6 \pm 0.6$	$19.9 \pm 0.4 \pm 0.8$	–
$B^0 \to K^+K^-$	$0.04 \pm 0.15 \pm 0.08$	$0.09^{+0.18}_{-0.13} \pm 0.01$	$0.39 \pm 0.16 \pm 0.12$†
$B^0_s \to \pi^+\pi^-$	–	< 12	< 1.2†
$B^0_s \to K^-\pi^+$	–	< 26	$5.0 \pm 0.7 \pm 0.8$†
$B^0_s \to K^+K^-$	–	$38^{+10}_{-9} \pm 7$	$24.4 \pm 1.4 \pm 4.6$†
$\Lambda^0_b \to p\pi^-$	–	–	$3.5 \pm 0.6 \pm 0.9$†
$\Lambda^0_b \to pK^-$	–	–	$5.6 \pm 0.8 \pm 1.5$†

Table 1.4: Summary of branching fractions in unit 10^{-6} of $B \to h^+h'^-$ decays at the time of the analysis from Babar [38], Belle [39, 40, 41], CDF[42, 43]. The symbol † labels the case when the relative branching fraction is converted to absolute branching fraction.

$\varphi_1 - \varphi_2$ and a non-trivial strong phase difference $\delta_1 - \delta_2$ are present. This kind of $\mathcal{C}P$ violation is referred to as "direct" $\mathcal{C}P$ violation, as it originates directly at the amplitude level of the considered decay. It is the B-meson counterpart of the effects that are probed through $\mathrm{Re}(\varepsilon'/\varepsilon)$ in the neutral kaon system,[1] and have been established with the help of $B^0 \to \pi^\mp K^\pm$ decays [44].

1.6 $\mathcal{A}_{\mathcal{C}P}(B \to h^+h'^-)$ measurements motivations

One of the topics of this work is the measurement of the $\mathcal{C}P$ violation of $B^0 \to K^+\pi^-$, $B^0_s \to K^-\pi^+$, $\Lambda^0_b \to p\pi^-$, and $\Lambda^0_b \to pK^-$ decay modes. The experimental situation at the time of the analysis is reported in tab. 1.3. The $\mathcal{A}_{\mathcal{C}P}(B^0 \to K^+\pi^-)$ was measured at b-factories with significance $> 5\sigma$, while the $\mathcal{A}_{\mathcal{C}P}(B^0_s \to K^-\pi^+)$, $\mathcal{A}_{\mathcal{C}P}(\Lambda^0_b \to p\pi^-)$, and $\mathcal{A}_{\mathcal{C}P}(\Lambda^0_b \to pK^-)$ were measured only at CDF, but they have not yet been observed. The study of this effect in less investigated areas, such as the

[1] In order to calculate this quantity, an appropriate low-energy effective Hamiltonian having the same structure as (1.12) is used.

D^0 and the B_s^0 sectors, is a very important field of research. Experimental results that deviates from predictions are the way to increase our understanding of the whole Standard Model framework. Actually, unexpected hints of $\mathcal{C}P$ violation in the D^0 system seem to have been found recently. Thus, nowadays is the adequate period to increase the effort in these kind of analysis in new windows, such as B_s^0 and Λ_b^0 sectors.

1.6.1 $\mathcal{A}_{\mathcal{C}P}(B^0 \to K^+\pi^-)$

The $B^0 \to K^+\pi^-$ decay mode receives contributions from penguin and tree topologies. Within the usual formalism the decay amplitude can be written as follows:

$$A(B^0 \to K^+\pi^-) = -P\left[1 - re^{i\delta}e^{i\gamma}\right], \tag{1.27}$$

where P describes the penguin amplitudes, r is the amplitude ratio between tree and penguin amplitudes, γ is the $\mathcal{C}P$ hadronic phase. The quark level transition originate from $\bar{b} \to \bar{u}u\bar{s}$, and contains a factor $V_{ub}^*V_{us}$. The penguin amplitude are dominated by a loop involving the t quark, thus the CKM factor is $V_{tb}^*V_{ts}$. Because the ratio $V_{ub}^*V_{us}/V_{tb}^*V_{ts} \approx 0.02$, the QCD penguin amplitudes are expected to dominate the $B^0 \to K^+\pi^-$ decay mode. EW penguin topologies are color–suppressed. In general, it can be observed that the feature of the dominance of QCD penguins applies to all $B \to \pi K$ modes. In particular, for both the $B^0 \to K^+\pi^-$ and $B^+ \to K^+\pi^0$ decays, EW penguins contribute in color–suppressed form and are hence expected to play a minor rôle. In this assumption, the $\mathcal{C}P$ asymmetry of the $B^+ \to K^+\pi^0$ is expected to be equal to the direct $\mathcal{C}P$ asymmetry in the $B^0 \to K^+\pi^-$ mode [6, 45, 46]. The experimental results [47], however, differ with a significance of more than 5σ.

$$\begin{aligned} \mathcal{A}_{\mathrm{CP}}^{\mathrm{dir}}(B^+ \to K^+\pi^0) &= +0.040 \pm 0.021 \\ \mathcal{A}_{\mathrm{CP}}^{\mathrm{dir}}(B^0 \to K^+\pi^-) &= -0.087 \pm 0.008 \end{aligned}$$

This has been for long time a puzzling discrepancy, and has been named the $K\pi$ puzzle. Simple extensions of the standard model could accommodate the discrepancy [48], but uncertainty on the contribution of higher-order SM amplitudes has prevented a firm conclusion [49]. Recently, Lipkin suggested a way [50] to accommodate this discrepancy within the SM, but ultimately the question about a possible NP explanation of this discrepancy is still open. High accuracy measurements of the violation of $\mathcal{C}P$ symmetry in charmless modes remains a very interesting subject of study and may provide useful information to our comprehension of this discrepancy.

1.6.2 $\mathcal{A}_{\mathcal{C}P}(B_s^0 \to K^-\pi^+)$

The $B_s^0 \to K^-\pi^+$ decay mode originates from a $\bar{b} \to \bar{d}$ transition, and it receives contributions from penguin and tree topologies. Within the usual formalism, the

decay amplitude can be written as follows:

$$A(B_s^0 \to K^-\pi^+) = P_s\sqrt{\epsilon}\left[1 - \frac{1}{\epsilon}r_s e^{i\delta_s}e^{i\gamma}\right] \tag{1.28}$$

Being the $B_s^0 \to K^-\pi^+$ the U–spin partner of the $B^0 \to K^+\pi^-$, the measurements of direct $\mathcal{C}P$ violation in $B_s^0 \to K^-\pi^+$ decays have been proposed as a nearly model-independent test for the presence of non-SM physics [4, 5]. The relationships between charged-current quark couplings in the SM predict a well-defined hierarchy between direct $\mathcal{C}P$ violation in $B^0 \to K^+\pi^-$ and $B_s^0 \to K^-\pi^+$ decays:

$$\Gamma(B_s^0 \to K^-\pi^+) - \Gamma(\overline{B}_s^0 \to K^+\pi^-) = \Gamma(\overline{B}^0 \to K^-\pi^+) - \Gamma(B^0 \to K^+\pi^-), \tag{1.29}$$

$$\mathcal{A}_{\mathcal{C}P}(B_s^0 \to K^-\pi^+) = -\mathcal{A}_{\mathcal{C}P}(B^0 \to K^+\pi^-) \times \frac{\mathcal{B}(B^0 \to K^+\pi^-)}{\mathcal{B}(B_s^0 \to K^-\pi^+)} \times \frac{\tau(B_s^0)}{\tau(B^0)}. \tag{1.30}$$

Using the $\mathcal{A}_{\mathcal{C}P}(B^0 \to K^+\pi^-) = -0.087 \pm 0.008$ average from the experimental measurements [47], $\mathcal{B}(B_s^0 \to K^-\pi^+) = (5.4 \pm 0.6) \times 10^{-6}$ and $\mathcal{B}(B^0 \to K^+\pi^-) = (19.55^{+0.54}_{-0.53}) \times 10^{-6}$ from [47], $\tau(B^0) = (1.519 \pm 0.007) \times 10^{-12}$ and $\tau(B_s^0) = (1.497 \pm 0.015) \times 10^{-12}$ from [51], eq. (12.11) predicts:

$$\mathcal{A}_{\mathcal{C}P}(B_s^0 \to K^-\pi^+)|^{SM} = 0.31 \pm 0.04. \tag{1.31}$$

The resulting $\mathcal{A}_{\mathcal{C}P}(B_s^0 \to K^-\pi^+)$ is a significant asymmetry of about 30%. Assuming this relationship valid only within the SM, a different configuration would be due to the presence of a different source of $\mathcal{C}P$ from NP. In addition, this large effect allows easier experimental investigations: at the time of the analysis, this $\mathcal{C}P$ violation was not yet observed and it is one of the topic of this thesis.

1.6.3 $\mathcal{A}_{\mathcal{C}P}(\Lambda_b^0 \to p\pi^-)$ and $\mathcal{A}_{\mathcal{C}P}(\Lambda_b^0 \to pK^-)$

The Λ_b^0 baryon is described by:

$$\Lambda_b^0 \sim bud \tag{1.32}$$

In a naive factorization approach the $\Lambda_b^0 \to p\pi^-$ and $\Lambda_b^0 \to pK^-$ are described in a similar way with respect to the b-mesons. The diagrams describing the transitions are the same as figs. 1.2–1.4 with the difference of having two spectator quarks (ud or $\bar{u}\bar{d}$) instead of only one quark. Using factorization it is possible to write an effective Hamiltonian as follows:

$$\mathcal{H}_{\text{eff}} = \frac{G_{\text{F}}}{\sqrt{2}}\left[V_{ub}V_{uq}^*\left\{C_1(\mu)Q_1^u(\mu) + C_2(\mu)O_2^u(\mu) - V_{tb}V_{tq}^*\sum_{i=3}^{10}C_i(\mu)O_i(\mu)\right\}\right] + h.c. \tag{1.33}$$

where $q = d, s$ and $C_i(\mu)$ are the Wilson coefficients for different transitions, evaluated at the renormalization scale μ. The first two elements are related to tree

diagrams, the sum is over QCD and electroweak penguins. The $\Lambda_b^0 \to p\pi^-$ is mediated by the $b \to u\bar{u}d$ tree or by a $b \to d$ penguin. On the contrary, the $\Lambda_b^0 \to pK^-$ is mediated by the $b \to u\bar{u}s$ tree or by a $b \to s$ penguin. Thus for the $\Lambda_b^0 \to p\pi^-$ the dominant contribution is expected to be from tree diagrams, while for the $\Lambda_b^0 \to pK^-$ the penguin QCD diagram is supposed to be the dominant one. While over the past two decades the b-meson $\mathcal{C}P$ asymmetries has been deeply and methodically investigated at the b-factories, the b-baryon system represents a new window to look at. The measurement of the $\mathcal{C}P$ violation in the $\Lambda_b^0 \to p\pi^-$ decay can be sensitive to NP in the Minimal Supersymmetric Standard Model (MSSM). SM predicts values of O(8%), while in R–parity violating MSSM scenarios [52]. suppressed values ($\approx 0.3\%$) are expected. Recent pQCD calculations [53], with large theoretical uncertainties, predict a central value of $\mathcal{A}_{\mathcal{C}P}(\Lambda_b^0 \to pK^-) \approx +5\%$, while the expected central value for the $\mathcal{A}_{\mathcal{C}P}(\Lambda_b^0 \to p\pi^-)$ is about $+30\%$.

1.7 $B^0_{(s)} \to h^+h'^-$ annihilation measurements motivations

The $B_s^0 \to \pi^+\pi^-$ and $B^0 \to K^+K^-$ decay modes are of special interest: all quarks in the final state are different from those in the initial state, so they can be mediated solely by amplitudes with penguin-annihilation (PA) and W-exchange (E) topologies (see fig. 1.6). They resisted attempts at quantitative prediction up to the present, and they are often simply neglected in calculations. Predictions for these amplitudes vary greatly between approaches, and even within the same approach. Estimates based on the QCDF approach are affected by significant uncertainties, due to end-point singularities. For the $B_s^0 \to \pi^+\pi^-$, Beneke et all [7] parameterize the divergent integral arising in the term $\mathcal{O}(\Lambda_{\rm QCD}/m_b)$ of eq. (1.17) using:

$$X_s^{PP} = (1 + \rho_s^{PP} e^{i\phi_s^{PP}}) \ln \frac{m_b}{\Lambda_h} \qquad \rho_s^{PP} \leq 1, \Lambda_h = 0.5 \text{ GeV} \tag{1.34}$$

where ϕ_s^{PP} is an arbitrary strong-interaction phase which may be coming from soft scattering, m_b and Λ_h are the normalization scales, and ρ_s^{PP} is a parameter coming from experimental constraints. Thus Beneke et al. predict $\mathcal{B}(B_s^0 \to \pi^+\pi^-) = (0.024^{+0.165}_{-0.024}) \times 10^{-6}$ and $\mathcal{B}(B^0 \to K^+K^-) = (0.013^{+0.087}_{-0.013}) \times 10^{-6}$ [7], in agreement with Yang et al., that also used QCDF but with a different solution to avoid end-point divergences, obtaining $\mathcal{B}(B_s^0 \to \pi^+\pi^-) = (0.124 \pm 0.028) \times 10^{-6}$ [54]. It can be noted as several approaches from QCDF, with different parameterization inputs, predict different central values ($\mathcal{B}(B_s^0 \to \pi^+\pi^-) = (0.26^{+0.01}_{-0.09}) \times 10^{-6}$ and $\mathcal{B}(B^0 \to K^+K^-) = (0.10^{+0.04}_{-0.04}) \times 10^{-6}$ [55] or $\mathcal{B}(B_s^0 \to \pi^+\pi^-) = 0.022 \times 10^{-6}$ [56]).

More recent perturbative QCD calculations (pQCD) provide more precise predictions, but they tend to be significantly larger than the predictions coming from QCDF: Ali et al. predict $\mathcal{B}(B_s^0 \to \pi^+\pi^-) = (0.57^{+0.18}_{-0.16}) \times 10^{-6}$ [57]; in the same approach Li, Lu, Xiao, and Yu calculate $\mathcal{B}(B_s^0 \to \pi^+\pi^-) = (0.42 \pm 0.06) \times 10^{-6}$, but with Sudakov resummation, and including contributions from electroweak and QCD

penguin amplitudes [58]. As a general comment, it can be noted in tab. 1.5 how the QCDF predictions are systematically lower than the pQCD ones. No calculations are yet available within the soft collinear effective theory (SCET) [59].

Mode	QCDF	pQCD
$B_s^0 \to \pi^+\pi^-$	$0.024^{+0.165}_{-0.024}$[7]	$0.57^{+0.18}_{-0.16}$ [57]
	0.124 ± 0.028 [54]	0.42 ± 0.06 [58]
	$0.26^{+0.01}_{-0.09}$ [55]	
	0.022[56]	
$B^0 \to K^+K^-$	$0.013^{+0.087}_{-0.013}$[7]	
	$0.10^{+0.04}_{-0.04}$ [55]	

Table 1.5: $\mathcal{B}(B_s^0 \to \pi^+\pi^-)$ and $\mathcal{B}(B^0 \to K^+K^-)$ theoretical prediction for different pQCD and QCDF approaches.

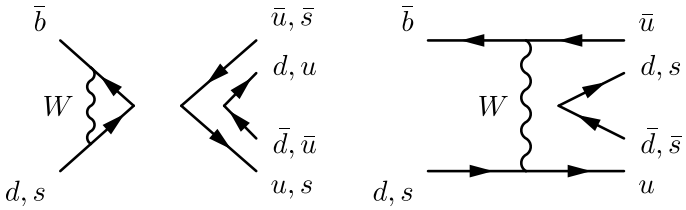

Figure 1.6: *PA* (left panel) and *E* (right panel) diagrams contributing to $B^0 \to K^+K^-$ and $B_s^0 \to \pi^+\pi^-$ decays.

The lack of knowledge of the size of annihilation-type amplitudes introduces irreducible uncertainties in the predictions for several decays of great interest in the search for new physics effects, such as $B^0 \to \pi^+\pi^-$ and $B_s^0 \to K^+K^-$ [60, 61, 62, 63]. Experimental investigation of the issue is therefore very desirable, and has the potential to enable a significant advancement of the field. A simultaneous measurement of branching fractions of both modes would be especially useful, as it would allow a better constraint on the strength of *PA* and *E* amplitudes [61] and would help to improve the pQCD and QCDF approaches calculations. At the time of the analysis, they have not yet been observed, the best upper limits at 90% CL being respectively 1.2×10^{-6} [42] and 0.41×10^{-6} [40]. The experimental situation of all the $B \to h^+h'^-$ decay modes at the time of the analysis is reported in tab. 1.4.

1.8 Current experimental status

If the *b*-hadrons experimental measurements were represented in a comedy drama, we would see different comedians playing in the stage. The main actors have been

for long time the two asymmetric e^+e^- b-factories at SLAC and KEK with their detectors BaBar and Belle, respectively. The second act of the play was represented at the Tevatron of Fermilab, where the CDF and D0 collaboration were able to produce relevant B-physics results. This was the experimental status at the time of the analysis, back in 2010. With about 9 fb^{-1} of data available, we expected to perform $\mathcal{A}_{CP}(B_s^0 \to K^-\pi^+)$, $\mathcal{A}_{CP}(\Lambda_b^0 \to p\pi^-)$ and $\mathcal{A}_{CP}(\Lambda_b^0 \to ph^-)$ measurements with a resolution of order 10%, and hopefully to obtain a first evidence for the $B_s^0 \to K^-\pi^+$ measurement. The goal was also to perform updated measurements of $\mathcal{A}_{CP}(B^0 \to K^+\pi^-)$ and of branching ratios, in particular for the yet unobserved annihilation modes. Starting 2011, new players from the LHC experiment at CERN entered the stage: in particular the LHCb experiment, devoted to the b-physics, becomes in a short time a main character. In addition, the b-factories refined their measurement strategies and provided updated results. The experimental status at the time of writing this thesis is reported in tab. 1.6 and tab. 1.7.

$\mathcal{A}_{CP}$	BABAR	Belle	CDF	LHCb
$B^0 \to K^+\pi^-$	$-10.7 \pm 1.6^{+0.6}_{-0.4}$	$-6.9 \pm 1.4 \pm 0.7$	$-8.6 \pm 2.3 \pm 0.9$	$-8.0 \pm 0.7 \pm 0.3$
$B_s^0 \to K^-\pi^+$	–	–	$39 \pm 15 \pm 8$	$27 \pm 4 \pm 1$
$\Lambda_b^0 \to pK^-$	–	–	$3 \pm 15 \pm 8$	–
$\Lambda_b^0 \to p\pi^-$	–	–	$37 \pm 17 \pm 3$	–

Table 1.6: Summary of $\mathcal{A}_{CP}$ of $B \to h^+h'^-$ decays in unit of % at the time of writing this thesis from Babar [35], Belle [64], CDF[37], LHCb[9].

Mode	BABAR	Belle	CDF	LHCb
$B^0 \to \pi^+\pi^-$	$5.5 \pm 0.4 \pm 0.3$	$5.0 \pm 0.2 \pm 0.2$	$5.0 \pm 0.3 \pm 0.3$†	$5.1 \pm 0.2 \pm 0.4$†
$B^0 \to K^+\pi^-$	$19.1 \pm 0.6 \pm 0.6$	$20.0 \pm 0.3 \pm 0.6$	–	–
$B^0 \to K^+K^-$	$0.04 \pm 0.15 \pm 0.08$	$0.09^{+0.18}_{-0.13} \pm 0.01$	$0.39 \pm 0.16 \pm 0.12$†	$0.11^{+0.05}_{-0.04} \pm 0.06$†
$B_s^0 \to \pi^+\pi^-$	–	< 12	< 1.2†	$0.95^{+0.21}_{-0.17} \pm 0.13$†
$B_s^0 \to K^-\pi^+$	–	< 26	$5.0 \pm 0.7 \pm 0.8$†	$5.4 \pm 0.4 \pm 0.6$†
$B_s^0 \to K^+K^-$	–	$38^{+10}_{-9} \pm 7$	$24.4 \pm 1.4 \pm 4.6$†	$23.0 \pm 0.7 \pm 2.3$†
$\Lambda_b^0 \to p\pi^-$	–	–	$3.5 \pm 0.6 \pm 0.9$†	–
$\Lambda_b^0 \to pK^-$	–	–	$5.6 \pm 0.8 \pm 1.5$†	–

Table 1.7: Summary of branching fractions in unit 10^{-6} of $B \to h^+h'^-$ decays at the time of writing the thesis from Babar [38], Belle [64, 39, 40, 41], CDF[42, 43] and LHCb[65]. The symbol † labels the case when the relative branching fraction is converted to absolute branching fraction.

Chapter 2

Experimental apparatus

This chapter describes the CDF II detector at the Fermilab TeVatron collider, used to collect the data analyzed in this work. We focused on the description of the tracking and the trigger system, for the crucial role they play in the analysis. A detailed description of the experimental apparatus can be found in Ref. [66].

2.1 The TeVatron collider

The Fermilab TeVatron was the world most powerful proton-antiproton collider, until the last collision occurred on September 30th, 2011. The TeVatron is located at the Fermi National Accelerator Laboratory (FNAL or Fermilab), about 50 km West from Chicago, Illinois, United States. It is an underground circular proton synchrotron 1 km in radius and represents the last stage of a system of accelerators, storage rings and transfer lines. While operating in collider mode, it collides bunches[1] of protons, circulating clockwise, against anti-protons accelerated counter-clockwise, both at energies of 980 GeV. The available center of mass energy $\sqrt{s}$ is thus equal to 1.96 TeV. The TeVatron produced its first collisions in 1985 and since then various periods of collider operations alternated with fixed-target operations and shut-down periods for the upgrades of the machine. The TeVatron collider operations periods are conventionally identified as a "Run": Run I, from 1992 to 1996, and Run II, from 2001 to the last collision. Between the two Runs the two detectors installed at TeVatron (called CDF and D0) undergone the most extensive upgrades. Table 2.1 reports a summary of the TeVatron operations and performances since its construction, dated back in 1983, until the last collision, on September 30th, 2011.

The performance of the TeVatron collider is evaluated in terms of two key parameters. The first is the center of mass energy $\sqrt{s}$ that defines the accessible phase-space for the production of resonances in the final states. The second is the instantaneous luminosity $\mathcal{L}$ that represents the coefficient of proportionality between the rate of a given process and its cross-section σ:

[1] A bunch is a collection of particles with the same energy gathered togheter.

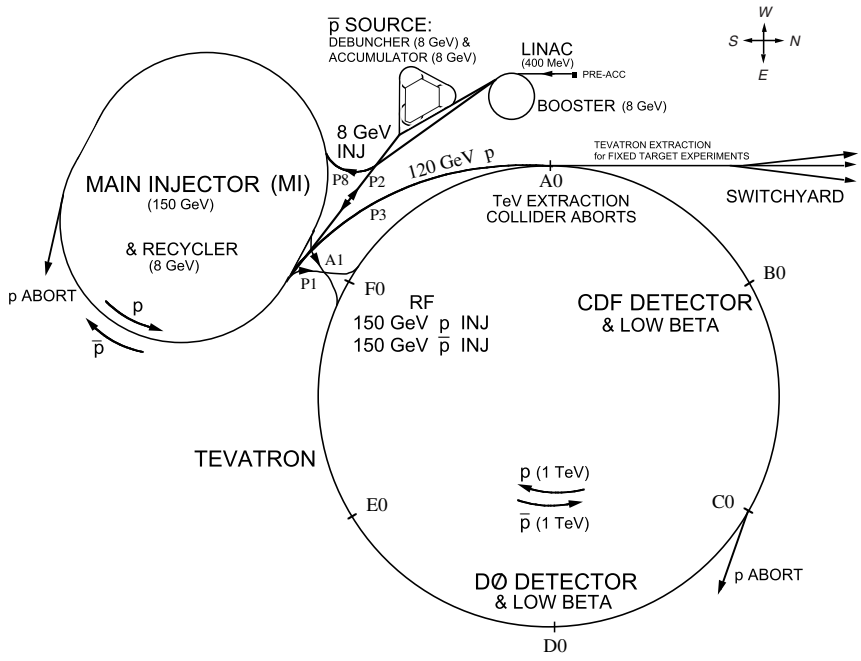

Figure 2.1: Illustration of the Fermilab TeVatron collider.

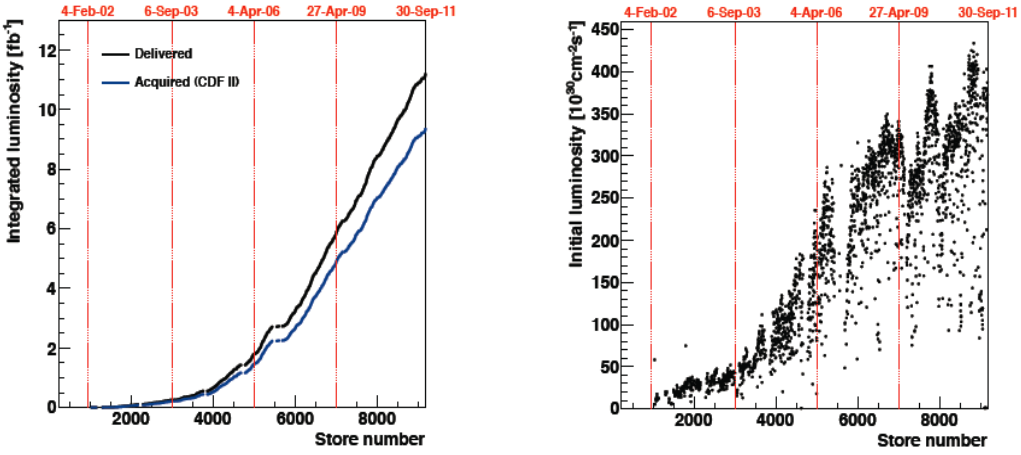

Figure 2.2: Integrated luminosity as a function of the time (or store number) (a). Initial luminosity as a function of the time (or store number) (b).

$$\text{rate [events s}^{-1}] = \mathcal{L}\ [\text{cm}^{-2}\text{s}^{-1}]\ \times\ \sigma\ [\text{cm}^2].$$

The time-integral of the luminosity (integrated luminosity) is therefore a measure of the expected number of events, n, produced in a finite time T:

$$n(T) = \int_0^T \mathcal{L}\sigma dt. \tag{2.1}$$

Date		$\sqrt{s}$[TeV]	$\mathcal{L}$[cm^{-2}s^{-1}]	$\int \mathcal{L}dt$ [pb]$^{-1}$
Mar 1983	End of the construction	-	-	-
Jul 1983	Proton energy 512 GeV	-	-	-
Oct 1983	fixed target program began	-	-	-
Feb 1984	Proton energy 800 GeV	-	-	-
Oct 1985	First $p\bar{p}$ collisions observed	1.6	10^{24}	-
Oct 1986	Proton energy 800 GeV	-	-	-
Jun 1988 -				
May 1989	Run 0	1.8	0.02×10^{32}	~ 4.5
1989-1992	Detectors upgrades	-	-	-
Aug 1992-				
Feb 1996	Run I	1.8/0.63	0.28×10^{32}	~ 180
Aug 2000	Beam energy 980 GeV	-	-	-
Mar 2001-				
Sep 2011	Run II	1.96	3.6×10^{32}	~ 10.000

Table 2.1: Chronological overview of the TeVatron operations and performance. The third column shows the peak luminosity.

Assuming an ideal head-on $p\bar{p}$ collision with no crossing angle between the beams, the instantaneous luminosity is defined as

$$\mathcal{L} = 10^{-5} \frac{N_p N_{\bar{p}} B f \beta\gamma}{2\pi\beta^* \sqrt{(\epsilon_p + \epsilon_{\bar{p}})_x (\epsilon_p + \epsilon_{\bar{p}})_y}} \mathcal{H}(\sigma_z/\beta^*) \qquad [10^{30}\text{cm}^{-2}\text{s}^{-1}]. \quad (2.2)$$

$\mathcal{L}$ depends on the following TeVatron parameters: the number of circulating bunches in the ring ($B = 36$), the revolution frequency ($f = 47.713$ kHz), the Lorentz relativistic factor (boost, $\beta\gamma = 1045.8$ at 980 GeV), the average numbers of protons ($N_p \approx 250\times10^9$) and antiprotons ($N_{\bar{p}} \approx 25\times10^9$) in a bunch, an empiric "hourglass" factor ($\mathcal{H} = 0.6$–0.7), which is a function of the ratio between the longitudinal r.m.s. width of the bunch ($\sigma_z \approx 60$ cm) and the "beta function" calculated at the interaction point ($\beta^* \approx 31$ cm), and the 95% normalized emittances of the beams ($\epsilon_p \approx 18\pi$ mm mrad and $\epsilon_{\bar{p}} \approx 13\pi$ mm mrad after injection).[2] At the TeVatron the limiting factor of the luminosity is the availability of antiprotons because it

[2]The hourglass factor is a parameterization of the longitudinal profile of the beams in the collision region, which assumes the shape of an horizontal hourglass centered in the interaction region. The beta function is a parameter convenient for solving the equation of motion of a particle through an arbitrary beam transport system. The emittance ϵ measures the phase-space occupied by the particles of the beam. Three independent two-dimensional emittances are defined. The quantity $\sqrt{\beta\epsilon}$ is proportional to the r.m.s. width of the beam in the corresponding phase plane. On-line measurements of the transverse emittances are performed at the TeVatron with various methods, including flying through the beam a 7 μm wire and by measuring the cascade of losses, which is proportional to the beam intensity, or detecting the synchrotron light radiated by the particles at the edge of a dipole magnet.

is difficult to produce and to compact them into bunches and to transfer them efficiently through the subsequent accelerator stages.

The TeVatron is an approximately circular synchrotron using 772 dipole, 2 half-pole, and 204 quadrupole superconducting magnets. Each is approximately 6 m long, 4 tons in mass, and is made of NbTi alloy filaments embedded in copper, kept at 4.3 K temperature by a large cryogenic system. A 4400 A current flows through each magnet to produce the 4.2 T magnetic field necessary to keep the (anti)protons on their orbit, while they are accelerated by eight radio-frequency cavities (RF) driven at approximately 53.105 Hz. Motions or friction by the about 4000 N/cm of outward pressure are avoided by epoxy-covered steel collars bound around the magnets.

The TeVatron provides beams for experiments in different modes (fixed-target, collider, etc.). For the purpose of this analysis, we describe the procedure of obtaining a continuos period of collider operation using the same collection of protons and antiprotons, called a store. Additional details can be found in Ref. [67].

2.1.1 Proton beam

H^- ions are produced by ionization of gaseous hydrogen and boosted to 750 keV by a commercial Cockroft-Walton accelerator. The proton beam, segmented into bunches, is then injected in a 150 m long linear accelerator *Linac* which increases their energy to 400 MeV. A carbon foil is used to strip the electrons from the H^- before the resulting protons are injected to the *Booster*. The Booster (see fig. 2.1) is a rapid cycling synchrotron (radius of 75.5 m) that accelerates the protons up to 8 GeV and compacts them into bunches of about $5 \cdot 10^{12}$ particles each. The protons are then transfered to a synchrotron, called the *Main Injector*, which brings their energy to 150 GeV. The last stage of the process is the transfer to the TeVatron this is the beginning of the process of final injection into the TeVatron.

2.1.2 Antiproton beam

While the energy of the protons bunches circulating in the Main Injector reaches 120 GeV, they are slammed to a rotating 7 cm thick nickel or copper target to produce antiprotons. The target rotates to be more resistant to the radiation. Spatially wide-spread antiprotons are produced (about one antiproton for every 10^6 protons on target) and focused into a beam via a cylindrical lithium lens which separates $\bar{p}$ from other charged interaction products. The emerging antiprotons have a bunch structure similar to that of the incident protons and are stored in a *Debuncher*. It is a storage ring where the momentum spread of the $\bar{p}$ is reduced while maintaining a constant energy of 8 GeV, via stochastic cooling stations. Many cycles of Debuncher cause the destruction of the bunch structure which results in a continuous beam of antiprotons. At the end of the process the monochromatic antiprotons are stored

in the *Accumulator* (see fig. 2.1) which is a triangle-shaped storage ring where they are further cooled and stored until the cycles of the Debuncher are completed. After 20 hours the number of antiprotons accumulated is sufficient to create 36 bunches with the required density. At this point the accumulation process is stopped in preparation for injection.

2.1.3 The injection and the collisions

When the antiproton accumulation process is stopped, a set of seven proton bunches is extracted from the Booster and are transfered to a synchrotron, called the *Main Injector*, which brings their energy to 150 GeV. Here the seven bunches are coalesced into a single bunch of about 300 $\times 10^9$ protons, and then injected into the TeVatron. This process is repeated until 36 proton bunches, separated by 396 ns, are loaded into the TeVatron central orbit. The electrostatic separators (about 30 pairs of metal plates) are then activated in the TeVatron in preparation for antiproton injection.

Four sets of 7-11 antiproton bunches are extracted from the Accumulator to the Main Injector, accelerated to 150 GeV, coalesced into four 30 $\times 10^9$ antiproton bunches separated by 396 ns, and then injected into the TeVatron where protons are counter-rotating. Protons and antiprotons circulate in the same enclosure, sharing magnet and vacuum systems. The electrostatic separators minimize the beam-beam interactions, by keeping the protons and antiprotons beams into two non-intersecting closed helical orbits separated by about 5 millimeters. This allows controlling each beam nearly independently.

When 36 bunches of both protons and antiprotons are circulating in the TeVatron the energy of the machine is increased in about 10 seconds from 150 to 980 GeV and the collisions begin at the two interaction points: DØ (where the homonym detector is located) and BØ (home of CDF II). Special quadrupole magnets (*low-β squeezers*) located at both extremities of the detectors along the beam pipe "squeeze" the beam to maximize luminosity inside the detectors. A roughly Gaussian distribution of the interaction region along the beam axis is achieved ($\sigma_z \approx 28$ cm) and its center is shifted on the nominal interaction point by the fine tuning of squeezers. The transverse shape of the interaction region has an almost circular spatial distribution with a diameter of $\sigma_{\mathrm{T}} \approx 30$ μm. Luminosity lifetime is increased by using electrostatic separators which separate transversely the proton and antiproton bunches except at the collision regions. Then the *'scraping'* takes place, a procedure which shapes the beam transverse profile to its optimized configuration, in order to avoid detector damages due to the tails of the $p(\bar{p})$ distributions entering the active volumes. The scraping is done by moving iron plates which act as collimators in the transverse plane toward the beam and sweep away the transverse beam halo. When the beam profile is narrow enough and the conditions are safely stable the detectors are powered and the data taking starts. This is the end

of the injection procedure called *'shot'*.
The inter-bunch crossing is 396 ns and this defines an overall time constant which influences the whole detector design: on this parameter depends the choice of the active parts, the design of the readout electronics, the structure of the trigger etc..
The number of overlapping interactions N for each bunch crossing is a Poisson-distributed variable dependent on the instantaneous luminosity and on the number of colliding bunches. At TeVatron luminosities of $\mathcal{L} \approx 10 \times 10^{31}$ cm^{-2}s^{-1} $\bar{N}$ is approximately 2.
Each time that at least one of the CDF II triggers fires, an *event* is labeled with an increasing number. Events are grouped into *'runs'*; a run is a period of continuous[3] operation of the CDF II Data Acquisition. Most parameter of the CDF II operations (e. g., the position of the beam) are stored in the database on a run-averaged format.
While collisions are taking place the luminosity decreases exponentially[4] because of the beam-gas and beam-halo interactions. In the meantime, antiproton production and storage continues. When the antiproton stack is sufficiently large ($\simeq 10^{12}$ antiprotons) and the circulating beams are degraded ($\sim$ 14 hours) the detector high-voltages are switched off and the store is dumped. The beam is extracted via a switch-yard and sent to an absorption zone. Beam abortion can occur also accidentally when the temperature of a superconducting magnet shift above the critical value and the magnet quenches destroying the orbit of the beams. The typical time between the end of a store and the beginning of collisions of the next one is typically 2 hr. During this time CDF II usually performs calibrations of the sub-detectors and test runs with cosmics.

2.1.4 TeVatron performance

The initial Run II goal (1996) was to achieve a luminosity of 5×10^{31} cm^{-2}s^{-1} and an integrated luminosity of 2 fb^{-1}. The final performance was well beyond this expectation. The peak luminosity exceeded regularly 2×10^{32} cm^{-2}s^{-1} (with a record of 4.3×10^{32} cm^{-2}s^{-1}, May 2011). Between February 2002 and September 2011 about 10 fb^{-1} of data were recorded on tape, representing the complete Run II data sample.

[3] Many different cases can require the DAQ to be stopped and restarted including the need to enable or disable a subdetector, a change in the trigger Table, a problem in the trigger/DAQ chain etc..

[4] The decrease is about a factor of 2.5-5 for a store ($\sim$ 10-20 hrs), depending from the initial luminosity also.

2.2 CDF II detector

The CDF II detector is a large multi-purpose solenoidal magnetic spectrometer designed with an approximately cylindric symmetry and it is installed at the BØ interaction point of the TeVatron (see fig. 2.1). CDF II consists of five main sub-detector systems: tracking, particle identification, calorimetry, muon identification and luminosity detector. These systems are used to determine energy, momentum and, whenever possible, the identity of a broad range of particles produced in the $p\bar{p}$ collisions.

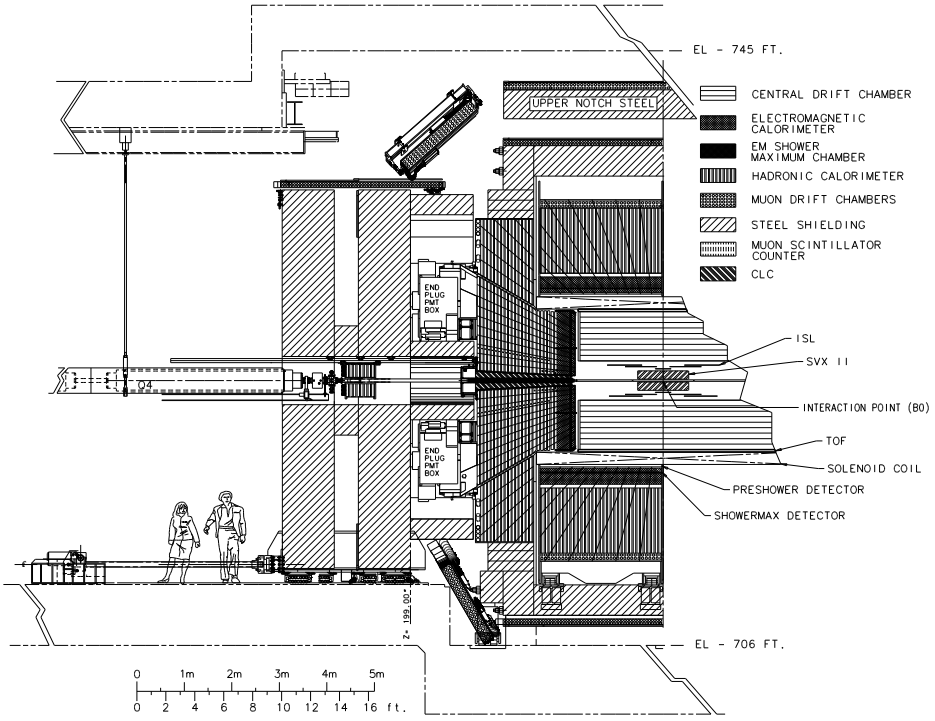

Figure 2.3: Elevation view of one half of the CDF II detector.

2.2.1 Coordinates and notation in CDF II

CDF II adopts a right-handed cartesian coordinates system with the origin in the BØ interaction point, assumed coincident with the center of the drift chamber. The

positive z-axis lies along the nominal beam-line pointing toward the proton direction (east). The (x, y) plane is therefore perpendicular to either beams, with positive y-axis pointing vertically upward and positive x-axis in the horizontal plane of the TeVatron pointing radially outward with respect to the center of the ring.

Since the colliding beams of the TeVatron are unpolarized, the resulting physical observations are invariant under rotations around the beam line axis. Thus, a cylindrical (r, ϕ, z) coordinates system is particularly convenient to describe the detector geometry. Throughout this thesis, *longitudinal* means parallel to the proton beam direction (i.e., to the z-axis), and *transverse* means perpendicular to the proton direction, i.e., in the $(x, y) \equiv (r, \phi)$ plane.

Since the protons and antiprotons are composite particles, the actual interaction occurs between individuals partons (valence or sea quarks and gluons) contained within them. Each parton carries a varying fraction of the (anti)proton momentum, not known on a event-by-event basis. As a consequence of the possible imbalance in the longitudinal components of the momenta of interacting partons, possible large velocities along $\hat{z}$ for the center-of-mass of the parton-level interaction may occur. In the hadron collisions environment, it is customary to use a variable invariant under $\hat{z}$ boosts as an unit of relativistic phase-space, instead of the polar angle θ. This variable is the *rapidity* defined as

$$Y = \frac{1}{2}\ln\left[\frac{\mathrm{E} + \mathrm{pcos}(\theta)}{\mathrm{E} - \mathrm{pcos}(\theta)}\right], \tag{2.3}$$

where $(E, \vec{p})$ is the energy-momentum four-vector of the particle. Under a $\hat{z}$ boost to an inertial frame with velocity β, the rapidity of a particle transforms linearly, according to $Y \to Y' \equiv Y + \tanh^{-1}(\beta)$, therefore Y is invariant since $dY \equiv dY'$. However, a measurement of rapidity still requires a detector with accurate identification capabilities because of the mass term entering E. Thus, for practical reasons, it is often preferred to substitute Y with its approximate expression η in the ultra-relativistic limit ($p >> m$), usually valid for products of high-energy collisions:

$$Y \to \eta + \mathcal{O}(m^2/p^2), \tag{2.4}$$

where the *pseudo-rapidity* $\eta \equiv -\ln[\tan(\theta/2)]$ is only function of the momenta. As the event-by-event longitudinal position of the actual interaction is distributed around the nominal interaction point with 30 cm r.m.s width, it is useful to distinguish the *detector pseudo-rapidity*, η_{det}, measured with respect to the (0,0,0) nominal interaction point, from the *particle pseudo-rapidity*, η, measured with respect to the z_0 position of the real vertex where the particle originated[5].

Other convenient variables are the transverse component of the momentum with respect to the beam axis (p_{T}), the "transverse energy" (E_{T}), and the approximately Lorentz-invariant angular distance ΔR, defined as

$$\vec{p}_{\mathrm{T}} \equiv (p_x, p_y) \to p_{\mathrm{T}} \equiv p\sin(\theta), \quad E_{\mathrm{T}} \equiv E\sin(\theta), \quad \text{and} \quad \Delta R \equiv \sqrt{\eta^2 + \phi^2}. \tag{2.5}$$

[5] An idea of the difference is given by considering that $\eta_{\mathrm{det}} \approx \eta \pm 0.2$ if the particle was produced a $z = 60$ cm from the nominal interaction point

2.2.2 Overview

CDF II (see fig. 2.3) is a three-story, 5000-ton approximately cylindric assembly of sub-detectors, $\sim$ 15 m in length, $\sim$ 15 m in diameter. The flow of final state particles in energetic hadronic collisions is well described by quantities of (pseudo)rapidity, transverse component of the momentum with respect to the beam axis and azimuthal angle around this axis. Consequently CDF II detector was designed and constructed with an approximately cylindrically symmetric layout both in the azimuthal plane and in the *"forward"* ($z > 0$) - *"backward"* ($z < 0$) directions with spatial segmentation of its subcomponents roughly uniform in pseudorapidity and azimuth.
CDF II is composed of several specialized sub-systems each one designed to perform a different task, arranged in a standard layout for multipurpose detectors; starting from the interaction point, particle emitted within the acceptance region encounter in sequence: a thin wall beryllium[6] vacuum chamber, a high precision tracking system, a time of flight detector, a solenoidal magnet, sampling calorimeters and muon detectors. Its capabilities include high resolution charged particle tracking, electron and muon identification, low momentum π/K separation, precise secondary vertices proper time measurements, finely segmented sampling of energy flow coming from final state hadrons, electrons or photons, identification of ν's via transverse energy imbalance. The detector is divided conventionally into two main polar regions. In the following we shall refer to the detector volume contained in the $|\eta_{det}| < 1$ as the *central region*, while the *forward region* indicates the detector volume comprised in $1 < |\eta_{det}| < 3.6$.

A comprehensive description of the CDF II detector and its subsystems is given in Ref. [66]. In the following, we emphasize the tracking and the trigger systems, which are the aspects of the detector more specific to this analysis.

2.2.3 Tracking system

At CDF the tracking system provides measurements of the particle trajectory, referred to as a track. This allows the determination of the charge and the momenta of the particles which are essential for the analysis presented in this work, where mesons decaying to two charged particles are studied. In particular, the only physics objects used in this analysis are the tracks. Within an uniform axial magnetic field in vacuum, the trajectory of a charged particle produced with non-zero initial velocity in the bending plane of the magnet is described by an helix. The arc of an helix described by a charged particle in the magnetic volume of CDF is parameterized using three transverse, and two longitudinal parameters:

C – signed helix (half)-curvature, defined as $C \equiv \frac{q}{2R}$, where R is the radius of the

[6] The beam pipe is made of beryllium because it has the best mechanical qualities with the lowest nuclear interaction cross section.

helix. This is directly related to the transverse momentum: $p_{\mathrm{T}} = \frac{cB}{2|C|}$;

$\boldsymbol{\varphi_0}$ – ϕ direction of the particle at the point of closest approach to the z-axis;

$\boldsymbol{d_0}$ – signed impact parameter, i. e., the distance of closest approach to the z-axis, defined as $d_0 \equiv q(\sqrt{x_c^2 + y_c^2} - R)$, where (x_c, y_c) are the coordinates of the center-guide;

$\boldsymbol{\lambda}$ – the helix pitch, i. e., $\cot(\theta)$, where θ is the polar direction of the particle at the point of its closest approach to the z-axis. This is directly related to the longitudinal component of the momentum: $p_z = p_{\mathrm{T}} \cot(\theta)$;

$\boldsymbol{z_0}$ – the z coordinate of the point of closest approach to the z-axis.

The trajectory of a charged particle satisfies the following equations [68]:

$$x = r\sin(\varphi) - (r + d_0)\sin(\varphi_0) \tag{2.6}$$

$$y = -r\cos(\varphi) + (r + d_0)\cos(\varphi_0) \tag{2.7}$$

$$z = z_0 + s\lambda, \tag{2.8}$$

where s is the projected length along the track, $r = 1/2C$, and $\varphi = 2Cs + \varphi_0$. The reconstruction of a charged-particle trajectory consists of determining the above parameters through an helical fit of a set of spatial measurements ("hits") reconstructed in the tracking detectors by clustering and pattern-recognition algorithms. The helical fit takes into account field non-uniformities and scattering in the detector material.

Three-dimensional charged particle tracking is achieved through an integrated system consisting of three silicon inner subdetectors and a large outer drift-chamber, all contained in a superconducting solenoid. (see fig. 2.4).

In the central region ($|\eta_{\mathrm{det}}| \lesssim 1$), 7 silicon samplings (one in the (r, ϕ) view plus six in the (r, ϕ, z) view), and 96 chamber samplings (48 (r, ϕ) plus 48 (r, z)) are available between 1.6 and 132 cm. In the forward and backward regions ($1 \lesssim |\eta_{\mathrm{det}}| \lesssim 2$), 8 silicon samplings (one in the (r, ϕ) view plus seven in the (r, ϕ, z) view) are available between 1.6 and 29 cm, along with partial information from the chamber.

The high number of samplings over the 88 cm lever arm of the chamber ensure precise determination of curvature, azimuth, and pseudo-rapidity of the tracks in the central region. The chamber provides also track seeds for pattern-recognition in silicon.

The innermost tracking device, i. e., the Layer ØØ (LØØ), is a light-weight silicon layer placed on the beam-pipe. It recovers the degradation in resolution of the reconstructed vertex position due to multiple scattering on the SVXII read-out electronics and cooling system, installed within the tracking volume. The LØØis made of state-of-the-art radiation-tolerant sensors, and it will extend the lifetime of

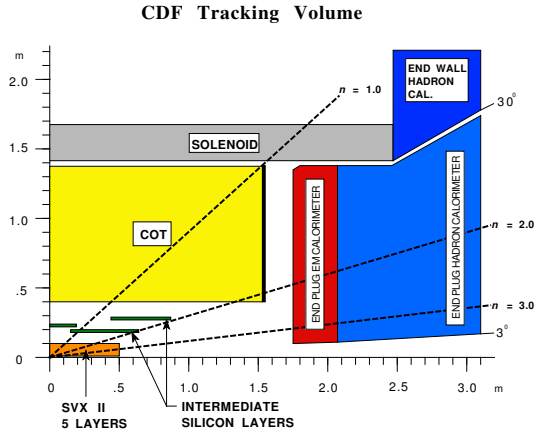

Figure 2.4: Elevation view of one quadrant of the inner portion of the CDF II detector showing the tracking volume surrounded by the solenoid and the forward calorimeters.

the whole system when the effects of radiation damage will degrade the performance of the inner SVXII layers. The integrated design of the tracking system allowed commonality of components among subdetectors (read-out chip, support structures, etc.) thus simplifying the construction and the operation.

The core of the silicon detector is the Silicon VerteX detector (SVXII). It provides five three-dimensional measurements that extend the lever arm by 41.5 cm toward the beam thus allowing more precise determination of the trajectories and identification of decay-vertices displaced from the beam-line. The SVXII has an outer and an inner extension.

The outer extension, i. e., the Intermediate Silicon Layers (ISL), provides a single (double) three-dimensional silicon measurement in the central (forward-backward) region, at intermediate radial distance from the chamber. The ISL allows efficient linking between tracks reconstructed in the chamber and hits detected in the SVXII, and extends the track finding at pseudo-rapidities $1 \lesssim |\eta_{\rm det}| \lesssim 2$, where the chamber coverage is marginal.

The total amount of material in the silicon system, averaged over ϕ and z, varies roughly as $\frac{0.1X_0}{\sin(\theta)}$ in the $|\eta_{\rm det}| \lesssim 1$ region, and roughly doubles in $1 \lesssim |\eta_{\rm det}| \lesssim 2$ because of the presence of cables, cooling bulk-heads, and portions of the support frame.[7] The average amount of energy loss for a charged particle is roughly 9 MeV. The total heat load of the silicon system is approximately 4 kW. To prevent thermal expansion, relative detector motion, increased leakage-current, and chip failure due to thermal heating, the silicon detectors and the associated front-end electronics are held at roughly constant temperature ranging from -6°C to -10°C for LØØ and SVXII, and around 10°C for ISL, by an under-pressurized water and ethylene-glycol

[7] The symbol X_0 indicates the radiation length.

coolant flowing in aluminum pipes integrated in the supporting structures.[8]

The magnet

A 1.4116 T solenoidal magnetic field is maintained in the region $r < 150$ cm $|z| < 250$ cm by circulating a 4650 A current through 1164 turns of a Nb-Ti/Cu superconducting coil. The field is oriented along the positive $\hat{z}$ direction and is uniform at the 0.1% level in the $|z| < 150$ cm volume where tracking measurements are made (see fig. 2.4). The tiny non-uniformities, mapped out during detector construction, are treated as a small perturbation within the track fitting software. The field is continuously monitored via nuclear magnetic resonance probes during data taking and any deviation from the mapped values is applied as a correction to measured track momenta. The threshold to escape radially the magnetic field for a particle is $p_{\mathrm{T}} > 0.3$ GeV/c while the trajectory of a $p_{\mathrm{T}} = 30$ GeV/c particle deviates only 1.6 cm from a straight path of 150 cm. The solenoid is 4.8 m in length, 1.5 m in radius, 0.85 X_0 in radial thickness[9] and is cooled by forced flow of two-phase helium. Outside the coil the field flux is returned through a steel yoke to avoid having the fields interfere with the proper operations of the calorimeter's photo-multiplier tubes.

2.2.4 Layer ØØ (LØØ)

Layer ØØ (LØØ) is the innermost layer of the microvertex silicon detector [69]. It consists of one layer of single sided AC-coupled silicon sensors which covers the beryllium beam pipe along 80 cm longitudinally. The state-of-the-art 7.85 cm long silicon sensors of LØØ can be biased to very high ($\mathcal{O}$(500 V)) voltages allowing to maintain a good signal-to-noise ratio even after high integrated radiation dose ($\mathcal{O}$(5 MRad)). The radiation hardness of such sensors allowed their installation at radii of 1.35 and 1.62 cm supported by a mechanical structure in direct contact with the beam pipe. The LØØ strips are parallel to the beam axis allowing the first sampling of the track within the $r - \phi$ plane, the inter-strip pitch is 25 μm but the read-out strip are alternated with floating ones resulting in 50 μm of readout pitch.
The signals of the 13,824 channels are fed via special optical fiber cables to the front-end electronic which is placed in a region separated from the sensors and less exposed to the radiation. The operation temperature of this device is around 0^oC maintained by a forced flux of under-pressurized[10] gas through tiny aluminum pipes installed in between the sensor and the beam-pipe. The cooling circuit increases the total mass of the LØØ which is about $1\%X_0$ where pass the cooling pipes and

[8] The pressure of the cooling fluid is maintained under the atmospheric pressure to prevent leaks in case of damaged cooling pipes.

[9] This has to be intended for normally incident particles.

[10] The pressure of the cooling fluid is maintained under the atmospheric pressure to avoid dangerous leaks of fluid in case of damaged cooling pipe.

reduces to $0.6\%X_0$ where only sensors contribute.

2.2.5 Silicon VerteX detector II (SVXII)

The Silicon VerteX detector II (SVXII) [70] is a fine resolution silicon microstrip vertex detector which provides five 3D samplings of a track between 2.45 and 10.6 cm of radial distance from the beam (see fig. 2.4). Its cylindrical geometry coaxial with the beam is segmented along z into three *'mechanical barrels'* for a total length of 96 cm which provides complete geometrical coverage within $|\eta_{\rm det}| < 2$ (see fig. 2.5(a)). Each barrel consists of twelve azimuthal wedges each of which subtends approximately[11] 30^o. One wedge of a given barrel comprises 5 concentric and equally spaced layers of silicon sensors installed at radii 2.45 (3.0), 4.1 (4.6), 6.5 (7.0), 8.2 (8.7), and 10.1 (10.6) cm from the beam as shown in (see fig. 2.5(b)).

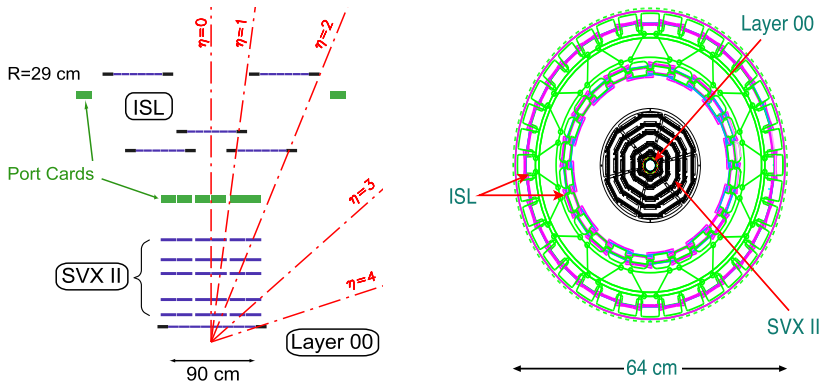

Figure 2.5: Schematic illustration of the silicon system, in the (r, z) plane (a) and in the (r, ϕ) plane (b). z dimension not to scale.

Sensors in a layer are arranged into independent readout units, called *'ladders'* (or electrical barrels). The ladder components are two double sided rectangular 7.5 cm long sensors and the *hybrid* which is a multilayer board where all the front end electronics, biasing circuits and fan-out are allocated. The two silicon sensors, accurately aligned along their major axis, are glued end-to-end on a carbon-fiber support, with wirebonds connections joining the strips on one sensor to the strips of the next. It results in strips with an effective length of 15 cm in turn wirebonded to the front-end electronics of the hybrid which is mounted at one end of the carbon fiber support. Two ladders are longitudinally juxtaposed head-to-head within a barrel's layer, in order to leave the two hybrids at the two outside extremities of the barrel.
The active surface consists of double-sided, AC-coupled silicon sensors having mi-

[11] There is a small overlap between the edges of two adjacent wedges, which helps in wedge-to-wedge alignment.

crostrips implanted on a 300 μm thick, high resistivity bulk. Bias is applied through integrated polysilicon resistors. There are three different possible sort of strip orientations in each sensor's side: $r-\phi$ (axial) strips oriented parallel to the beam axis, small angle stereo (SAS) strips whose orientation is tilted by 1.2^o with respect to the beam axis and the 90^o stereo strips which lie in the transverse plane. All the five layers have axial strips on one side, three of the other sides have 90^o stereo and two have SAS strips.
The charge pulse from each strip flows to a channel of SVX3D, the radiation-hard front-end chip [71]. SVX3D operates readout in "sparse-mode" which means that only signals above a threshold are processed. SVX3D samples the pedestal event-by-event and subtracts it from the signal. The discriminated differential pulse from each one of the 405,504 channels is preamplified, ADC-converted to a digital string and fed through neighbor-logic[12] to the DAQ chain. The measured average signal-to-noise ratio is S/N $\geq$ 10, with a single hit efficiency greater than 99%.
To prevent thermal expansion, relative detector motion, increased leakage current and chip failure due to thermal heating the SVX II is held at roughly constant temperature of 10-15^{o}C through the operation of a water-glycol cooling system whose pipes run all below the detector. The average material of SVX II corresponds to $5\%X_0$.

2.2.6 Intermediate Silicon Layers (ISL)

The Intermediate Silicon Layer [72] detector is a silicon tracker placed at intermediate radial distance between the SVXII and the drift chamber (see fig. 2.4). The polar coverage extends to $|\eta_{\rm det}| < 2$. In the central region ISL consist of a single layer of silicon installed over a cylindrical barrel at radius of 22 cm. In the forward region, two layers of silicon are placed on concentric barrels at radii of 20 and 28 cm. Each silicon layer is azimuthally divided into a 30^o wedge structure matching that of SVXII. The basic readout unit is the ISL *ladder* which is similar to the SVXII ladder but consists of three, instead of two, sensors wirebonded in series resulting in a total active length of 25 cm.
ISL employs 5.7$\times$ 7.5 cm^2 double sided AC-coupled 300 μm thick sensors. Each sensor has axial strips on one side and SAS strips on the other. As in SVXII, signals from the 303,104 channels are read by SVX3D chips. Average mass of the detector is $2\%X_0$ for normally incident particles.

2.2.7 Central Outer Tracker (COT)

The outermost tracking volume [73] of CDF II is a large open cell drift chamber called the Central Outer Tracker (COT).
The COT has a coaxial bi-cylindrical geometry and extends, within the central

[12] In presence of a channel over threshold also the signal of the neighbor channels is accepted allowing clustering of the hits.

region, from 44 to 132 cm radially from the beam axis. The chamber contains 96 radial layers of 0.40 μm diameter gold-plated tungsten sense (anode) wires arranged into 8 *"superlayers"*. Each superlayer samples the path of a charged particle at 12 radii (spaced 0.762 cm apart) where sense wires are strung. Four superlayers have their constituent sense wires oriented parallel to the beam axis in order to measure the hit coordinates in the $r-\phi$ plane. These are radially interleaved with four *stereo* superlayers having wires canted at angles of either $+3^o$ or -3^o with respect to the beamline. Combined readout of stereo and axial superlayers allows the measurement of the $r-z$ hit coordinates.
Each superlayer is azimuthally segmented into open drift cells. A drift cell, as shown in fig. 2.6, contains a row of 12 sense wires alternating with thirteen 0.40 μm diameter gold-plated tungsten potential wires which control the gain on the sense wires, optimizing the electric field intensity. The cathode of the detection circuit is the *field panel* which closes the cell along the azimuthal direction. It is made of gold on a 0.25 mm thick Mylar sheet and defines the fiducial volume of a cell. The electric field strength is 2.5 kV/cm. Innermost and outermost radial extremities

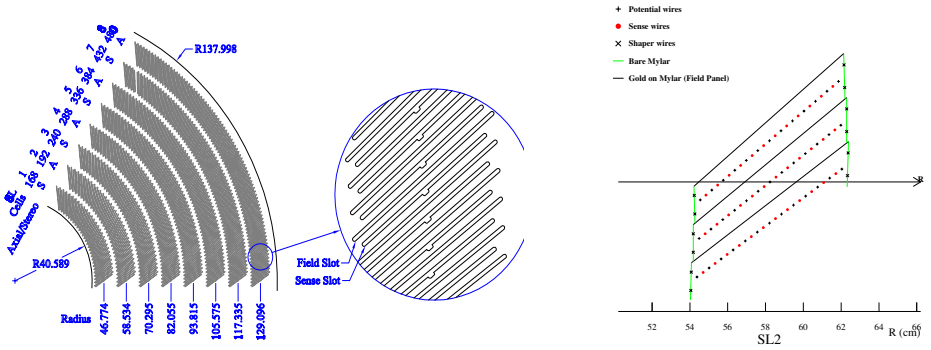

Figure 2.6: A 1/6 section of the COT end-plate (a). For each super-layer is given the total number of cells, the wire orientation (axial or stereo), and the average radius [cm]. The enlargement shows in details the slot were wire planes (sense) and field sheet (field) are installed. Sketch of an axial cross-section of three cells in super-layer 2, (b). The arrow shows the radial direction.

of a cell are closed both mechanically and electrostatically by the *shaper panels*, which are Mylar strips carrying field-shaping wires attached. The architecture of the cell allows the containment of a possible broken wire inside only one cell and its dimensions bound to 0.9 cm the maximum drift distance.
Wire planes are not aligned with $\hat{r}$. A 35^o azimuthal tilt is provided in order to offset the Lorentz angle of the drift paths which results from the combined effect of crossed electrical and magnetic field and the characteristics of the gas mixture. Moreover the tilted-cell geometry helps in the drift-velocity calibration as every high-p_{T} (radial) track samples the full range of drift distances within each super-

layer. Further benefit of the tilt is that the left-right ambiguity[13] is cleared-up for track coming from the origin since the ghost track in each superlayer appears rotated of a large azimuthal angle becoming unfittable by pattern recognition. The volume of the COT is filled with a Ar(50%)/Ethane(50%) gas mixture. Drift electrons follow approximately azimuthal trajectories at speed $v \approx 100$ μm/ns. The resulting maximum drift time is about 100 ns, well smaller than the inter-bunch spacing 396 ns, providing the read-out and processing of the COT data available for the Level 1 trigger.
The analog pulses from the 30,240 sense wires flow to preamplifiers where are amplified and shaped. The discriminated differential output encodes charge information in its width to be used for dE/dx measures and is fed to a TDC which records leading and trailing edge of the signals in 1 ns bins. COT has 99% efficiency on tracks with measured single hit resolution $\sigma_{\rm hit} \simeq 175$ μm and $p_{\rm T}$ resolution is $\sigma_{p_{\rm T}}/p_{\rm T}^2 \simeq 0.13\%$ GeV/c^{-1}. The material of the COT is about 1.6% X_0 for tracks at normal incidence.

Performance of tracking system

For this analysis, only COT-seeded silicon tracks were used, because the pattern recognition algorithms that use stand-alone silicon information would have given marginal contribution for two reasons. First, the impact of silicon stand-alone tracking becomes important in the region $1 \lesssim |\eta| \lesssim 2$ where the COT coverage is incomplete. This region of acceptance is already excluded in our analysis, since the trigger that collects $B^0_{(s)} \to h^+h'^-$ events uses the COT information (see sec. 2.4). Secondly, the algorithms for silicon stand-alone tracking were not yet optimized as of this analysis.

All tracks were first fit in the COT and then extrapolated inward to the silicon. This approach guarantees fast and efficient tracking with high track purities. The greater radial distance of the COT with respect to the silicon tracker results in a lower track density and consequent fewer accidental combination of hits in the track reconstruction. A concise overview of the tracking algorithms is given in the following, see Ref. [75] for more details.

COT performance

The COT efficiency for tracks is typically 99%. The single-hit resolution is 140 μm, including a 75 μm contribution from the ≈ 0.5 ns uncertainty on the measurement of the $p\bar{p}$ interaction time. Internal alignments of the COT cells are maintained within 10 μm using cosmic rays. Curvatures effects from gravitational and electrostatic sagging are under control within 0.5% by equalizing the difference of E/p between

[13] Each pulse on a given wire has a two fold ambiguity corresponding to the two incoming azimuthal drift trajectories. The signals from a group of nearby radially wires will satisfy the configuration for two tracks, one from the actual particle trajectory and another "ghost track" originated by the two fold ambiguity.

electrons and positrons as a function of $\cot(\theta)$. The typical resolutions on track parameters are: $\sigma_{p_T}/p_T^2 \approx 0.0015$ $(\mathrm{GeV}/c)^{-1}$, $\sigma_{\varphi_0} \approx 0.035°$, $\sigma_{d_0} \approx 250$ μm, $\sigma_\theta \approx 0.17°$, and $\sigma_{z_0} \approx 0.3$ cm for tracks fit with no silicon information or beam constraint.

Performance of the silicon detectors

The silicon information improves the impact parameter resolution of tracks which, depending on the number (and radial distance) of the silicon hits, may reach $\sigma_{d_0} \approx 20$ μm (not including the transverse beam size). This value, combined with the $\sigma_T \approx 30$ μm transverse beam size, is sufficiently small with respect to the typical transverse decay-lengths of heavy flavors (a few hundred microns) to allow separation of their decay-vertices from production vertices. The silicon tracker improves also the stereo resolutions up to $\sigma_\theta \approx 0.06°$, and $\sigma_{z_0} \approx 70$ μm, while the transverse momentum and the azimuthal resolutions remain approximately the same of COT-only tracks.

2.3 Other CDF II subdetectors

In this section the subdetectors not used in this analysis are briefly discussed.

2.3.1 Time of Flight detector

The Time of Flight detector (TOF) is a cylindrical array made of 216 scintillating bars [76] and it is located between the external surface of the COT and the cryostat containing the superconducting solenoid. Bars are 280 cm long and oriented along the beam axis all around the inner cryostat surface at an average radial distance of 138 cm. Both longitudinal sides of the bars collect the light pulse into PMT and measure accurately the timing of the two pulses. The time between the bunch crossing and the scintillation signal in these bars defines the β of the charged particle while the momentum is provided by the tracking. PID information is available through the combination of TOF information and tracking measurements. The measured mean time resolution is now 110 ps. This guarantees a separation between charged pions and kaons with $p_T \lesssim 1.6$ GeV/c equivalent to 2σ, assuming Gaussian distributions. Unfortunately, in high ($\mathcal{L} \gtrsim 5 \times 10^{31}$ cm^{-2}s^{-1}) luminosity conditions, the occupancy of the single bars determines a degradation in efficiency, which is about 60% per track.

2.3.2 Calorimeters

Outside the solenoid, scintillator-based calorimetry covers the region $\eta_{\mathrm{det}} \leq 3.6$, and is devoted to the measurement of the net energy deposition of photons, electrons and hadrons using the *shower sampling* technique.

The basic structure consists of alternating layers of passive absorber and plastic scintillator. Neutral particles and charged particles with a transverse momentum greater than about 350 MeV/c are likely to escape the solenoid's magnetic field and penetrate into the CDF II calorimeters. Here particles undergo energy loss, striking the absorber material, and produce daughter particles which also interact in a cascade process, giving rise to a *shower* of particles. Showers propagate through many layers of absorber before they exhaust their energy generating a detectable signal, roughly proportional to the number of particles in the shower, within the active scintillator layers. The sum of the signals collected by all the sampling active layers is proportional to the energy of the incident particle.
The CDF II calorimeters are finely segmented in solid angle around the nominal collision point, and coarsely segmented radially outward from the collision point (in-depth segmentation.) Angular segmentation is organized in projective *towers*. Each tower has a truncated-pyramidal architecture having the imaginary vertex pointing to the nominal interaction point and the base is a rectangular cell in the ($\eta_{\rm det}$, ϕ) space. Radial segmentation of each tower instead consists of two compartments, the inner (closer to the beam) devoted to the measure of the electromagnetic component of the shower, and the outer devoted to the measure of the hadronic fraction of energy. These two compartments are read independently through separated electronics channels.
A different fraction of energy release in the two compartments distinguishes photons and electrons from hadronic particles. CDF II calorimetry is divided in several independent subsystems presented in the following subsections.

Central region: CEM, CHA, WHA

The radial extension of the calorimeters in the central region is 1.73 $m < r < 3.5$ m. The Central ElectroMagnetic calorimeter (CEM) [77] is constructed as four azimuthal arches (NE, NW, SE, SW) each of which subtends 180^o and is divided into twelve 15^o wedges. A wedge consists of 31 layers of 5 mm thick polystyrene scintillator interleaved with 30 aluminum-clad lead 3.2 mm thick sheets, divided along $\eta_{\rm det}$ into ten towers ($\Delta\eta_{\rm det} \approx 0.11$ per tower). To maintain a constant thickness in X_0, compensating the $\sin(\theta)$ variation between towers, some lead layers are replaced with increasing amounts of acrylic as a function of $\eta_{\rm det}$[14]. Light from each tower is collected by sheets of acrylic wavelength shifter at both azimuthal tower boundaries and guided to two phototubes per tower. The spatial resolution of the CEM is about 2 mm. The outer two towers in one wedge (known as *chimney towers*) are missing to allow solenoid access, for a resulting total number of 478 instrumented towers.
At a radial depth of $5.9X_0$, which is approximately the depth corresponding to the peak of shower development, the CEntral Strip multi-wire proportional chambers

[14]The number of lead layers varies from 30 in the innermost ($|\eta_{\rm det}| \approx 0.06$) tower to 20 in the outermost ($|\eta_{\rm det}| \approx 1.0$).

(CES) measure the transverse shower shape with ~ 1.5 cm segmentation. A further set of multi-wire proportional chambers, the Central Pre-Radiator (CPR) [78] is located in the gap between outer surface of the solenoid and the CEM. It monitors eventual photon conversions started before the first CEM layer. Phototube gains are calibrated once per store using an automated system of Xenon or LED light flashers.
The hadronic compartment is the combination of two sub-systems: the Central HAdronic (CHA) and Wall HAdronic (WHA) [79] calorimeters. Analogously as in the CEM, in both systems four "C"-shaped arches contain 48 wedges. Each CHA wedge is segmented into 9 η_{det} towers matching in size and position the CEM towers. The WHA wedge instead consists of 6 towers of which three are matching CHA towers. Radially a CHA tower is constructed of 32 layers of 2.5 thick steel absorber alternating with 1.0 cm thick acrylic scintillator. WHA towers structure is similar but there are only 15 layers of absorber which is 5.1 cm thick.

The total thickness of the electromagnetic section corresponds to approximately $19X_0$ ($1\lambda_{\text{int}}$, where λ_{int} is the pion nuclear absorption length in units of g cm^{-2}), for a relative energy resolution $\sigma_E/E = 13.5\%/\sqrt{E\sin(\theta)}\oplus 2\%$.[15] The total thickness of the hadronic section corresponds to approximately $4.5\lambda_{\text{int}}$, for an energy resolution of $\sigma_E/E = 50\%/\sqrt{E\sin(\theta)}\oplus 3\%$ for the central, and $\sigma_E/E = 75\%/\sqrt{E\sin(\theta)}\oplus 4\%$ for the end-wall.

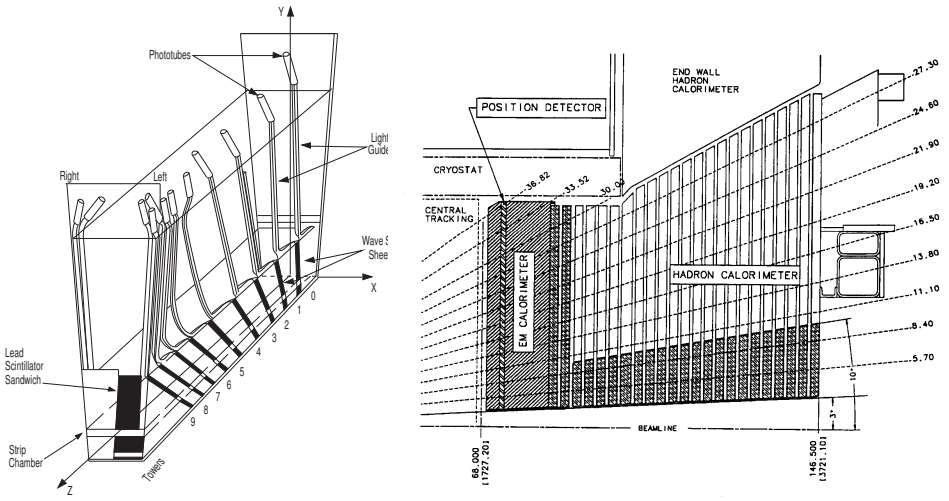

Figure 2.7: Schematic illustration of an azimuthal sector of the central electromagnetic calorimeter (a). Elevation view of one quarter of the plug calorimeter (b).

[15] The first term is called the "stochastic" term and derives from the intrinsic fluctuations of the shower sampling process and of the PMT photo-electron yield. The second term, added in quadrature, depends on the calorimeter non-uniformities and on the uncertainty on the calibrations. All energies are in GeV.

Forward region: PEM, PHA

The coverage of the $1.1 \leq |\eta_{\text{det}}| \leq 3.6$ region relies on the scintillating tile *Plug* calorimeter [80] which is composed of two identical devices, one installed in $\eta_{\text{det}} > 0$ region and the other in the $\eta_{\text{det}} < 0$. Each of these two halves has electromagnetic and hadronic compartments (see fig. 2.7(b)).
In each half the absorber of the Plug ElectroMagnetic calorimeter (PEM) consists in 23 *"doughnuts"*-shaped lead plates, 2.77 m in outer diameter, which have a central hole where the beam pipe is allocated. Each plate is made out of 4.5 mm thick calcium-tin-lead sandwiched between two 0.5 mm thick stainless-steel sheets. Between the absorber plates are inserted the 4 mm thick scintillator *tiles* organized azimuthally in 15^o triangularly-shaped wedges. The signal of each tile is collected independently by embedded wavelength-shifter fibers which guide it to the photomultipliers. A preshower detector consist of a thicker (10 mm) amount of scintillator installed in the first layer of PEM, while shower maximum sampling is performed at radial depth of $\sim 6X_0$ by two tilted layers of scintillator strips (pitch 5 mm).
Each half of the hadronic compartment, Plug HAdronic calorimeter (PHA), is azimuthally subdivided in 12 wedge-shaped modules each subtending 30^o. In depth each module consists of 23 layers of 5 cm thick iron absorber alternated with 6 mm scintillator layers. Within each sampling layer the scintillator is arranged in tiles similar to those used in the PEM.

The total thickness of the electromagnetic section corresponds to approximately $21X_0$ ($1\lambda_{\text{int}}$), for an energy resolution of $\sigma_E/E = 16\%/\sqrt{E\sin(\theta)} \oplus 1\%$.[16] The total thickness of the hadronic section corresponds to approximately $7\lambda_{\text{int}}$, for an energy resolution of $\sigma_E/E = 74\%/\sqrt{E\sin(\theta)} \oplus 4\%$.

2.3.3 Muon systems

CDF II is equipped with scintillating counters and drift tubes [81] installed at various radial distances from the beam to detect muons and shielded by the iron structure of the inner detector. Scintillators serve as trigger and vetoes while the drift chambers measure the ϕ coordinate using the absolute difference of drift electrons arrival time between two cells, and the z coordinate by charge division.
These systems cover the whole range of pseudorapidity $|\eta_{\text{det}}| < 2$ and are used only to identify the penetrating muon reconstructing a small segment of their path (*stub*) sampled by the chambers. The momentum measurement is performed by pointing back the stub to the corresponding, track in the COT. The shield is constituted by the iron of the calorimeter, the return yoke and further steel walls intended to filter out the punch-through of hadrons. Different muon sub-systems cover different geometrical regions. In the $|\eta_{\text{det}}| < 0.6$ region moving outward from the beam we encounter the inner CMU (Central MUon detector) chambers at radial distance of

[16] See footnote at pag. 37 for an explanation of terms.

3.5 m. Approximately $5.4\lambda_{\rm int}(\pi)$ of material[17] separate the luminous region from the CMU resulting in about 1/220 high energy hadrons traversing the calorimeter unchecked. In order to recognize and discard them, the CMP (Central Muon uPgrade) chambers lie in the same $\eta_{\rm det}$ region separated radially from the CMU by a 60 cm thick wall of steel achieving a rejection of 95% of the fake muons.
The muon coverage in the $0.6 < |\eta_{\rm det}| < 1$ volume is ensured by the CMX (Central Muon eXtension) chambers, embedded in scintillator counters and placed at radius of 3.5 m. The Intermediate MUon (IMU) detectors are instead drift tubes covering the pseudorapidity range of $1 < |\eta_{\rm det}| < 2.0$.
CDF II triggers on muons only emerging at $|\eta_{\rm det}| < 1.5$ where the muon coverage is segmented with sufficient granularity to survive high occupancies. The granularity of muon devices in the forward regions is less fine and not adequate for triggering, but sufficient for offline muon assignation to high $p_{\rm T}$ tracks going through that region.

2.3.4 Cherenkov Luminosity Counters

The luminosity ($\mathcal{L}$) is inferred from the average number of inelastic interactions per bunch crossing ($\overline{N}$) according to $\overline{N} \times f_{\rm b.c.} = \sigma_{\rm p\bar{p}-in.} \times \varepsilon \times \mathcal{L}$, where the bunch-crossing frequency ($f_{\rm b.c.}$) is precisely known from the Tevatron RF, $\sigma_{\rm p\bar{p}-in.} = 59.3 \pm 2.3$ mb is the inelastic $p\bar{p}$ cross-section resulting from the averaged CDF and E811 luminosity-independent measurements at $\sqrt{s} = 1.8$ TeV [82], and extrapolated to $\sqrt{s} = 1.96$ TeV, and ε is the efficiency to detect an inelastic scattering.

The Cherenkov Luminosity Counters (CLC) are two separate modules, covering the $3.7 \lesssim |\eta_{\rm det}| \lesssim 4.7$ range symmetrically in the forward and backward regions [83]. Each module consists of 48 thin, 110–180 cm long, conical, isobutane-filled Cherenkov counters. They are arranged around the beam-pipe in three concentric layers and point to the nominal interaction region. The base of each cone, 6–8 cm in diameter and located at the furthest extremity from the interaction region, contains a conical mirror that collects the light into a PMT, partially shielded from the solenoidal magnetic field. Isobutane guarantees high refraction index and good transparency for ultraviolet photons. With a Cherenkov angle $\theta_C = 3.4°$, the momentum thresholds for light emission are 9.3 MeV/c for electrons and 2.6 GeV/c for charged pions. Prompt charged particles from the $p\bar{p}$ interaction are likely to traverse the full counter length, thus generating large signals and allowing discrimination from the smaller signals of particles emitter at the same angle due to the beam halo or to secondary interactions. In addition, the signal amplitude distribution shows distinct peaks for different particle multiplicities entering the counters. This allows a measurement of $\overline{N}$ with 4.4% relative uncertainty in the luminosity range $10^{31} \lesssim \mathcal{L} \lesssim 10^{32}$ cm^{-2}s^{-1}. This accuracy, combined with the 4% relative

[17] This defines also a $p_{\rm T}$ threshold for muons reaching the CMU which is approximately 1.4 GeV/c.

uncertainty on the inelastic $p\bar{p}$ cross-section, results in an instantaneous luminosity measured with 5.9% relative uncertainty. This uncertainty does not affect the results of this analysis since ratios of branching fractions, instead of absolute branching fractions, are measured.

2.4 Trigger system and data acquisition

The trigger system plays a fundamental role in hadron collider experiments, because the typical collision rate is much higher than the rate at which data can be stored on tape.

At the typical TeVatron instantaneous luminosity approximately 2.6×10^6 inelastic collisions per second occur, corresponding on average to one interaction per bunch crossing. The interbunch space is 396 ns, corresponding to a collision rate of about 2.5 MHz. Unfortunately, the storage rate attainable at CDF II is well below this value: the writing cannot proceed faster than about 100 Hz. Thus, the read-out system faces the challenge of reducing the 2.5 MHz rate to 100 Hz. This is achievable evaluating the partial information provided by the detector in real time and rejecting uninteresting events, representing the majority of collision events[18]. The CDF II Data AcQuisition system (DAQ) is divided into three levels, represented in fig. 2.8, each receiving data events from the previous one. Each level provides a rate reduction sufficient to allow for processing in the next level with minimal deadtime[19].

2.4.1 Data acquisition

Prior to any trigger level, the bunched structure of the beam is exploited to reject cosmic ray events by gating the front end electronics of all subdetectors in correspondence of the bunch crossing. The front end electronics of each subdetector has a 42 cells deep pipeline synchronized with the TeVatron clock cycle, set to 132 ns. The TeVatron clock picks up a timing marker from the synchrotron RF and forwards this bunch crossing signal to the trigger and to the front end electronics. Since the inter bunch time is 396 ns, three times the TeVatron clock cycle, the pipeline can collect data corresponding to a maximum of 14 bunch crossings. The pipeline depth gives the amount of time that Level 1 (L1) trigger has to decide to accept or reject an event otherwise the buffer content is overwritten: 14×396 ns $= 5.5$ μs. An event accepted by the L1 is passed to the Level 2 (L2) buffer, where the number of buffers in the pipeline is 4, that gives 4×5.5 μs $= 22$ μs. This means that if an event is

[18] For example, the b production cross section is 10^{-3} times smaller than the generic $p\bar{p}$ inelastic one.

[19] Since the read-out of the entire detector needs about 2 ms on average, after the acquisition of one event another 5,000 interactions approximately occur and remain unrecorded. The percentage of events which are rejected solely because the trigger is busy processing previous events is referred to as trigger deadtime.

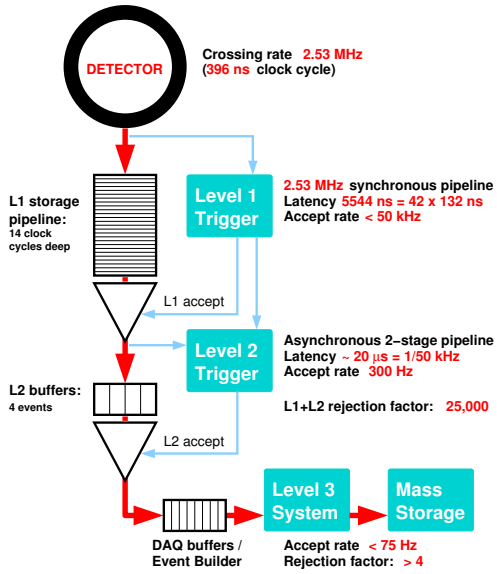

Figure 2.8: Functional block diagram of the CDF II trigger and data acquisition systems.

accepted by the L1 and the L2 does not have a free buffer, deadtime will incur. L2 output rate is low enough to avoid in general deadtime problem in the connection between L2 and Level 3 (L3). It is now useful to define some relevant quantities used in the trigger selection, giving the reasons why they are useful in our analysis. All quantities are calculated in the laboratory frame, and are illustrated in fig. 2.9. For the present description we neglect the curvature of particles with momentum $\sim$1 GeV/c.

Transverse momentum ($\vec{p}_{\mathrm{T}}$) – the projection of the momentum vector onto the transverse plane, calculated in the point of closest approach between the track and the beam line. This quantity is the simplest discriminant between heavy-flavor signals and background because, in $p\bar{p}$ collisions, charged particles from b-hadron decays have average transverse momenta higher than particles from generic QCD-backgrounds. Another useful quantity used in the selection is the scalar sum of the transverse momenta of the two particles $\Sigma p_{\mathrm{T}} \equiv p_{\mathrm{T}}(1) + p_{\mathrm{T}}(2)$.

Primary vertex – the space-point of the reconstructed primary $p\bar{p}$ interaction, where the b-quark, once produced, quickly hadronizes to a b-hadron pair.

Secondary vertex – the space point in which the decay of a long-lived particles occurs. The components of its displacement with respect to the primary vertex

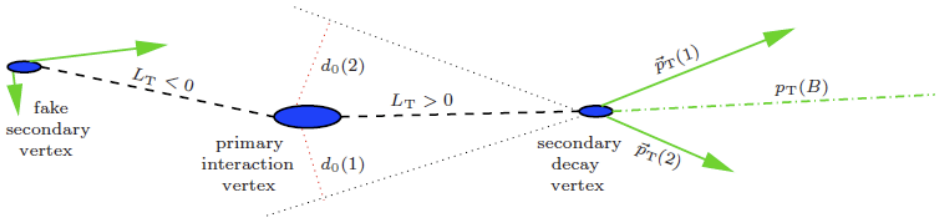

Figure 2.9: Illustration of a $p\bar{p}$ event containing a two-body decay, projected into the transverse plane. Ellipses indicate vertices, arrows indicate the transverse momenta (i. e., the direction) of charged particles. Nothing is to scale.

in the transverse plane are indicated by the vector $\vec{x}_v = \vec{\beta}_T \gamma ct = (\vec{p}_T/m)ct$, for a particle of mass m and momentum p that decays at time t after its production.

Transverse decay-length (L_T)– the displacement of the secondary vertex with respect to the primary one, projected onto the transverse momentum vector of the decaying particle ($\vec{p}_T(B)$). The transverse displacement of the secondary vertex ($\vec{x}_v$) may not be collinear with $\vec{p}_T(B)$ because of the measurement uncertainties. Thus, the transverse decay-length,

$$L_T \equiv \frac{\vec{p}_T \cdot \vec{x}_v}{p_T}, \tag{2.9}$$

is usually preferred to $\vec{x}_v$ as an estimator of transverse decay-length travelled before decay. This quantity is typically positive for a true long-lived decays, while it is negative or positive with almost equal probability for decays from a fake secondary vertex or for combinations of prompt tracks, although in the latter case its value is comparable with its resolution.

Impact parameter (d_0) – the component of the distance of closest approach

between a track and the primary vertex in the transverse plane. This is a signed quantity defined as

$$d_0 \equiv \frac{\hat{z} \cdot (\vec{p}_{\mathrm{T}} \wedge \vec{x}_v)}{p_{\mathrm{T}}}, \tag{2.10}$$

where the scalar product with the unit vector pointing toward the proton direction ($\hat{z}$) determines its sign and the symbol "$\wedge$" indicates the cross product. The impact parameter is typically different from zero for products of long-lived decays, while it is comparable with the convolution of its resolution and the transverse size of the beam for particles produced in the vicinity of the primary vertex (prompt background).

Azimuthal opening angle ($\Delta\varphi_0$) – the opening angle between the two outgoing particles projected in the transverse plane. The distribution of this quantity in $B^0_{(s)} \to h^+h'^-$ decays depends on the distributions in impact parameter and transverse momentum. However, it has generally a slowly-varying shape for signal candidates, while it shows two enhancements around 0° and 180° for background candidates. Pairs of quasi-collinear tracks are found in hadronic jets, due to light-quark fragmentation, or in highly occupied regions of the detector, due to combinations of fake tracks; pairs of azimuthally-opposed tracks are found in back-to-back jets of generic QCD background.

In the following, we give a brief description of the three levels of the trigger.

Level 1

At L1, a synchronous system of custom designed hardware processes a simplified subset of data in three parallel streams to reconstruct coarse information from the calorimeters (total energy and presence of single towers over threshold), the COT (two dimensional tracks in the transverse plane), and the muon system (muon stubs, i. e., segments of hits in the muon chambers). A decision stage combines the information from these low resolution physics objects, called primitives, into more sophisticated objects, e. g. track primitives are matched with muon stubs, or tower primitives, to form muon, electron, or jet[20] objects, which then undergo some basic selections.

The eXtremely Fast Tracker (XFT) Using information from the COT, at L1, the eXtremely Fast Tracker (XFT) [84, 85] reconstructs trajectories of charged particles in the (r, φ) plane for each proton-antiproton bunch crossing. The XFT is a custom processor that uses pattern matching to first identify short segments of tracks and then to link them into full-length tracks. After classifying the hits of

[20] A particle jet is a flow of secondary particles produced in a spatially collimated form, as a consequence of the hadronization of partons produced in the hard collisions.

the four axial super-layers in prompt (0-66 ns) or delayed hits (67-220 ns), depending upon the observed drift-time within the cell, track segments are reconstructed in each axial super-layer. A pattern-matching algorithm searches for coincidences between the observed combinations of hits in each super-layer (a minimum of 11 out of 12 hits is required) and a set of predetermined patterns. If a coincidence between segments crossing four superlayers is found, two-dimensional XFT tracks are reconstructed by linking the segments. The segments are compared with a set of about 2,400 predetermined patterns corresponding to all tracks with $p_T > 1.5$ GeV/c originating from the beam-line. The comparison proceeds in parallel in each of the 288 azimuthal 1.25° sectors in which XFT logically divides the chamber. If no track is found using all four super-layers, then the best track found in the innermost three super-layers is output. The track-finding efficiency and the fake-rate with respect to the offline tracks depend on the instantaneous luminosity and were measured to be about 96% and 3%, respectively, at $\mathcal{L} \simeq 10^{31}$ cm^{-2} s^{-1}. The observed momentum resolution is $\sigma_{pT}/p_T \approx 1.7\%$ (GeV/c)$^{-1}$, and the azimuthal resolution is $\sigma_{\varphi_6} \approx 0.3°$, where φ_6 is the azimuthal angle of the track measured at the sixth COT super-layer, located at 106 cm radius from the beam-line. Events are selected for further processing when two XFT-tracks satisfying trigger criteria on basic variables are found. The variables are the product of any combination of two particles charges (opposite or same sign), the opening angle of the two tracks in the transverse plane ($\Delta\varphi_6$), the two particles' transverse momenta and their scalar sum.

Level 2

At L2, an asynchronous system of custom designed hardware processes the time ordered events accepted by the L1. Additional information from the shower maximum strip chambers in the central calorimeter [74] and from the axial layers of the SVX II detector is combined with L1 primitives to produce L2 primitives. A rough energy clustering is done in the calorimeters by merging the energies in adjacent towers to the energy of a seed tower above threshold. L1 track primitives matched with consistent shower maximum clusters provide refined electron candidates whose azimuthal position is known with 2° accuracy. Information from the (r, φ) sides of the SVX II is combined with L1 tracks primitives to form two dimensional tracks with resolution similar to the offline one. Finally, an array of programmable processors makes the trigger decision, while the L2 objects relative to the following event accepted at L1 are already being reconstructed.

Silicon Vertex Trigger (SVT) The Silicon Vertex Trigger (SVT) detects impact parameters of the charged particles, which is faster than fully reconstructing the decay vertices, but still provides information on the lifetime of the decaying particle[86]. This feature is of crucial importance for this analysis, because b-hadrons decays are characterized by longer decay lengths with respect to light

flavour decays or other backgrounds. The full spatial resolution of silicon detectors is used to discriminate $\mathcal{O}(100\ \mu\text{m})$ impact parameters from the $\mathcal{O}(10\ \mu\text{m})$ beam spot. Since the silicon signals are digitized only after the L1 accept decision, the SVT is used at L2. Here the information from the SVX II detector and the output tracks of the XFT are incorporated into the trigger track reconstruction by the SVT. It first finds charge clusters in the silicon, by converting a list of channel numbers and pulse heights into charge-weighed hit centroids. These information are then used by a pattern recognition algorithm, which is formed of two subsequent stages. First, a low-resolution stage is implemented by grouping together adjacent detector channels into "super-bins". Their width in the azimuthal direction is programmable, with 250-700 μm typical values. A set containing about 95% of all super-bin combinations compatible with the trajectory of a charged particle with $p_T > 2$ GeV/c originated from the beam-line ("patterns") is calculated in advance from simulation and stored in a special design memories called Associative Memories (AMs). For each azimuthal sector, the 32,768 most probable patterns are stored. Online, an algorithm detects low-resolution candidate tracks, called "roads", by matching super-bins containing hits with the stored patterns. A road is a combination four excited super-bins in different SVX II layers plus the XFT track parameters, which are logically treated as additional hits (see fig. 2.10 (a)).

A maximum of 64 roads per event, each one having a maximum of 8 hits per super bin, is output. At this stage, pattern recognition is done during detector readout with no additional processing time. The resolution is coarse enough to reduce the fraction of accidental combinations, but fine enough to separate most tracks. Once a track is confined to a road, most of the pattern recognition is done, leaving the remaining ambiguities, as multiple hits in the same superbin, to the stage of track fitting.

In principle, no exact linear relation exists between the transverse parameters of a track in a solenoidal field, and the coordinates at which the track intersects a radial set of at detector planes. But for $p_{\text{T}} > 2$ GeV/c, $|d_0| < 1$ mm and $|\Delta\phi_0| < 150°$, a linear fit biases the reconstructed d_0 by at most a few percent. The trackfitting process exploits this feature by expanding the non-linear constraints and the parameters of the real track to first order with respect to the reference track associated to each road. A linear expansion in the hit positions of both the track parameters and the χ^2 is used. The fit process is thus reduced to computing a few scalar products, which is done within 250 ns per track. The needed constants, which depend on detector geometry and alignments, are evaluated in advance and stored in an internal memory. The output of the SVT are the reconstructed parameters of the twodimensional track in the transverse plane: p_{T}, ϕ_0 and d_0. The list of parameters for all found tracks is sent to L2 for trigger decision.

The SVT measures the impact parameter with a r.m.s. width $\sigma_{d_0}(SVT) \approx 35\ \mu$m with an average latency of 24 μs. This resolution is comparable with the offline one, for tracks not using L00 hits, and yields a distribution of impact pa-

rameter of prompt tracks with respect to the z axis with $\sigma_{d_0}(SVT) \approx 47$ μm when combined with the transverse beamspot size, as shown in fig. 2.10 (b). The SVT

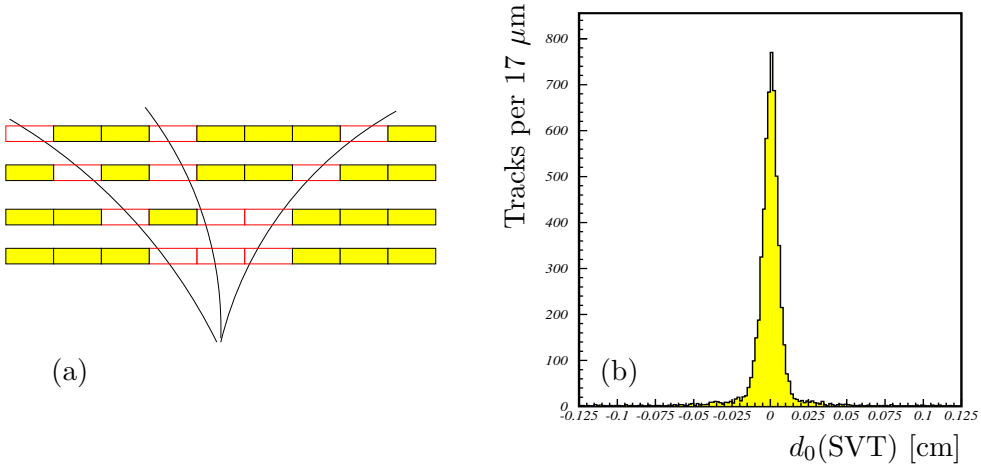

Figure 2.10: Illustration of roads in the transverse plane (a). Impact parameter distribution as measured by SVT (b).

efficiency is higher than 85%.[21] The impact parameter is a quantity measured with respect to the beam. If the actual beam position in the transverse plane is shifted by an amount d_{beam} with respect to the origin of the SVT reference frame, all prompt tracks appear to SVT as having $\mathcal{O}(d_{beam})$ impact parameters. This is relevant since the beam is usually displaced from its nominal $(0, 0, z)$ position. Between TeVatron stores, $\mathcal{O}(500\mu\text{m})$ displacements in the transverse plane and $\mathcal{O}(100\mu\text{rad})$ slopes with respect to the detector axis may occur. In addition, the beam can drift by $\mathcal{O}(10\mu\text{m})$ in the transverse plane even during a single store. However, a simple geometric relation prescribes that the impact parameter of a track, calculated with respect to a point displaced from its production vertex, is a sinusoidal function of its azimuthal coordinate:

$$d_0 = y_0 \cos\phi_0 - x_0 \sin\phi_0, \tag{2.11}$$

where (x_0, y_0) are the coordinates of the production vertex. Using eq. (2.11) SVT measures the actual coordinates of the beam position with respect to the detector system and subtracts them from the measured impact parameters, in order to provide physical impact parameters. Using about 10^5 tracks every 30 seconds, six transverse beam positions (one for each SVXII semi-barrel) are determined online. The six samplings (one for each SVX II barrel) along the z direction provide a measurement of the slope of the beam with respect to the nominal z axis. For the proper measurement of impact parameters, the beam slope is more harmful than the transverse drift, because it breaks the cylindrical symmetry of the system. The SVT does not have access to the z_0 coordinate of tracks. For each track, only the

[21] Efficiency definied as the ratio between the number of tracks reconstructed by SVT and the XFT-macthed offline silicon tracks.

longitudinal coordinate of the SVX II halfbarrel that detected the track is known. But halfbarrels are too long (16 cm) to allow for a reliable correction of the beam slope. When significant slopes are observed, the TeVatron beam division is alerted and they apply a corrective action on the magnets.

Level 3

The digitized output relative to the L2 accepted event reaches L3 via optical fibers and it is fragmented in all subdetectors. The output of L2 is collected by a custom hardware switch that arranges it in the proper order and transfers it to commercial computers, organized in a modular and parallelized structure of 16 subsystems. The ordered fragments are assembled in the event record, a block of data that univocally corresponds to a bunch crossing and is ready for the analysis of the L3 software. The L3 trigger uses a simpler tracking algorithm and preliminary calibrations relative to the ones used off-line and re-tests the criteria imposed by L2. In addition, the difference in z of the two tracks at the point of minimum distance from the primary vertex, Δz_0 , is required not to exceed 5 cm, removing events where the pair of tracks originate from different collisions within the same crossing of p and $\bar{p}$ bunches.

If an event satisfies the L3 requirements, the corresponding event record is transferred to mass storage at a maximum rate of 20 MB/s. A fraction of the output is monitored in real time to search for detector malfunctions, to derive calibrations constants and to graphically display events. The L3 decision is made after the full reconstruction of the event is completed and the integrity of its data is checked.

2.5 Operations and data quality

The proper operation of the detector and the quality of the on-line data-taking is continuously ensured by "crews" of five members of the CDF Collaboration plus one technician who alternate on duty with eight-hours shifts, plus several subdetector experts available on request. The on-line crew, in communication with the Tevatron crew, ensures smooth data-acquisition, monitors the crucial parameters of all subdetector, and intervenes in case of malfunctions. The average data-taking efficiency is 85%. The inefficiency is approximately equally shared in a 5% arising at the beginning of the store, when the detector is not powered while waiting for stable beam conditions, a 5% due to trigger deadtime, and a 5% due to unexpected detector or DAQ problems.

When no beam is present, cosmic-rays runs are taken, or calibrations of the subdetectors are done. During the Tevatron shut-down periods, the crew coordinates and helps the work of experts that directly access the detector.

Each time that at least one of the trigger paths fires, an "event" is labeled with a progressive number. Events are grouped into runs, i. e., periods of continuous data-taking in constant configurations of trigger table, set of active subdetectors

and so forth.[22] Several parameters of the operations (e. g., beam-line position and slope, set of calibrations, etc.) are stored in the database on a run-averaged format.

All data manipulations occurring some time after the data are written to permanent memories are referred to as *off-line* processes, as opposed to the on-line operations which take place in real time, during the data-taking. The most important off-line operation is the processing with a centralized *production* analysis that generates collections of high-level physics objects suitable for analysis, such as tracks, vertices, muons, electrons, jets, etc. from low-level information such as hits in the tracking subdetectors, muon stubs, fired calorimeter towers, etc. [87]. During the production, more precise information about the detector conditions (e. g., calibrations, beam-line positions, alignment constants, masks of malfunctioning detector-channels, etc.) and more sophisticated algorithms are used than those available at the Level-3 of the trigger. The production may be repeated when improved detector information or reconstruction algorithms become available: this typically occurs once or twice every year. The reprocessing uses large farms of commercial processors that reconstruct approximately 10^7 events per day employing approximately 2–5 s per event with 1 GHz CPU.[23] The added information increases the event size by typically 20% after production.

To ensure homogeneous data-taking conditions, each run undergoes a quality inspection. On-line shift operators, off-line production operators, and subdetector experts certify in what fraction of data the running conditions for all relevant subdetectors are compliant to physics-quality standards.

When detectable problems of the detector occur, the data-taking is quickly stopped, so very short runs are likely to contain corrupted data. Runs with fewer than 10^8 live Tevatron clock-cycles, or fewer than 10^4 (10^3) Level-1 (Level-2) accepts, or containing data corresponding to an integrated luminosity $\int \mathcal{L}dt < 1$ nb^{-1} are excluded from physics analysis. On-line shift operators further exclude the runs in which temporary or test trigger tables were used.[24] Runs whose data underwent problems or software crashes during the production are excluded off-line.

Accurate integrated luminosity measurements are ensured in physics-quality data by requiring the CLC to be operative during the data-taking and by verifying that a set of luminosity and beam-monitor probe quantities are within the expected ranges. Shift operators ensure that Level-1 and Level-2 trigger operate correctly and that the rate of SVXII data corruption errors is smaller than 1%.[25]

[22] The data acquisition might need to be interrupted and recovered for several motivations, including the need for enabling or disabling a subdetector, the need for a change in the trigger table, a problem in the DAQ chain etc.

[23] The event size, and the processing-time increase roughly linearly with the instantaneous luminosity.

[24] It is sometimes necessary to test new configurations of the trigger selections in a real data-taking condition to monitor trigger rates, performance and so on.

[25] The read-out of the silicon detector and the proper integration of the information in the on-line infrastructure is a complex operation which, occasionally, leads to a certain fraction of data to be

SVT experts verify that the on-line fit and subtraction of the beam position is done correctly and that the SVT occupancy is within the expected limits. In addition, higher level quantities, such as event yields of $J/\psi \to \mu^+\mu^-$, $D^0 \to K^-\pi^+$, and $D^{*+} \to D^0\pi^+$ decays are monitored on-line and are required to be within the expected ranges. For analyses that use COT information, the minimum integrated luminosity required is 10 nb^{-1} and the fraction of noisy COT channels is required to be smaller than 1%.

improperly processed.

Chapter 3

Sample selection

This chapter describes the reconstruction and selection of the sample of $B \to h^+h'^-$ decay candidates used in the measurements of $\mathcal{C}P$ asymmetries.

3.1 Introduction

The analysis of $B \to h^+h'^-$ decay modes uses the full CDF data sample, collected between December 2004 (run 190697) and September 2011 (run 312510). After the application of standard CDF data-quality requirements (see sec. 2.5), the sample size corresponds to an integrated luminosity of 9.3 fb^{-1}. $B \to h^+h'^-$ decay modes have a relatively simple topology: two charged particles decay from a B^0 or a B_s^0 meson or a Λ_b^0 baryon. The $B \to h^+h'^-$ decays lack most of the standard discriminating features: there are no leptons in the final states, so it is impossible to use the good CDF muon and electron identification capability; in addition, there aren't intermediate resonances that could be used to provide useful kinematics constraints. Furthermore, the final states are pions, protons or kaons, which are the most common particles present in the background: the signal to background ratio in these conditions is $\mathcal{O}(10^{-9})$. As explained, the trigger bandwidth available at CDF II is not sufficient to record all events, so it is necessary to select on-line the interesting decay modes. The strategy to reject undesirable events exploits the information of the decay time of the heavy particles, subject of this analysis. The b-hadrons decay length is $\mathcal{O}(400\ \mu m)$, typically longer with respect to the light flavour or other backgrounds decays. If the momentum of the b-hadron has a sufficiently large component in the plane transverse to the beam-line, the displacement between production and decay positions of the b-hadron can be measured with the silicon tracker. The Displaced-Tracks Trigger introduced in sec. 2.4 is therefore used in this analysis.

3.2 The displaced-tracks trigger

The data have been collected with the Displaced-Tracks Trigger, that is composed by several trigger *paths*. A trigger path is a well defined sequence of Level-1, Level-2, Level-3 requirements. Specifically, this analysis uses more than 50 different trigger paths, that can be classified into two different groups sharing similar requirements: the `B_PIPI` (or `med`) and the `B_PIPI_HIGHPT` (or `high`) paths. The main difference between the two groups are the different requirement in transverse momentum of the two tracks ($p_{\mathrm{T}}(1,2)$) and $\sum p_{\mathrm{T}} = p_{\mathrm{T}}(1)+p_{\mathrm{T}}(2)$. At high luminosity, with higher purity, but less efficiency, the `B_PIPI_HIGHPT` selection is employed. As the luminosity decreases over the course of a store, trigger bandwidth becomes available and the `B_PIPI` is utilized to fill the available trigger bandwidth and maximize the signal yield. In the following, we will briefly describe the two trigger paths requirements. At each level of the trigger, more complete information are added, to obtain higher efficiency while having larger background rejection. This is achieved using parameters capable of discrimination between our $B \to h^{+}h^{'-}$ signals and background. Kinematics requirements are applied on the sample to select only candidates in the desirable kinematic region. Additional information, such as the track's charge, the opening angle between tracks and the impact parameter, are applied to reject background events having different distributions. Other requirements, such as the tracks fit quality or the decay length, complete the set of requirements, as reported in tab. 3.1.

Version	Level 1	Level 2	Level 3
`med`	$p_{\mathrm{T}}(1,2) > 2.0$ GeV/c	confirmed	confirmed
	$\sum p_{\mathrm{T}} > 5.5$ GeV/c	confirmed	confirmed
	Track's opposite charge	confirmed	confirmed
	$0° < \Delta\phi_6 < 135°$	$20° < \Delta\phi_0 < 135°$	confirmed
		0.01 cm $< d_0(1,2) <$ 0.1 cm	confirmed
		$L_T(B) > 200$ μm	confirmed
		$\lvert d_0(B)\rvert < 140$ μm	confirmed
		$\chi^2_{SVT} < 25$	confirmed
			$\lvert\Delta z_0\rvert < 5$ cm
			$\lvert\eta(1,2)\rvert < 1.2$
			$4 < m_{\pi\pi} < 7$ GeV/c^2
`high`	$p_{\mathrm{T}}(1,2) > 2.5$ GeV/c	confirmed	confirmed
	$\sum p_{\mathrm{T}} > 6.5$ GeV/c	confirmed	confirmed

Table 3.1: Selections for the two displaced triggers used in this work. The two trigger paths share all the requirements, except for the p_{T} and $\sum p_{\mathrm{T}}$ requirements as discussed. The labels (1,2) refers to requirements applied to both tracks, while the other criteria refer to track-pairs. Finally $m_{\pi\pi}$ is the invariant mass calculated in assumption of two pions in the final state.

Over the course of a TeVatron store, the available trigger bandwidth varies because trigger rates decrease as instantaneous luminosity falls. Higher trigger rates at high luminosity arise from both a larger rate for real physics processes as well as a larger fake trigger rate due to multiple $p\bar{p}$ interactions. To fully exploit the available trigger bandwidth, for the work of this thesis we employed two prescaled[1] variants of the displaced-tracks trigger. In addition, to better use the trigger bandwidth, a dynamic prescale (DPS) has been added to particularly high trigger accept-rates. The DPS adjusts the prescale factor according to the instantaneous luminosity, since the instantaneous luminosity of the store decreases with time. This is due to the interactions of the proton and anti-proton bunches with the residual gas in the beam-pipe and due to the degradation process of the transverse section of bunches in many hours of collisions. The dynamic prescale factor decreases along the store to keep the trigger bandwidth fully occupied.

`B_CHARM` trigger paths

In this work we also used different data samples, as control samples or to extract efficiency corrections. One of the sample used is the $D^0 \to h^+h'^-$ decay modes, where the h can be a pion or a kaon. These decays are kinematically and topologically similar to the $B^0_{(s)} \to h^+h'^-$ decay modes: in both the decay channels start with a meson (the b-hadron or the D^0) and end with pions or kaons. Also, the kinematical requirements in the trigger selections are similar, making the $D^0 \to h^+h'^-$ a reliable control sample. The selection used to collect the $D^0 \to h^+h'^-$ sample is collectively called `B_CHARM`: to fully exploit the available trigger bandwidth, there are three main variants of the displaced tracks trigger. The three selections are referred to as the low p_{T}, medium p_{T} and high p_{T} selections, according to their requirements on minimum transverse momentum. The `B_CHARM` medium p_{T} trigger path has similar requests to the `B_PIPI` trigger paths, while the `B_CHARM` high p_{T} is similar to the `B_PIPI_HIGHPT`. Table 3.2 summarizes the requirements.

3.3 Extraction of the $B \to h^+h'^-$ signal

The first step of the off-line analysis consists in applying a baseline selection to the events collected by the `B_PIPI` and `B_PIPI_HIGHPT` trigger paths. Trigger requirements are reapplied using high-resolution off-line quantities to remove the $B \to h^+h'^-$ candidates not satisfying the trigger selection.

3.3.1 Tracks

This analysis is based on tracks. Tracks are reconstructed by the standard CDF II production executable using LØØ, SVXII, ISL and COT hits, the detailed magnetic

[1] Prescaling a trigger of a factor $< N$ means to accept randomly 1 event every N events.

Version	Level 1	Level 2	Level 3
Low	$p_{\mathrm{T}}(1,2) > 2.0$ GeV/c $\sum p_{\mathrm{T}} > 4$ GeV/c Track's opposite charge $0^\circ < \Delta\phi_6 < 90^\circ$	$p_{\mathrm{T}}(1,2) > 2.0$ GeV/c $\sum p_{\mathrm{T}} > 4$ GeV/c Track's opposite charge $2^\circ < \Delta\phi_0 < 90^\circ$ 100 μm $< d_0(1,2) <$ 1000 μm $L_T(B) > 200$ μm	$p_{\mathrm{T}}(1,2) > 2.0$ GeV/c $\sum p_{\mathrm{T}} > 4$ GeV/c Track's opposite charge $2^\circ < \Delta\phi_0 < 90^\circ$ 100 μm $< d_0(1,2) <$ 1000 μm $L_T(B) > 200$ μm $\lvert\Delta z_0\rvert < 5$ cm $\lvert\eta(1,2)\rvert < 1.2$
Medium	$p_{\mathrm{T}}(1,2) > 2$ GeV/c $\sum p_{\mathrm{T}} > 5.5$ GeV/c	$p_{\mathrm{T}}(1,2) > 2$ GeV/c $\sum p_{\mathrm{T}} > 5.5$ GeV/c	$p_{\mathrm{T}}(1,2) > 2$ GeV/c $\sum p_{\mathrm{T}} > 5.5$ GeV/c
High	$p_{\mathrm{T}}(1,2) > 2.5$ GeV/c $\sum p_{\mathrm{T}} > 6.5$ GeV/c	$p_{\mathrm{T}}(1,2) > 2.5$ GeV/c $\sum p_{\mathrm{T}} > 6.5$ GeV/c	$p_{\mathrm{T}}(1,2) > 2.5$ GeV/c $\sum p_{\mathrm{T}} > 6.5$ GeV/c

Table 3.2: Selections for the `B_CHARM` triggers used in this work. When the three triggers share the requirements, only the difference are reported. The labels (1,2) refers to requirements applied to both tracks, while the other criteria refer to track-pairs.

map of the tracking volume, and taking into account the measured angular and translation mis-alignments among LØØ, SVXII, ISL, COT and the beam-line. Since the measurements described in this thesis are not lifetime-based, but they are decay rate measurements and since the lifetime information enters only in the selection (see tab. 3.1) through the cuts on impact parameter and decay transverse length, the improvement due to the LØØ hits is marginal, as already proved in the previous version of this analysis [88]. We therefore used only tracks whose reconstruction included silicon hits of SVXII, ISL. Mis-alignments and noise hits in the silicon detectors and in the COT cause a contamination of fake or mis-reconstructed tracks. The fraction of such undesirable tracks was reduced by selecting tracks reconstructed using at least 40 hits in the COT layers. Each track was also required to result from a converged helix-fit with a positive error matrix.

The default 3-D silicon tracking code uses a stepwise fit that starts from a COT track pointing to the silicon detector fiducial volume and progressively adds hits within the search road[2] as the fit moves from the outer silicon radii to the inner radii. We required the tracks to be associated to at least 3 hits in the axial, at least 2 hits in 90° and at least 1 hit in small angle stereo silicon super-layers. The requirement of tracks with sufficient $r - z$ information reduces the contamination from those tracks coming from two distinct heavy-flavors in the event, which have sizable impact parameter but are separated along the z direction. This additional requirement has a $\sim 90\%$ efficiency on signal yield while it reduces the background by a factor $\simeq 2$. The error matrix of the track fit in the COT is estimated by default disregarding the effect of multiple scattering in the COT. According to the standard CDF prescriptions, we compensated for this approximation by refitting the tracks, after rescaling the covariance matrix of the COT track with an appropriate set of empirical scale factors. The rescaled COT track is used to seed the refit of the combined COT-SVXII tracks. The refitting uses the algorithm based on

[2]Silicon hits are searched in a 4σ-wide extrapolation of the COT track in the silicon layers, where σ are the uncertainties on the estimated track parameters.

the Kalman filtering [89] and includes energy-loss corrections for kaons, pions and protons, according to the chosen mass assignment for each particle. The refitting procedure, the tracking alignments, and the GEANT description of the detector material have been carefully studied and validated by independent analyses for the measurement of b-hadron masses [90].

3.3.2 Trigger confirmation

Since SVT tracks are reconstructed with a different fitting algorithm with respect to the off-line tracks, the sample selected by the off-line analysis may contain candidates which did not satisfy the trigger selection ("volunteers"). Since the Monte Carlo does not reproduce volunteers, we need to exclude them also from data. They were excluded by requiring the matching[3] between the off-line track pair forming the $B \to h^+h'^-$ candidate and two SVT tracks in each event; then the complete set of trigger requirements was applied to the SVT quantities of the matched tracks, thus repeating the real trigger decision in the off-line analysis.

3.3.3 Reconstruction of $B \to h^+h'^-$ candidates

The off-line reconstruction of $B \to h^+h'^-$ candidates was solely based on tracking, disregarding any form of particle identification. The use of particle identification is reserved for later, within an overall fit of the sample, in order to keep a high selection efficiency. In each event, the two particle invariant mass was computed for all possible pairs of oppositely-curved tracks satisfying the criteria described in sec. 3.3.1 and 3.3.2. We used the measured momenta and we arbitrarily assigned the charged-pion mass to both tracks. The two tracks were constrained by the vertex fit algorithm to originate from a common vertex in the 3-D space. In case of a converged vertex-fit with satisfactory quality, the pair was promoted to a $B \to h^+h'^-$ candidate, and retained for further processing. During reconstruction we reapplied the trigger selection off-line quantities in addition with other kinematics informations: for example, we rejected tracks reconstructed outside the SVT fiducial acceptance ($|\eta| \leq 1$), and pairs with a positive product of impact parameters. The cuts optimization procedure has been specifically made to optimize the probability of discovery and limit setting of the $B_s^0 \to K^-\pi^+$ mode. It was developed in the previous version of this analysis: a more detailed description of the optimization technique, based on the Minimum Variance Bound method, is reported in [88]. The selection is also well-suited to measure all the observables related to rare modes ($B_s^0 \to \pi^+\pi^-$, $B^0 \to K^+K^-$, $\Lambda_b^0 \to p\pi^-$, and $\Lambda_b^0 \to pK^-$). In the final set of cuts the trigger requirements (see tab. 3.1) were tightened, and two variables with good separation power signal to background are added: the isolation of the B candidate ($I(B)$) and the 3-D vertex quality ($\chi^2_{3D}(B)$).

[3] The algorithm required proximity in curvature and azimuthal opening angle between SVT tracks and off-line tracks.

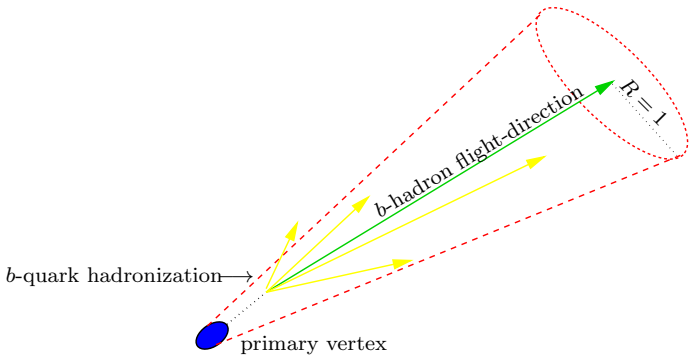

Figure 3.1: Illustration of the fragmentation of a b-quark into a b-hadron. The isolation cone is shown in red, the directions of the charged particles produced in the fragmentation are shown in yellow.

Isolation of the B meson ($I(B)$)

One of the useful variable used to discriminate the $B \to h^+h'^-$ signals from the background in the off-line selection is the "isolation". Given their hard fragmentation, b-hadrons tend to carry a larger fraction of the transverse momentum of the particles produced in the fragmentation, with respect to lighter hadrons [91]. We used an estimator of the fraction of momentum carried by the b-meson:

$$I(B) = \frac{p_{\mathrm{T}}(B)}{p_{\mathrm{T}}(B) + \sum\limits_{i \neq j : B \to j}^{R} p_{\mathrm{T}}(i)}, \tag{3.1}$$

where the sum in the right-hand term of the denominator runs over all fragmentation tracks, identified as tracks (other than those of the B candidate decay-chain) satisfying standard track-quality requirements and found in a local region around the flight direction of the B candidate. Such region is parameterized as a cone in the $(\eta - \phi)$ space, unitary in radius ($R = \sqrt{\phi^2 + \eta^2} = 1$), whose apex is the primary vertex and the axis collinear with $\vec{p}_{\mathrm{T}}(B)$ (see fig. 3.1). When the decay products of the b-meson are contained in the cone, $I(B)$ is just the fraction of transverse momentum within the cone carried by the b-meson. Candidates with large isolation are more likely to be b-mesons than candidates with low isolation, as shown by the comparison in fig. 3.2. The introduction of the isolation adds further complexity in the analysis: its distribution depends on the mechanism of hadronization of the b-quark, which is not described by the signal-only simulation, as will be discussed in chap. 4. Therefore real data has been used to characterize this observable; for more details, see [88].

3-D vertex quality (χ^2_{3D})

Vertexing includes a large amount of information and it is sensitive to many issues, including alignments, geometry and track parameter errors. A quantity that sum-

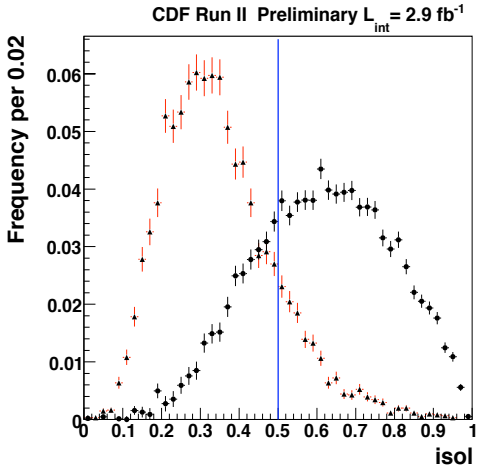

Figure 3.2: Isolation distribution for background-only events (red triangles) extracted from high mass sidebands and signal events (black dots) extracted from a sideband subtraction procedure. The line shows the cut required in the final selection of the sample.

marizes all information of the three-dimensional vertex fit quality is the $\chi^2/1$ d.o.f. of the vertex fit. The χ^2_{3D} is the minimum χ^2 resulting from the vertex fit minimization, when in the minimization all 3-D tracking information from the drift chamber and silicon detectors is used. This variable rejects a large amount of combinatorial background with an high efficiency for the signal.

List of cuts

The final selections are reported in tab. 3.3. The final samples contain just one $B \to h^+h'^-$ candidate per event. The invariant mass distribution of the candidates (with the pion mass assigned to both tracks) is shown in fig. 3.3.

3.3.4 Sample composition

The invariant $\pi\pi$-mass distribution provides a first insight on the sample composition. Contributions to the background may in principle include mixture of rare events from heavy-flavors, light-quarks, resolution tails and so forth. In the signal region, at about the nominal masses of the b-mesons, we expect a peak corresponding to the presence of the $B \to h^+h'^-$ decay channels. To give a rough estimate of the signal yield and of the purity of the sample, a simple χ^2-binned fit was performed. Two Gaussian shapes were assumed to parametrize the two "signal" peaks, while two different distributions were used to parameterize the distinct background components visible in the distribution: an exponential for the background sparse in

Quantity of the track	Units	Requirement
Axial silicon hits	–	≥ 3
90° silicon hits	–	≥ 2
Small angle stereo silicon hits	–	≥ 1
Total COT hits	–	≥ 40
p_{T}	GeV/c	$> 2.0(2.5)$
$\lvert\eta\rvert$	–	< 1.0
Impact parameter	μm	[120, 1000]
Quantity of the candidate		
Product of track's charges	e^2	-1
Product of track's impact parameter	$\mu\mathrm{m}^2$	< 0
Transverse decay length	μm	> 350
Scalar sum of track's p_{T}	GeV/c	> 5.5 (6.5)
Impact parameter	μm	< 60
Track's azimuthal separation	Degrees	[20°, 135°]
$\lvert\eta\rvert$	–	< 1.0
Isolation	–	> 0.525
χ^2_{3D} of the vertex fit	–	< 5
$m_{\pi^+\pi^-}$	GeV/c^2	[5.0, 5.8]

Table 3.3: Summary of the final selection requirements.

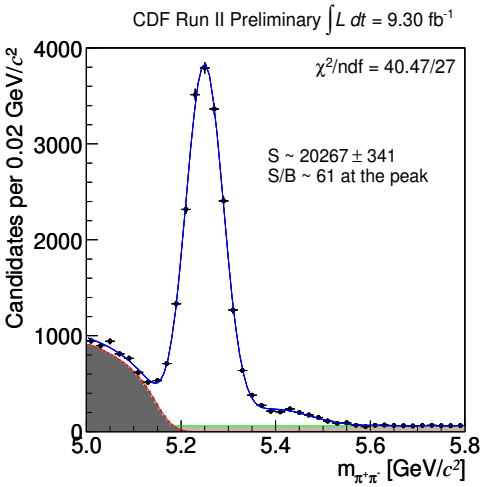

Figure 3.3: Invariant $\pi\pi$-mass distribution of the events passing the final selection. Two Gaussians (signal) plus exponential (combinatoric background, light grey) plus a smeared Argus (physics background, dark grey) fit function is overlaid. For Argus function definition see text or Ref. [92].

all the mass window and an *Argus* function[4] convoluted with a Gaussian distribu-

[4] $\mathrm{Argus}(x;c,m) = \frac{1}{\mathrm{Norm}} \cdot [xe^{-c(\frac{x}{m})^2}\sqrt{1-(\frac{x}{m})^2}]$ if $x \leq m$, $\mathrm{Argus}(x;c,m) = 0$ if $x > m$. See Ref. [92].

tion centered at zero with a width equal to the mass resolution (≈ 25 MeV/c^2) for the events with $m_{\pi^+\pi^-} < 5.16$ GeV/c^2, where a change in the slope is clearly visible. We estimate a yield of $20,267 \pm 341$ $B \to h^+h'^-$ events. The standard deviation of the main gaussian is $\sigma = 39.8 \pm 0.4$ MeV/c^2 and the purity is $S/B \approx 61$ at the peak.

Signal composition

The observed width of the main gaussian, corresponding to the region of $B^0_{(s)} \to h^+h'^-$ signal, is approximately 39 MeV/c^2, much larger than what expected from the simulation for a single decay $\approx$ 25 MeV/c^2 (e.g., $B^0 \to \pi^+\pi^-$ or $B^0 \to K^+\pi^-$). This indicates that the main peak visible in fig. 3.3 is the overlap of signals from different B^0 and B^0_s decay modes with different proportions. Theoretical and experimental knowledge at the time of this analysis (see tabs. 1.4 and 1.5) predict sizable contributions of $B^0 \to \pi^+\pi^-$, $B^0 \to K^+\pi^-$, and $B^0_s \to K^+K^-$ for the main bulk near 5.25 GeV/c^2, while $B^0_s \to K^-\pi^+$, $\Lambda^0_b \to p\pi^-$, and $\Lambda^0_b \to pK^-$modes populate a smaller peak at a higher masses (5.4 - 5.5 GeV/c^2) than the main peak. Smaller contributions come also from the $B^0_s \to \pi^+\pi^-$ and the yet unobserved $B^0 \to K^+K^-$ modes. A $B^0_s \to \pi^+\pi^-$ signal is expected at the nominal B^0_s mass (5.3663 GeV/c^2), while a $B^0 \to K^+K^-$ signal would appear as a small enhancement around 5.18 GeV/c^2.

Background composition

The invariant $\pi\pi$-mass distribution indicates the presence of two different kinds of backgrounds:

combinatorial background – it is mostly composed of random pairs of charged particles, displaced from the beam-line, accidentally satisfying the selection requirements. Its dominant sources include generic QCD background of light-quark decays, lepton pairs from Drell-Yan processes, pairs of mis-measured tracks, combinations of a mis-measured track with a track from an heavy-flavor decay, or combinations of two tracks originated from two independent heavy-flavor decays of the event ($b\bar{b}$ and $c\bar{c}$ production). This is consistent with the smooth, slowly decreasing invariant $\pi\pi$-mass distribution in the signal sample for masses above 5.5 GeV/c. In this region, as well as in the signal region, the combinatorial component is the prominent source of background.

Partially-reconstructed heavy-flavor decays – (referred to also as "physics background") a change in the slope of the mass distribution of the signal sample, at masses just smaller than the signal mass, indicates the presence of an additional background source. This contribution has been interpreted as mis-reconstructed b-hadron decays: these are multi-body b-hadron decays (e. g., $B^0 \to \rho^\mp\pi^\pm$, $B^0 \to \rho^-K^+$, $B^0_s \to \rho^\mp\pi^\pm$, $B^0_s \to \rho^+K^-$ and many others), in

which only two tracks were reconstructed, resulting in the typical shoulder-shape, that is suppressed around 5.15 GeV/c^2, because their contribution is kinematically limited to the $m_{\pi^+\pi^-} < m_{B^0_{(s)}}$ region.

However, this one-dimensional binned fit is only a qualitative tool to estimate the yield and the purity of the sample in a quick way. The Gaussian distributions used to describe the signal peaks are not adequate to describe the overlapping of the different signals. In order to obtain the branching fraction measurements, that are the subject of this analysis, it is necessary to separate the contributions of the different signal components. Therefore, a very accurate study of $B \to h^+h'^-$ simulated samples is needed to understand the sample composition. Chapter 4 describes the $B \to h^+h'^-$ simulated samples obtained using the CDF official Monte Carlo, and how they were specifically tuned for the purposes of the analysis.

Chapter 4

Monte Carlo Simulation

A sample of simulated $B \to h^+h'^-$ decays is needed to study the kinematics information of the different signal components. We used the official CDF II simulation, that takes into account all the changes of detector (changes of the silicon coverage, of the XFT and the SVT configurations) and trigger configurations during the data-taking. We provide here a short overview of the CDF II simulation used in this analysis, while more details can be found in [93].

4.1 CDF II simulation

Hadrons generation

The BGENERATOR[94] and the PYTHIA[95] packages can be used to generate the $b-$hadrons. The BGENERATOR package simulates only the production and the decay of b-hadrons: no fragmentation products, pile-up events[1] or collision remnants are simulated, allowing a fast processing. Thus no information about QCD backgrounds or fragmentation can be extracted from the simulated samples. In the PYTHIA package this information is available, but a large amount of computing power would be needed to generate background samples of adequate size for this analysis, with $\mathcal{O}(10^9)$ rejection factors of background. Also, using this package in precision measurement would require extensive checking. So we decided to use the simpler approach of using BGENERATOR to simulate the signals, while we extracted the background information from collision data.

Given a spectrum in rapidity and transverse momentum, BGENERATOR can create and fragment heavy quarks (a single q or a qq pair). The single quark generation follows the theory from P. Nason, S. Dawson and R. K. Ellis [96, 97], while the quark pair generation the ones from M. Mangano, P. Nason and G. Ridolfi [98].

We generated 30 millions events for each decay ($B^0 \to \pi^+\pi^-$, $B^0 \to K^+\pi^-$,

[1] During a single bunch crossing there may be more than one registered collisions. These multiple interactions are said to be "piling-up'.

$\overline{B}^0 \to K^-\pi^+$, $B^0 \to K^+K^-$, $B_s^0 \to \pi^+\pi^-$, $B_s^0 \to K^-\pi^+$, $\overline{B}_s^0 \to K^+\pi^-$, $B_s^0 \to K^+K^-$, $\Lambda_b^0 \to p\pi^-$, $\overline{\Lambda}_b^0 \to \overline{p}\pi^+$, $\Lambda_b^0 \to pK^-$, and $\overline{\Lambda}_b^0 \to \overline{p}K^+$). We included also the effect of QED radiation in the final state with the loss of energy from soft photon emission from charged final state particles (final state radiation FSR). This effect is modeled in Monte Carlo through PHOTOS [99, 100], an algorithm that includes leading and next to leading order calculations of the QED effects of the soft-photon radiation. For the $\Lambda_b^0 \to ph^-$ modes we turned off the soft photon emission because of the presence of a proton in the final state. The expected yield of $\Lambda_b^0 \to ph^-$ decays are about a factor 10 smaller than the $B^0 \to \pi^+\pi^-$ yield, thus we neglect the effect of the FSR (already small) for these rare modes.

Fragmentation was turned off and the rapidity and $p_{\rm T}(B)$ distributions were taken from an external histogram containing a smooth fit to the data published in CDF Run II measurement [101], according to the CDF standard prescription. Decays were forced to $B_{(s)}^0 \to h^+h'^-$ and $\Lambda_b^0 \to ph^-$ using the EvtGen package and we took into account the differences between decays, as the input masses and the lifetimes.

Input masses and lifetimes in the Monte Carlo

Since the selection relies on both impact parameter and transverse decay length cuts, the choice of the B lifetimes in the Monte Carlo is important for the correct determination of the efficiencies. We use the PDG 2010 [51] value of $c\tau(B^0) = 457.2 \pm 2.7$ μm for the B^0 lifetime and $c\tau(\Lambda_b^0) = 417 \pm 11$ μm for the Λ_b^0 lifetime. For the $B_s^0 \to K^-\pi^+$ lifetime we used the PDG 2010 value measured on semileptonic decays: $c\tau(B_s^0) = 441 \pm 8$ μm. The choice of the $c\tau(B_s^0 \to K^+K^-)$ is less straightforward because in principle it depends both on the $\mathcal{C}P$ content of this mode and on the value of $\Delta\Gamma_s/\Gamma_s$ which are both unknown so far. One can write:

$$\Gamma(B_s^0(t) \to K^+K^-) + \Gamma(\overline{B}_s^0(t) \to K^+K^-) \propto R_H e^{-\Gamma_{H(s)}t} + R_L e^{-\Gamma_{L(s)}t} \qquad (4.1)$$

where R_H (R_L) is the relative fraction of "heavy" ("light") mass eigenstate for this mode. However in literature [102] the $B_s^0 \to K^+K^-$ mode is expected to be dominated by the "short" eigenstate, with a "long"eigenstate contribution smaller than 5%. Therefore we calculated the value of $c\tau(B_s^0 \to K^+K^-)$ used in our analysis using the following assumptions:

- the $B_s^0 \to K^+K^-$ mode is 100% "short" eigenstate;
- $\Delta\Gamma_s/\Gamma_s = 0.092^{+0.051}_{-0.054}$ [51];
- the semileptonic widths for B_s^0 and B^0 mesons are equal, according to the Standard Model: $\Gamma_s = \Gamma_d$.

From these assumptions we extracted the following relation:

$$c\tau(B_s^0 \to K^+K^-) = \frac{c}{\Gamma_s^{short}} = \frac{c}{\Gamma_s + \Delta\Gamma_s/2} = \frac{c}{\Gamma_d + 0.12 \cdot \Gamma_d/2} \quad (4.2)$$

$$= [437 \pm 2.7\ (\Gamma_d) \pm 11\ (\Delta\Gamma_s^{SM})]\ \mu m \quad (4.3)$$

We split the uncertainty on $c\tau(B_s^0 \to K^+K^-)$ into the part coming from the uncertainty on Γ_d, which contributes 0.6%, and the part coming from the 0.05 uncertainty on $\Delta\Gamma_s/\Gamma_s$ expected from the SM. We assume $c\tau(B_s^0 \to \pi^+\pi^-) = c\tau(B_s^0 \to K^+K^-)$, because $\pi^+\pi^-$ final state is a CP even (+1) eigenstate as the $B_s^0 \to K^+K^-$.

Table 4.1 reports the input masses and lifetimes used to generate the simulated samples. The values are taken from PDG 2010 [51]. Once the generation is done, we

Mode	m [MeV/c^2]	$c\tau$ [μm]
B^0	5279.5	457
$B_s^0 \to \pi^+\pi^-$	5366.3	437
$B_s^0 \to K^-\pi^+$	5366.3	441
$B_s^0 \to K^+K^-$	5366.3	437
Λ_b^0	5620.2	417

Table 4.1: Summary of the input masses and lifetimes in the simulation.

proceed in simulating the detector characteristics, in order to reproduce interactions with materials and subdetectors responses. GEANT takes care of the full detector simulation.

Detector and trigger simulation

The generated sample was processed using the GEANT simulation modeling the detector geometry and materials (GEANT v3, [103]). GEANT receives in input the positions, the four-momenta and the identities of the simulated particles with enough lifetime to exit the beam pipe. It simulates their paths in the detector, modeling their interactions (bremsstrahlung, multiple scattering, nuclear interactions, photon conversions...) and the consequent generation of signals on a single channel basis. Then the actual trigger logic is simulated. The detector and trigger configuration undergo variations during data-taking (for example, after a TeVatron shut down period). For a more detailed simulation of the actual experimental conditions, the simulation has been interfaced with the online database that reports, on a run by run basis, all known changes in configuration (position and slope of the beam line, relative misalignments between subdetectors, trigger table used...) and local or temporary inefficiencies in the silicon tracker (active coverage, noisy channels...). This allows a realistic simulation for any possible subset of data. The output of the simulated data mimics the structure of collision data, allowing the reconstruction with the same programs used for real collision data.

4.2 $B \to h^+h'^-$ simulated sample data-tuning

The official CDF Monte Carlo is sophisticated enough to reproduce with good accuracy real collision data samples. However, since by construction there exists no simulation that is able to reproduce perfectly the data, we need to investigate possible differences between data and Monte Carlo. For example, we know that the Monte Carlo has no access to the information relative to the prescales applied during the data-taking: as a consequence, we need to rescale the simulated distribution using information from data. Another tuning has to be done for the mass resolution of the simulated distributions, found to be narrower with respect to the correspondent data ones. Next subsections sec. 4.2.1, sec. 4.2.2, and sec. 4.2.3 describe the tunings performed on the Monte Carlo distributions.

4.2.1 $B \to h^+h'^-$ sample trigger composition

As introduced in sec. 3.2, the $B \to h^+h'^-$ sample is collected using two different trigger paths, `med` and `high`, whose main differences are the following requirements:

$$\begin{array}{rcl} \sum p_{\mathrm{T}} & > & 5.5 \text{ GeV}/c, \quad p_{\mathrm{T}}(1,2) > 2.0 \text{ GeV}/c \quad (\texttt{med}) \\ \sum p_{\mathrm{T}} & > & 6.5 \text{ GeV}/c, \quad p_{\mathrm{T}}(1,2) > 2.5 \text{ GeV}/c \quad (\texttt{high}). \end{array} \tag{4.4}$$

The `high` requirements are tighter than the `med` ones, and therefore all the events triggered by the `high` path would also be triggered `med` path. A pictorial representation is given in fig. 4.1(a). The presence of prescales complicates this picture. Prescaling a trigger of a factor N means to accept randomly 1 event every N events, therefore it is possible that one event satisfying the `high` path requirements (thus automatically satisfying `med` path requirements) is not accepted by the `med` path. This feature makes our sample the result of a linear combination between the two different kinematics (scenarios) where the relative fractions are known thanks to the trigger bits[2]. There are approximately an overlap of 41% ($\mathrm{M} \cap \mathrm{H}$) of events in common, a fraction of exclusive `med` of 26% ($\mathrm{M} \cap \bar{\mathrm{H}}$), and a fraction of exclusive `high` of 33% ($\bar{\mathrm{M}} \cap \mathrm{H}$). Using this notation the total sample is $\mathrm{M} \cup \mathrm{H}$. A pictorial representation is given in fig. 4.1(b).

We described how the only difference between the `med` and `high` paths are the different thresholds in p_{T}(tracks) and in $\sum p_{\mathrm{T}}$ observables. Consequently, the momenta related distributions show an enhancement, in correspondence of the turn on of the trigger (see fig. 4.2). The knowledge of this characteristic is crucial in our analysis, since the momentum distributions will be used in a fit of composition (as will be described in sec. 5.6). To avoid technical difficulties in the parameterization of the distributions with the enhancement, we divided the sample in two statistically independent sub-samples $\texttt{A} \equiv \mathrm{M}$ and $\texttt{C} \equiv \bar{\mathrm{M}} \cap \mathrm{H}$: using this notation the total sample is $\texttt{A} \cup \texttt{C}$ (see fig. 4.3). By definition the first sample `A` is pure `med` kinematics,

[2] That is, the numerical label associated to a unique trigger path.

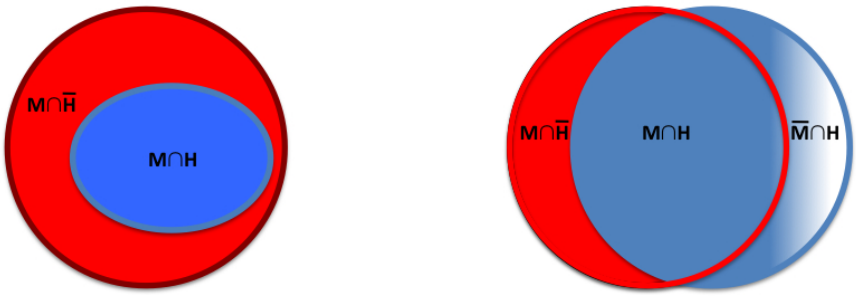

(a) (b)

Figure 4.1: Illustration of trigger scenarios relationships in absence of prescales (a), and in presence of prescales (b). In red, the events triggered exclusively by `med` path, in blue events triggered simultaneously by `med` and `high` paths, and in light blue events triggered exclusively by `high` path.

with events triggered by `med` path, and this is independent on the trigger bit of the `high` path. The second sample `C` is a pure `high` kinematics, since these events were triggered (*unprescaled bit*) simultaneously by the `med` and the `high` paths, but they are written on tape (*prescaled bit*) only as `high`. For these reasons, the two samples are independent samples, with different features. Thus all the technical work of this thesis, such as simulations comparisons, parameterizations and so forth is performed independently on the two trigger scenarios. When possible, for the convenience of the reader we will avoid the insertion of all the plots doubled: typically, we will show plots from the more abundant `A` sample. The other relevant plots can be found in the appendices.

4.2.2 $p_T(B)$ reweighting of the Monte Carlo.

We observed a discrepancy in the $p_{\mathrm{T}}(B)$ spectrum between simulated b-hadrons candidates and real data (see fig. 4.4). The $p_{\mathrm{T}}(B)$-distribution in the data has been determined by applying the standard procedure of sideband subtraction to the $B \to h^+h'^-$ sample described in chap. 3. Only the upper mass sideband has been used in the procedure to avoid the contamination of the partially/misreconstructed B decays in the lower mass sideband, that are only a small effect under the signal region. The observed discrepancy can be mainly explained by the fact that the data candidates have been selected requiring isolated b-hadrons candidates ($I_B > 0.525$), while simulated candidates do not have any information about fragmentation process, since only signal decays modes have been generated. By construction, the isolation variable is strongly related to the $p_{\mathrm{T}}(B)$ distribution. We therefore reweighted the Monte Carlo $p_{\mathrm{T}}(B)$ distribution in order to obtain a better agreement between the simulation and the data. The simulated inclusive $p_{\mathrm{T}}(B)$ distribution has been reweighted bin by bin to the distribution observed on data. We assumed the same

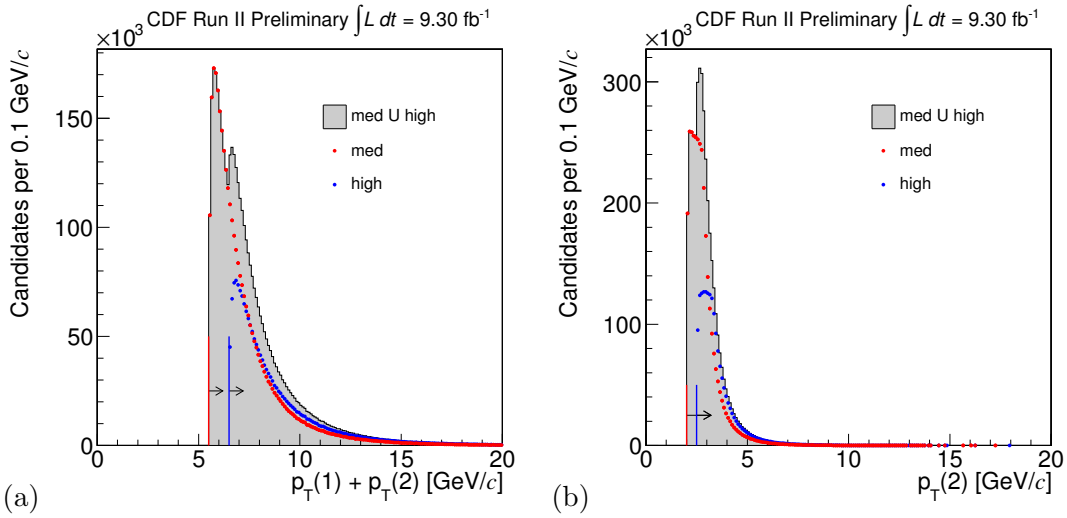

Figure 4.2: Data $\sum p_{\mathrm{T}}$ (a) and $p_{\mathrm{T}}(2)$ distribution after trigger requirements. The arrows refer to the `med` and `high` thresholds, respectively $\sum p_{\mathrm{T}} > 5.5$ and $p_{\mathrm{T}} > 2.0$ GeV/c and $\sum p_{\mathrm{T}} > 6.5$ and $p_{\mathrm{T}} > 2.5$ GeV/c.

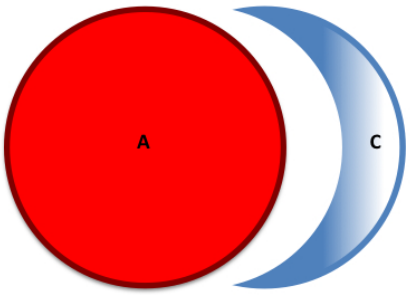

Figure 4.3: Pictorial representation of subsamples `A` and `C`.

effect of the isolation for all $B^0_{(s)} \to h^+h'^-$ signals [104]. Since the sculpting due to the isolation requirement has been observed to be the main source of discrepancy, the described reweighting is also able to adjust the other smaller data-MC differences, such as the ones due to inaccuracies in the input kinematic spectrum.

4.2.3 Mass resolution.

We checked the reliability of our simulation using huge samples available of $D^0 \to h^+h'^-$ decays, selected and reconstructed with the same strategy of $B^0_{(s)} \to h^+h'^-$ decays which are used in this analysis. We checked that the simulation reproduces all kinematic features of two body charmless decays, and in particular if the invariant

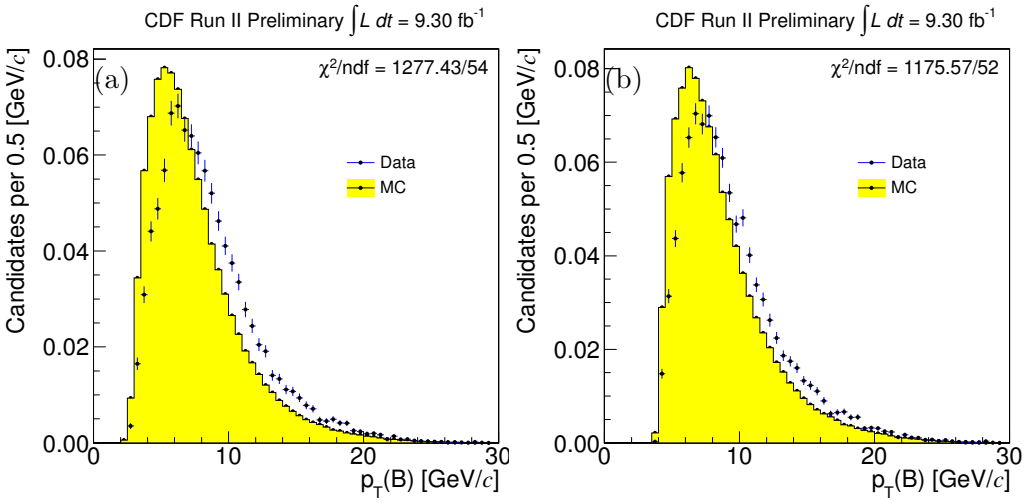

Figure 4.4: Data-simulation comparison of the $p_{\mathrm{T}}(B)$ distribution after reweighting for the run distribution. `med` (a) and `high` (b) scenarios. Yellow histograms are Monte Carlo, dots with errors are data.

mass line-shape is well simulated. In particular, we are interested in checking the squared mass, because this will be the variable used in the fit of composition, as described in chap. 5. By the comparison of the invariant mass peak of the $D^0 \to K^-\pi^+$ decays with its relative simulated peak we noticed that the simulated squared mass width is narrower than that observed in data by a factor ≈ 1.094. This factor is extracted with a procedure performed in two steps: 1) we first fit the template of the square invariant mass from simulation using the probability density function (p.d.f.) exploited for the fit of composition, that will be described in eq. (6.1). The result of the fit is reported in fig. 4.5(a); 2) in the second step, we use the same p.d.f. to fit data in which we apply the following variable change $x \to (x - m)/s$ where m and s are the only free parameters of the signal shape. For the background we used an exponential function whose normalization and slope are free to vary in the fit. We found $m = -0.284 \pm 0.002$ and $s = 1.094 \pm 0.001$ and the result is reported in fig. 4.5(b). We fit about 7×10^6 $D^0 \to K^-\pi^+$. The agreement between data and our model is very satisfactory.

The scale factor extracted in such a way refers to the $D^0 \to K^-\pi^+$ decays, while we are interested on how the square invariant mass scales in the $B^0 \to K^+\pi^-$ decays (and in general in all $B^0_{(s)} \to h^+h'^-$ decays). To move from D^0 to B mesons we used the Fast Monte Carlo described in Ref. [105]. The Fast Monte Carlo is a C++ code based on the official CDF Monte Carlo which generates the decay of a generic B or D meson into two scalar or pseudo-scalar particles. Since the FMC is not able to reproduce all the official Monte Carlo features, such as trigger configurations or temporary inefficiencies of the detector, it is very fast, but it is still found to be reliable for what concerns the kinematics observables. We generated several samples

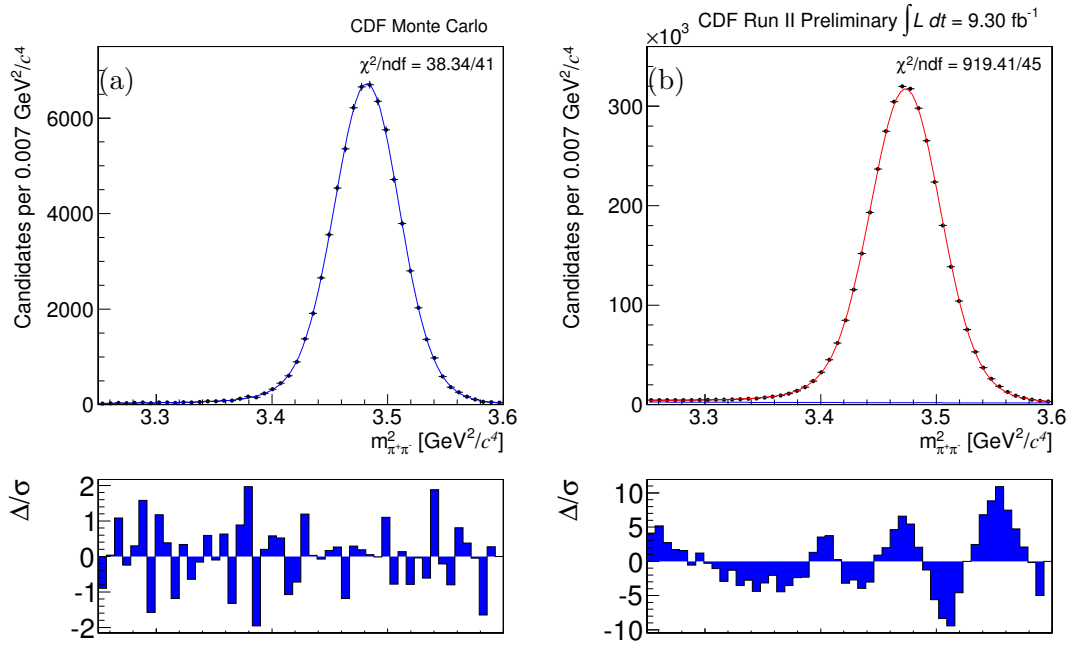

Figure 4.5: Comparison of square mass resolution between data and simulation using $D^0 \to K^-\pi^+$. (a) Parameterization of the square mass line shape from simulation. (b) Fit to data to extract m and s.

of $D^0 \to K^-\pi^+$ and $B^0 \to K^+\pi^-$ in which we scaled the curvature resolution function using a global scale factor. Then we looked at the square invariant mass for both decays to understand how the mass resolution varies as a function of scaled curvature. Table 4.2 shows the curvature scale factor, the RMS of the $D^0 \to K^-\pi^+$ (and $B^0 \to K^+\pi^-$) squared invariant mass, and the ratio between the scaled RMS and the unscaled RMS for the $D^0 \to K^-\pi^+$ (and $B^0 \to K^+\pi^-$) decays. From tab. 4.2 we extract the scale factor for the $B^0_{(s)} \to h^+h'^-$ decays. We then enlarged the Monte Carlo templates using a scale factor of $s = 1.103$, which corresponds to a mass scale factor of 1.094 for the $D^0 \to K^-\pi^+$ decays, and a scale factor of 1.11 for the curvature resolution. The enlarged templates will be used for the templates of the fit of composition as described in chap. 6. This study was performed using `med` scenario requirements. The results agree with the ones obtained from an equivalent study performed using `high` scenario requirements.

Check of the method using $\Upsilon(1s) \to \mu^+\mu^-$ sample

We checked the correctness of the method using data and Monte Carlo samples of $\Upsilon(1s) \to \mu^+\mu^-$. We chose this sample because the $\Upsilon(1s)$ mass $m_{\Upsilon(1s)} = 9.5$ GeV/c^2 is larger than the b-mesons masses ~ 5.3 GeV/c^2, extrapolating the results of the method in another mass region. By the comparison of the invariant mass peak

scaling	RMS [GeV$^2/c^4$]	ratio
1.00	0.0368	1
1.05	0.0382	1.038
1.09	0.0396	1.075
1.10	0.0397	1.079
1.11	0.0403	1.095
1.12	0.0405	1.100
1.13	0.0408	1.108
1.14	0.0411	1.118
1.15	0.0416	1.132

scaling	RMS [GeV$^2/c^4$]	ratio
1.00	0.282	1
1.05	0.293	1.041
1.09	0.306	1.085
1.10	0.308	1.092
1.11	0.311	1.103
1.12	0.311	1.102
1.13	0.316	1.121
1.14	0.320	1.135
1.15	0.322	1.143

Table 4.2: Studies on mass resolution of the $D^0 \to K^-\pi^+$ (left) and $B^0 \to \pi^+\pi^-$ (right) using the FMC. The first column reports the curvature scale factor, the second column the RMS of the square invariant mass, the third column the ratio between the scaled RMS and the unscaled RMS.

of the $\Upsilon(1s)$ decays with its relative simulated peak we extracted the resolution factor. The extraction has been done with the same two steps procedure used for the $D^0 \to h^+h'^-$: 1) we first fit the template of the square invariant mass from simulation using the standard p.d.f. of eq. (6.1) as reported in fig. 4.6(a), 2) and then we use this p.d.f. to fit data in which we apply the following variable change $x \to (x - m)/s$ where m and s are the only free parameters of the signal shape. For the background we used an exponential function whose normalization and slope are free to vary in the fit. We found $s_\Upsilon = 1.122 \pm 0.001$ and the result of a fit on $900,000$ $\Upsilon(1s)$ decays is reported in fig. 4.6(b). The check demonstrates an accuracy in the our method of evaluating the resolution at level of 2%. Because the $\Upsilon(1S)$ has higher mass with respect to the B decays, and there is larger background in the sample, a conservative systematic uncertainty will be assessed in sec. 11.2.8 as a consequence of the discrepancies observed.

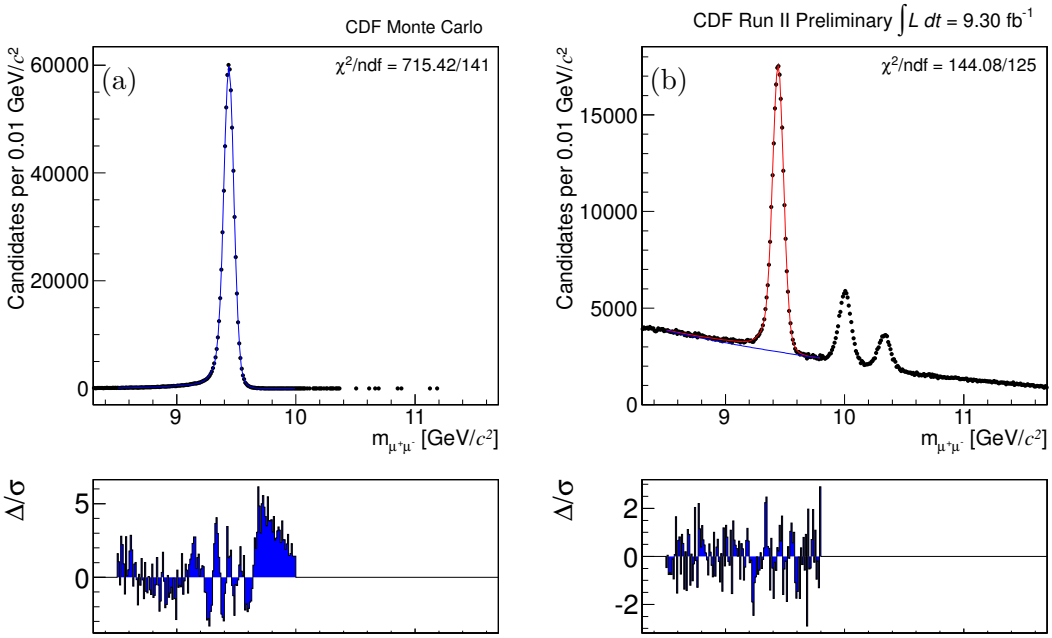

Figure 4.6: $\Upsilon(1s) \to \mu^+\mu^-$ distribution from Monte Carlo (a) and data (b). Fit function overlaid.

4.3 Comparison data - Monte Carlo

We report the comparison plots between data sideband subtracted and $B \to h^+h'^-$ simulated modes: each mode is normalized to the branching fractions derived from the current experimental results (see tab. 1.4). Plots for the `med`, figs. 4.7–4.9, and for the `high` scenario, figs. 4.10–4.12. The agreement between data and simulation for all interesting kinematic variables is satisfactory, although small residual discrepancies can be observed (for example in the $d_0(B)$ distributions). This achievement is important, because the simulated kinematic distributions information will be used in a fit of composition to disentangle the signal decay modes.

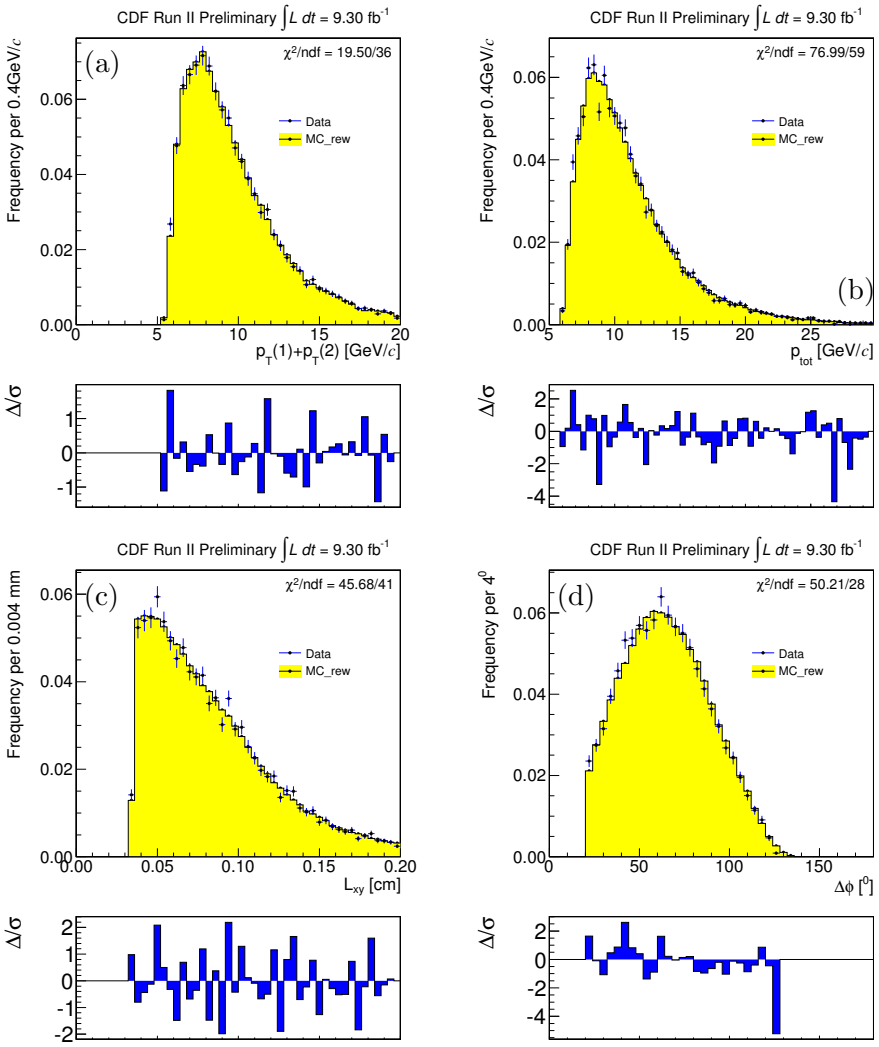

Figure 4.7: Comparison of background-subtracted distributions in $B^0_{(s)} \to h^+h'^-$ decays and equivalent Monte Carlo distributions for the `med` scenario: $\sum p_{\mathrm{T}}$ (a), p_{tot} (b) L_{T} (c), $\Delta\varphi_0$ (d). Data (points with error bars) are compared with reweighted Monte Carlo simulation (filled histogram).

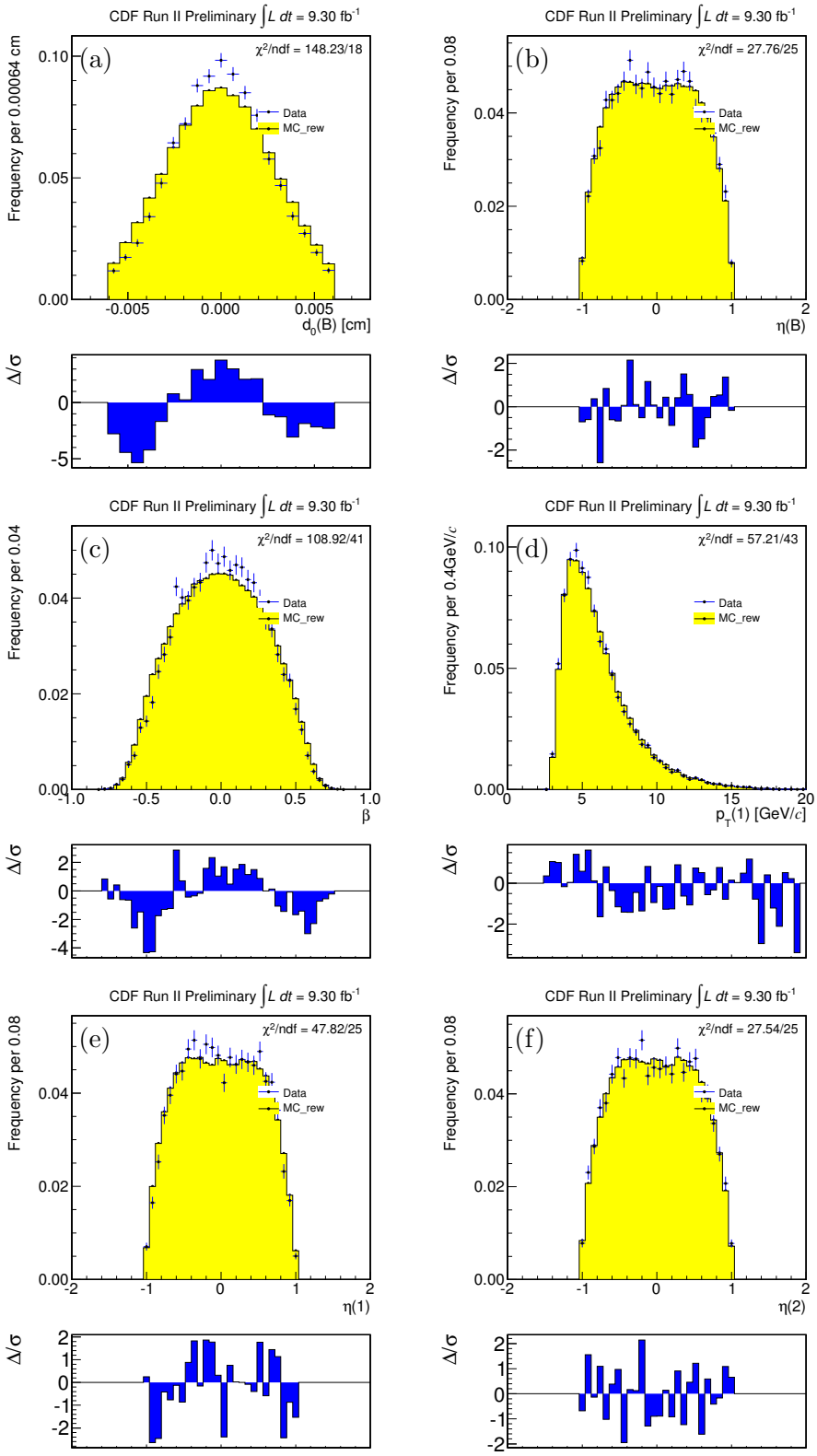

Figure 4.8: Comparison of background-subtracted distributions in $B^0_{(s)} \to h^+h'^-$ decays and equivalent Monte Carlo distributions for the `med` scenario: $d_0(B)$ (a), $\eta(B)$ (b), β (c), $p_{\rm T}(1)$ (d), $\eta(1)$ (e), $\eta(2)$ (f). Data (points with error bars) are compared with reweighted Monte Carlo simulation (filled histogram).

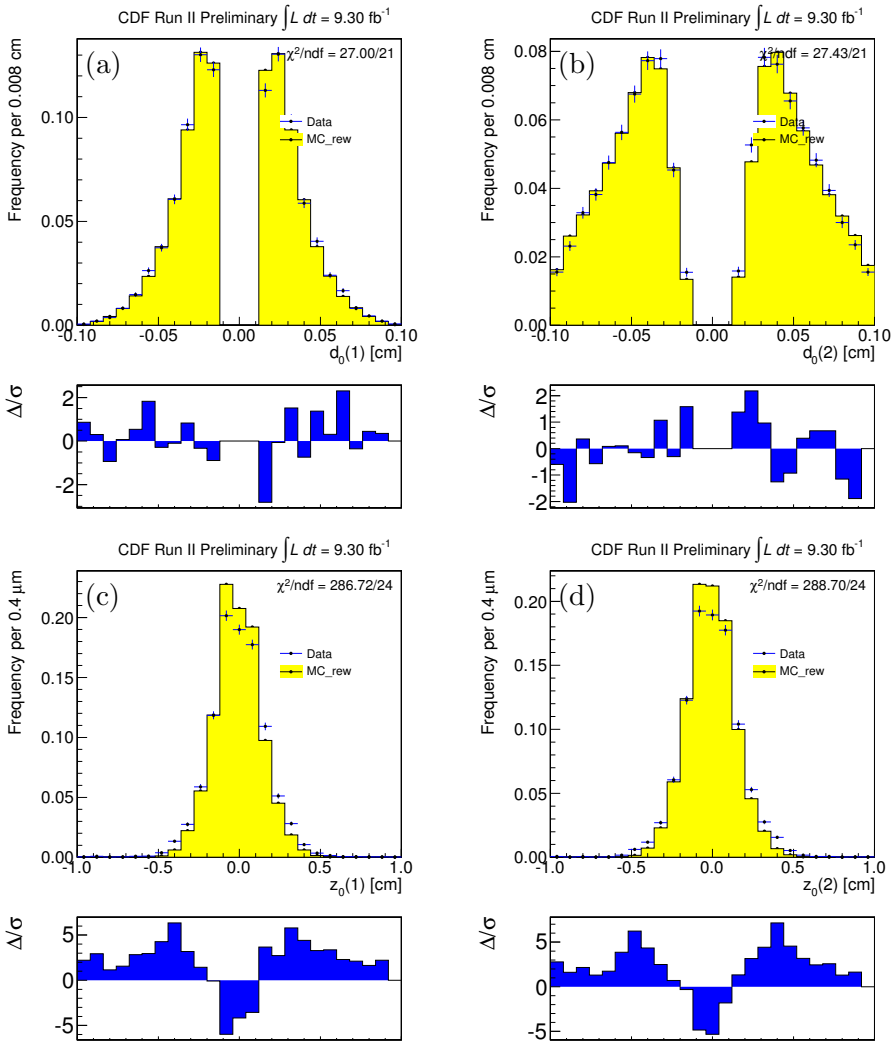

Figure 4.9: Comparison of background-subtracted distributions in $B^0_{(s)} \to h^+h'^-$ decays and equivalent Monte Carlo distributions for the `med` scenario: $d_0(1)$ (a), $d_0(2)$ (b), $z_0(1)$ (c), $z_0(2)$ (d). Data (points with error bars) are compared with reweighted Monte Carlo simulation (filled histogram).

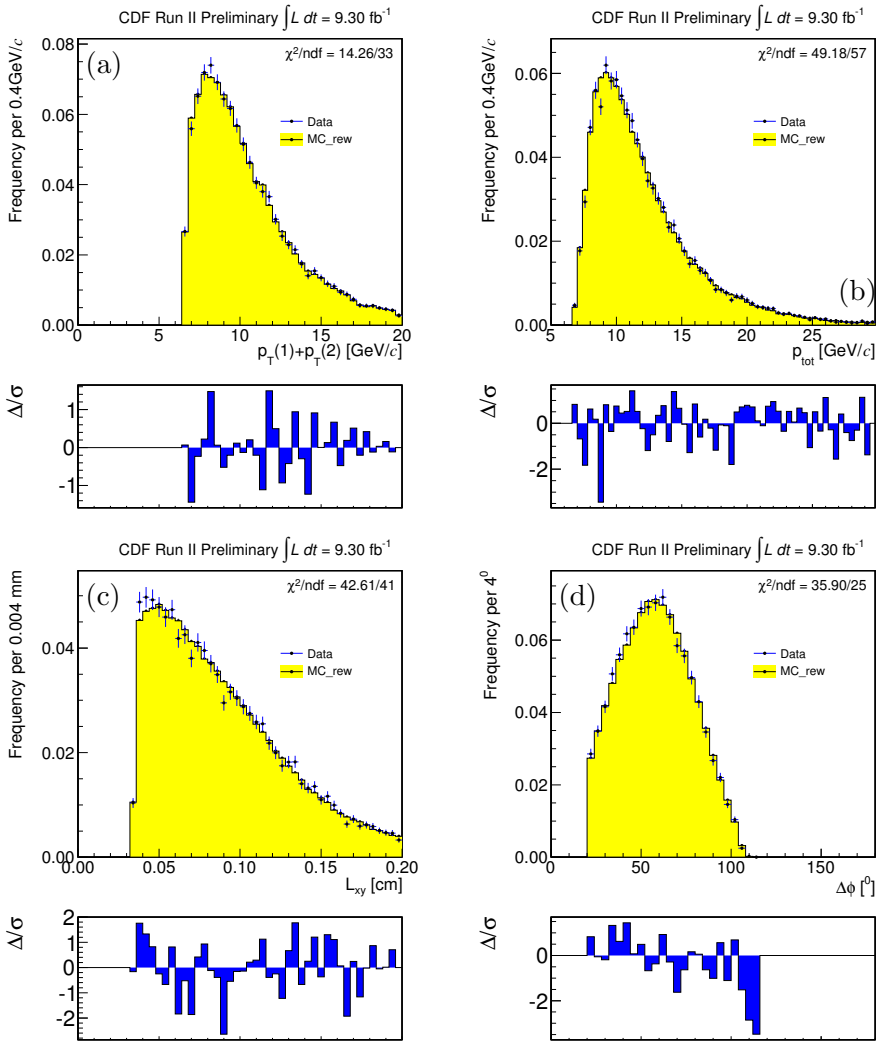

Figure 4.10: Comparison of background-subtracted distributions in $B^0_{(s)} \to h^+h'^-$ decays and equivalent Monte Carlo distributions for the `high` scenario: $\sum p_{\mathrm{T}}$ (a), p_{tot} (b) L_{T} (c), $\Delta\varphi_0$ (d). Data (points with error bars) are compared with reweighted Monte Carlo simulation (filled histogram).

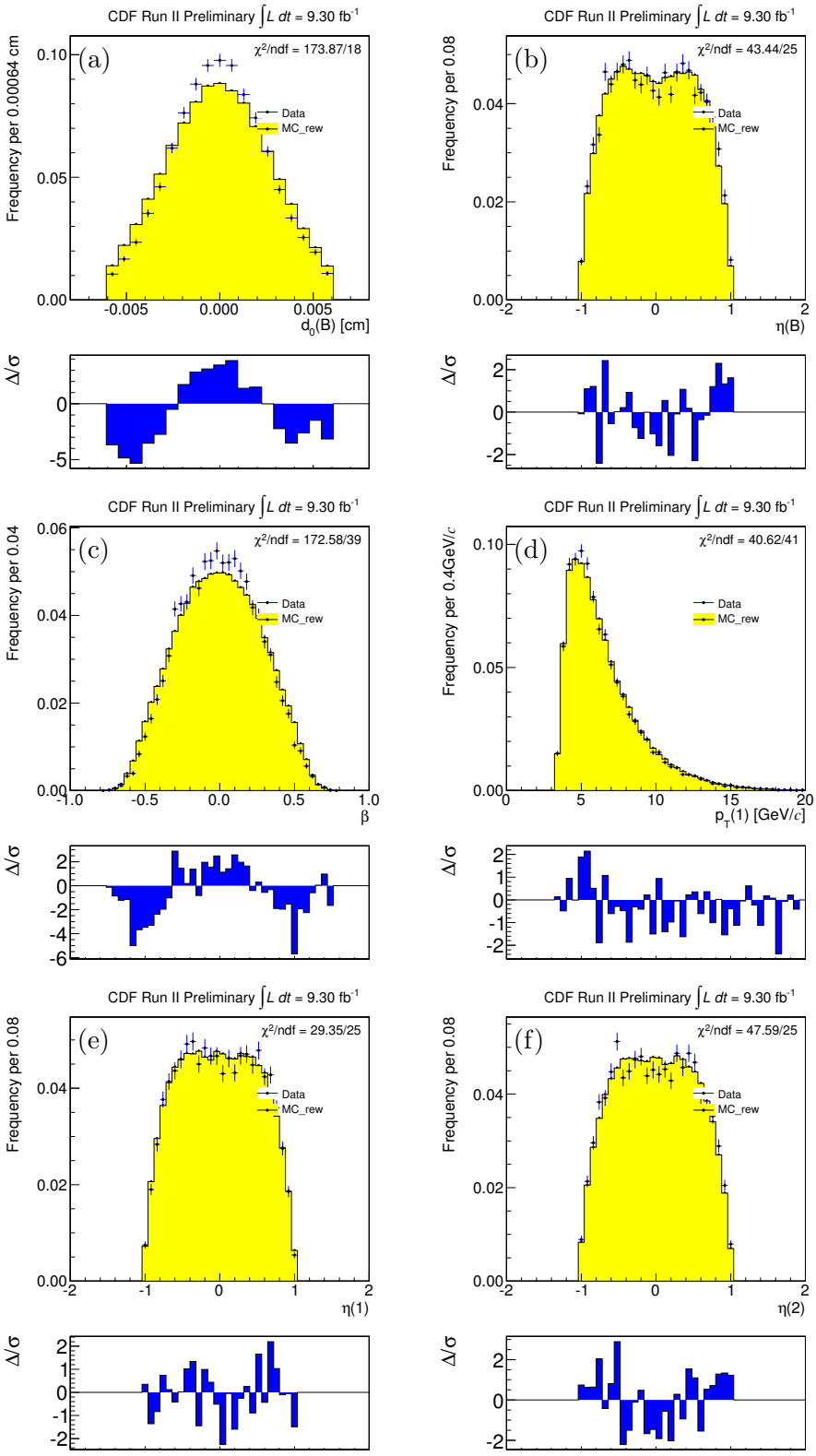

Figure 4.11: Comparison of background-subtracted distributions in $B^0_{(s)} \to h^+h'^-$ decays and equivalent Monte Carlo distributions for the `high` scenario: $d_0(B)$ (a), $\eta(B)$ (b), β (c), $p_{\mathrm{T}}(1)$ (d), $\eta(1)$ (e), $\eta(2)$ (f). Data (points with error bars) are compared with reweighted Monte Carlo simulation (filled histogram).

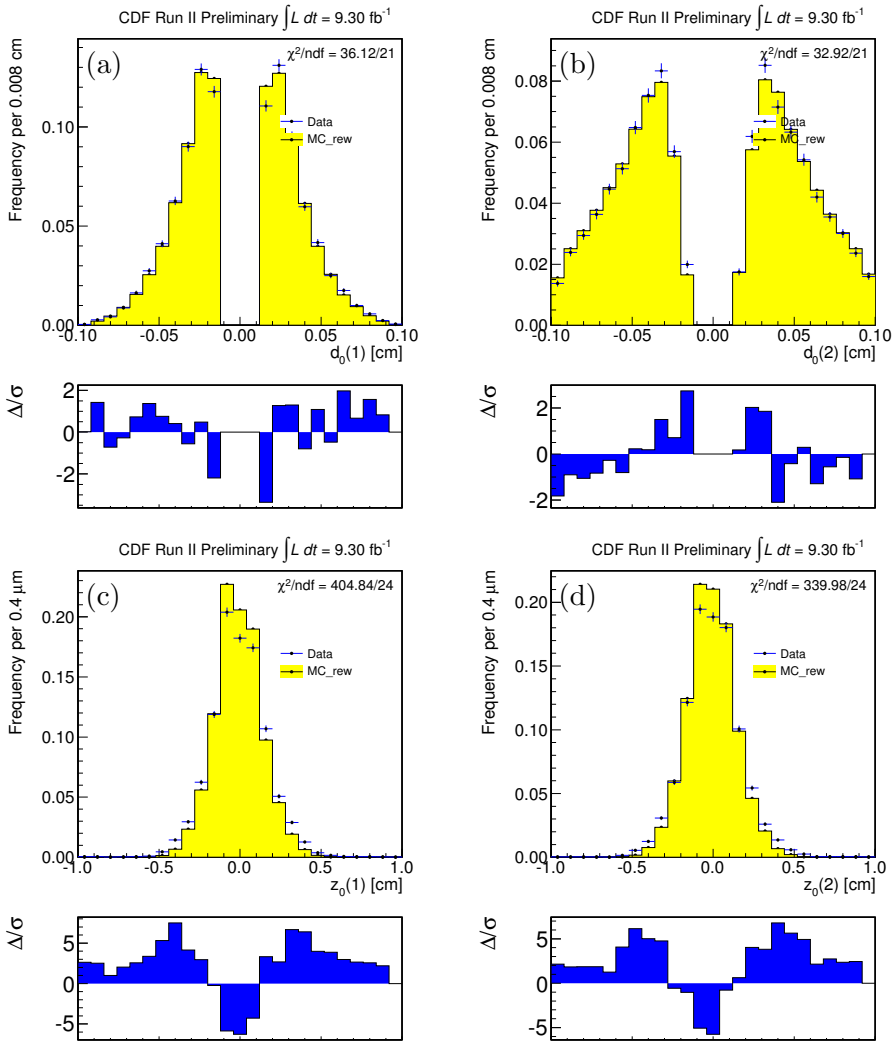

Figure 4.12: Comparison of background-subtracted distributions in $B^0_{(s)} \to h^+h'^-$ decays and equivalent Monte Carlo distributions for the `high` scenario: $d_0(1)$ (a), $d_0(2)$ (b), $z_0(1)$ (c), $z_0(2)$ (d). Data (points with error bars) are compared with reweighted Monte Carlo simulation (filled histogram).

4.4 First look at the Monte Carlo mass distributions

Before going into the details of the analysis used to perform the $\mathcal{CP}$ and $\mathcal{B}$ measurements, we consider the mass distributions of the simulated events. Figure 4.13 shows the invariant $\pi\pi$-distribution of the simulated events, where each mode is normalized: we used the branching fractions derived from the current experimental results (see tab. 1.4). It is evident how all the different $B^0_{(s)} \to h^+h'^-$ decay modes overlap in a single peak, whose dominant contribution are given by $B^0 \to K^+\pi^-$, $B^0 \to K^+K^-$, and $B^0_s \to K^+K^-$. This single-peaking structure is expected, and it is due to the broadening of the invariant mass distributions of modes with wrong assigned final state masses, as discussed in sec. 3.3.4. It would be difficult to disentangle the different decay modes by means of mass information only.

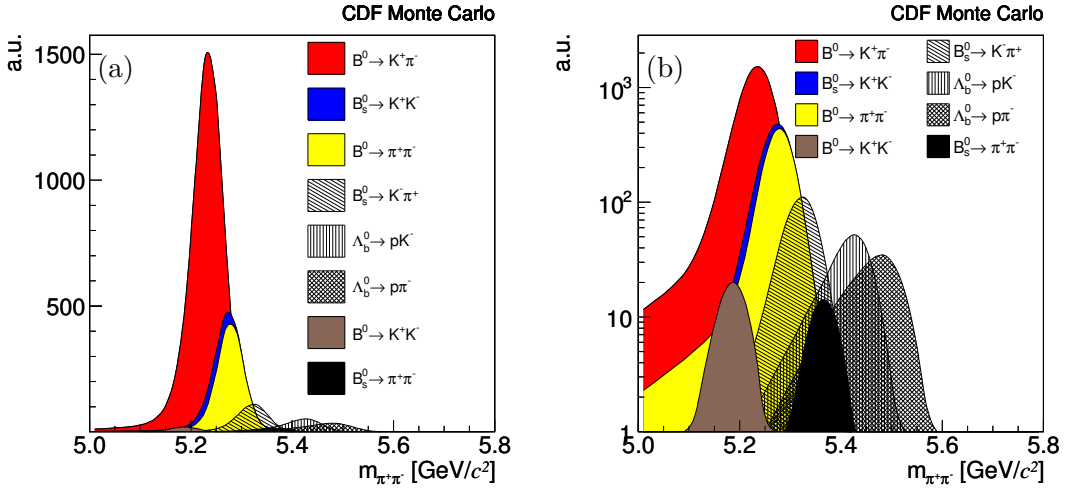

Figure 4.13: Invariant $\pi\pi$-mass distribution of the simulated events. Linear scale (a) and log scale (b).

Chapter 5

Separation of $B \to h^+ h'^-$ modes

This chapter describes the methodology used to discriminate the different contributes present in the data sample. The resolution in mass and in particle identification information is not sufficient for an event-by-event separation. Therefore we will combine them to increase as much as possible the separation between the signals and the backgrounds, and between the different $B \to h^+ h'^-$ decay modes.

5.1 Separation strategy

In a decay of a neutral particle into two charged bodies of momenta $\vec{p}_+$ and $\vec{p}_-$ and masses m_+ and m_-, where the symbol $+(-)$ labels the positively (negatively) charged particle, the invariant mass is defined as follows:

$$m^2_{m_+m_-} = \left(\sqrt{p_+^2 + m_+^2} + \sqrt{p_-^2 + m_-^2}\right)^2 - (\vec{p}_+ + \vec{p}_-)^2 \tag{5.1}$$

Assigning the pion mass to the outgoing particles, we obtain the $\pi\pi$ invariant mass:

$$m^2_{m_\pi m_\pi} = \left(\sqrt{p_+^2 + m_\pi^2} + \sqrt{p_-^2 + m_\pi^2}\right)^2 - (\vec{p}_+ + \vec{p}_-)^2 \tag{5.2}$$

Figure 5.1 shows the data invariant $\pi\pi$-distribution compared with the same distribution from Monte Carlo simulation described in chap. 4, where each mode is normalized using the current experimental knowledge (see tab. 1.4). Figure 5.1 shows that the different decays are too closely spaced to be solved: they appear overlapping in a single peak, broader than the expected $\mathcal{O}(25\ \mathrm{MeV}/c^2)$ mass resolution for an individual decay. In fact, given a specific mass assignment for the outgoing particles, the invariant mass distributions of modes with wrong assigned masses are broadened. The broadening is inevitable and it is due to the invariant mass dependence on the momenta of the outgoing particles. For example, if we assign to the outgoing particle the π mass, the mass r.m.s. width is about 25 MeV/c^2 for the properly reconstructed $B^0 \to \pi^+\pi^-$ and $B_s^0 \to \pi^+\pi^-$ simulated

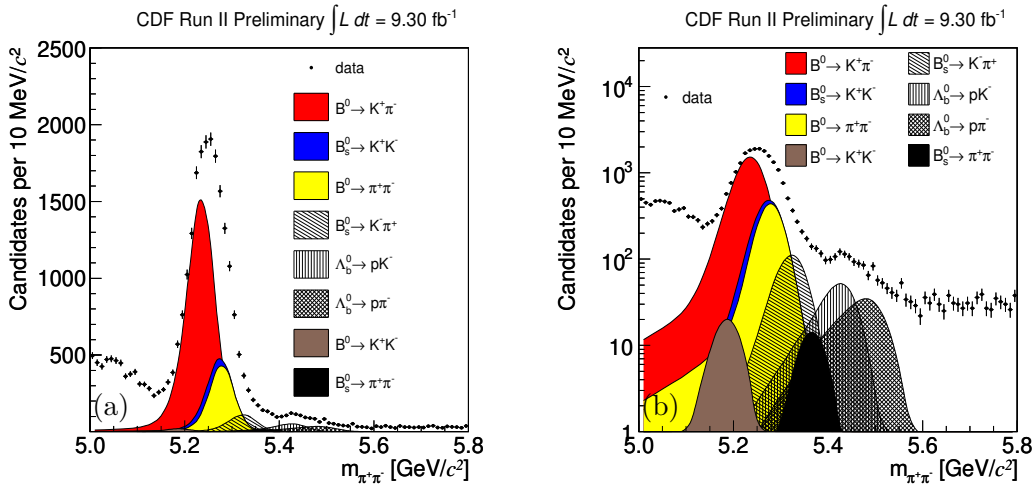

Figure 5.1: Comparison invariant $\pi\pi$-mass distribution for data and simulation. Linear (a) and logarithmic scale (b).

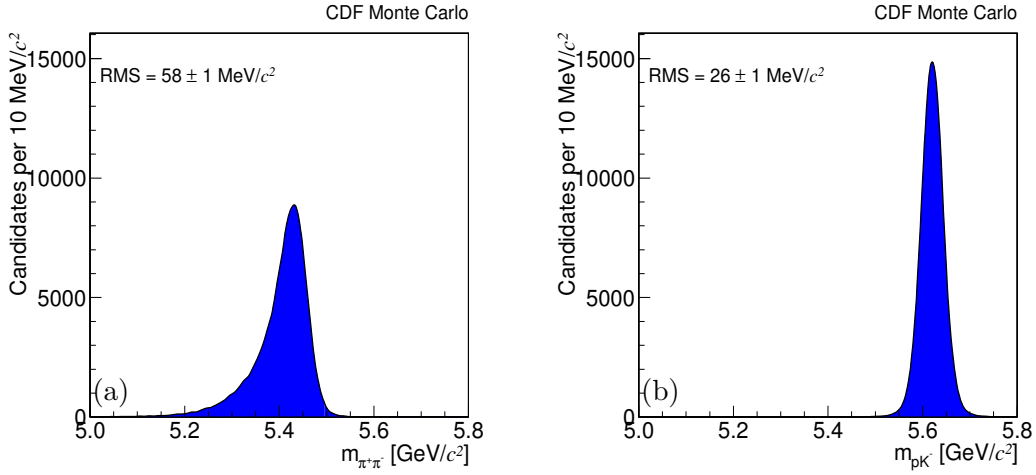

Figure 5.2: Comparison of invariant $\pi\pi$-mass distribution (a) and pK-mass distribution (b) of simulated $\Lambda_b^0 \to pK^-$ decay modes.

modes, while the widths of the misreconstructed modes are larger: it is approximately equal to 38 MeV/c^2 for the $B^0 \to K^+\pi^-$ and $B_s^0 \to K^-\pi^+$ modes, where only one mass assignment is uncorrect, while it is maximally larger $\approx$ 58 MeV/c^2. for $\Lambda_b^0 \to pK^-$ mode, where both assignments are uncorrect. Figure 5.2 shows the comparison of the widths of $\Lambda_b^0 \to pK^-$ mass distribution for the uncorrect $\pi\pi$ mass assignment (a) and of the correct pK mass assignment (b). In conclusion, to distinguish the different decay modes the mass distribution is not sufficient, despite the excellent CDF II mass resolution[1]. That holds whatever choice of mass assignment

[1]See for instance the observed mass widths $\sigma_m \approx 14$ MeV/c^2 in $J/\psi \to \mu\mu$ decays, or $\sigma_m \approx 9$ MeV/c^2/ in $D^0 \to h^+h'^-$ decays.

to the outgoing particles and even with an infinitely precise mass resolution. We therefore need additional information to distinguish the different contributions of the $B \to h^+h'^-$ data sample. We have the possibility to use all the information available, but it is preferable to have a tool to select only those variables capable of maximum discrimination. The identification performance of a variables x (or a set of variables $x_1, x_2...$) relies on the difference in the distributions between the classes of events to be identified. Such difference is generally expressed in terms of a separation between those distributions.

5.1.1 Separation power

The conventional way to quote the separation is to provide an estimation of the distance between the centers of the distributions in units of their standard deviations (σ). The reliability of this estimation degrades increasingly as the distributions deviate from the Gaussian shape. In presence of long tails or strongly asymmetric distributions, the separation estimated with this approach is not reliable. In addition, this choice has limited applicability: if the information is given in form of a multi-dimensional observable, no straightforward and unambiguous way to quote the separation is provided. Since in our analysis we will use multi-dimensional distributions, we chose a different approach [106]. Suppose that one uses a particular information in a sample of N events given by the sum of two different class of events, A and B. The fraction f are A events and a fraction $1-f$ are B events (see fig. 5.3). An unambiguous characterization of the separation power is given by quoting the minimum achievable σ_f, that is the statistical uncertainty on the fraction f. This

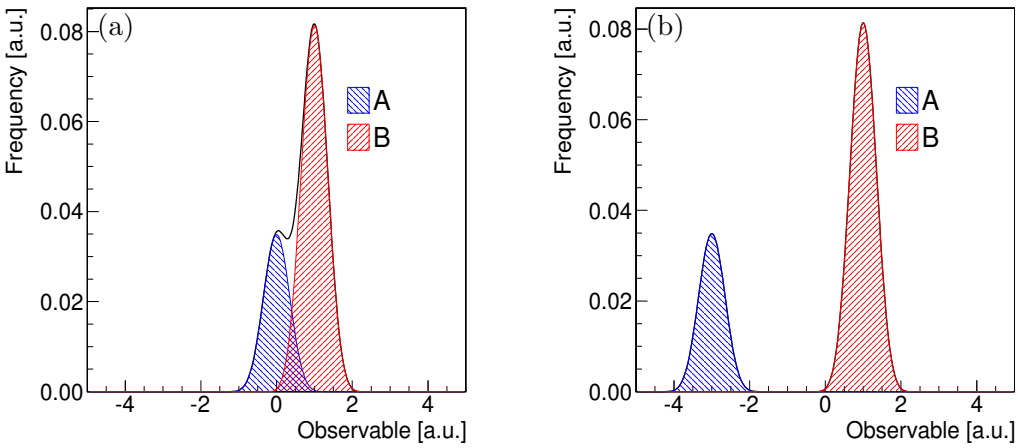

Figure 5.3: Illustration of the x variable in case of partial (a) and complete (b) event separation.

resolution is bounded from above by the value $\sigma_f^{\text{best}} = \sqrt{f(1-f)/N}$ obtained in

the ideal case of classes of events being totally separated, i. e., the distributions of the chosen observable having zero overlap (see fig. 5.3(b)). In this limiting case, the only uncertainty in assigning an event to one of the two classes comes from the Binomial fluctuation due to the finite sample-size.

We quote the separation between A and B events as the ratio of the ideal case resolution with respect to the observed resolution $s = \sigma_f^{\text{best}}/\sigma_f$. The resolution σ_f can in principle be determined by repeating a maximum Likelihood fit of the fraction f on a sufficient number of pseudo-experiments that simulate the experimental data, and evaluating the spread of results around the input values. An approach exploiting the Minimum Variance Bound (MVB)[106, 107] can also be used: choosing a variable x to separate the classes of events, in the simple case of two classes, the MVB is written as follows:

$$\sigma_f^2 = \frac{1}{N}\left[\int \frac{(\wp_A(x) - \wp_B(x))^2}{f\wp_A(x) + (1-f)\wp_B(x)}dx\right]^{-1}, \tag{5.3}$$

where $\wp_A(x)$ and $\wp_B(x)$ are the probability distributions of x, normalized to unit area, for A and B events respectively (see fig. 5.3).[2] Following our approach, the separation power of the variable x in the given sample is determined by evaluating

$$s = \sigma_f^{\text{best}}/\sigma_f = \sqrt{f(1-f)\int \frac{(\wp_A(x) - \wp_B(x))^2}{f\wp_A(x) + (1-f)\wp_B(x)}dx}. \tag{5.4}$$

This quantity is independent of the sample size, but depends on the true values of fractions as generally happens for resolutions. This is also intuitive, since an easier separation is expected among populations similar in size. The quantity s ranges from zero, i. e., no separation corresponding to completely overlapping distributions, to one, i. e., the maximum achievable separation in the given sample. The quantity s is well-defined whatever the shape and the dimensionality of the observable distributions involved. In addition, any s value can be analytically converted in an "equivalent $n\sigma$ separation" to quote, in a more conventional way, the separation in σ units one would have observed if the distributions of the chosen variable were Gaussian. The achieved separation power depends on the variable (i. e., x) used to measure it, and a wise choice of the variable (or set of variables) may enhance the actual separation. For the specific goals of this analysis, the set of observables must have the maximum separation power possible to distinguish:

- between signals and backgrounds;
- between different signals contributing to the $B \to h^+h'^-$ peak: kinematics differences between modes will be exploited in a strategy described in sec. 5.2. Charged particle identification information is an additional tool used to increase the separation power: we will explain the strategy in sec. 5.3.

[2] The symbol x may stand for a set of many variables, discrete or continuous, and the integral extends over the whole x domain.

5.2 Kinematic separation

Separation power can be exploited using kinematic differences between decay modes. Obviously, one useful information is the mass difference between B^0, B_s^0 and Λ_b^0 decay modes, respectively $m_{B^0} \approx 5.30$ GeV/c^2, $m_{B_s^0} \approx 5.36$ GeV/c^2 and $m_{\Lambda_b^0} \approx 5.62$ GeV/c^2. However, we explained in the previous sections that using a single mass-assignment for all events will lead to the broadening of the mass resolution. As a consequence, the mass information alone is not sufficient to allow discrimination between the different decay modes, overlapping each others. Now let us consider the invariant mass definition of eq. (5.1): it is written as a function of the masses of the final states and the momenta. In addition, we have also the charge information of the final state particles. Thus the structure of the eq. (5.1) gives the opportunity to add, in a simple way, other kinematics information: the momentum and the charge of the final state particles. In particular, for the $\mathcal{C}P$ measurements, having a variable capable of discriminating between $\mathcal{C}P$ conjugates final states ($K^+\pi^-$ and $K^-\pi^+$, ph^- and $\overline{p}h^+$) is of fundamental importance.

Consider the invariant mass for any mass assignment $m_{m_+m_-}$ from eq. (5.1) and the invariant mass in assumption of $\pi\pi$ in the final state given on eq. (5.2). Their difference can be written as:

$$\begin{aligned} m^2_{\pi\pi} - m^2_{m_+m_-} &= (m^2_\pi + m^2_\pi) - (m^2_+ + m^2_-) + \\ 2 \cdot \left(\sqrt{p^2_+ + m^2_\pi} \cdot \sqrt{p^2_- + m^2_\pi} - \sqrt{p^2_+ + m^2_+} \cdot \sqrt{p^2_- + m^2_-} \right) \end{aligned} \tag{5.5}$$

where, for simplicity, we used $m^2_{\pi\pi} \equiv m^2_{m_\pi m_\pi}$ (following the same notation, $m^2_{K\pi} = m^2_{m_K m_\pi}$ and so forth for the other $B^0_{(s)} \to h^+h'^-$ decay modes). The relation eq. (5.5) allows writing the invariant mass of any possible decay $m^2_{m_+m_-}$ as a function of three variables: the invariant $\pi\pi$ mass squared $m^2_{\pi\pi}$ and the momenta p_+ and p_-. So for each event (i. e., for each set of observed $m^2_{m_+m_-} = m^2_{\pi\pi}$, p_+ and p_-) eq. (5.5) takes different forms, depending on the decay mode one is referring to. In particular, the presence of the final state particles charge information introduces differences in the functional form between a decay mode and its $\mathcal{C}P$ conjugate: for example, for the $\overline{B}^0_s \to K^+\pi^-$ mode $m_+ = m_{K^+}$, $m_- = m_{\pi^-}$, $p_+ = p_{K^+}$, $p_- = p_{\pi^-}$ and $m^2_{m_+m_-} = m^2_{B^0_s}$. On the contrary, for the $B^0_s \to K^-\pi^+$ mode $m_+ = m_{\pi^+}$, $m_- = m_{K^-}$, $p_+ = p_{\pi^+}$, $p_- = p_{K^-}$[3]. This difference in the functional form translates into different trends in the distributions making possible to obtain separation power between the different decay modes. As an alternative, we could evaluate the invariant mass with the correct mass assignment and use all of them in the fit of composition. With this strategy, large correlations between the likelihood terms would arise. In addition, this choice would increase the number of variables in the fit of composition. For these reasons we decided not to follow this strategy.

Given the structure of the relation eq. (5.5), it is possible to use a set of less

[3] In assumption of trascurable Cabibbo suppressed decay modes $B^0_s \to K^+\pi^-$. Same holds for the other decay modes.

correlated variables. We define a charge momentum asymmetry:

$$\beta \equiv \frac{p_+ - p_-}{p_+ + p_-} = \frac{p_+ - p_-}{p_{\rm tot}} \tag{5.6}$$

where $p_{\rm tot}$ is the scalar sum of the momentum of the final state particles. β takes values in the finite interval [-1,1] and $p_{+(-)}$ can be written as a function of β, $p_{\rm tot}$:

$$p_+ = \frac{1+\beta}{2} \cdot p_{\rm tot} \tag{5.7}$$

$$p_- = \frac{1-\beta}{2} \cdot p_{\rm tot} \tag{5.8}$$

Using a change of variables, eq. (5.5) can be written as

$$\begin{aligned} m^2_{m_+m_-} &= m^2_{\pi\pi} - 2m^2_\pi + (m^2_+ + m^2_-) + \\ &-2 \cdot \left(\sqrt{\left(\tfrac{1+\beta}{2} p_{tot}\right)^2 + m^2_\pi} \cdot \sqrt{\left(\tfrac{1-\beta}{2} p_{tot}\right)^2 + m^2_\pi} \right) + \\ &+2 \cdot \left(\sqrt{\left(\tfrac{1+\beta}{2} p_{tot}\right)^2 + m^2_+} \cdot \sqrt{\left(\tfrac{1-\beta}{2} p_{tot}\right)^2 + m^2_-} \right) \end{aligned} \tag{5.9}$$

Using eq. (5.9) it is possible to calculate the analytical expressions for the $m^2_{m_+m_-}$ of each $B \to h^+h'^-$ decay, as a function of β and $p_{\rm tot}$: for example, the $m^2_{m_+m_-}$ for the $B^0_s \to K^-\pi^+$ mode is written as follows:

$$\begin{aligned} m^2_{\pi K} &= m^2_{\pi\pi} - 2m^2_\pi + (m^2_\pi + m^2_K) + \\ &-2 \cdot \left(\sqrt{\left(\tfrac{1+\beta}{2} p_{tot}\right)^2 + m^2_\pi} \cdot \sqrt{\left(\tfrac{1-\beta}{2} p_{tot}\right)^2 + m^2_\pi} \right) + \\ &+2 \cdot \left(\sqrt{\left(\tfrac{1+\beta}{2} p_{tot}\right)^2 + m^2_\pi} \cdot \sqrt{\left(\tfrac{1-\beta}{2} p_{tot}\right)^2 + m^2_K} \right) \end{aligned}$$

Using eq. (5.9) we can summarize all the kinematic information and the charge information in just three, loosely correlated variables ($m^2_{\pi\pi}, \beta$ and $p_{\rm tot}$)[4]. Figure 5.4 shows the distributions of $m^2_{\pi\pi}$ as a function of β, visualizing the differences between the kinematic distributions of the different modes due to the mass-momentum correlation. In spite of the smearing effect of the mass resolution, the different trends of the different modes are clearly visible. A general feature of these plots is that the slopes are enhanced at the boundaries of the β domain ($|\beta| \approx 1$), suggesting that the kinematic separation is more effective in the decays where the momenta of the final particles are strongly unbalanced. Differences between $B^0 \to K^+\pi^-$ and $\overline{B}^0 \to K^-\pi^+$ decays, between $B^0_s \to K^-\pi^+$ and $\overline{B}^0_s \to K^+\pi^-$ decays and between $\Lambda^0_b \to p\pi^-(\Lambda^0_b \to pK^-)$ and $\overline{\Lambda}^0_b \to \overline{p}\pi^+(\overline{\Lambda}^0_b \to \overline{p}K^+)$ are also visible. The latter are used to measure the $\mathcal{C}P$-violating decay-rate asymmetry in these modes. The shape of the $B^0 \to \pi^+\pi^-(B^0_s \to \pi^+\pi^-)$ mode is a straight line centered at the $B^0(B^0_s)$ meson mass, since the chosen mass assignment is correct for this mode.

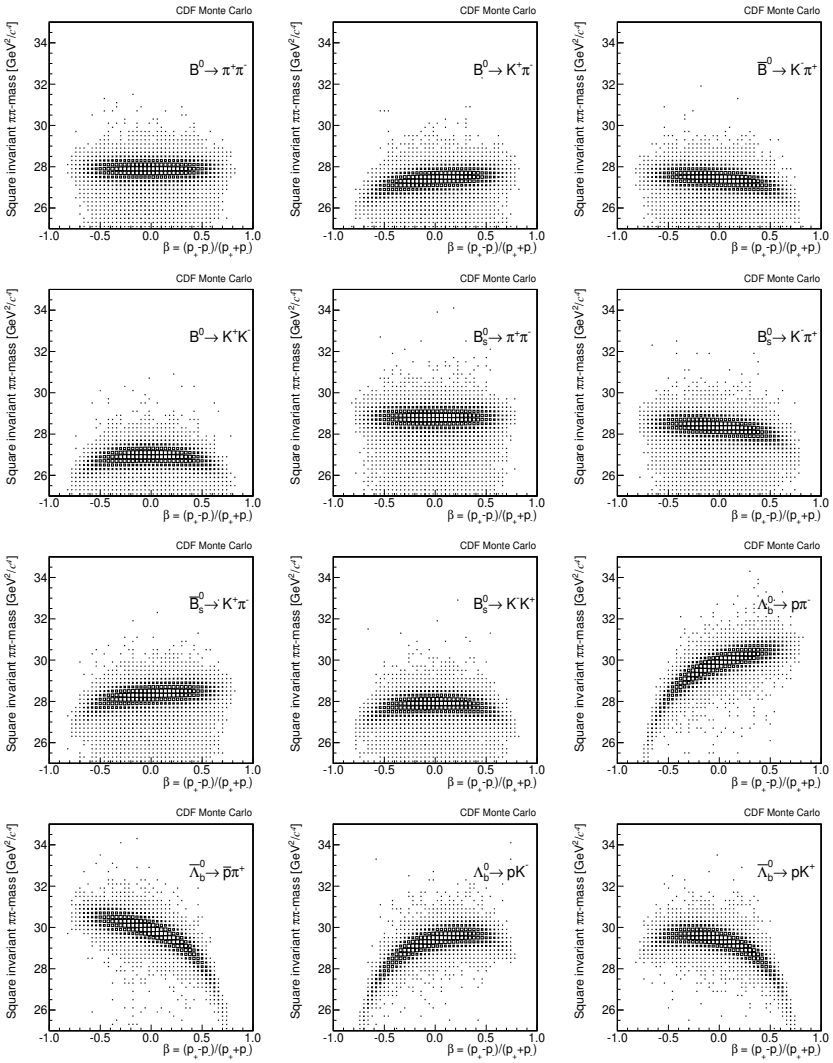

Figure 5.4: Square invariant $\pi\pi$-mass of the simulated $B^0_{(s)} \to h^+h'^-$ and $\Lambda^0_b \to ph^-$ decays as a function of β.

Figure 5.6 shows the maximum separation power among the modes, that is between the $B^0 \to K^+K^-$ and the $\Lambda^0_b \to p\pi^-$ decay modes, and the minimum separation power between $B^0 \to \pi^+\pi^-$ and $B^0_s \to K^+K^-$ where the mass wrong assignment to the kaon final particles has the effect of counter-balancing the wrong mass assignment in m_{B_s}. The two resulting mass shapes are very similar: only a small tail is visible for the $B^0_s \to K^+K^-$ decay modes, due to the momentum dependence of the $m^2_{\pi\pi}$. In tab. 5.1 we reported the list of the separation powers between the different $B \to h^+h'^-$ decay modes.

[4]The correlation between p_+ and p_- is $\approx 5.0\%$, while the correlation between β and $p_{\rm tot}$ is $\approx 0.2\%$

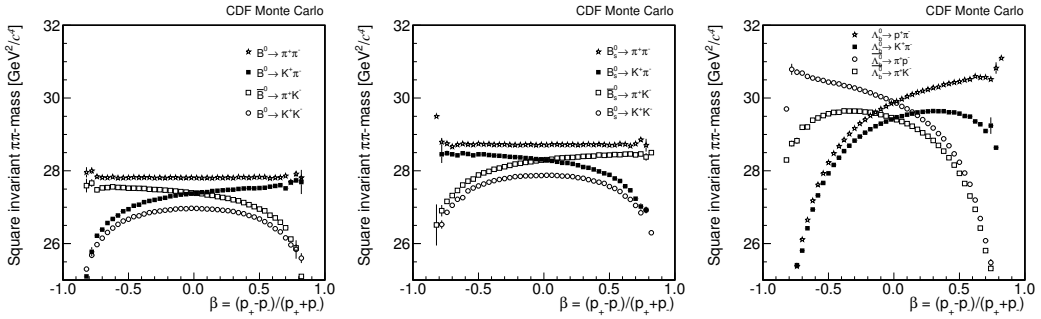

Figure 5.5: Profile plots of the square invariant $\pi\pi$-mass as a function of charged momentum asymmetry β for all simulated signal modes.

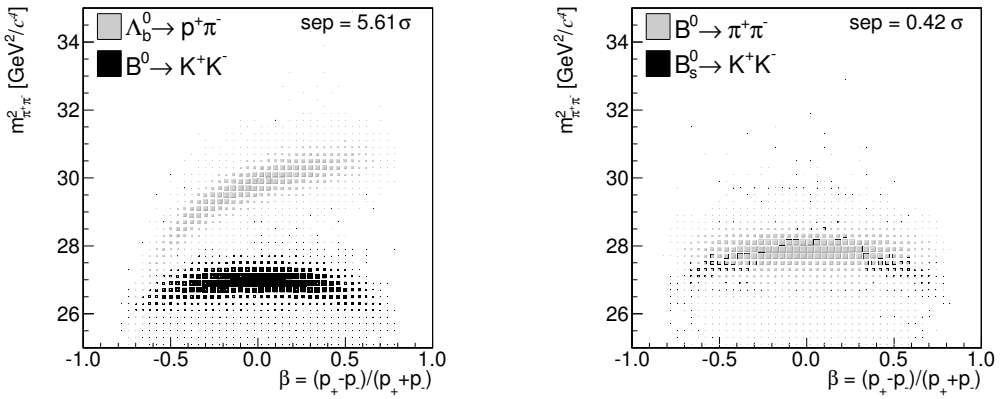

Figure 5.6: Joint distribution for β (abscissa) and $m^2_{\pi^+\pi^-}$ (ordinate) observables of simulated $B^0 \to K^+K^-$ and $\Lambda_b^0 \to p\pi^-$ (left panel), $B^0 \to \pi^+\pi^-$ and $B_s^0 \to K^+K^-$ (right panel) decay modes.

mode	$B^0\to$ $\pi^+\pi^-$	$B^0\to$ $K^+\pi^-$	$\overline{B}^0\to$ π^+K^-	$B^0\to$ K^+K^-	$B_s^0\to$ $\pi^+\pi^-$	$B_s^0\to$ π^+K^-	$\overline{B}_s^0\to$ $K^+\pi^-$	$B_s^0\to$ K^+K^-	$\Lambda_b^0\to$ $p\pi^-$	$\bar{\Lambda}_b^0\to$ $\bar{p}\pi^+$	$\Lambda_b^0\to$ pK^-	$\bar{\Lambda}_b^0\to$ $\bar{p}K^+$
$B^0\to\pi^+\pi^-$	0											
$B^0\to K^+\pi^-$	1.66σ	0										
$\overline{B}^0\to K^-\pi^+$	1.66σ	0.98σ	0									
$B^0\to K^+K^-$	3.17σ	1.77σ	1.77σ	0								
$B_s^0\to\pi^+\pi^-$	2.96σ	3.77σ	3.77σ	4.28σ	0							
$B_s^0\to K^-\pi^+$	1.62σ	2.80σ	3.05σ	3.99σ	1.64σ	0						
$\overline{B}_s^0\to K^+\pi^-$	1.58σ	3.05σ	2.80σ	3.99σ	1.64σ	0.95σ	0					
$B_s^0\to K^+K^-$	$\mathbf{0.42}\sigma$	1.66σ	1.66σ	3.28σ	3.04σ	1.70σ	1.70σ	0				
$\Lambda_b^0\to p\pi^-$	4.10σ	4.99σ	4.56σ	$\mathbf{5.61}\sigma$	2.92σ	3.40σ	3.70σ	4.56σ	0			
$\overline{\Lambda}_b^0\to\overline{p}\pi^+$	4.10σ	4.56σ	4.99σ	5.61σ	2.92σ	3.90σ	3.40σ	4.56σ	2.25σ	0		
$\Lambda_b^0\to pK^-$	3.70σ	4.99σ	4.10σ	5.25σ	2.08σ	2.85σ	3.05σ	3.70σ	1.70σ	2.20σ	0	
$\overline{\Lambda}_b^0\to\overline{p}K^+$	3.70σ	4.10σ	4.99σ	5.25σ	2.08σ	3.05σ	2.94σ	3.90σ	2.20σ	1.74σ	1.96σ	0

Table 5.1: Kinematics separation power in unit of σ between $B\to h^+h'^-$ decays, extracted from the $m^2_{\pi\pi}$ versus β distributions. In bold, we reported the minimum and the maximum separation powers found between the $B\to h^+h'^-$ decay modes.

The separation power among the modes given by the $p_{\rm tot}$ variable is small, order $\mathcal{O}(m/p)$, and since it is not possible to visualize in a three-dimensional space a four-dimensions surface ($m^2_{\pi\pi}, \beta, p_{\rm tot}$ and $z-$axis), in the figures only the correlations between the invariant $\pi\pi$-mass and β are plotted. $p_{\rm tot}$ has a limited separation power for the signal modes, but it provides some discrimination between signals and background, as you can see from fig. 5.7 (right). Figure 5.7 (left) shows the difference between the combinatorial background $m^2_{\pi\pi}$ versus β distribution, sparse in all the mass region, and the simulated $B^0 \to \pi^+\pi^-$ decay modes $m^2_{\pi\pi}$ versus β distribution, peaking in the region corresponding to the nominal B^0 mass: a separation power of about 2.4 σ is evaluated. It is evident how it would be impossible, relying only in the kinematics information, to disentangle the different $B \to h^+h'^-$ decay modes, and to perform accurate measurements of $\mathcal{C}P$ violations and $\mathcal{B}$. Therefore, we need additional information: a common strategy to discriminate between particles is the use of Particle Identification (PID).

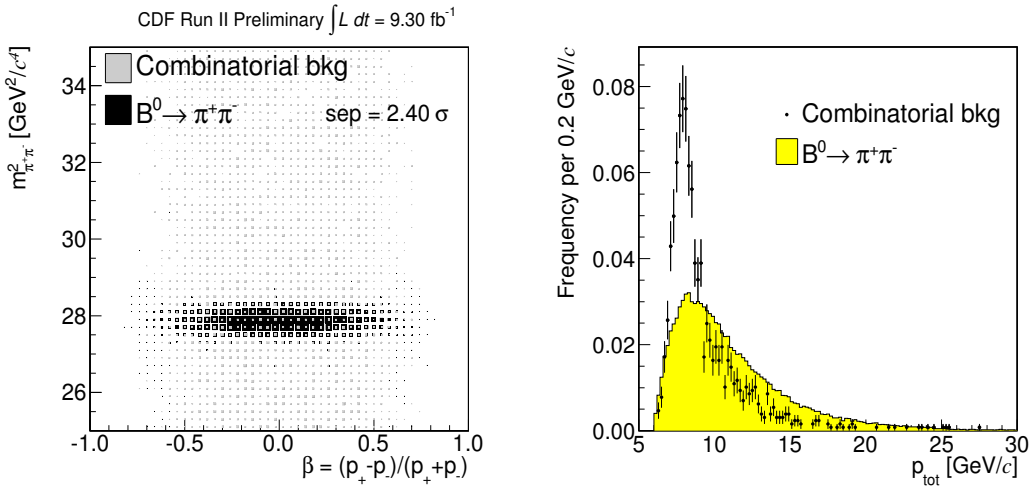

Figure 5.7: Comparison between combinatorial background distributions and simulated $B^0 \to \pi^+\pi^-$ decay modes: β versus $m^2_{\pi\pi}$ on the left, $p_{\rm tot}$ on the right.

5.3 Particle Identification (PID) separation

Identification of hadrons is difficult at CDF II, since the detector was designed for high-p_{T} physics measurements [108], and not optimized for these capabilities[5]. For charged particles with $p_{\mathrm{T}} \gtrsim 2$ GeV/c, a reasonably effective separation can be obtained from the rate of energy loss through ionization (dE/dx) in the gas that fills the active volume of the drift chamber (the COT, introduced in chap. 2). We would like to exploit the dE/dx information to obtain a variable statistically discriminating between charged particles such as pion, kaons and protons. In this way we can obtain separation power between the final states of the $B \to h^+h'^-$ decays modes consisting in particle pairs: for instance, between $\pi^+\pi^-$ and K^+K^-, or between $\pi^+\pi^-$ and pK^-, but in particular between π^+K^- and $K^+\pi^-$. The last separation power would be fundamental for $\mathcal{C}P$ measurements, because allows discriminating between the $B^0 \to K^+\pi^-$ and $\overline{B}^0 \to K^-\pi^+$ decay modes, where the separation from the kinematics information is not large. Let us suppose the possibility to obtain such a variable for positively- and negatively-charged particles, and suppose this variable can allow a statistical separation power between kaons and pions of about 1.4σ. The separation between a final state between a couple of K^+K^- and a couple $\pi^+\pi^-$ would be about $\sqrt{2} \cdot 1.4\sigma \approx 2\sigma$. The same holds for $\mathcal{C}P$ related states, for example between the couple $K^+\pi^-$ and $K^-\pi^+$. Obtaining this variable is actually possible: it is called "kaonness" $\kappa_{+(-)}$, and will be described in detail in chap. 7. The protons κ distribution are observed to be very similar to the kaon's one, thus proton are almost indistinguishable from kaons using dE/dx information. To appreciate the separation power among the signal modes achievable, we report the κ_+ versus κ_- distributions in fig. 5.8, extracted from control samples (the details will be described in chap. 7). The use of the κ is important for the aim to separate the different $B \to h^+h'^-$ contributions, in particular if we consider that the kinematics and the dE/dx are perfectly complementary. For example the kinematic separation power between the $B^0 \to \pi^+\pi^-$ and $B_s^0 \to K^+K^-$ modes is almost null (see fig. 5.6), while the dE/dx power separation is maximum, about 2σ (see fig. 5.8). In tab. 5.2 we reported the list of the separation powers between the different $B \to h^+h'^-$ decay modes.

[5] The TOF is the only detector entirely devoted to this function, but its performance is marginal for particles with momenta greater than 2.0 GeV/c. Similarly, specific ionization from the silicon tracker is of little help, because its identification power is only effective for particles with $p_{\mathrm{T}} \lesssim$ 800 MeV/c

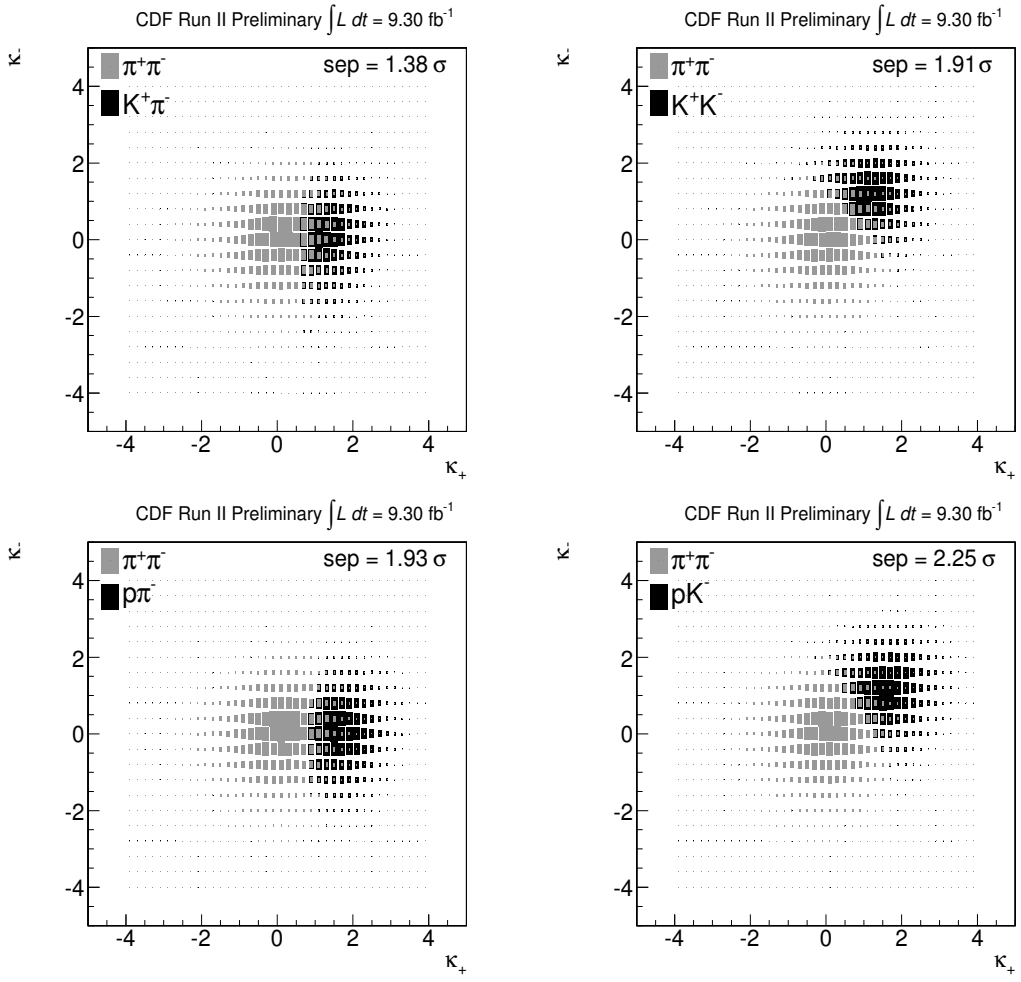

Figure 5.8: κ_+ versus κ_- distributions for different pairs of final state particles.

final states	$\pi^+\pi^-$	$K^+\pi^-$	π^+K^-	K^-K^-	$p\pi^-$	$\pi^+\bar{p}$	pK^-	$K^+\bar{p}$
$\pi^+\pi^-$	0							
$K^+\pi^-$	1.38σ	0						
π^+K^-	1.38σ	2.02σ	0					
K^+K^-	1.91σ	1.38σ	1.38σ	0				
$p\pi^-$	1.93σ	0.54σ	2.42σ	1.53σ	0			
$\pi^+\bar{p}$	1.93σ	2.42σ	0.54σ	1.53σ	2.75σ	0		
pK^-	2.25σ	1.40σ	1.90σ	0.54σ	1.38σ	2.15σ	0	
$K^+\bar{p}$	2.25σ	1.81σ	1.44σ	0.54σ	1.96σ	1.44σ	0.77σ	0

Table 5.2: PID separation power in unit of σ between $B \to h^+h'^-$ decays, extracted from the κ_+ versus κ_- distributions.

5.4 Combining information to separate the $B \to h^+h'^-$ modes

We discussed how, separately, the kinematic distributions and the PID information do not allow to distinguish the different decay modes contribution to the $B \to h^+h'^-$ peak. Thus it is necessary to use all the information available. The strategy followed combines the dE/dx and the kinematics information all together in a multidimensional Likelihood fit. This strategy is particularly convenient, if we consider that the kinematics and the PID information are complementary, and the same holds for the separation obtained from them. To have a glimpse of the global separation achievable with this strategy, we report in tab. 5.3 the separation between the $B \to h^+h'^-$ decay modes evaluated assuming the kinematic information as completely independent of PID information. This is a good approximation of the final separation power expected. In the modes where the kinematics is similar (for instance between the $B^0 \to \pi^+\pi^-$ and $B_s^0 \to K^+K^-$ modes) and thus the kinematic separation power is not large, the PID information makes possible to obtain an appreciable separation power (about 2σ). The same holds for the $B \to h^+h'^-$ decay modes with the same final states, indistinguishable using PID information, but with different kinematics, such as $B^0 \to K^+K^-$ and $B_s^0 \to K^+K^-$.

To obtain the PID and kinematics information of the different $B \to h^+h'^-$ decay modes is only the first step of the analysis, that also is complicated by the presence of the backgrounds (combinatorial and physics). In sec. 5.5 we report a brief analysis overview, underlining the crucial points of the work, while sec. 5.6 describes the structure of fit of composition used to disentangle the different $B \to h^+h'^-$ decay modes between themselves and also between the backgrounds.

mode	$B^0\to$ $\pi^+\pi^-$	$B^0\to$ $K^+\pi^-$	$\overline{B}^0\to$ π^+K^-	$B^0\to$ K^+K^-	$B_s^0\to$ $\pi^+\pi^-$	$B_s^0\to$ π^+K^-	$\overline{B}_s^0\to$ $K^+\pi^-$	$B_s^0\to$ K^+K^-	$\Lambda_b^0\to$ $p\pi^-$	$\bar{\Lambda}_b^0\to$ $\bar{p}\pi^+$	$\Lambda_b^0\to$ pK^-	$\bar{\Lambda}_b^0\to$ $\bar{p}K^+$
$B^0 \to \pi^+\pi^-$	0											
$B^0 \to K^+\pi^-$	2.20σ	0										
$\overline{B}^0 \to K^-\pi^+$	2.20σ	2.25σ	0									
$B^0 \to K^+K^-$	3.70σ	2.24σ	2.24σ	0								
$B_s^0 \to \pi^+\pi^-$	2.96σ	4.01σ	4.01σ	4.69σ	0							
$B_s^0 \to K^-\pi^+$	2.12σ	3.45σ	3.05σ	4.22σ	2.14σ	0						
$\overline{B}_s^0 \to K^+\pi^-$	2.10σ	3.05σ	3.45σ	4.22σ	2.14σ	2.23σ	0					
$B_s^0 \to K^+K^-$	1.96σ	2.16σ	2.16σ	3.28σ	3.59σ	2.19σ	2.19σ	0				
$\Lambda_b^0 \to p\pi^-$	4.53σ	5.02σ	5.16σ	5.81σ	3.50σ	4.17σ	3.74σ	4.81σ	0			
$\overline{\Lambda}_b^0 \to \bar{p}\pi^+$	4.53σ	5.16σ	5.02σ	5.81σ	3.50σ	3.94σ	4.17σ	4.81σ	3.55σ	0		
$\Lambda_b^0 \to pK^-$	4.33σ	5.18σ	4.52σ	5.28σ	3.06σ	3.43σ	3.36σ	3.74σ	2.19σ	3.07σ	0	
$\overline{\Lambda}_b^0 \to \bar{p}K^+$	5.47σ	4.33σ	5.18σ	5.28σ	3.06σ	3.54σ	3.45σ	3.94σ	2.95σ	2.26σ	2.11σ	0

Table 5.3: Separation power in unit of σ between $B \to h^+h'^-$ decays, extracted from the kinematics and PID information.

5.5 Analysis overview

In the next chapters we describe in details the analysis used to obtain the $\mathcal{C}P$ and the $\mathcal{B}$ results. The challenge is to disentangle the different decay modes between themselves and between the background (physics and combinatorial). In particular, the rarer decay modes ($B_s^0 \to \pi^+\pi^-$, $B^0 \to K^+K^-$, $B_s^0 \to K^-\pi^+$, and $\Lambda_b^0 \to ph^-$) represent together at most 10% of the $B \to h^+h'^-$ events and are hidden by the other more abundant $B \to h^+h'^-$ modes ($B^0 \to K^+\pi^-$, $B^0 \to \pi^+\pi^-$, and $B_s^0 \to K^+K^-$). The following points are crucial for the search:

- **mass resolution description**; high accuracy of mass distribution comprehension is needed. The $B_s^0 \to \pi^+\pi^-$, $B^0 \to K^+K^-$, $B_s^0 \to K^-\pi^+$ and $\Lambda_b^0 \to ph^-$ decay modes are rarer with respect the modes dominating the peak, i. e., the $B^0 \to K^+\pi^-$, $B^0 \to \pi^+\pi^-$ and $B_s^0 \to K^+K^-$. In particular, the more abundant mode $B^0 \to K^+\pi^-$ represents about 50% of the all signal peak. Its tails hide the other interesting decays, and the results of the analysis may strongly depend on the detailed shape on the invariant mass distribution. An accurate description of the mass line shape, including the tails, is crucial to obtain correct results. The kinematics templates will be described in detail in chap. 6.

- **PID**; the PID information is a fundamental information for two reasons. At first, it is necessary to disentangle the rarer modes ($B_s^0 \to K^-\pi^+$, $B_s^0 \to \pi^+\pi^-$, $B^0 \to K^+K^-$ and $\Lambda_b^0 \to ph^-$) from the other $B \to h^+h'^-$ modes: that would be impossible relying only on the kinematic information. Secondly, it is fundamental to distinguish the charge conjugates modes: $B^0 \to K^+\pi^-$ from $\overline{B}^0 \to K^-\pi^+$, $B_s^0 \to K^-\pi^+$ from $\overline{B}_s^0 \to K^+\pi^-$ and so on. An accurate description of the PID information is then crucial to obtain correct results. The PID templates will be described in detail in chap. 7.

- **physics background**; the $B^0 \to K^+K^-$ search is made more difficult by the overlapping of the partially reconstructed decay modes. Some of them are not yet measured and have large theoretical uncertainties, some others have large uncertainties on the $\mathcal{B}$ measurements. Thus the final state composition is not known with high accuracy and this diminishes the effect of using the PID information. In addition, the left tail of the $B^0 \to K^+\pi^-$ and of the $B^0 \to K^+K^-$ distributions overlap with the tail of the physics background modes. The kinematic limits of the physics background mass distribution are unknown a priori, because we do not know the exact composition of the physics background. An inaccurate description of the physics background mass distribution can therefore strongly affect the $\mathcal{B}(B^0 \to K^+K^-)$ result, and can also influence the shape of the $B^0 \to K^+\pi^-$ distribution. To obtain correct results, an accurate description of the template modes has been done in sec. 6.2.

5.6 Fit of composition

We used the following five discriminating observables:

1. $\boldsymbol{m^2_{\pi\pi}}$ – square invariant mass of the pair with pion mass assignments[6];
2. $\boldsymbol{\beta}$ – charged-momentum asymmetry between the two particles;
3. $\boldsymbol{p_{\rm tot}}$ – scalar sum of the particle momenta;
4. $\boldsymbol{\kappa_+}$ – kaonness[7] (function of the dE/dx) of the positively charged particle;
5. $\boldsymbol{\kappa_-}$ – kaonness of the negatively charged particle.

The Likelihood function $\mathscr{L}$ is the product of the Likelihoods $\mathscr{L}_i$ of all events:

$$\mathscr{L}(\vec{\theta}) = \prod_{i=1}^{N} \mathscr{L}_i(\vec{\theta}|\vec{x}_i) \tag{5.10}$$

where the index i runs over the events. N is the total number of events passing the final selection, $\vec{\theta}$ is the vector of parameters that we want to estimate, $\vec{x}$ is the vector of the discriminating observables $\vec{x}_i = \{m^2_{\pi\pi}, \beta, p_{\rm tot}, \kappa_+, \kappa_-\}_i$.
The Likelihood of each event is written as the sum of a signal term and a background term:

$$\mathscr{L}_i = b \cdot \mathscr{L}_i^{\rm bck} + (1-b) \cdot \mathscr{L}_i^{\rm sig}. \tag{5.11}$$

The index sig (bck) labels the part of the function that describes the signal (background) term; b is the fraction of background events and $1-b$ is the fraction of the $B \to h^+h'^-$ events ($b \in \vec{\theta}$). The Likelihood of the signal events is factorized as a product of three probability density functions (p.d.f.'s):

$$\mathscr{L}^{\rm sig} = \sum_{j=1}^{s} f_j \cdot \wp_j^m(m^2_{\pi\pi}|\beta, p_{tot}) \cdot \wp_j^p(\beta, p_{\rm tot}) \cdot \wp_j^{\rm PID}(\kappa_+, \kappa_-|\beta, p_{\rm tot}), \tag{5.12}$$

in which the index j runs over the twelve expected components: $B^0 \to \pi^+\pi^-$, $B^0 \to K^+\pi^-$, $\overline{B}^0 \to K^-\pi^+$, $B^0_s \to K^-\pi^+$, $\overline{B}^0_s \to K^+\pi^-$, $B^0_s \to K^+K^-$, $B^0 \to K^+K^-$, $B^0_s \to \pi^+\pi^-$, $\Lambda^0_b \to p\pi^-$, $\overline{\Lambda}^0_b \to \overline{p}\pi^+$, $\Lambda^0_b \to pK^-$, $\overline{\Lambda}^0_b \to \overline{p}K^+$[8]. The parameters f_j are their fractions (of the total signal), and are determined by the fit. From the $(s-1)$ independent fractions resulting by the normalization condition,

$$f_s = 1 - \sum_{j=1}^{s-1} f_j, \tag{5.13}$$

[6] It is particular convenient to use the square invariant $\boldsymbol{\pi\pi}$-mass ($\boldsymbol{m^2_{\pi\pi}}$) instead of the more commonly used invariant $\boldsymbol{\pi\pi}$-mass ($\boldsymbol{m_{\pi^+\pi^-}}$) because eq. (5.9), given $\boldsymbol{\beta}$ and $\boldsymbol{p_{\rm tot}}$, is a linear transformation, when square masses are considered as variables. This implies that the jacobian $\boldsymbol{|dm^2_{\pi\pi}/dm^2_j| = 1}$ instead of a complicated function of $\boldsymbol{\beta}$ and $\boldsymbol{p_{\rm tot}}$ different for each signal.

[7] The variable "kaonness" will be properly described in chap. 7, together with the correspondent template.

[8] C-conjugate modes are considered distinct for decays in $K\pi$, $p\pi$ and pK final states that are distinguishable on the basis of the final particle types.

we determined the yield of each mode. We conventionally label as $\wp^m$ the term that describes the invariant-mass distributions ("mass term"), $\wp^p$ the term that describes the momentum distributions ("momentum term"), and $\wp^{\mathrm{PID}}$ the term that models the dE/dx density ("PID term"). This factorization is not trivial since the three terms of the p.d.f. are inter-related by the dependencies between mass, momentum, and dE/dx observables.

The Likelihood of the background factorizes in a similar way to the signal term, and it consists of the sum of two contributions:

$$\mathscr{L}^{\mathrm{back}} = \sum_{l=\mathrm{A,E}} f_l \cdot \wp_l^m(m^2_{\pi\pi}|\beta, p_{\mathrm{tot}}) \cdot \wp_l^p(\beta, p_{\mathrm{tot}}) \cdot \wp_l^{\mathrm{PID}}(\kappa_+, \kappa_-|\beta, p_{\mathrm{tot}}), \tag{5.14}$$

where the index l runs over the different kinds of background, combinatorial ($l = E$) and physics ($l = A$) background. The parameters f_l are their fractions (of the total background) and are determined by the fit. From the normalization condition results $f_{\mathrm{E}} = 1 - f_{\mathrm{A}}$. In Equations (5.11)–(5.14) the functional dependence on the vector $\vec{\theta}$ was omitted, since in the equations we wrote explicitly some terms of this vector, as f_i, f_{A} and b. The kinematic templates will be discussed in detail in chap. 6, while in chap. 7 we will report the modeling of the PID observables.

Simultaneous fit of `A` and `C` samples

The probability density function of the fit of composition we wrote keeps into account only one kinematics, for instance the one of the `A` subsample. As explained in detail in sec. 3.1, the data sample is composed by two different kinematics, the `med` and the `high` ones, corresponding to two independent subsamples `A` and `C`. Therefore we can perform a simultaneous fit of these two sub-samples and we can write the total Likelihood function $\mathscr{L}$ of all events:

$$\mathscr{L}(\vec{\theta}) = \prod_{i=1}^{N_{\mathrm{A}}} \mathscr{L}_i^{\mathrm{A}}(\vec{\theta}_{\mathrm{A}}|\vec{x}_i) \cdot \prod_{i=1}^{N_{\mathrm{C}}} \mathscr{L}_i^{\mathrm{C}}(\vec{\theta}_{\mathrm{C}}|\vec{x}_i) \tag{5.15}$$

where the index i runs over the events. N_{A} is the number of events of `A` sample, N_{C} is the number of events of `C` sample, and where $N = N_{\mathrm{A}} + N_{\mathrm{C}}$ is the total number of events. $\vec{\theta}_{\mathrm{A(C)}}$ is the vector of parameters that we want to estimate, $\vec{x}$ is the vector of the discriminating observables $\vec{x}_i = \{m^2_{\pi\pi}, \beta, p_{\mathrm{tot}}, \kappa_+, \kappa_-\}_i$.

The likelihood function written in such a way does not keep into account the poissonian uncertainty due to the finite size of the total sample N and the binomial uncertainty due to the fact we splitted the sample in two subsamples $N = N_{\mathrm{A}} + N_{\mathrm{C}}$. This means that we have to consider N as a Poisson variable with mean ν and and that N_{A} and N_{C} are binomially distributed, with a probability p to have N_{A}, and $1 - p$ to have N_{C} events, when the sum is constrained to be, in our specific case,

equal to N. Then the new extended Likelihood function can be written as:

$$\mathscr{L}(\nu, p, \vec{\theta}) = \frac{\nu^N}{N!} e^{-\nu} \cdot \frac{N!}{N_{\rm A}!(N - N_{\rm A})!} p^{N_{\rm A}} (1-p)^{N-N_{\rm A}} \cdot \prod_{i=1}^{N_{\rm A}} \mathscr{L}_i^{\rm A}(\vec{\theta}_{\rm A}|\vec{x}_i) \cdot \prod_{i=1}^{N_{\rm C}} \mathscr{L}_i^{\rm C}(\vec{\theta}_{\rm C}|\vec{x}_i) \tag{5.16}$$

and if we define $n_{\rm A}$ and $n_{\rm C}$ as

$$n_{\rm A} = \nu p \tag{5.17}$$

$$n_{\rm C} = \nu(1-p) \tag{5.18}$$

the Likelihood function can be rewritten as a function of $n_{\rm A(C)}$, instead of ν and p, that are the observables we want to estimate. Other parameters remain unchanged, as described in the previous sections, except that they are much more since we are fitting two different kinematics. They did not double because some of them are in common between the two samples. The p.d.f for all signal and background components are parameterized as described in next chapters, respectively for `med` and `high` scenarios, as two different analyses.

Chapter 6

Kinematics templates

As introduced in chap. 5, a very accurate description of the kinematics distributions is needed to disentangle the rarer decay modes ($B^0 \to K^+K^-$, $B_s^0 \to \pi^+\pi^-$, $B_s^0 \to K^-\pi^+$, and $\Lambda_b^0 \to ph^-$) from the surrounding and more abundant others $B \to h^+h'^-$ decay modes. This chapter describes the kinematic templates used in the Likelihood fit: we extracted the templates of the $B \to h^+h'^-$ decay modes and of the physics background using the official CDF Monte Carlo simulation. The combinatorial background templates are extracted directly from data.

6.1 $B \to h^+h'^-$ signal templates

6.1.1 Probability density function of the signal mass term

Using the mass information in a Likelihood fit requires modeling the distributions of the desired observable. The squared invariant $\pi\pi$-mass distribution of the non-$\pi\pi$ components depends on the mass shift, which is a function of the charged-momentum asymmetry β and of the scalar sum of the momenta $p_{\rm tot}$ of the decay products. It is due to mis-assigned masses of the outgoing particles, as discussed in sec. 5.2. We will account for this effect by writing a $\pi\pi$-mass p.d.f. as a conditional probability density function for a given charged-momentum asymmetry and scalar sum of the momenta.

Using the simulated sample described in chap. 4, we parameterized the squared invariant mass distribution m_j^2, computed with the correct mass assignment ($j = B^0 \to \pi^+\pi^- \Longrightarrow m_j^2 = m_{\pi\pi}^2$; $j = B^0 \to K^+\pi^- \Longrightarrow m_j^2 = m_{K\pi}^2$; etc.), using the following analytical function:

$$\begin{aligned}\mathcal{R}_j(m_j^2) &= f_{\rm bulk}^j \left[f_1^j \mathscr{G}(m_j^2; m_{H_j^0}^2 + \delta_1^j, \sigma_1^j) + (1 - f_1^j)\mathscr{G}(m_j^2; m_{H_j^0}^2 + \delta_2^j, \sigma_2^j) \right] \\ &\quad + (1 - f_{\rm bulk}^j)\mathscr{T}(m_j^2; b^j, c^j, m_{H_j^0}^2 + \delta_1^j) \end{aligned} \tag{6.1}$$

where:

$$\mathscr{G}(x;\mu,\sigma) = \frac{1}{\sqrt{2\pi}\sigma} e^{-\frac{1}{2}\left(\frac{x-\mu}{\sigma}\right)^2} \tag{6.2}$$

$$\mathscr{T}(x;b,c,\mu) = \frac{1}{K} e^{b(x-\mu)} \cdot \mathrm{Erfc}(c(x-\mu)) \tag{6.3}$$

$$K = \int_{x_1}^{x_2} e^{b(x-\mu)} \cdot \mathrm{Erfc}(c(x-\mu))dx \tag{6.4}$$

$$\mathrm{Erfc}(x) = 1 - \mathrm{Erf}(x) = \frac{2}{\sqrt{\pi}} \int_x^{+\infty} e^{-t^2} dt. \tag{6.5}$$

in which the index j runs over all components. We used a sum of two Gaussians to parameterize the bulk of the distribution, while the long lower-mass tail due to the soft photon emission is parameterized with the function in eq. (6.3). f^j_{bulk} is the relative fraction of the double-Gaussian bulk with respect to the total (bulk plus tail), while $1 - f^j_{\mathrm{bulk}}$ is the fraction of the tail term. f^j_1 is the relative fraction of the more abundant Gaussian labeled with the index 1 with respect to the sum of two Gaussians, while $\sigma^j_{1(2)}$ is the the width of the Gaussian 1(2). $\delta^j_{1(2)}$ is the shift from the squared mass value of the hadron H^0_j ($j = B^0 \to \pi^+\pi^- \Longrightarrow m^2_{H^0_j} = m^2_{B^0}$; $j = B^0_s \to K^+K^- \Longrightarrow m^2_{H^0_j} = m^2_{B^0_s}$; etc.). The values of the parameters $\{f_{\mathrm{bulk}}, f_1, \sigma_2, \delta_1, \delta_2, b, c\}_j$ are fixed in the fit; they were extracted from the MC simulation described in the previous sections. Figures 6.1–6.4 show the squared invariant mass kinematic templates for all the $B \to h^+h^{'-}$ decay modes.

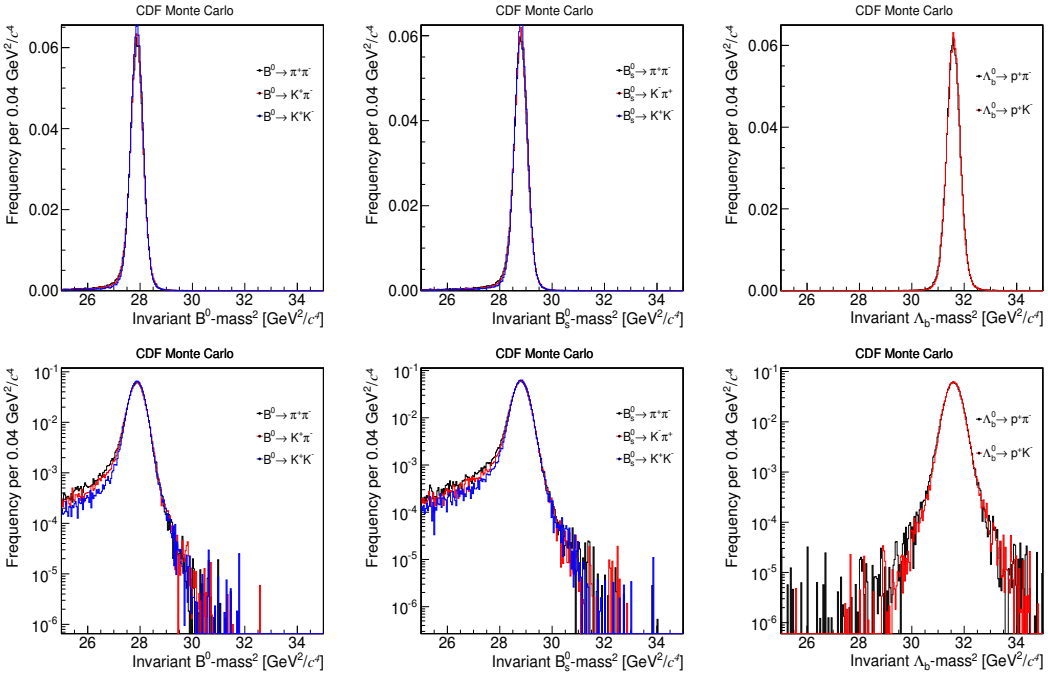

Figure 6.1: Squared invariant mass distribution of the simulated $B \to h^+h'^-$ histograms. Linear (top) and logarithmic (bottom) scale.

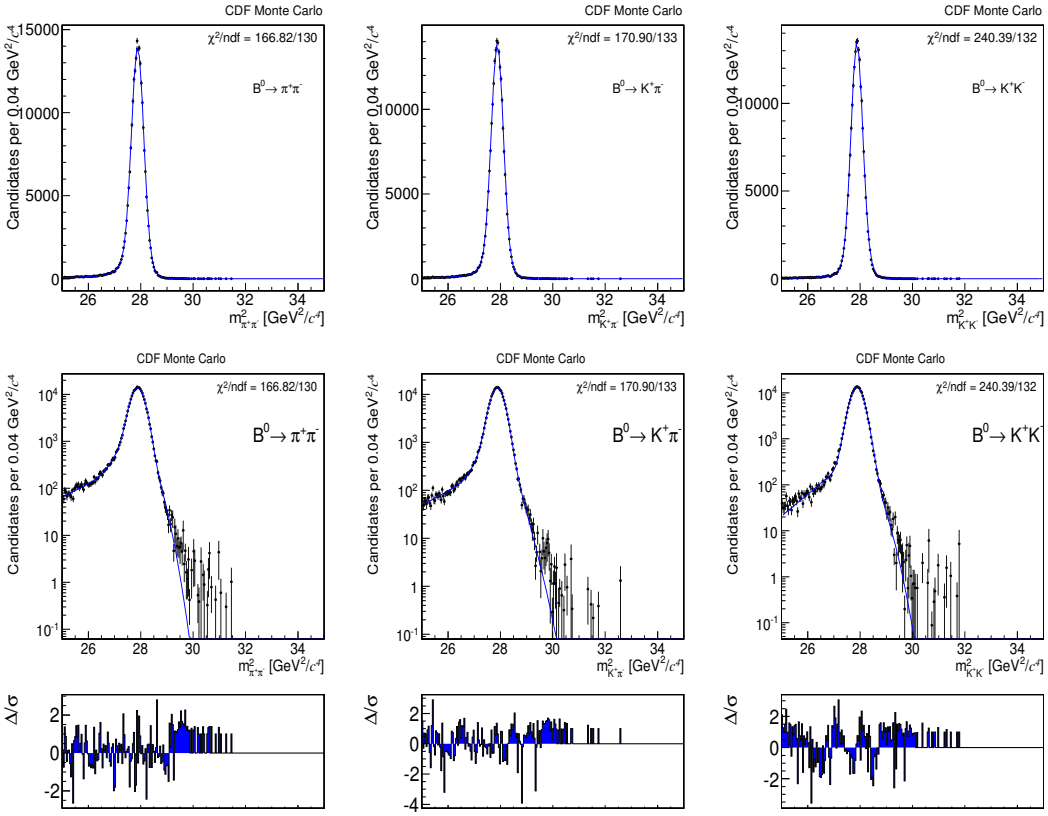

Figure 6.2: Squared invariant mass distribution of the simulated $B^0 \to h^+h'^-$ decays. On the top linear scale, on the bottom logarithmic scale. The template is overlaid.

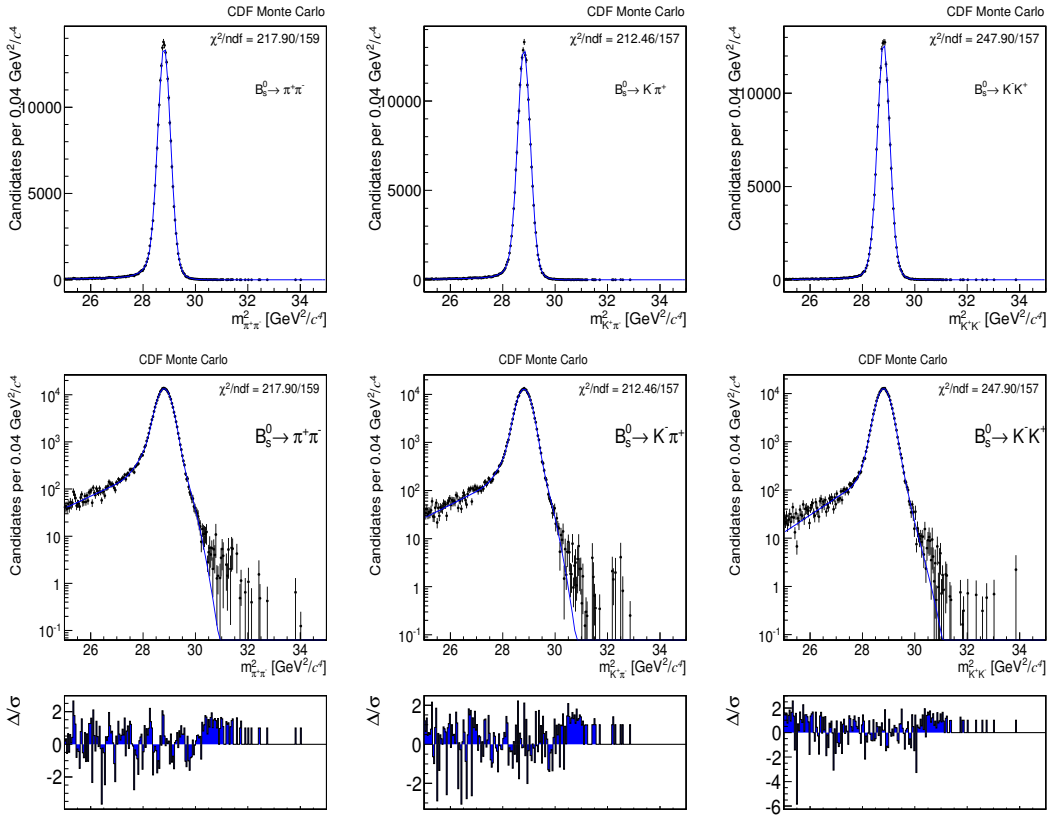

Figure 6.3: Squared invariant mass distribution of simulated $B_s^0 \to h^+h'^-$ decays. On the top linear scale, on the bottom logarithmic scale. The template is overlaid.

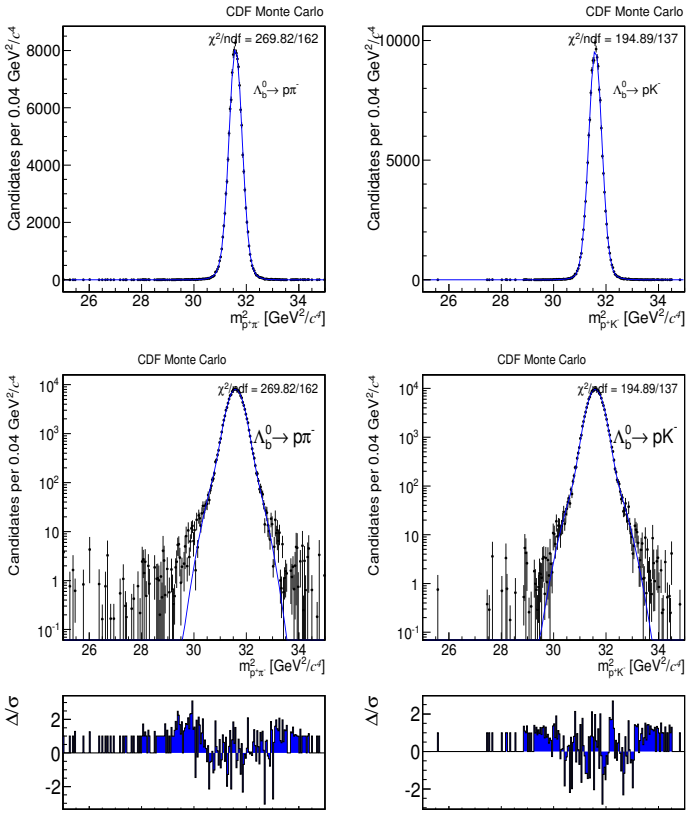

Figure 6.4: Squared invariant mass distribution of the simulated $\Lambda_b^0 \to ph^-$ decays. On the top linear scale, on the bottom logarithmic scale. The template is overlaid.

The distribution of the signal mass term $\mathcal{R}_j(m_j^2)$ was written, in eq. (6.1), as a function of different mass observables m_j^2, because for each decay mode (j) we have a different invariant mass variable. In sec. 5.2 we discussed why it is convenient to write the different squared mass assignments m_j^2 as a function of a single invariant mass observable $m_{\pi\pi}^2$ and the momenta observables β and $p_{\rm tot}$. Therefore, for each jth decay mode we can write the probability density function as a function of $m_{\pi\pi}^2$ given β and $p_{\rm tot}$, through a simple change of variables $m_j^2 \to m_{\pi\pi}^2$:

$$\mathcal{R}_j(m_j^2) \;=\; \mathcal{R}_j(m_j^2(m_{\pi\pi}^2)) \times \frac{dm_{\pi\pi}^2}{dm_j^2} = \mathcal{R}_j(m_{\pi\pi}^2|\beta, p_{\rm tot}), \tag{6.6}$$

where $\frac{dm_{\pi\pi}^2}{dm_j^2} = 1$. With this substitution we can write the probability density of the signal mass term as follows:

$$\begin{aligned}\wp_j^m(m_{\pi\pi}^2|\beta, p_{\rm tot}) \;=\; & f_{\rm bulk}^j \Big[f_1^j \mathscr{G}(m_{\pi\pi}^2 - \Delta_{\beta,p_{\rm tot}}^j; m_{H_j^0}^2 + \delta_1^j, \sigma_1^j) \\ & + (1 - f_1^j)\mathscr{G}(m_{\pi\pi}^2 - \Delta_{\beta,p_{\rm tot}}^j; m_{H_j^0}^2 + \delta_2^j, \sigma_2^j)\Big] \\ & + (1 - f_{\rm bulk}^j)\mathscr{T}(m_{\pi\pi}^2 - \Delta_{\beta,p_{\rm tot}}^j; b^j, c^j, m_{H_j^0}^2 + \delta_1^j). \end{aligned} \tag{6.7}$$

$$\tag{6.8}$$

where $\Delta_{\beta,p_{\rm tot}}^j = 2m_\pi^2 - (m_+^2 + m_-^2) + 2\left(\sqrt{\left(\frac{1+\beta}{2}p_{tot}\right)^2 + m_\pi^2} \cdot \sqrt{\left(\frac{1-\beta}{2}p_{tot}\right)^2 + m_\pi^2}\right) - 2\left(\sqrt{\left(\frac{1+\beta}{2}p_{tot}\right)^2 + m_+^2} \cdot \sqrt{\left(\frac{1-\beta}{2}p_{tot}\right)^2 + m_-^2}\right)$ from eq. (5.9).

Momentum dependence of the $m_{\pi\pi}^2$ resolution

So far we treated the invariant mass resolution as independent of the momentum observables, however the invariant mass resolution depends on the momentum of the mother particle and therefore, on the momenta of the decay products. We explicitly introduced this dependence to keep into account the changes of the mass resolution as a function of our momentum observables β and $p_{\rm tot}$ (less than 10 MeV$^2/c^4$ as a function of β and about 80 MeV$^2/c^4$ as a function of $p_{\rm tot}$, spanning the range $5.5 \lesssim p_{\rm tot} \lesssim 35$ GeV$/c$). The variation as a function of β is a small residual dependence on $p_{\rm tot}$, since selecting different regions in β we bias our sample toward high $p_{\rm tot}$ values.

The choice of β and $p_{\rm tot}$ as variables in the fit rather than equivalent p_+ and p_- variables turns out to be very convenient in this case, because β and $p_{\rm tot}$ are almost independent observables, and this is reflected in the factorizability of the momenta mass resolution dependence. The mass resolution can be written as the product of two independent functions of β and $p_{\rm tot}$: $\sigma(\beta, p_{\rm tot}) \approx \sigma_\beta(\beta) \cdot \sigma_{p_{\rm tot}}(p_{\rm tot})$. Since the variation as a function of β is small, in the $\wp(m_{\pi\pi}^2)$ we neglected this dependence. The $p_{\rm tot}$ dependence was parameterized with a straight line. Figure 6.5 shows the $m_{\pi\pi}^2$ resolution, as a function of $p_{\rm tot}$, for $B^0 \to K^+\pi^-$ decay mode as an example.

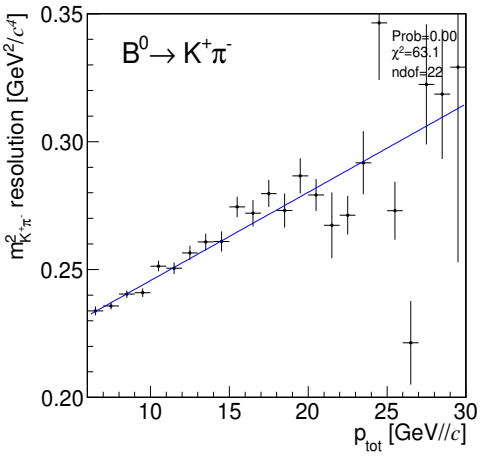

Figure 6.5: Dependence of the squared mass resolution on $p_{\rm tot}$ for the $B^0 \to K^+\pi^-$ decays parameterized with a first order degree polynomial.

The values σ_1^j and σ_2^j extracted in the parameterization of $\wp_j^m(m_j^2)$ (see eq. (6.1)) are averaged along all momenta: $\sigma_1^j \to \sigma_{01}^j$ and $\sigma_2^j \to \sigma_{02}^j$. Then we introduced the $p_{\rm tot}$ dependence in the fit and the new momentum dependent values for σ_1^j and σ_2^j to insert in eq. (6.1) become:

$$\begin{aligned} \sigma_1^j &= \sigma_{01}^j \cdot \left(1 + \frac{b_1^j}{\sigma_{01}^j}(p_{\rm tot} - \langle p_{\rm tot}\rangle)\right) \\ \sigma_2^j &= \sigma_{02}^j \cdot \left(1 + \frac{b_1^j}{\sigma_{02}^j}(p_{\rm tot} - \langle p_{\rm tot}\rangle)\right) \end{aligned} \tag{6.9}$$

where the index j runs over all possible signal modes and $\langle p_{\rm tot}\rangle$ is the average $p_{\rm tot}$ value.

6.1.2 Probability density function of the signal momentum term

The momentum p.d.f. is extracted from the simulated signal samples described in chap. 4. Selection requirements and kinematic correlations between the outgoing particles cause the domain and shape of the β distribution to vary as a function of $p_{\rm tot}$. In fact, both momenta (p_+ and p_-) are necessarily larger than 2(2.5) GeV/c, and their sum is larger than 5.5(6.5) GeV/c, because of the trigger requirements on their transverse momenta. This translates into the following conditions on β and $p_{\rm tot}$:

$$p_\pm = p_{\rm tot}\left(\frac{1\pm\beta}{2}\right) > 2(2.5)\ \text{GeV}/c \quad \text{and} \quad p_{\rm tot} > 5.5(6.5)\ \text{GeV}/c. \tag{6.10}$$

Thus the domain of the joint distribution $\beta, p_{\rm tot}$ is defined by eq. (6.10), explicitly:

$$p_{\rm tot} > \frac{4(5)}{1-\beta}\ \text{GeV}/c \tag{6.11}$$

$$p_{\rm tot} > \frac{4(5)}{1+\beta}\ \text{GeV}/c \tag{6.12}$$

The domain is visible in fig. 6.6(a) (for scenario `med`) and in fig. 6.6(b) (for scenario `high`). For these reasons, the β distribution varies as a function of $p_{\rm tot}$. Table 6.1

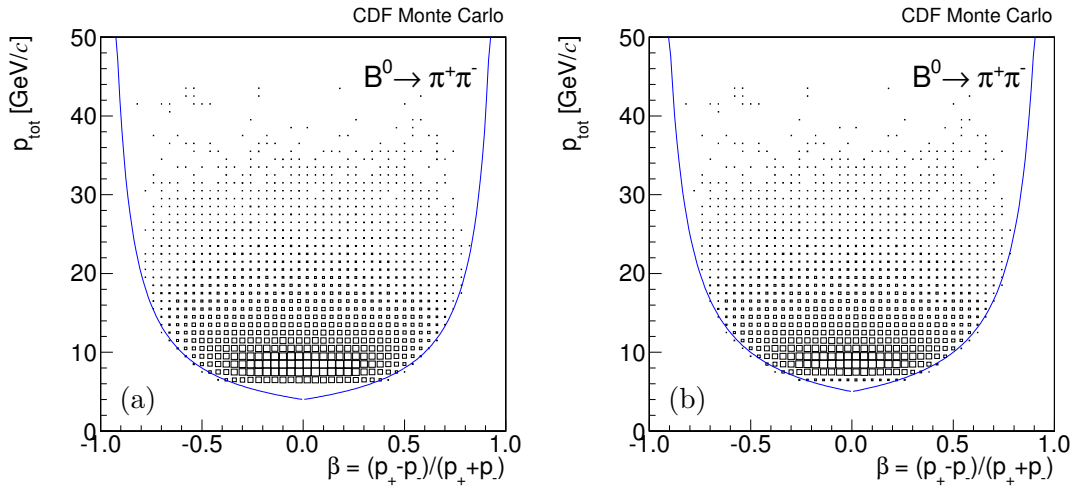

Figure 6.6: β versus $p_{\rm tot}$ distribution for the $B^0 \to \pi^+\pi^-$ simulated decay modes for `med` (a) and `high` (b) scenarios. The function overlaid corresponds to the domain requirements $p_{\rm tot}$ = 4(5)/(1-β) and $p_{\rm tot}$ = 4(5)/(1+β).

reports the variation of β in function of different slice of $p_{\rm tot}$. The domain requirements translate into an increasing RMS of the β distribution with the increasing of $p_{\rm tot}$. Figure 6.7 shows the distribution of the β variable as a function of $p_{\rm tot}$, spanning the range $p_{\rm tot} < 30$ GeV/c, for the $B^0 \to \pi^+\pi^-$ decay mode.

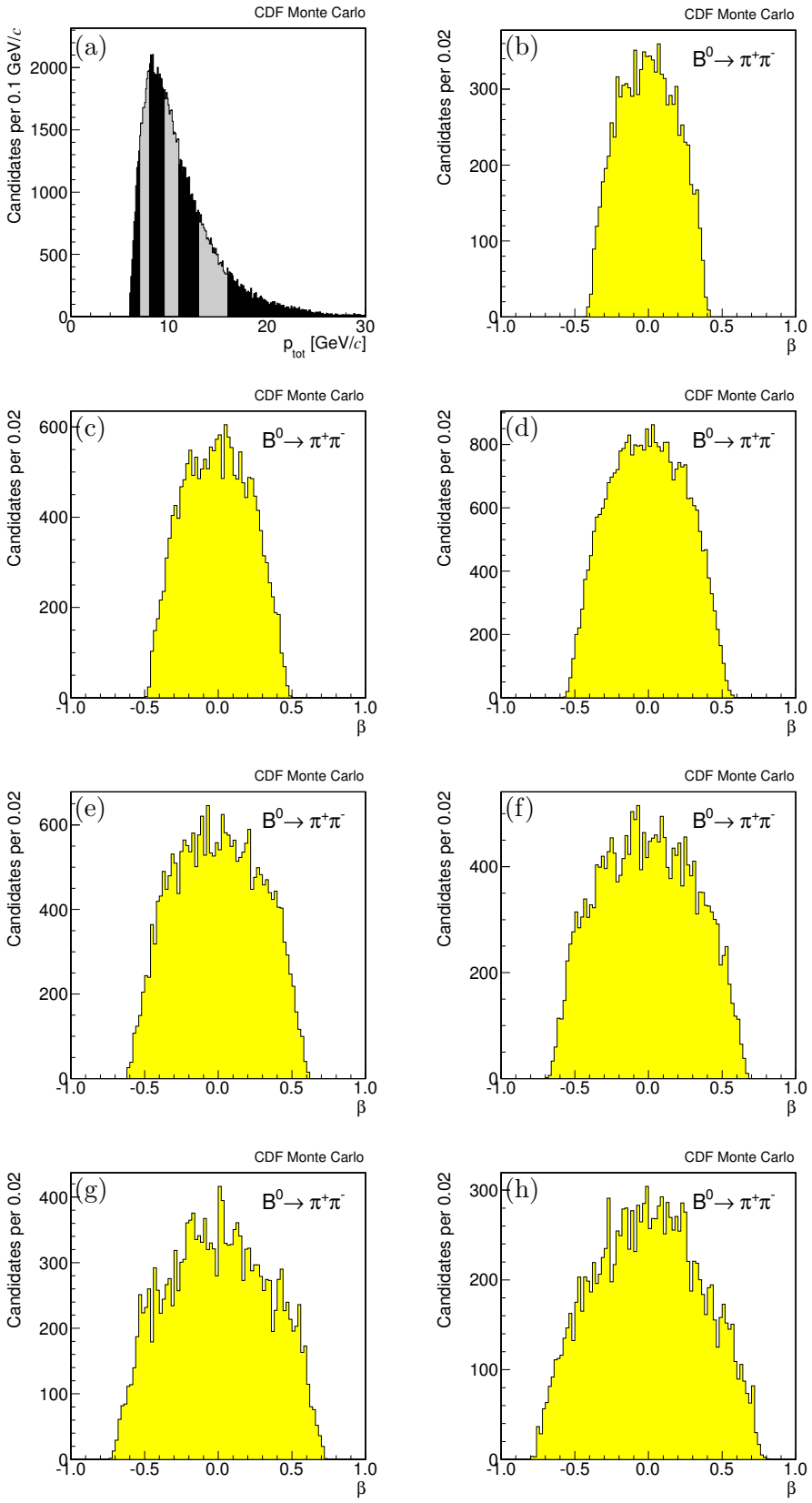

Figure 6.7: $p_{\rm tot}$ distribution of simulated $B^0 \to \pi^+\pi^-$ decays, divided for the different $p_{\rm tot}$ ranges (a). β distribution of simulated $B^0 \to \pi^+\pi^-$ decays spanning different $p_{\rm tot}$ ranges: $p_{\rm tot} < 7$ GeV/c (b), $7 < p_{\rm tot} < 8$ GeV/c (c), $8 < p_{\rm tot} < 9.5$ GeV/c (d), $9.5 < p_{\rm tot} < 11$ GeV/c (e), $11 < p_{\rm tot} < 13$ GeV/c (f), $13 < p_{\rm tot} < 16$ GeV/c (g), $p_{\rm tot} > 16$ GeV/c (h).

$p_{\rm tot}$ interval (GeV/c)	mean	rms
$p_{\rm tot} < 7.0$	0.00	0.19
$7.0 < p_{\rm tot} < 8.0$	0.01	0.22
$8.0 < p_{\rm tot} < 9.5$	0.00	0.25
$9.5 < p_{\rm tot} < 11.0$	0.00	0.28
$11.0 < p_{\rm tot} < 13.0$	0.01	0.31
$13.0 < p_{\rm tot} < 16.0$	0.00	0.34
$p_{\rm tot} > 16.0$	0.00	0.35

Table 6.1: β mean and RMS as a function of $p_{\rm tot}$.

Performing the parameterization of such a joint distribution is challenging: the β dependence on $p_{\rm tot}$ must be reproduced by the fit function. To simplify the problem, we define two new variables, β' for `med` and β'' for `high` path:

$$\beta' = \beta \cdot \frac{p_{\rm tot}}{p_{\rm tot} - 4}; \qquad \beta'' = \beta \cdot \frac{p_{\rm tot}}{p_{\rm tot} - 5} \tag{6.13}$$

The definition of these two variables incorporates the β dependence on $p_{\rm tot}$ due to the trigger requirements. Therefore the β' and β'' dependence on $p_{\rm tot}$ is almost null (see fig. 6.8): for example, the correlation factor between β' and $p_{\rm tot}$ is $\approx 0.5\%$ for $B^0 \to \pi^+\pi^-$ simulated decay modes. Still, as you can see in fig. 6.9, a small depen-

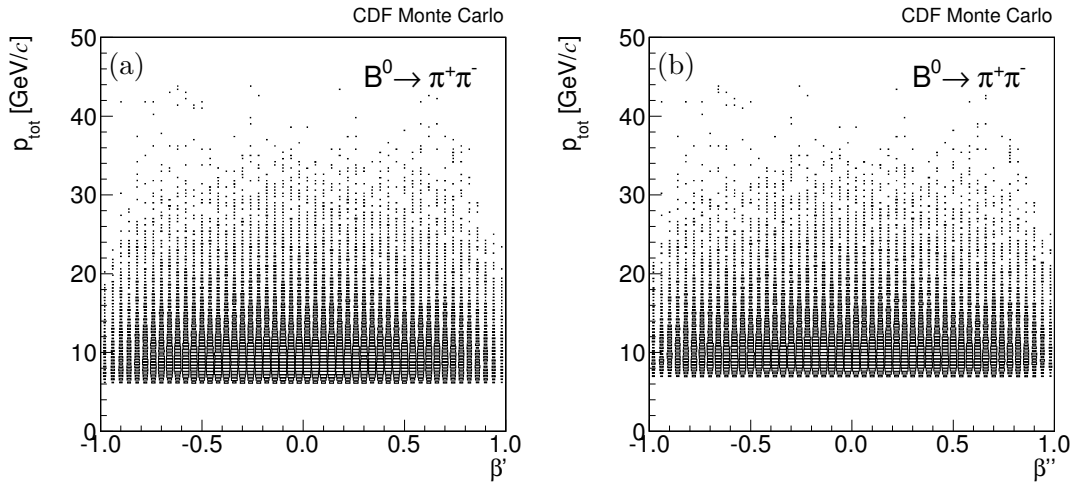

Figure 6.8: β' versus $p_{\rm tot}$ distribution for the $B^0 \to \pi^+\pi^-$ simulated decay modes for `med` sample (a). β'' versus $p_{\rm tot}$ distribution for the $B^0 \to \pi^+\pi^-$ simulated decay modes for `high` sample (b).

dence between β' and $p_{\rm tot}$ is unavoidable (the same holds for β''): the RMS of the distribution decreases with the increasing of $p_{\rm tot}$. Thus, we wrote a bi-dimensional function where the β' term is able to vary in function of $p_{\rm tot}$, to take into account the small dependence discussed. To avoid repetitions, from now on we will describe

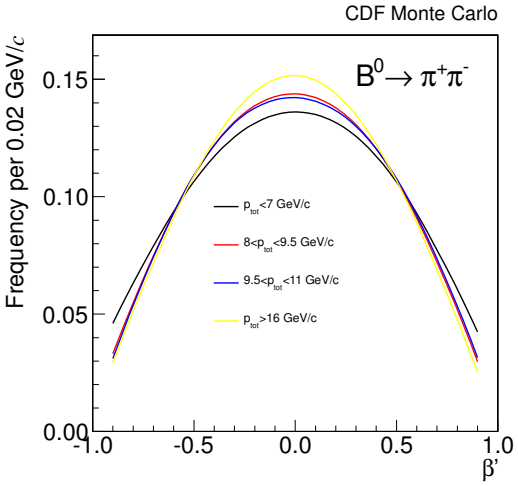

Figure 6.9: β' distributions of $B^0 \to \pi^+\pi^-$ decays in different $p_{\rm tot}$ intervals.

only the procedure used to obtain the scenario `med` p.d.f.s. The same method has been used for the scenario `high` p.d.f.s. We followed a three steps strategy: in the first step, we fitted the $p_{\rm tot}$ distribution using the Laguerre polynomials[1]. In the second step, we fitted the $p_{\rm tot}$-integrated β' distribution using the Chebyshev polynomials[2]. In the final step, we fitted the $(\beta', p_{\rm tot})$ joint distribution with a bidimensional function using the information obtained from the previous steps.

$p_{\rm tot}$ parameterization

We empirically chose a parameterization of $p_{\rm tot}$ density, whose parameters were determined with a binned fit of simulated events distributions. The technical challenge is to reproduce the shape behaviour: a rapid turn on due to the trigger requirements is followed by a smoothly declining tail (fig. 6.10 (a)). Thus the p.d.f.$(p_{\rm tot})$ is written as the product of an exponential function times a 6th-degree Laguerre polynomial:

$$\wp_j^p(p_{\rm tot}) \;=\; \frac{1}{N_j}\left(e^{c_j p_{\rm tot}} \sum_{l=0}^{6} a_{lj} L_l(p_{\rm tot})\right) \tag{6.14}$$

where the index j labels the dependence on the decay mode and N_j is a normalization term. The exponential part reproduces the tail of the distribution, while the Laguerre polynomials parameterize the turn on region.

[1] $L_n(x) = \frac{e^x}{n!}\frac{d^n}{dx^n}(e^{-x}x^n)$
[2] $T_n(x) = \cos(n \cdot \arccos(x))$

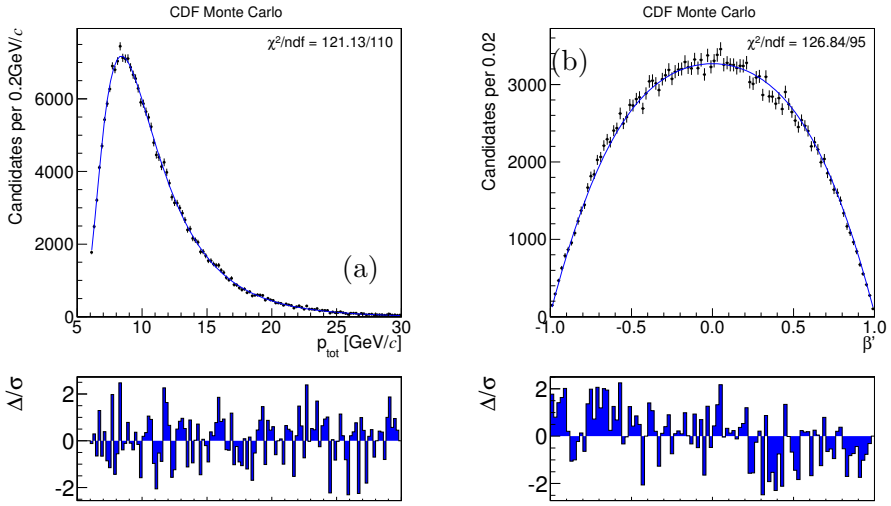

Figure 6.10: Fit of $p_{\rm tot}$ distribution (a) and β' distribution (b) for $B^0 \to \pi^+\pi^-$ simulated decays.

β' parameterization

The $p_{\rm tot}$-integrated β' p.d.f. is written as a 6th degree Chebyshev polynomial, where the parameters b_i, with $i = 0...6$, are free to vary. We chose these functions because they are a set of orthogonal polynomials in the interval [-1,1], that is the β' domain. The fit function agreement with respect to the data distribution is satisfactory (see fig. 6.10 (b)).

$$\wp_j(\beta') \quad = \quad \sum_{m=0}^{6} b_{mj} T_m(\beta'), \tag{6.15}$$

Bidimensional β',$p_{\rm tot}$ parameterization

In the final step of this procedure we wrote a bidimensional function parameterizing the joint p.d.f. $\wp(\beta',p_{\rm tot})$. The parameters are fixed to the corresponding parameters of the one–dimensional functions obtained in the first two steps. To take into account the a small β' dependence on $p_{\rm tot}$, we let the Chebyshev parameters b_{mj} vary in function of $p_{\rm tot}$:

$$b_{mj} \to b_{mj}(1 + d^1_{mj} \cdot p_{\rm tot} \ + d^2_{mj} \cdot p^2_{\rm tot} + d^3_{mj} \cdot p^3_{\rm tot} + d^4_{mj} \cdot p^4_{\rm tot}) \tag{6.16}$$

This method allows us to satisfactorily reproduce the simulated distribution, because the variations with respect to the b_{mj} values are small. As a matter of fact, the d^k_{mj} coefficients decrease as the $p_{\rm tot}$ power increases. Thus the momentum p.d.f.

of the j^{th} signal mode is written as:

$$\begin{aligned}\wp_j^p(\beta', p_{\text{tot}}) &= \wp_j(p_{\text{tot}}) \times \wp_j(\beta'|p_{\text{tot}}) \\ &= \frac{1}{K_j}\left(e^{c_j p_{\text{tot}}} \sum_{l=0}^{6} a_{lj} L_l(p_{\text{tot}})\right) \times \left(\sum_{m=0}^{6} b_{mj}(p_{\text{tot}}) T_m(\beta')\right),\end{aligned} \tag{6.17}$$

where the p_{tot} density is the product of an exponential function times a 6th-degree Laguerre polynomial, whereas the conditional p.d.f. of β is a 6th-degree Chebyshev polynomial in β'. The index j of the a_{lj}, b_{mj}, and c_j parameters denotes their dependence on the decay mode. While a_{lj} and c_j are constants, b_{mj} is a function of p_{tot} through a 4th-degree polynomial $b_{mj} = \sum_{k=0}^{4} d_{mj}^k p_{\text{tot}}^k$, where d_{mj}^k are constants. The normalization factor K_j for each mode is calculated with a numerical two-dimensional integration of the p.d.f. in the appropriate domain of β' and p_{tot}.

Since in the Likelihood function the parameters chosen are $m_{\pi\pi}^2, \beta, p_{\text{tot}}, \kappa_+, \kappa_-$ and not β' (nor β''), we rewrote eq. (6.17) in function of β. Thus the momentum p.d.f. of the j^{th} signal mode used in the Likelihood fit is written as follows:

$$\begin{aligned}\wp_j^p(\beta, p_{\text{tot}}) &= \wp_j(p_{\text{tot}}) \times \wp_j(\beta'(\beta)|p_{\text{tot}}) \times \frac{d\beta'}{d\beta} \\ &= \frac{1}{K_j}\left(e^{c_j p_{\text{tot}}} \sum_{l=0}^{6} a_{lj} L_l(p_{\text{tot}})\right) \times \left[\sum_{m=0}^{6} b_{mj}(p_{\text{tot}}) T_m\left(\beta \frac{p_{\text{tot}}}{p_{\text{tot}} - 4}\right)\right] \times \frac{p_{\text{tot}}}{p_{\text{tot}} - 4},\end{aligned} \tag{6.18}$$

Figure 6.11 shows the distribution of the scalar sum of momenta as a function of the momentum imbalance of the simulated $B^0 \to \pi^+\pi^-$ mode. Similar distributions are obtained for all signal modes. These are fitted to the functions of eq. (6.18) to obtain the momentum templates. We checked the agreement between the model and the simulated distributions by overlaying the templates to the β-distributions of simulated data integrated in the p_{tot} variable (see fig. 6.11), and, as a further check, sampled in different p_{tot} ranges (fig. 6.12). We performed the same parameterization for all the $B \to h^+h^{'-}$ decay modes, for both `med` and `high` kinematics. To not weight down the text, only the plots for simulated $B^0 \to K^+\pi^-$ and $\overline{B}^0 \to K^-\pi^+$ are reported in appendix A. Similar plots are obtained for all the other $B \to h^+h^{'-}$ modes.

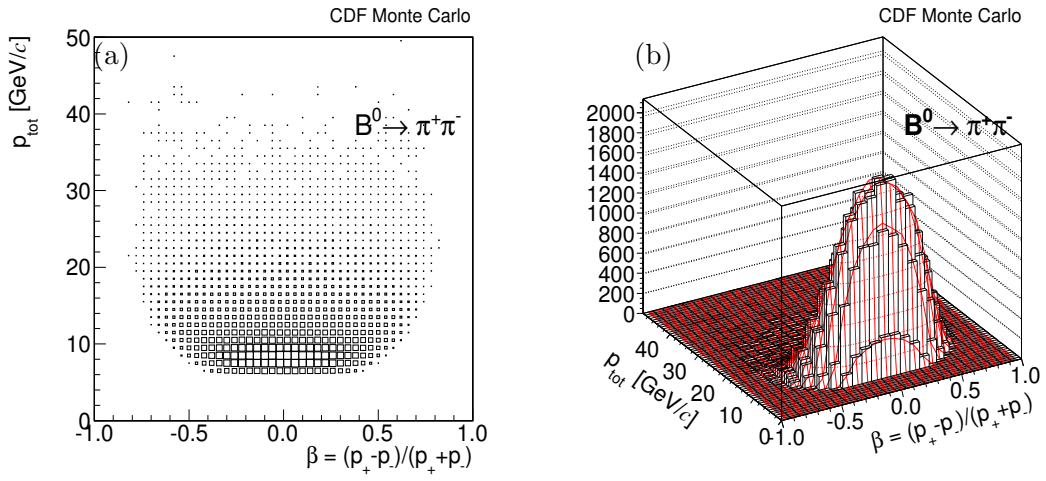

Figure 6.11: Distribution of the scalar sum of the momenta as a function of the charged-momentum asymmetry in the $B^0 \to \pi^+\pi^-$ simulated decays (a). The projection (red) is overlaid (b).

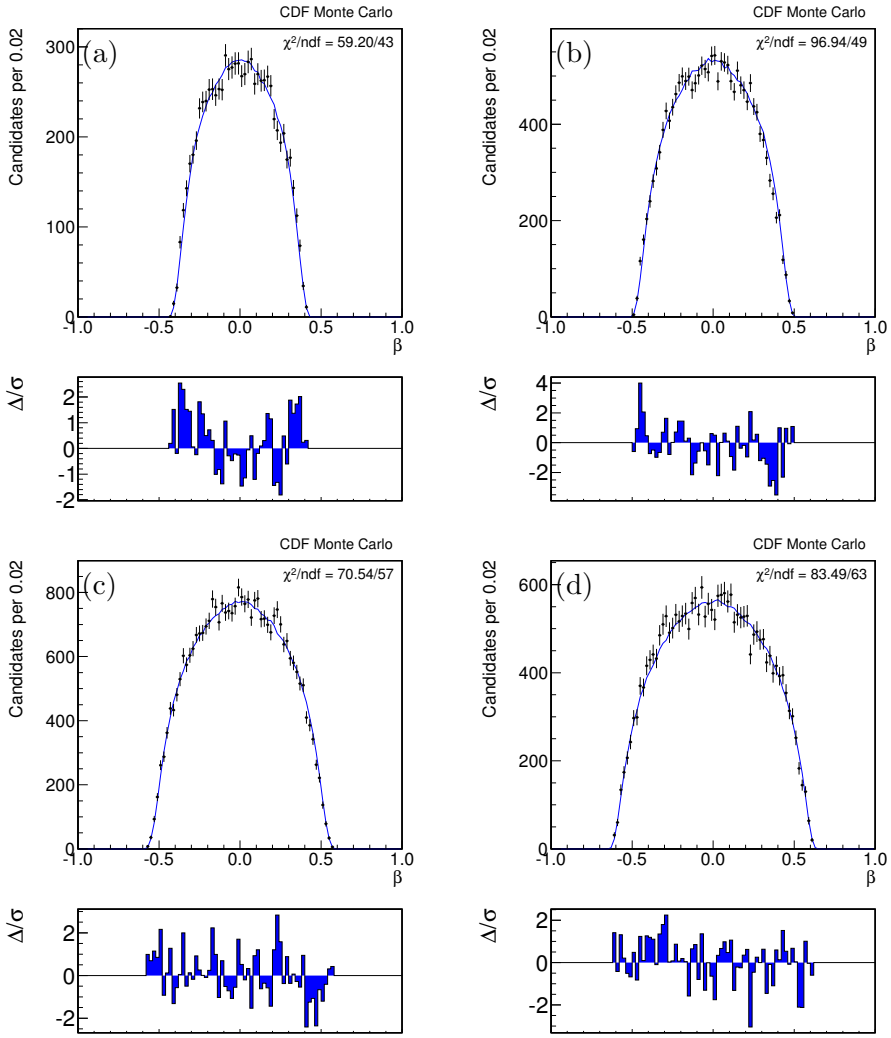

Figure 6.12: β distribution of simulated $B^0 \to \pi^+\pi^-$ decays spanning different $p_{\rm tot}$ ranges: $p_{\rm tot} < 7$ GeV/c (a), $7 < p_{\rm tot} < 8$ GeV/c (b), $8 < p_{\rm tot} < 9.5$ GeV/c (c), $9.5 < p_{\rm tot} < 11$ GeV/c (d).

6.2 Physics background template

6.2.1 Physics background simulation

The main contribution to the partially-reconstructed heavy flavor decays comes from decay modes $B^+ \to h_1^+ h_2^- h_3^+$, $B^0 \to h_1^+ h_2^- h_3^0$ and $B_s^0 \to h_1^+ h_2^- h_3^0$, where $h = \pi$ or K, and $B^0 \to \pi^- \ell^+ \nu_\ell$ and $B_s^0 \to K^- \ell^+ \nu_\ell$. In particular, they include also all the decay modes involving an intermediate resonance as a ρ or a K^* meson plus a pion or a kaon: $B^+ \to \rho^- \pi^+$, $B^+ \to \rho^0 K^+$, $B^0 \to \rho^\mp \pi^\pm$, $B^0 \to \rho^- K^+$, $B_s^0 \to \rho^\mp \pi^\pm$, $B_s^0 \to \rho^+ K^-$ (where $\rho \to \pi\pi$) and $B^+ \to K^{*0} \pi^+$, $B^+ \to K^{*+} \pi^0$, $B^0 \to K^{*+} \pi^-$, $B^0 \to K^{*0} \pi^0$ (where $K^* \to K\pi$) and many others. Many branching fractions of the decays involving the B^+ and B^0 mesons were measured at the B-Factories [51] while those of the B_s^0 mesons are still unknown with large theoretical uncertainties. For these reasons, we simulated only some of the decays listed above, in particular those involving the ρ meson resonance which represent about 50% of the low-mass bump (see fig. 6.14). We summed the contributions according to their relative branching fractions. For the B^+ and B^0 we used the measured values from [51]. We generated 5 millions events for each of the following decay:

- $\mathcal{B}(B^0 \to \rho^- K^+) = (8.4^{+1.6}_{-2.2}) \times 10^{-6}$;
- $\mathcal{B}(B^0 \to \rho^\mp \pi^\pm) = (23.0 \pm 0.023) \times 10^{-6}$;
- $\mathcal{B}(B^+ \to \rho^0 K^+) = (3.7 \pm 0.5) \times 10^{-6}$;
- $\mathcal{B}(B^+ \to \rho^- \pi^+) = (8.3 \pm 1.2) \times 10^{-6}$;
- $\mathcal{B}(B^0 \to \pi^- e^+ \nu_e) = (142 \pm 0.06) \times 10^{-6}$;
- $\mathcal{B}(B^0 \to \pi^- \mu^+ \nu_\mu) = (142 \pm 0.06) \times 10^{-6}$;
- $\mathcal{B}(B_s^0 \to \rho^+ K^-) = (24.5^{+15.2}_{-12.9}) \times 10^{-6}$.

For the same reasons explained for the signal simulation, also the physics background sample has to be reweighted for $p_{\mathrm{T}}(B)$ distribution of data sideband-subtracted in order to obtain a better agreement between the simulation and the data. The simulated $p_{\mathrm{T}}(B)$ distribution has been reweighted bin by bin to the distribution observed on data sideband subtracted, extracted in the region $m_{\pi^+\pi^-} < 5.16$ GeV/c^2. Then we checked that the agreement between data and simulation for the kinematic variables used in the fit of composition is satisfactory. The comparison plots are reported fig. 6.13.

6.2.2 Probability density function of the physics bkg mass term

The $m^2_{\pi\pi}$ distribution was modeled with the convolution of a resolution function, a Gaussian centered in zero with the width of an individual signal mode ($\sigma_{\mathrm{exp}} \approx$

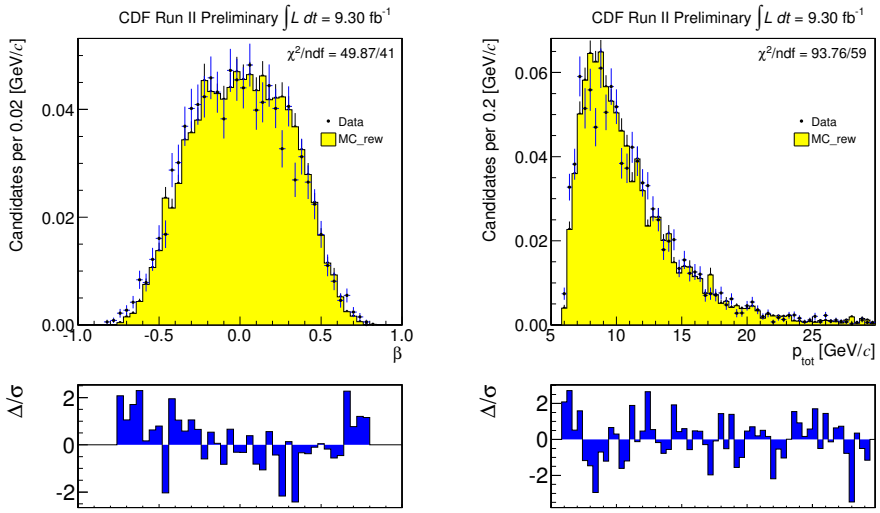

Figure 6.13: Comparison plots of $p_{\rm tot}$ and β distributions between the physics bkg simulated sample (full histograms) and data in $m_{\pi^+\pi^-} < 5.16$ GeV/c^2 sideband subtracted (dots).

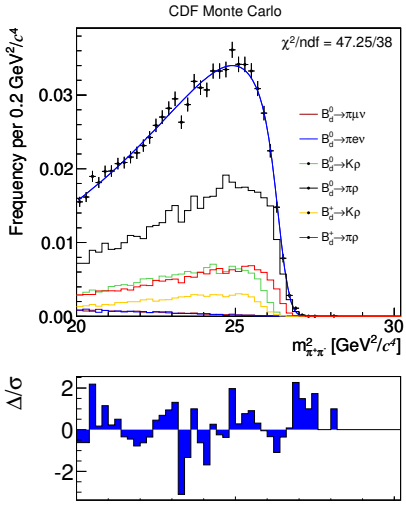

Figure 6.14: Squared invariant $\pi\pi$-mass distribution of simulated $B^+ \to h_1^+ h_2^- h_3^+$ and $B^0 \to h_1^+ h_2^- h_3^0$ decay modes, the fit function (eq. (6.19)) is overlaid.

0.25 GeV$^2/c^4$), and an Argus function [92], whose cut-off falls just on the left-hand side of the $B^0_{(s)} \to h^+ h'^-$ peak:

$$\wp^m_{\rm A}(m^2_{\pi\pi}|\beta, p_{\rm tot}; m^2_{\rm A}, c_{\rm A}) = \mathscr{G}(m^2_{\pi\pi}; 0, \sigma_{\rm exp}) * \mathscr{A}(m^2_{\pi\pi}; m^2_{\rm A}, c_{\rm A}), \qquad (6.19)$$

$$\mathscr{A}(m^2_{\pi\pi};m_{\rm A},c_{\rm A}) = \begin{cases} \frac{1}{K_{\rm A}}\cdot\left[m^2_{\pi\pi}\cdot\sqrt{1-\left(\frac{m^2_{\pi\pi}}{m^2_{\rm A}}\right)^2}\cdot e^{-c_{\rm A}\cdot\left(\frac{m^2_{\pi\pi}}{m^2_{\rm A}}\right)^2}\right] & \text{if } m^2_{\pi\pi} < m^2_{\rm A}, \\ 0 \quad \text{if } m^2_{\pi\pi} > m^2_{\rm A}, \end{cases} \tag{6.20}$$

where the normalization $K_{\rm A}$ is:

$$K_{\rm A} = \int_{a^2}^{m^2_{\rm A}} m^2_{\pi\pi}\cdot\sqrt{1-\left(\frac{m^2_{\pi\pi}}{m^2_{\rm A}}\right)^2}\cdot e^{-c_{\rm A}\cdot\left(\frac{m^2_{\pi\pi}}{m^2_{\rm A}}\right)^2} dm^2_{\pi\pi} \quad \text{with} \quad a^2 \leq m^2_{\rm A}. \tag{6.21}$$

Although the Argus function reproduces well the mass line shape of an inclusive data sample of multibody partially-reconstructed decays, it introduces some problem in the convergence of the fit. The convolution of eq. (6.19) is performed numerically, with a sum of a finite number of terms. Therefore the likelihood function has several terms with an infinite derivative at the value of the cut-off $m^2_{\rm A}$. To solve this problem the minimization of the cut-off is done repeating the fit with different fixed cut-off values. The chosen cut-off value, $m^2_{\rm A} = 26.64$ GeV$^2/c^4$, is the minimum of the $-2\log(\mathscr{L})$ profile obtained repeating the central fit where the cut-off value (fixed in the fit) spans the range $[26.4, 26.8]$ GeV$^2/c^4$ with a step of 0.001 GeV$^2/c^4$. This corresponds to 400 different central fits. The likelihood profile reported in fig. 11.2 shows a parabolic behaviour as expected for a regular likelihood. A systematic uncertainty is assessed on the observable of interest taking the difference between the the central fit (minimum of the profile) and the fits intersecting the horizontal line at $-2\Delta\log(\mathscr{L}) = 4$, corresponding to a of 95% confidence interval. More details on the systematics will be reported in sec. 11.2.6. Since in the most part of these

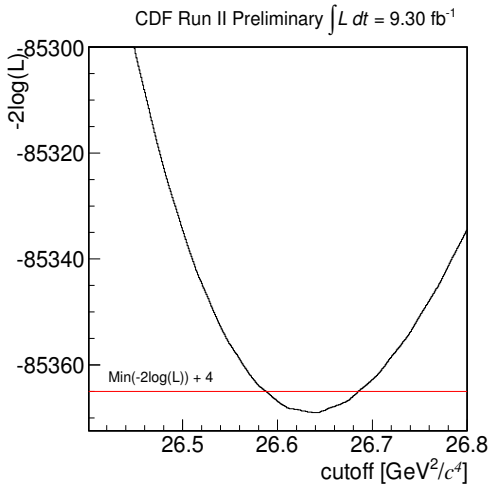

Figure 6.15: $-2\log(\mathcal{L})$ as a function of the cut-off value $m^2_{\rm A}$.

fits, performed for the cut-off likelihood scan, the parameter $c_{\rm A}$ goes to its limit, which is zero, we decide to fix this parameter to zero in the central fit, simplifying

the expression in eq. (6.19). $c_{\rm A}$ is necessary only when the shape of partially-reconstructed decays at lower masses goes down. As a further cross-check, we verified that a simple one-dimensional fit of just the mass shape of the $B^0_{(s)} \to h^+h'^-$ candidates yields, for the Argus function, similar estimated parameters as the full composition fit.

6.2.3 Probability density function of the physics bkg momentum term

As for the signal, the momentum p.d.f. of the physics background is written as:

$$\begin{aligned} \wp^{\rm E}(\beta, p_{\rm tot}) &= \wp(p_{\rm tot}) \times \wp(\beta|p_{\rm tot}) \times \frac{d\beta'}{d\beta} \\ &= \frac{1}{K}\left(e^{c_{\rm E}p_{\rm tot}} \sum_{l=0}^{6} a^{\rm E}_l L_l(p_{\rm tot})\right) \times \left[\sum_{m=0}^{6} b^{\rm E}_m(p_{\rm tot}) T_m\left(\beta \frac{p_{\rm tot}}{p_{\rm tot}-4}\right)\right] \times \frac{p_{\rm tot}}{p_{\rm tot}-4}, \end{aligned} \tag{6.22}$$

where the $p_{\rm tot}$ density is the product of an exponential function times a 6th-degree Laguerre polynomial, whereas the conditional p.d.f. of β is a 6th-degree Chebyshev polynomial in β scaled by a factor $(p_{\rm tot})/(p_{\rm tot}-4)$ deriving from the constraint on the domain of β given by eq. (6.10) for the `med` scenario. For the `high` scenario, the scale factor is $(p_{\rm tot})/(p_{\rm tot}-5)$. While $a^{\rm E}_l$ and $c_{\rm E}$ are constants, $b^{\rm E}_m$ is a function of $p_{\rm tot}$ through a 4th-degree polynomial $b^{\rm E}_m = \sum_{k=0}^{4} d^{\rm E}_{mk} p^k_{\rm tot}$, where $d^{\rm E}_{mk}$ are constants. The normalization factor K is calculated with a numerical two-dimensional integration of the p.d.f. in the appropriate domain of β and $p_{\rm tot}$. We checked the agreement between model and data by overlaying the template to the β-distribution of the background events, sampled in different $p_{\rm tot}$ ranges (fig. 6.16).

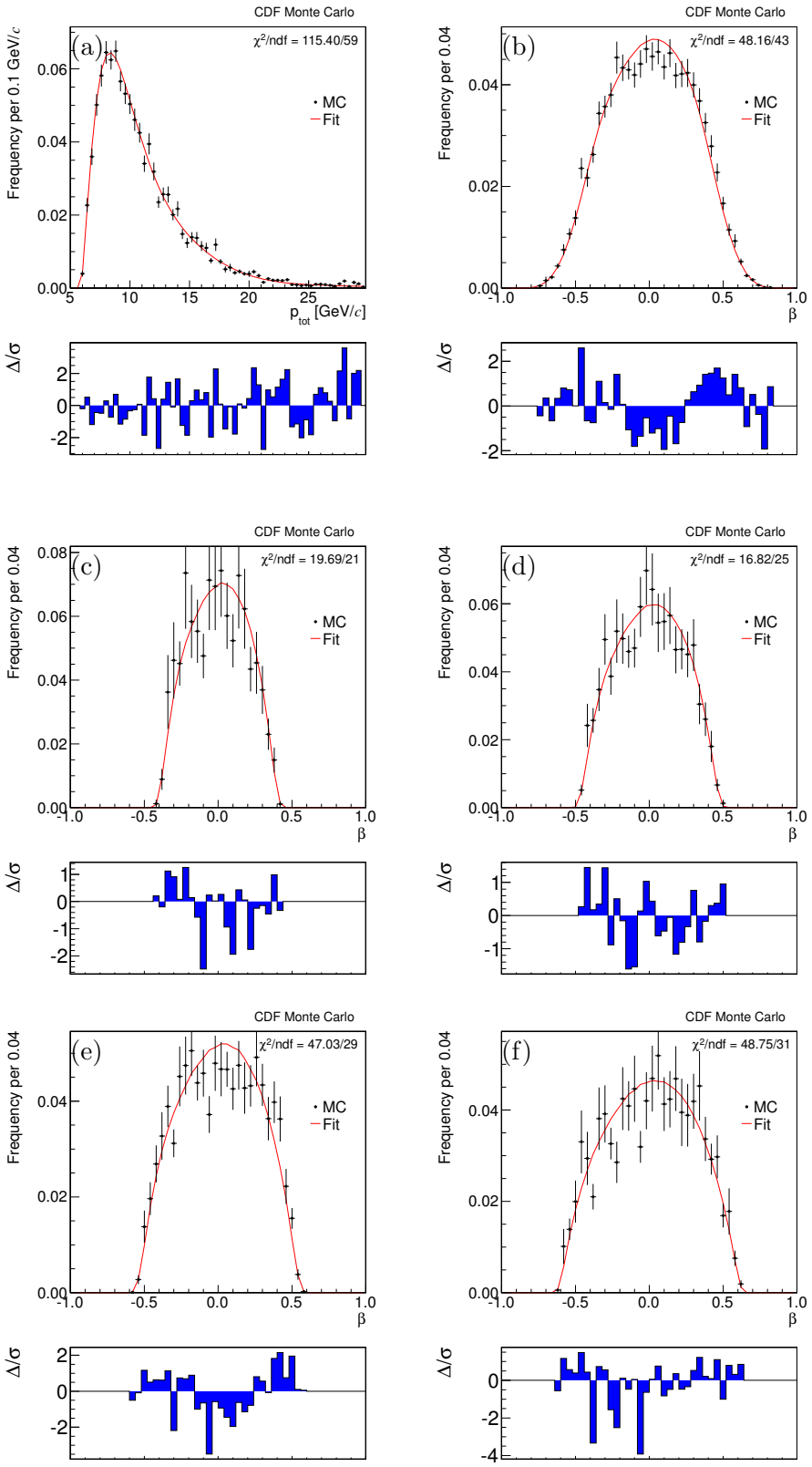

Figure 6.16: p_{tot} distribution (a) and β distribution (b) of simulated physics background decays, with the fit function overlaid. β distribution spanning different p_{tot} ranges: $p_{\mathrm{tot}} < 7$ GeV/c (c), $7 < p_{\mathrm{tot}} < 8$ GeV/c (d), $8 < p_{\mathrm{tot}} < 9.5$ GeV/c (e), $9.5 < p_{\mathrm{tot}} < 11$ GeV/c (f), with the fit function overlaid.

6.3 Combinatorial background template

Combinatorial background templates were extracted directly from data. A sample of pure combinatorial background is expected in the region with $m_{\pi^+\pi^-} > 5.6$ GeV/c^2, where the $\Lambda_b^0 \to ph^-$ contributions are kinematically limited. By construction, this sample is not accurate in reproducing the kinematic distributions ($m^2_{\pi\pi}$, β and $p_{\rm tot}$) in the whole mass range, spanning in a range $m_{\pi^+\pi^-}$ [5.0, 5.8] GeV/c^2. In order to choose an independent sample where to extract the templates, we studied an alternative sample of two generic random tracks extracted from the same $B \to h^+h'^-$ data, and compared this with the combinatorial background visible at higher masses.

6.3.1 The inverted χ^2 sample

We looked at the distributions of the events passing the final selection (continuous line in fig. 6.17, labeled as "signal sample") and the corresponding distribution of the events with "opposite-χ^2" requirement. The opposite-χ^2 sample contains events that pass the final selections of tab. 3.3 except for the requirement on the 3-D vertex quality, which is "reversed" to $\chi^2 > 40$ (see fig. 6.17, dashed line). The opposite-χ^2 sample is enriched of "unphysical" decays, i. e., decays which have two tracks with an identical kinematics on the transverse plane to the $B \to h^+h'^-$ modes but coming from two distinct heavy-flavors in the event, which have sizable impact parameter but are separated along the z direction. This threshold was chosen to

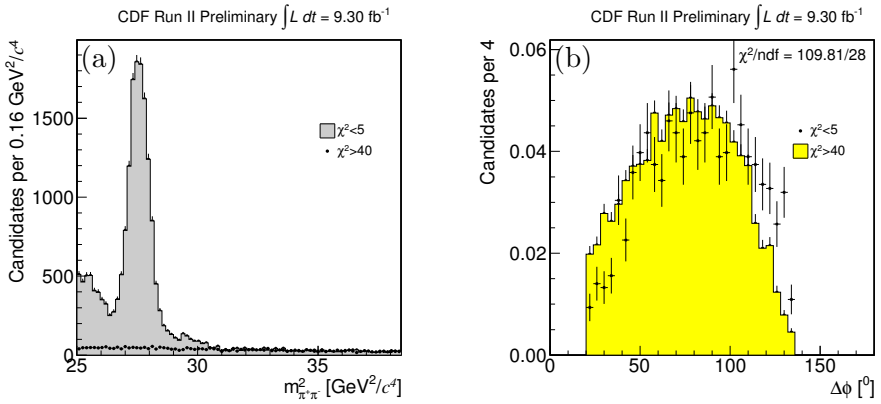

Figure 6.17: Squared invariant $\pi\pi$-mass distribution (a) and azimuthal angle $\Delta\phi$ distribution (b) of the events passing the final optimized selection (full histrograms, $\chi^2_{3D} < 5$) and events passing the final optimized selection with an opposite requirement on the 3-D vertex quality (point with error), $\chi^2_{3D} > 40$. The $\Delta\phi$ distributions have been selected requiring events lying at higher masses than the peak (right-hand side of the signal).

remove as much as possible the contamination of $B \to h^+h^{'-}$ signal events and to obtain a reasonable statistics of background events. To check if the invariant-mass shape of these random pairs of tracks is slightly dependent (or independent) on the χ^2 cut value, we compared distributions for the main kinematic variables in the same mass range requiring events lying at higher masses than the peak, right-hand side of the signal. While we observed small discrepancies comparing momenta observables of the two background samples, the lifetime related observables are not compatible. Indeed, inverting the χ^2 cut value means selecting tracks with an unsatisfactory vertex fit, so lifetime related distributions (such as $d_0(B)$ or $L_{\rm T}$ distributions) in disagreement with the ones of the events passing the standard cuts selection are expected. However, we are interested only in the mass line shape, whose features depend, at the first order, on the momenta distributions: the lifetime related observables distributions enter only at higher order level. Therefore we reweighted the $\Delta\phi$ distribution of the the opposite-χ^2 sample to the one of the signal sample (the comparison of $\Delta\phi$ distributions before the reweighting is shown in fig. 6.17(b)). Then a good agreement is found between momenta observables, as shown in fig. 6.18. Thus, the opposite-χ^2 sample provides an useful model of the mass and momenta shapes of the combinatorial background of the signal sample in the whole mass range.

6.3.2 Probability density function of the combinatorial bkg mass term

Given the slope of the distribution shown in fig. 6.17, the squared invariant $\pi\pi$-mass of the combinatorial background was modeled with a decreasing exponential:

$$\wp_E^m(m^2_{\pi\pi}|\beta, p_{\rm tot}; c_{\rm E}) = \frac{1}{\int_a^b e^{c_{\rm E} m^2_{\pi\pi}} dm_{\pi^+\pi^-}} \cdot e^{c_{\rm E} m^2_{\pi\pi}} \tag{6.23}$$

whose slope $c_{\rm E}$ has been extracted with an one-dimensional fit of the squared invariant $\pi\pi$-mass distribution of the opposite-χ^2 sample. In the central fit, the slope $c_{\rm E}$ of the combinatorial background mass shape is fixed. We checked that the slope extracted in this way is compatible with the slope obtained fitting the events lying at masses ($m^2_{\pi\pi} > 31.5$ GeV/c^2) higher than the $B \to h^+h^{'-}$ peak (right-hand side of the signal). We estimate respectively for `med` and `high`:

$$\begin{aligned} c_{\rm E}^{\rm A} &= -0.064 \pm 0.003 \ ({\rm GeV}^2/c^4)^{-1} \\ c_{\rm E}^{\rm C} &= -0.060 \pm 0.004 \ ({\rm GeV}^2/c^4)^{-1}. \end{aligned} \tag{6.24}$$

6.3.3 Probability density function of the combinatorial bkg momentum term

As for the signals, the momentum p.d.f. of the background is written as a joint p.d.f. $\wp(\beta, p_{\rm tot})$. The combinatorial background $p_{\rm tot}$ distribution shown in fig. 6.19

has a different shape respect to the signal distribution: in particular, the mean and the RMS have lower values.

Thus we empirically chose a different parameterization: instead of the product between Laguerre polynomials and an exponential function used for the signals, we use the sum of three Gaussians. This has been done because of the technical difficulties on parameterizing the very rapid turn at low momentum. The momentum p.d.f. of the background is written as:

$$\begin{aligned}\wp^{\mathrm{E}}(\beta, p_{\mathrm{tot}}) &= \wp(p_{\mathrm{tot}}) \times \wp(\beta|p_{\mathrm{tot}}) \times \frac{d\beta'}{d\beta} \\ &= \frac{1}{K}\left(\sum_{l=1}^{3} f_l^{\mathrm{E}} \mathscr{G}(p_{\mathrm{tot}}; \mu_l, \sigma_l)\right) \times \sum_{m=0}^{6} b_m^{\mathrm{E}}(p_{\mathrm{tot}}) T_m\left(\beta \frac{p_{\mathrm{tot}}}{p_{\mathrm{tot}} - 4(5)}\right) \times \frac{p_{\mathrm{tot}}}{p_{\mathrm{tot}} - 4},\end{aligned} \tag{6.25}$$

where the p_{tot} density is the sum of three gaussians $\mathscr{G}$ (defined in eq. (6.2)), whereas, as for the signal, the conditional p.d.f. of β is a 6th-degree Chebyshev polynomial in β scaled by a factor $(p_{\mathrm{tot}})/(p_{\mathrm{tot}} - 4(5))$ deriving from the constraint on the domain of β given by eq. (6.10). While μ_l and σ_l are constants, b_m^{E} is a function of p_{tot} through a 4th-degree polynomial $b_m^{\mathrm{E}} = \sum_{k=0}^{4} d_{mk}^{\mathrm{E}} p_{\mathrm{tot}}^k$, where d_{mk}^{E} are constants. The normalization factor K is calculated with a numerical two-dimensional integration of the p.d.f. in the appropriate domain of β and p_{tot}.

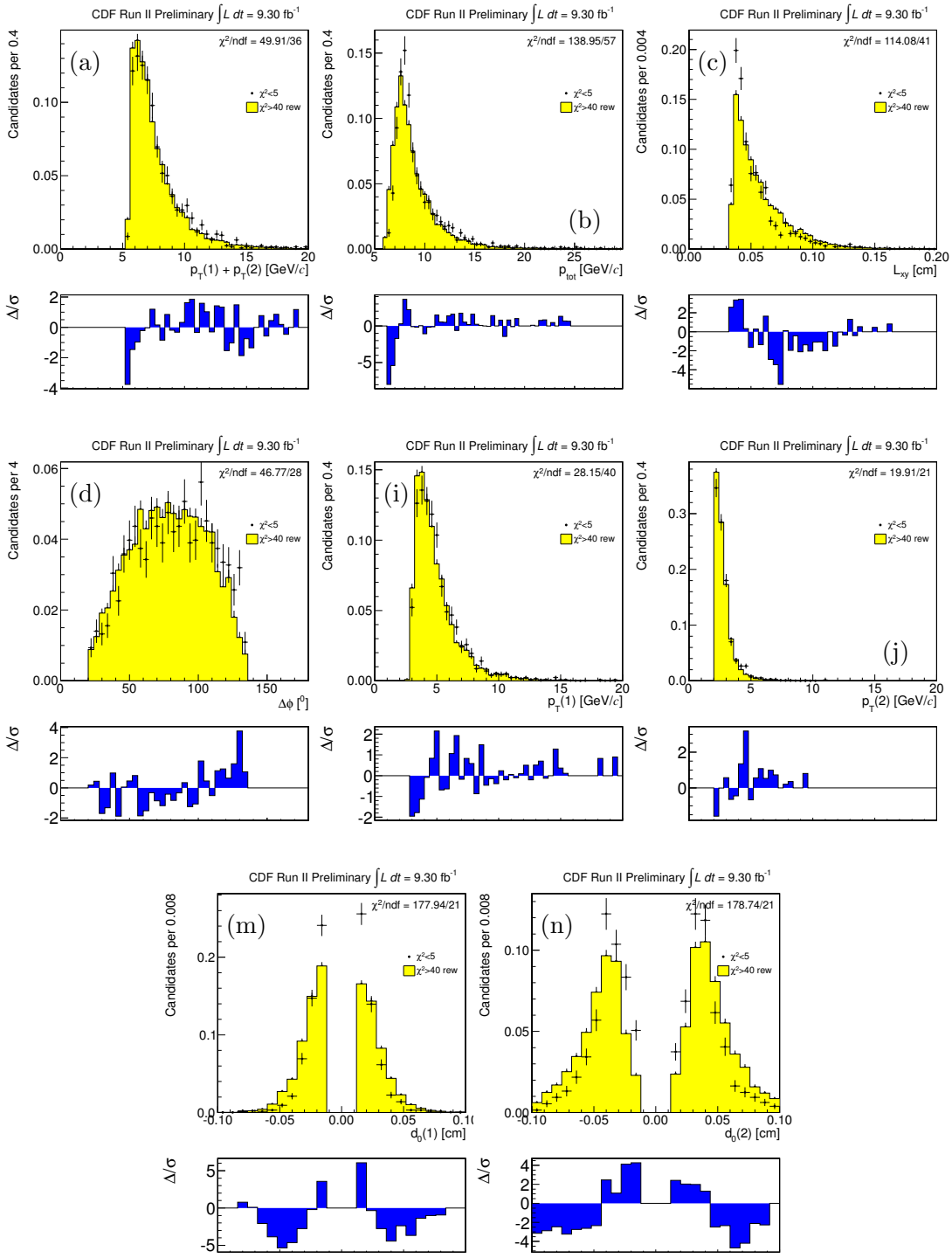

Figure 6.18: Comparison of distributions between the combinatorial signal sample and the opposite-χ^2 sample reweighted using the $\Delta\phi$ distribution: $\sum p_{\mathrm{T}}$ (a), p_{tot} (b) L_{T} (c), $\Delta\varphi_0$ (d), β (g), $p_{\mathrm{T}}(1)$ (i), $p_{\mathrm{T}}(2)$ (j), $d_0(1)$ (m), $d_0(2)$ (n).

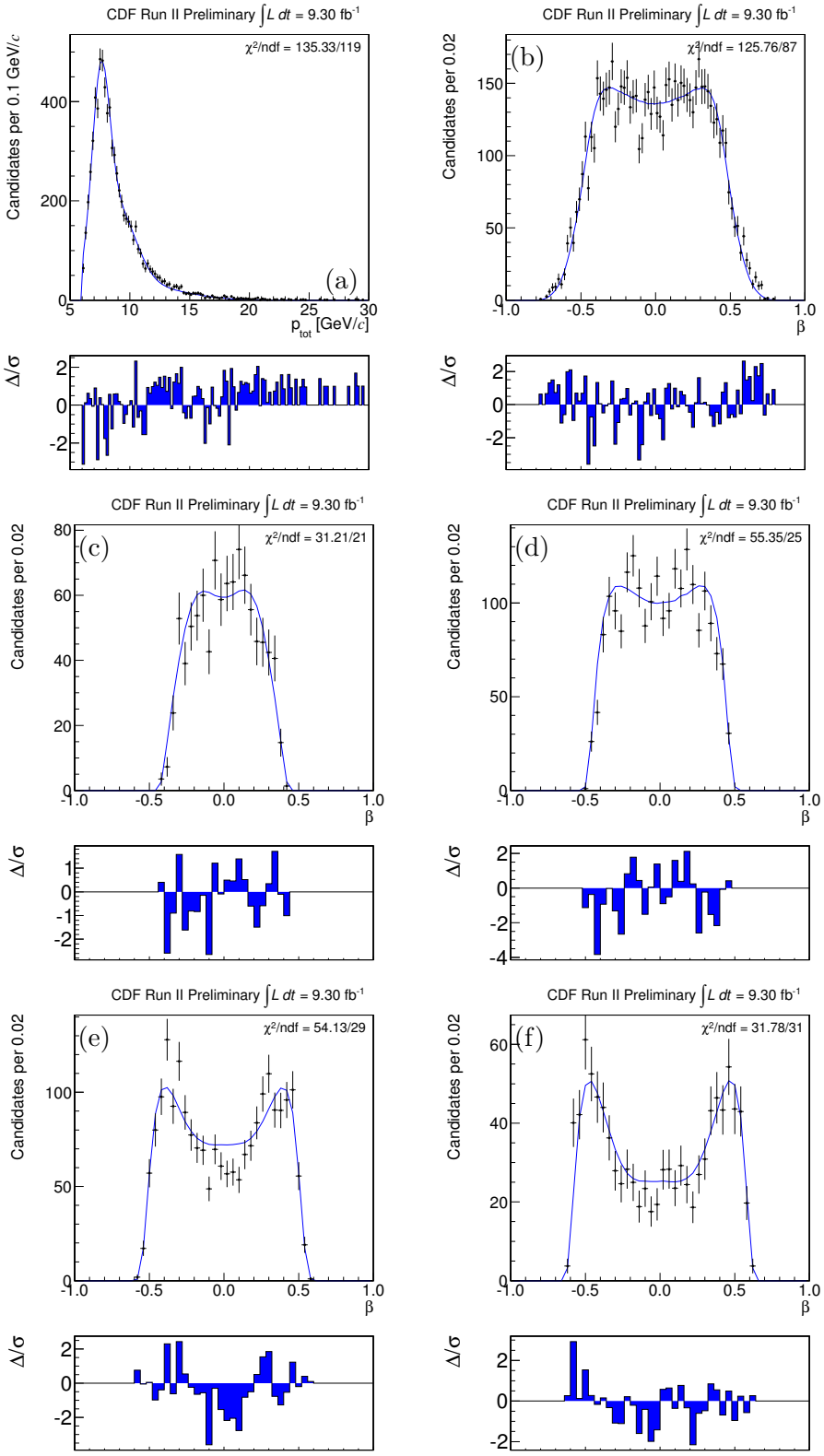

Figure 6.19: $p_{\rm tot}$ distribution (a) and β distribution (b) of combinatorial background, with the fit function overlaid. β distribution in different $p_{\rm tot}$ ranges: $p_{\rm tot}<$ 7 GeV/c (c), 7 $< p_{\rm tot}<$ 8 GeV/c (d), 8 $< p_{\rm tot}<$ 9.5 GeV/c (e), 9.5 $< p_{\rm tot}<$ 11 GeV/c (f).

Chapter 7

PID templates

A detailed description of the dE/dx information is crucial for this analysis: adding the PID to the kinematics information allows gaining separation power between decay modes with different final states, even when the separation power due to kinematics information is almost null. This chapter describes the work we especially made for the $B \to h^+h'^-$ analysis.

7.1 dE/dx control data samples

To parameterize the templates to model the dE/dx response of each particle we used CDF data, exploiting the available control samples. In order to describe correctly the signal and the background we need a model for all particle involved. The $B \to h^+h'^-$ modes decay into kaons, protons or pions. In addition, in the background we expect also the presence of muons and electrons.

pions and kaons – For pions and kaons a sample of $\simeq 2.7 \times 10^6$ $D^0 \to K^-\pi^+$ decays from the decay chain $D^{*+} \to D^0\pi^+ \to [K^-\pi^+]\pi^+$ was used. This sample was introduced in sec. 4.2.3 since it was used as control sample in the parameterization of the invariant mass distribution. The signal reconstruction is based solely on tracking and on the information of the identity of D^0 decay-products provided by the charge of the soft pion. One $D^0 \to K^-\pi^+$ and one $\overline{D}^0 \to K^+\pi^-$ candidate were formed for each pair of oppositely-curved tracks found in the XFT fiducial region ($|\eta| < 1$). The list of all requirements is reported in tab. 7.1. Candidates with reconstructed invariant mass within 8 MeV/c^2 of the world–average D^0 mass [51] were combined with a third charged particle with $p_{\rm T} > 0.4$ GeV/c (soft pion) to form a $D^{*+} \to D^0\pi^+$ candidate. The charged pion mass is assigned to the like-sign pair of particles. To select a very pure sample, the analysis has been restricted to candidates found within ± 0.8 MeV from the world average $D^{\star+}$ mass [51]. The invariant $D^0\pi$-mass distribution resulting is shown in fig. 7.2(a). A simple binned χ^2-fit of the distribution to a double Gaussian function for the signal, over a

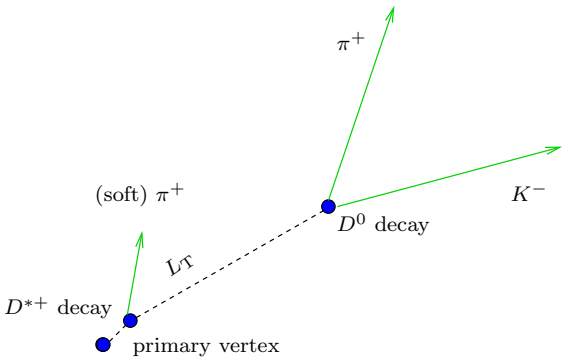

Figure 7.1: Schematic sketch of the $D^{*+} \to D^0\pi^+ \to [K^-\pi^+]\pi^+$ decay chain in the plane transverse to the proton beam direction.

straight line function for the background, provides an estimate of about 2.7 M signal events, over a very low background that includes random triplets of tracks satisfying accidentally the selection requirements and random tracks combined with a real D^0 (fake D^{*+}). The $D^0 \to h^+h'^-$ decay sample is thus almost ideal for calibrations and parameterizations: the resulting signal sample is huge and pure at 99% level. Moreover, the sample was collected by the `B_CHARM`(`B_CHARM_HIGHPT`) triggers (see sec. 3.2), a path belonging, along with the `B_PIPI`(`B_PIPI_HIGHPT`) path, to the Displaced-Tracks Trigger. A large fraction of trigger requirements is common to these two paths. Most trigger-dependent effects on the dE/dx of $B^0_{(s)} \to h^+h'^-$ final states are automatically accounted for the calibration and for the templates parameterization.

protons – A sample of $\Lambda \to p\pi^-$ decays was used to calibrate the proton response. These two-body decays were reconstructed with the same prescription of the $B^0_{(s)} \to h^+h'^-$ decays, (see chap. 3) and were collected using the same `B_PIPI`(`B_PIPI_HIGHPT`) trigger path (see sec. 3.2). It is important to notice that the $\Lambda \to p\pi^-$ decays are *volunteers* in the `B_PIPI`(`B_PIPI_HIGHPT`) trigger path, because one of two tracks in the final state (in most of cases the pion) does not satisfy the trigger requirements. This is due to the small energy available in the Λ rest frame ($m_\Lambda - m_p - m_\pi \simeq 38$ MeV/c^2). The trigger requirements on the transverse momentum of the particle $p_\mathrm{T} > 2$ GeV/c, on the scalar sum of the transverse momenta of the particles $\sum p_\mathrm{T} > 5.5$ GeV/c and on the invariant $\pi\pi$-mass requirement $4 < m_{\pi^+\pi^-} < 7$ GeV/c^2 suppress almost totally the signal. For these reasons, the trigger cuts confirmation was required only for the proton. To select a pure sample of $\Lambda \to p\pi$, the analysis has been restricted to candidates found within ± 3.6 MeV from the world average Λ mass [51], and supplementary requirements were added to exclude the contamination of $K_s \to \pi\pi$ decays. The obtained sample is pure at 99.4% level. The invariant $p\pi$-mass distribution of the resulting samples selected with the requirement summarized in tab. 7.2 are shown in fig. 7.2(b).

Tracks	Units	Requirement
Axial Si hits	–	≥ 3
$90^\circ - z$ Si hits	–	≥ 2
SA Si hits	–	≥ 1
Axial COT hits	–	≥ 10
Stereo COT hits	–	≥ 10
Total COT hits	–	≥ 40
dE/dx COT hits	–	≥ 40
p_{T}	GeV/c	> 2.2
$\lvert\eta\rvert$	–	< 1.0
$\lvert d_0\rvert$	μm	[100, 1000]
D^0 candidates		
Has Primary Vertex	–	true
$q(1) \times q(2)$	e^2	-1
L_{T}	μm	> 200
$\sum p_{\mathrm{T}}$	GeV/c	> 4.5
$\lvert d_0\rvert$	μm	< 100
χ^2	–	< 30
χ^2_{xy}	–	< 15
$\lvert\eta\rvert$	–	< 1.0
$\Delta\varphi_0$	Degrees	[2°, 90°]
$m_{\pi^+\pi^-}$	GeV/c^2	[1.8, 2.4]
Soft Pion		
$\lvert z_0\rvert$	cm	< 1.5
$\lvert d_0\rvert$	cm	< 0.06
p_{T}	GeV/c	> 0.4
$\lvert\eta\rvert$	–	< 1.0
Total COT hits	–	≥ 30
dE/dx COT hits	–	≥ 40
Total Si hits	–	≥ 2

Table 7.1: Summary of the selection cuts for $D^0 \to h^+h'^-$ decays from $D^{*+} \to D^0\pi^+$. Variables names are self-explanatory.

A simple binned χ^2-fit of the distribution to a double Gaussian function for the signal, over a straight line function for the background, provides an estimate of about 518,000 signal events. The kinematics allows a total separation between $\Lambda \to p\pi^-$ and $\overline{\Lambda} \to \overline{p}\pi^+$.

electrons and muons – For particles with transverse momentum greater than 2 GeV/c and with the available dE/dx response the muons can be considered indistinguishable from pions. For this reason and since a large fraction of muons is unlikely, the background of muons and pions in this analysis will

be considered as an unique background of pions. In the pion background we incorporated also the electrons component, since a very small fraction of electrons in the $B^0_{(s)} \to h^+h'^-$ background is expected, coming from semileptonic decays of heavy flavors.

Quantity of the track	Units	Requirement
$p_{\mathrm{T}}(\mathrm{p})$	GeV/c	> 2.0
$\lvert\eta(p)\rvert$	–	< 1.0
$\lvert d_0(p)\rvert$	μm	[100, 1000]
Quantity of the candidate		
$q(p) \times q(\pi)$	e^2	-1
$d_0(p) \times d_0(\pi)$	$\mu\mathrm{m}^2$	< 0
$\mathrm{corr}((d_0(p), d_0(\pi)))$	μm	< 51
L_{T}	cm	$[0.5, 2.2]$
$\sum p_{\mathrm{T}}$	GeV/c	> 1.1
$\lvert d_0\rvert$	μm	< 70
$\lvert z_0(p) - z_0(\pi)\rvert$	cm	< 2
χ^2_{T}	–	< 10
$m_{p\pi}$	GeV/c^2	[1.10, 1.13]
$m_{\pi\pi}$	GeV/c^2	$[0.35, 1.5]$
$\lvert m_{\pi\pi} - m_{K^0_s}\rvert$	GeV/c^2	> 0.0126

Table 7.2: Summary of the off-line selection used to reconstruct the $\Lambda \to p\pi^-$ decays. $\mathrm{corr}(d_0(p), d_0(\pi))$ is a variable related to the correlation between the proton and the pion impact parameters. It selects a region in the two-dimensional space $(d_0(p), d_0(\pi))$, for more details see [110].

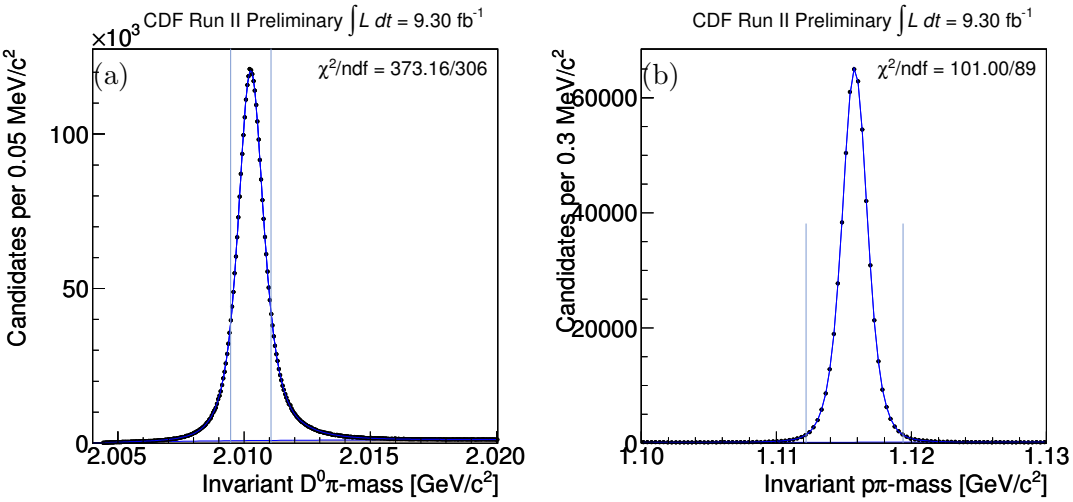

Figure 7.2: Invariant $K\pi$-mass of the $D^0 \to K^-\pi^+$ reconstructed from $D^{*+} \to D^0\pi^+ \to [K^-\pi^+]\pi^+$ decays passing the selection summarized in tab. 7.1 (a). Invariant $p\pi$-mass for the $\Lambda \to p\pi^-$ decays passing the selection summarized in tab. 7.2. The lines represent the mass windows requirements added to purify the sample.

7.2 Universal Curves

The average total energy-loss per unit length of a particle (heavier than the electron) of charge q traversing a gas volume with velocity $c\beta$ is approximated by the Bethe-Bloch formula [111]:

$$\left\langle \frac{dE}{dx} \right\rangle = \frac{4\pi N e^4}{m_e c^2 \beta^2} q^2 \left[\ln\left(\frac{2 m_e c^2 \beta^2 \gamma^2}{I} \right) - \beta^2 - \frac{\delta(\beta)}{2} \right], \tag{7.1}$$

where N is the electron density in the medium, m_e (e) is the electron mass (charge), I is the mean excitation energy of the medium atoms, and $\delta(\beta)$ is the correction that accounts for the density effect at high velocities. To a good approximation, the most probable dE/dx value of a charged particle is a function of its velocity. If the momentum of the particle is measured, the mass can also be determined. In the COT, the signal induced on each sense-wire depends on the amount of ionization charge produced by the passage of the charged particle near the wire. It is measured in nanoseconds because it is encoded as the digital pulse-width between the leading and the trailing-edge time of the hit. Multiple samplings along the trajectory of the charged particle allow a more reliable estimation of dE/dx, which has usually a broad distribution. The COT samples a maximum of 96 dE/dx measurements per track, from which a 80% truncated mean is calculated to avoid the adverse effect of long positive tails in the estimation of the average dE/dx.

The empirical equation that better models the COT average energy-loss as a function of velocity is the following variant of the Bethe-Bloch curve:

$$\left\langle \frac{dE}{dx} \right\rangle = \frac{1}{\beta^2} \left[c_1 \ln\left(\frac{\beta\gamma}{b + \beta\gamma} \right) + c_0 \right] + a_1(\beta - 1) + a_2(\beta - 1)^2 + C, \tag{7.2}$$

with a_i, b, c_j, and C parameters extracted from data. The above function has all the features that are present in the Bethe-Bloch curve (eq. (7.1)). The parameters c_0 and c_1 represent the intensities of the $1/\beta^2$ fall and of the relativistic rise. The parameter b is associated with the COT gas properties, e. g., mean excitation energy of the gas atoms, etc.. The parameters a_1 and a_2 provide a further adjustment, especially in the low $\beta\gamma$ region. Figure 7.3 shows average values of the dE/dx as a function of $\beta\gamma$, separately for pions, kaons, and protons, divided into positively- and negatively-charged particles. Fit of these curves (with a_i, b, c_j, and C free parameters) with the empiric modification of the Bethe- Bloch curve in eq. (7.2) are overlaid (blue line). The fits are in agreement with those obtained using the CDF official parameterization up to 3fb^{-1}. Figure 7.4 shows the summary for universal curves as a function of the momentum for all kind of particles separated by charge. While for electrons we used the old parameterization as it is in the CDF official functions up to 3 fb^{-1}, we explicitly updated up to 9 fb^{-1} the parameterizations for protons, kaons and pions using the samples described in sec. 7.1. Currently, our parameterizations are the CDF official functions, and are used in different kinds of analysis. Details on this work are reported in the appendix B.

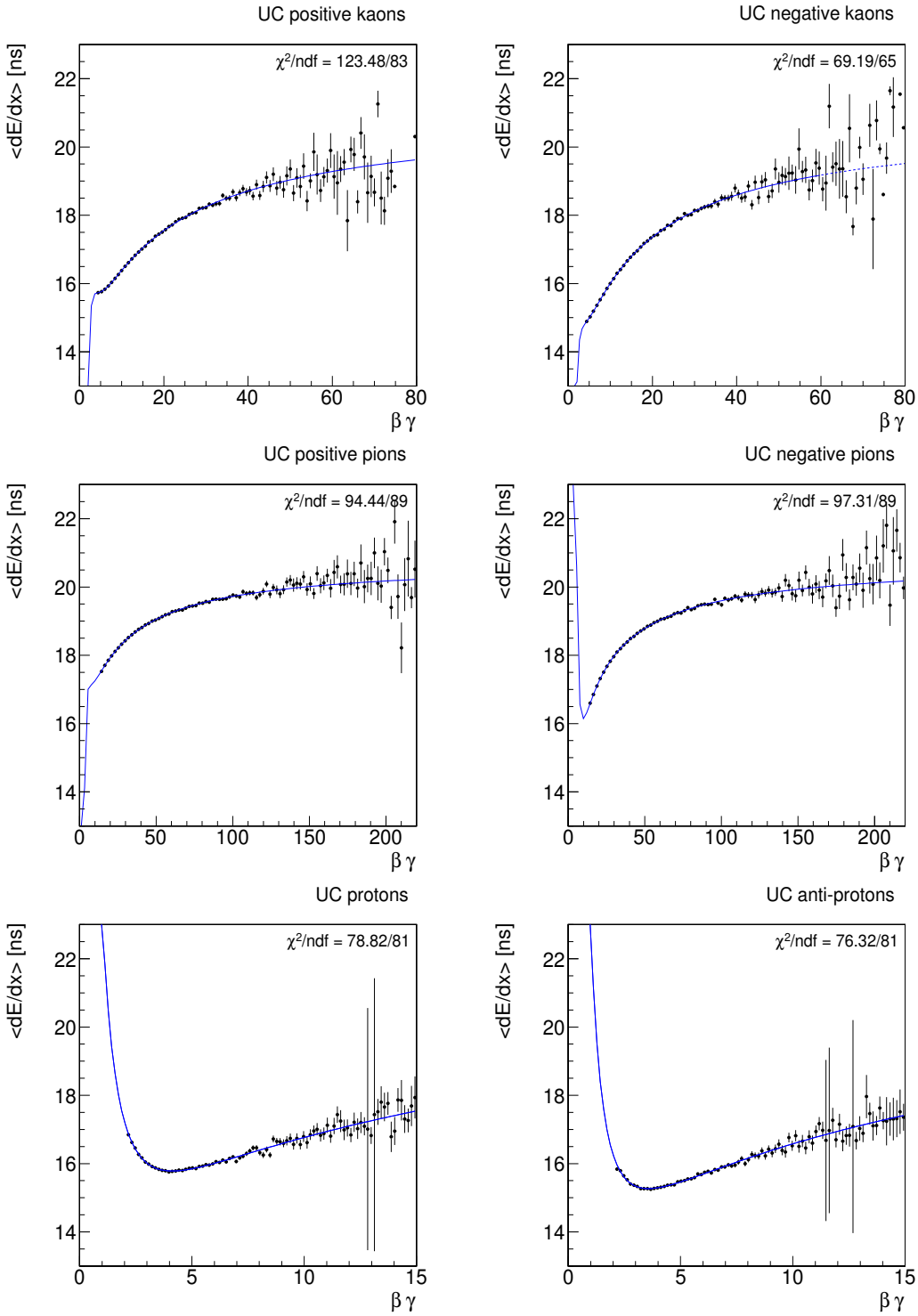

Figure 7.3: Parameterization (blue) of the Universal Curves for charged pions and kaons from $D^0 \to K^-\pi^+$ decays; protons from $\Lambda \to p\pi^-$ decays.

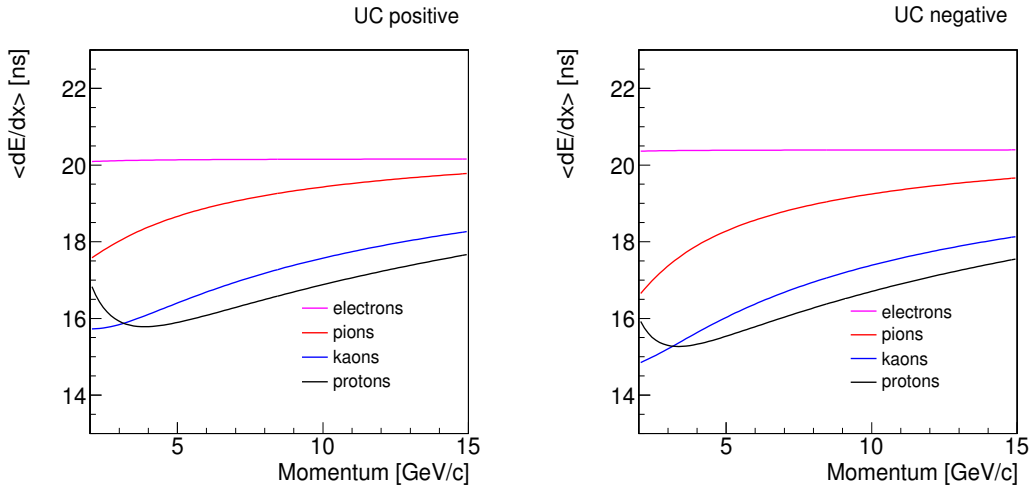

Figure 7.4: Universal curves as a function of particle momentum.

The individual charge collections output by the COT are subject to several corrections (*hit-level* corrections), applied in the off-line production, to eliminate a number of detector related conditions: hit merging, electronic pedestal subtraction, path-length correction high-voltage correction, z correction, angle and drift distance corrections, wire correction, super-layer correction, and pressure correction. An exhaustive description of these corrections can be found in [112, 113]. In addition to the hit-level corrections [113] an accurate calibration of the uniformity of the dE/dx response in time and over the chamber volume was required. These were determined using track-oriented parameters (like φ_0, η, hit multiplicity and time) which allowed complementary corrections accounting for some "macroscopic" effects (i.e. the track length dependence). We especially checked that the CDF official calibration, performed up to about 3 fb^{-1}, is valid for the $B^0_{(s)} \to h^+h'^-$ analysis purpose, up to more than 9 fb^{-1}. The details of this check are reported in appendix B. This improved the PID performance in terms of *separation power* to distinguish different classes of particles and reduced the effects due to the *correlations* between the dE/dx response of tracks. Understanding the dE/dx correlations is crucial to avoid bias in the estimate of physical observables.

7.3 dE/dx residual correlations

As introduced in sec. 5.3, in the fit of composition we will use the information given by the dE/dx. This strategy is completely inherited by the previous version of this analysis and has been reported in detail in [88], we just updated the distributions and checked the correctness of updated results. The dE/dx residual (in m_A mass hypothesis) of a charged particle with momentum p and observed specific energy-loss

dE/dx_{obs}, is defined as follows:

$$\delta_A = \frac{dE}{dx}_{\text{obs}} - \frac{dE}{dx}_A, \tag{7.3}$$

where dE/dx_{obs} is the observed specific energy-loss and dE/dx_A is the expected dE/dx in hypothesis of a particle with mass A, determined from the empirical function eq. (7.2) modeling the COT average energy loss, evaluated at $\beta\gamma = p/m_A$.

With an ideal PID detector, no correlation is expected between independent measurements. A non-vanishing correlation indicates the presence of residual dE/dx gain variations from event to event. An uncorrected gain variation would induce a correlation between the observed ionizations of distinct particles, through the inevitable correlations present in the calibration sample. The presence of correlations is dangerous for the present analysis. While a small separation power only degrades the statistical uncertainty on the relative fractions of the different signal modes, a large correlation strongly biases the central values. Therefore this effect was carefully studied. Figure 7.5 shows the distribution of the residual for kaons (with kaon hypothesis) as a function of the residual for pions (with pion hypothesis) and the same two-dimensional distribution of the residual for protons (with proton hypothesis) as a function of the residual for pions (with pions hypothesis). A non-zero, positive correlation is visible from the shape of the distributions, corresponding to a correlation coefficient $\rho \simeq 8\%$ for kaons and pions from $D^0 \to K^-\pi^+$ decays and $\rho \simeq 11\%$ for protons and pions from $\Lambda \to p\pi^-$ decays (see fig. 7.5).[1] The sources of correlation can be divided into two groups:

Global effects – these are all the effects unrelated to the kinematics. Suppose the dE/dx shows gain variations as a function of the instantaneous luminosity: $\frac{dE}{dx} = \frac{dE}{dx}(\beta\gamma, \mathcal{L})$. Then, since the kaon and the pion from a D^0 decay are reconstructed in the same event (e. g., in the same conditions of luminosity), their observed dE/dx would appear correlated by the common dependence on luminosity. This may apply to a variety of global variables, such as time, pressure or temperature of the gas, and so forth.

Local effects – these are all effects related to kinematics. Suppose that the dE/dx shows gain variations as a function of the azimuthal angle of emission of the particle: $\frac{dE}{dx} = \frac{dE}{dx}(\beta\gamma, \varphi_0)$. Then, since the azimuthal angle of a kaon and a pion from a D^0 decay are correlated by the kinematic of the decay and by the selection cuts, their observed dE/dx would become correlated. This may apply to a variety of local variables, such as η, z_0, hit multiplicity, etc.

We investigated the combined effect of all possible residual gain variations by allowing for a generic, time-dependent common-mode fluctuation $c(t)$ that affects

[1] The correlation coefficient in this case is $\rho = \frac{E[\delta_\pi \times \delta_{K(p)}] - E[\delta_\pi] \times E[\delta_{K(p)}]}{\sigma_{\delta_\pi} \times \sigma_{\delta_{K(p)}}}$, in which $E[x]$ indicates the expected value of x, and σ are sample standard-deviations.

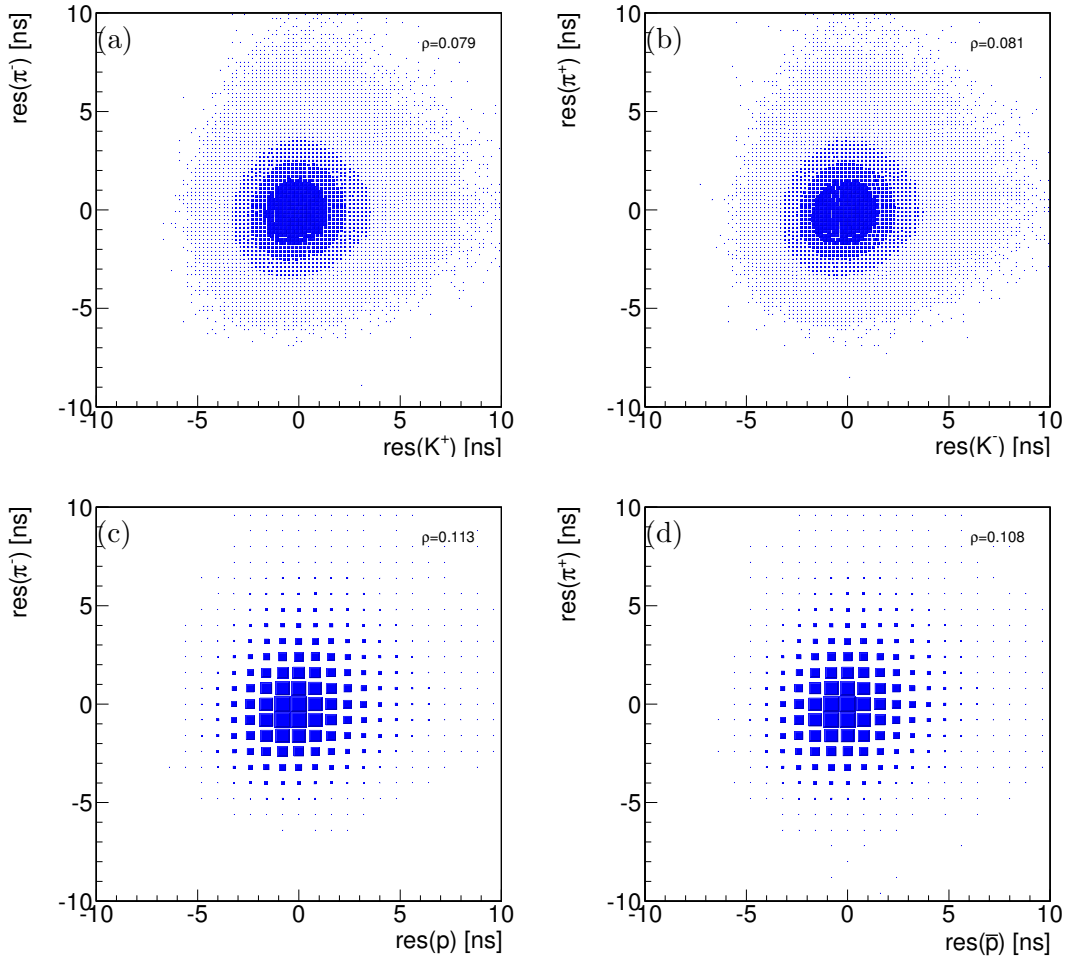

Figure 7.5: Residual for pions (with pion hypothesis) as a function of the residual for kaons (with kaon hypothesis) (a,b). Residual for pions (with pion hypothesis) as a function of the residual for protons (with proton hypothesis) (c,d).

and correlates the observed dE/dx values of the tracks in the event. In particular, we extracted the variance (σ_c^2) of the distribution of the common mode, as an estimator of the size of the correlation. We denote the probability distribution of the dE/dx residual for pions (with pion mass-hypothesis) as $\wp_\pi(\delta_\pi)$, with standard deviation σ_π. A similar notation is used for kaons. If δ_π and δ_K were independent variables, the probability distribution of their sum $(\delta_K + \delta_\pi)$ would satisfy

$$\wp(\delta_\pi + \delta_K) = \wp_\pi(\delta_\pi) * \wp_K(\delta_K), \tag{7.4}$$

in which the symbol $*$ indicates the Fourier convolution product.[2] Similarly, their difference $\delta_\pi - \delta_K$ would be distributed as

$$\wp(\delta_\pi - \delta_K) = \wp_\pi(\delta_\pi) * \wp_{-K}(-\delta_K), \tag{7.5}$$

[2]Henceforth, "convolution" always denote the Fourier convolution product.

where $\wp_{-K}(-\delta_K)$ is the distribution of the negative residual for kaons ($\frac{dE}{dx}_K - \frac{dE}{dx}_{\rm obs}$), whose variance satisfies the condition $\sigma^2_K = \sigma^2_{-K}$. Since the variance of a convolution product is the sum of variances of the convoluted distributions, the standard deviations of the distributions of sum and difference are equal:

$$\sigma_{\pi+K} = \sigma_{\pi-K} = \sqrt{\sigma^2_\pi + \sigma^2_K}. \tag{7.6}$$

On the other hand, if the two residuals are correlated by a common-mode fluctuation, the observed residual ($\delta^{\rm obs}$) is written as the sum of the intrinsic, uncorrelated residual with the common-mode shift:

$$\delta^{\rm obs}_\pi = \delta_\pi + c \quad \text{and} \quad \delta^{\rm obs}_K = \delta_K + c. \tag{7.7}$$

Therefore, the sum of the observed residuals, $\delta^{\rm obs}_\pi + \delta^{\rm obs}_K = \delta_\pi + \delta_K + 2c$, is distributed as

$$\wp(\delta^{\rm obs}_\pi + \delta^{\rm obs}_K) = \wp_\pi(\delta_\pi) * \wp_K(\delta_K) * \wp_c(2c), \tag{7.8}$$

whereas their difference, $\delta^{\rm obs}_\pi - \delta^{\rm obs}_K = \delta_\pi + c - \delta_K - c = \delta_\pi - \delta_K$, is distributed as

$$\wp(\delta^{\rm obs}_\pi - \delta^{\rm obs}_K) = \wp_\pi(\delta_\pi) * \wp_{-K}(-\delta_K). \tag{7.9}$$

Equations (7.8) and (7.9) show that, in presence of a common mode, the sum of residuals has greater variance than their difference, $\sigma^2_{\pi+K} > \sigma^2_{K-\pi}$. The standard deviation of the correlation is easily obtained:

$$\sigma_c = \frac{1}{2}\sqrt{\sigma^2_{\pi+K} - \sigma^2_{\pi-K}}. \tag{7.10}$$

Following eq. (7.10), we used the distributions of sum and difference of the observed residual to estimate the magnitude of time-dependent common modes. For $\Lambda \to p\pi^-$ decays, the standard deviation of the time-dependent common-mode is:

$$\sigma_c = \frac{1}{2}\sqrt{\sigma^2_{\pi+p} - \sigma^2_{\pi-p}}. \tag{7.11}$$

7.4 Model of the dE/dx distributions

Using the dE/dx information in a Likelihood fit requires modeling the distributions of the desired observables. It is convenient to stress the difference between *observed* dE/dx quantities, i. e., those affected by common-mode fluctuations, and *intrinsic* quantities, the quantities which would have been observed if the correlations were not present. Since the intrinsic residuals and the correlation are, by construction, independent variables (see eq. (7.7)), the (known) distribution of the observed residuals is the convolution of their unknown distributions:

$$\wp(\delta^{\text{obs}}) = \wp(\delta + c) = \wp(\delta) * \wp(c). \tag{7.12}$$

The model of the intrinsic residuals, $\wp(\delta)$, and of the correlations, $\wp(c)$, were extracted from the distributions of the observed residuals, $\wp(\delta^{\text{obs}})$, of pions and kaons from D^0 decays. We expanded each term of the right-hand side of eq. (7.12) in sum of Gaussian distributions, and we fit the distributions of the observed residuals to extract the unknown parameters. In practice, the first three terms of the expansion were sufficient to model accurately the intrinsic residuals and correlations:

$$\wp_K(\delta_K) = q' \cdot \mathscr{G}_{K'}(\delta_K) + q'' \cdot \mathscr{G}_{K''}(\delta_K) + (1 - q' - q'') \cdot \mathscr{G}_{K'''}(\delta_K) \tag{7.13}$$

$$\wp_\pi(\delta_\pi) = p' \cdot \mathscr{G}_{\pi''}(\delta_\pi) + p'' \cdot \mathscr{G}_{\pi''}(\delta_\pi) + (1 - p' - p'') \cdot \mathscr{G}_{\pi'''}(\delta_\pi) \tag{7.14}$$

$$\wp_c(c) = r \cdot \mathscr{G}_{c'}(c) + (1 - r) \cdot \mathscr{G}_{c''}(c) \tag{7.15}$$

where we used the following notation for the Gaussian distribution:

$$\mathscr{G}_s(x) = \mathscr{G}(x; \mu_s, \sigma_s) = \frac{1}{\sigma_s\sqrt{2\pi}} e^{-\frac{(x-\mu_s)^2}{2\sigma_s^2}}.$$

Independent parameterizations were assumed for the distributions of intrinsic residuals for positively and negatively-charged particles. Mean (μ), variance (σ^2) and fraction of each Gaussian were determined with a simultaneous, binned ML fit of the following combinations of observed residuals:

$$\wp_K(\delta_K^{\text{obs}}) = \wp(\delta_K) * \wp(c) = (\mathscr{G}_{K'} + \mathscr{G}_{K''} + \mathscr{G}_{K'''}) * (\mathscr{G}_{c'} + \mathscr{G}_{c''}) \tag{7.16}$$

$$\wp_\pi(\delta_\pi^{\text{obs}}) = \wp(\delta_\pi) * \wp(c) = (\mathscr{G}_{\pi'} + \mathscr{G}_{\pi''} + \mathscr{G}_{\pi'''}) * (\mathscr{G}_{c'} + \mathscr{G}_{c''}) \tag{7.17}$$

$$\wp(\delta_\pi^{\text{obs}} + \delta_K^{\text{obs}}) = (\mathscr{G}_{\pi'} + \mathscr{G}_{\pi''} + \mathscr{G}_{\pi'''}) * (\mathscr{G}_{K'} + \mathscr{G}_{K''} + \mathscr{G}_{K'''}) * (\mathscr{G}_{2c'} + \mathscr{G}_{2c''}) \tag{7.18}$$

$$\wp(\delta_\pi^{\text{obs}} - \delta_K^{\text{obs}}) = (\mathscr{G}_{\pi'} + \mathscr{G}_{\pi''} + \mathscr{G}_{\pi'''}) * (\mathscr{G}_{-K'} + \mathscr{G}_{-K''} + \mathscr{G}_{-K'''}), \tag{7.19}$$

where the relative normalization factors (p, q, r) were included in the fit, but omitted above for a clearer notation. If in the equations above (eqs. (7.13)–(7.19)) we replace the kaon index (K) with the proton index (p) we obtain the equivalent relations to model the probability density functions of protons and pions from $\Lambda \to p\pi^-$ decay. In this case we parameterized a different correlation function with respect to the $D^0 \to K^-\pi^+$ case since we used a different sample.

The technique used to extract the parameters of the dE/dx templates, of the intrinsic residuals and correlation, is based on an iterative method of one-dimensional binned fits of the distributions of δ_π^{obs}, δ_K^{obs}, $\delta_\pi^{\text{obs}} + \delta_K^{\text{obs}}$ and $\delta_\pi^{\text{obs}} - \delta_K^{\text{obs}}$.

Figures 7.6 and 7.7 show a satisfactory agreement between the chosen model and the distributions of the observed residuals and correlations. Although we allowed for independent residual distributions for kaons, pions and protons (negative and positive particles) the extracted shapes are similar, all showing non-Gaussian positive tails. The differences between the residuals of positively and negatively-charged particles are tiny. These small differences between kaons and pions and between positively and negatively-charged particles have been ascribed to a systematic dependence of the dE/dx response on track curvature, caused by the geometric and electrostatic asymmetry of the COT drift-cells. For a given Lorentz boost, the trajectories of charged particles with different masses or charge have different curvatures, and are sensitive to the systematic effects in the efficiency of charge-collection of the COT sense-wires.

Figure 7.9 shows the extracted probability density functions for the correlation. We extracted two models for the correlation function: one from the $D^0 \to K^-\pi^+$ sample and the other one from the $\Lambda \to p\pi^-$ sample. Both models show a non negligible correlation, as expected from the distributions of the sum and the difference of the residuals. These correlation functions show small differences. The correlation function extracted from pions and kaons from $D^0 \to K^-\pi^+$ decays has a tighter RMS than the correlation extracted from protons and pions from $\Lambda \to p\pi^-$ decays. The core of the distribution is centered at zero for $D^0 \to K^-\pi^+$ decays, while it is shifted by ≈ 0.06 ns for $\Lambda \to p\pi^-$ decays (see fig. 7.9).

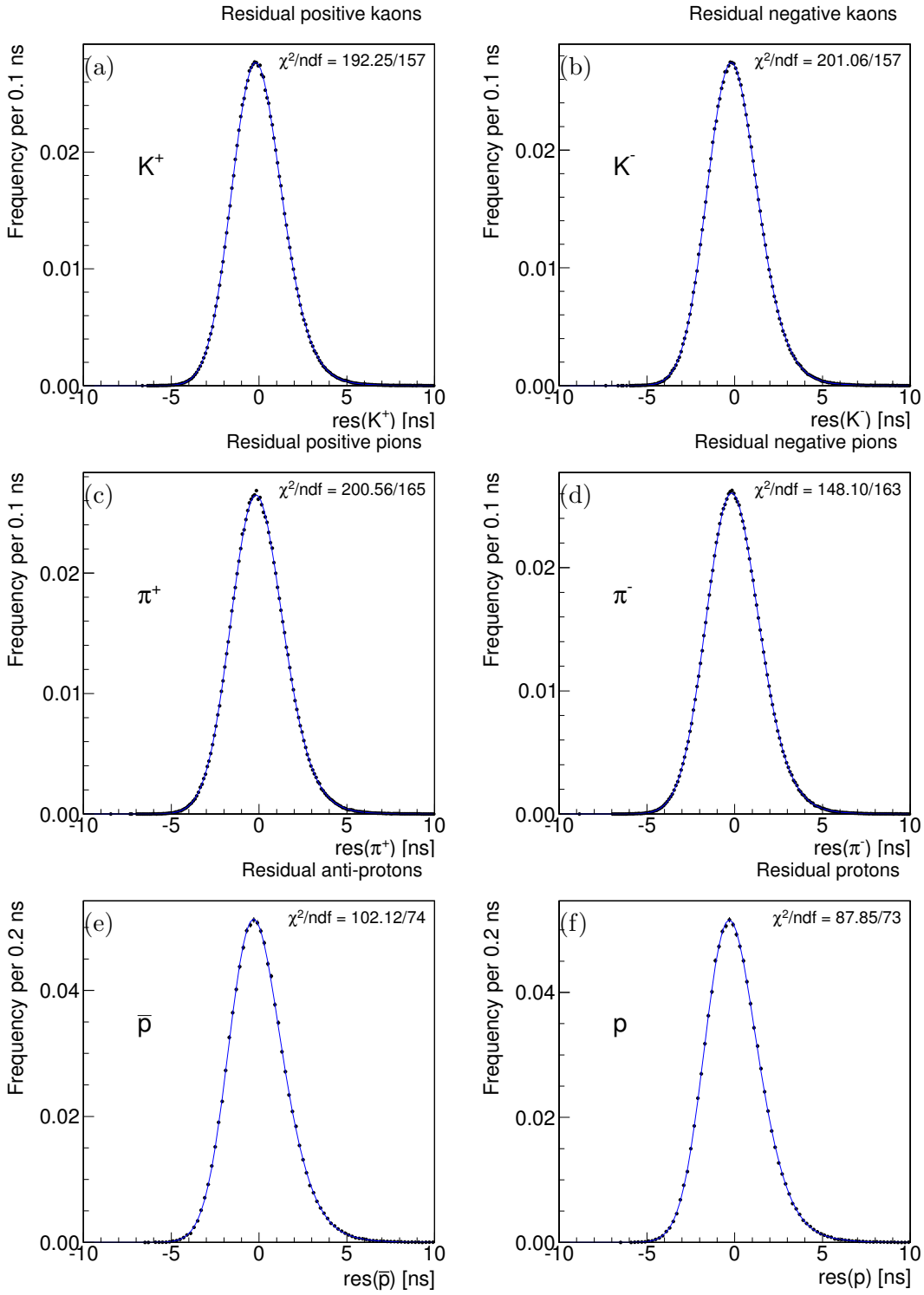

Figure 7.6: Distribution of observed dE/dx residual ($\wp(\delta^{\text{obs}}) = \wp(\delta + c) = \wp(\delta) * \wp(c)$), for pions (with pion mass hypothesis) (a,b), for kaons (with kaon mass hypothesis) (c,d) and for protons (with proton mass hypothesis) (e,f). The results of the fit to the functions in eq. (7.17) and eq. (7.16) are overlaid (blue, solid line).

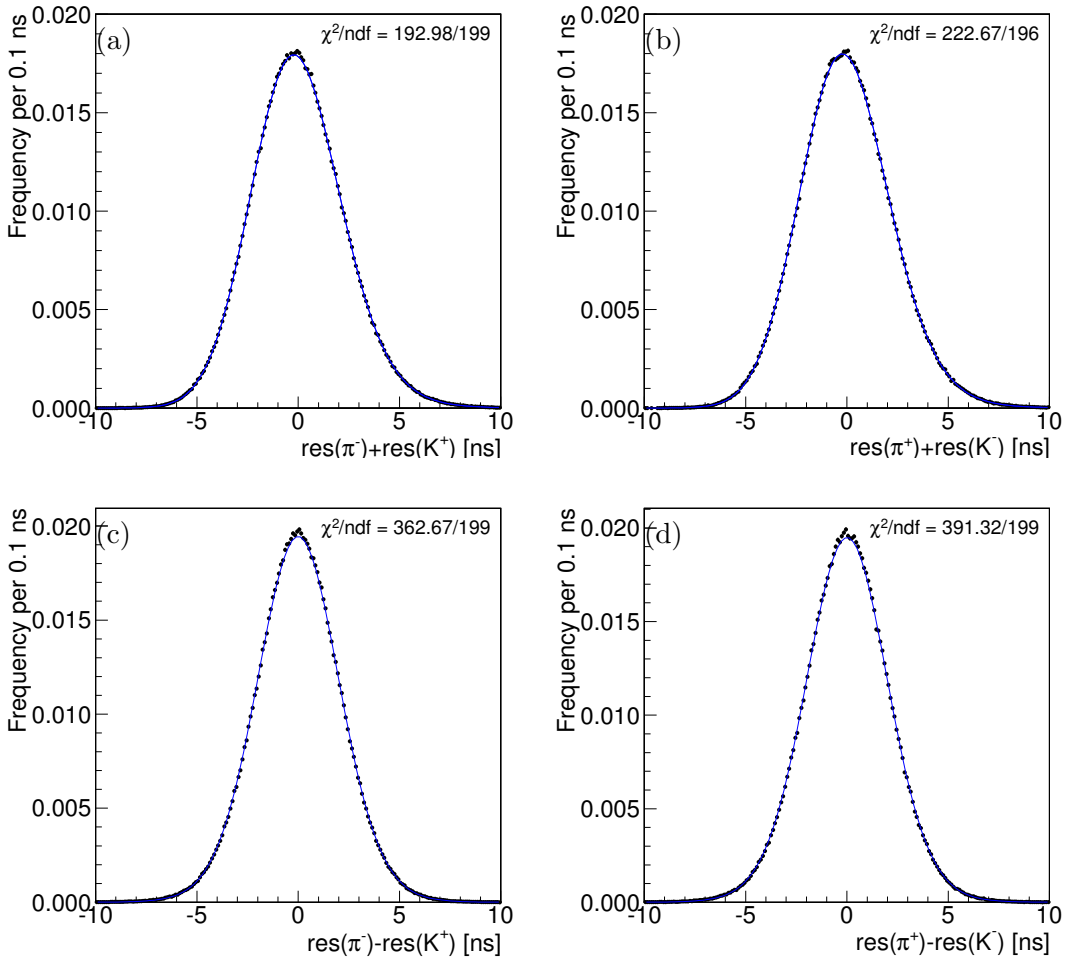

Figure 7.7: Distribution of the sum (a,b) and the difference (b,d) of the residuals for a kaon (in kaon hypothesis) and a pion (in pion hypothesis) from $D^0 \to K^-\pi^+$ decays. The results of the fit to the functions in eq. (7.18) and eq. (7.19) are overlaid (blue, solid line).

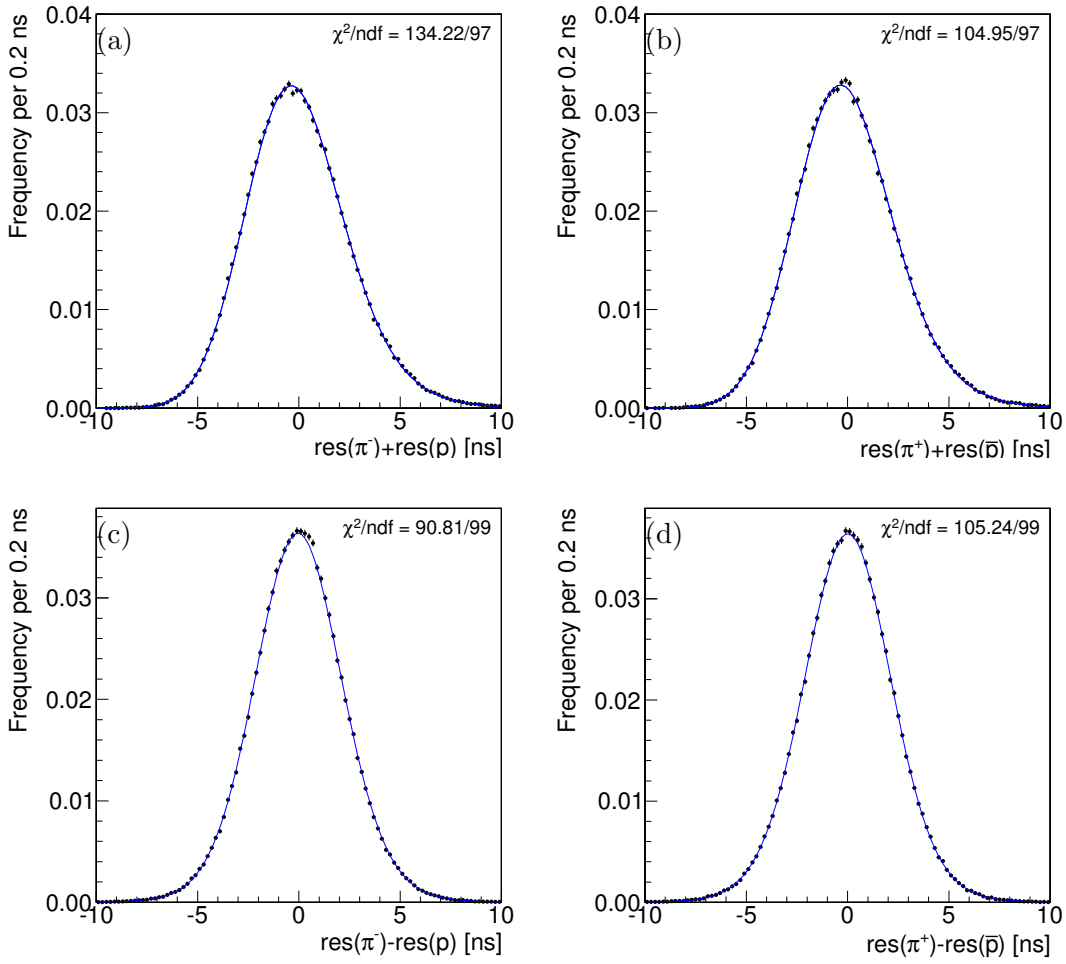

Figure 7.8: Distribution of the sum (a,b) and the difference (b,d) of the residuals for a proton (in proton hypothesis) and a pion (in pion hypothesis) from $\Lambda \to p\pi^-$ decays. The results of the fit to the functions in eq. (7.18) and eq. (7.19) are overlaid (blue, solid line).

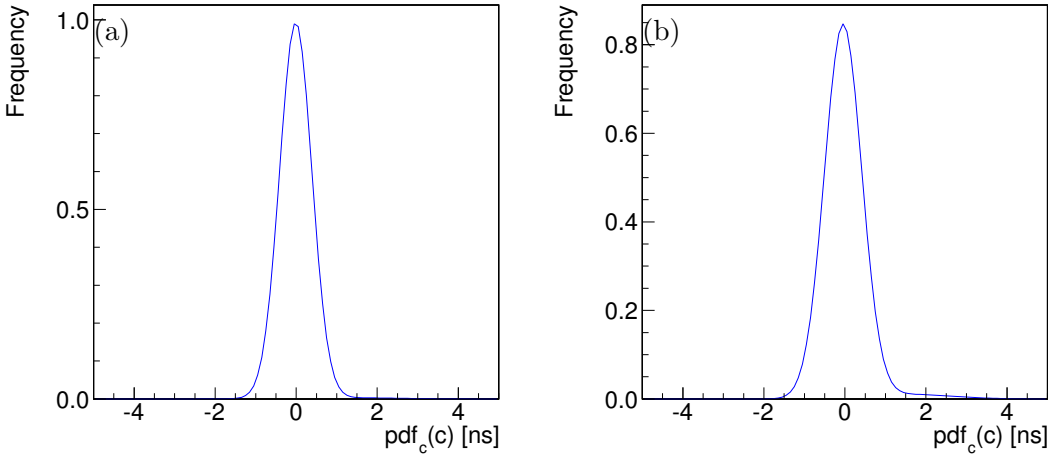

Figure 7.9: Correlation probability density functions for pions and kaons from $D^0 \to K^-\pi^+$ decays (a), for pions and protons from $\Lambda \to p\pi^-$ decays (b).

7.5 Probability density function of the signal PID term

The p.d.f. of the PID information can not be factorized in the probability densities of the two particles, because of the correlation between the observed dE/dx values. We therefore wrote a two-particle, joint p.d.f. that incorporates the probability densities of the intrinsic dE/dx observables of each particle, and of the correlation function. We used the shapes of the intrinsic residuals and correlation determined in sec. 7.4 to write the p.d.f., which results from a convolution integral plus a transformation of variables. The convolution combines the intrinsic dE/dx residuals of both particles in the final state l and m (δ_l and δ_m) through the p.d.f. of correlation, $\wp_c(c)$, yielding the following p.d.f. for the jth mode:

$$\begin{aligned}\wp_j(\delta_l^{\rm obs},\delta_m^{\rm obs}) = \wp_{H\to lm}(\delta_l^{\rm obs},\delta_m^{\rm obs}) &= [\wp_l(\delta_l)\times\wp_m(\delta_m)]*\wp_c(c)\\ &= \int_{-\infty}^{+\infty}\wp_l(\delta_l-c)\wp_m(\delta_m-c)\wp_c(c)dc,\end{aligned} \tag{7.20}$$

which, at this stage, is independent of momenta. The index j, which runs over all components, is splitted in three indices $H\to lm$ because the PID term depends only on the identity of particles in the final states of the jth mode and not on the initial mother particle $H = B^0, B_s^0$ or Λ_b^0. The indices $l, m = K^\pm$, $\pi^\pm$, p or $\bar{p}$ determine the choice of the shapes for intrinsic residuals within the integral. The p.d.f. in eq. (7.20) is function of a different set of observables for each mode, e. g., $(\delta_{\pi^+},\delta_{\pi^-})$ for the $B^0\to\pi^+\pi^-$ case, $(\delta_{K^+},\delta_{\pi^-})$ for the $B^0\to K^+\pi^-$ case and so on.

To avoid possible biases related to using different sets of observables in different terms of the Likelihood function δ_l and δ_m [109], we rewrote the Likelihood in terms of a single observable summarizing all the PID information, the "kaonness" κ, defined as:

$$\kappa = \frac{dE/dx_{\rm obs} - dE/dx_\pi}{dE/dx_K - dE/dx_\pi}. \tag{7.21}$$

The average of this quantity is, by construction, zero for pions and one for kaons, with almost momentum-independent distribution for both types of particles (see fig. 7.10). This is particularly convenient in our case, since all $B^0_{(s)}\to h^+h'^-$ modes have only pions and kaons in their final states, and also the background composition is expected to be dominated by these particles.

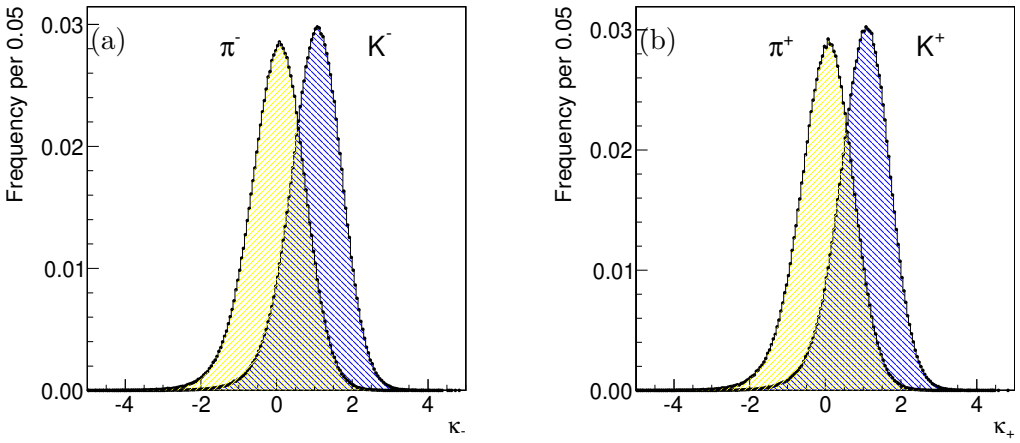

Figure 7.10: The kaonness κ for pion and kaons from $D^0 \to K^-\pi^+$ decays reconstructed from $D^{*+} \to D^0\pi^+ \to [K^-\pi^+]\pi^+$ decays. Negative particles (a), positive particles (b).

Changing variable from residual to kaonness induces an additional dependence on momentum in the PID term. In fact, for each particle type, the following relation holds:

$$\delta = (\kappa - \langle\kappa\rangle)\left(\frac{dE}{dx}_K - \frac{dE}{dx}_\pi\right) \equiv (\kappa - \langle\kappa\rangle)\,\Delta \tag{7.22}$$

where Δ indicates the difference between the expected dE/dx values evaluated in kaon and pion mass-hypothesis, which is function of momentum. The advantage to use the kaonness in lieu of the residuals in different hypothesis is that the kaonness is defined for all kind of particles in the same way. In fact the residuals in all mass hypothesis are function of kaonness and momentum particle. The joint p.d.f. as a function of κ is

$$\wp_{lm}(\kappa_+^{\rm obs}, \kappa_-^{\rm obs}) = \int_{-\infty}^{+\infty} \wp(\delta_l - c)\wp(\delta_m - c)\left|\frac{\partial(\delta_l, \delta_m)}{\partial(\kappa_+, \kappa_-)}\right|\wp_c(c)dc, \tag{7.23}$$

where $\delta \equiv \delta(\kappa)$. Following the same notation of chap. 5 where we labeled the outgoing particles according to the charge, index "+" labels the kaonness (κ_+) of the positive particle, while index "-" labels the corresponding quantities of the negative particle. After writing out the Jacobian, the above equation becomes

$$\wp_{lm}(\kappa_+^{\rm obs}, \kappa_-^{\rm obs}) = \int_{-\infty}^{+\infty} \wp(\delta_l - c)\wp(\delta_m - c)\Delta_1\Delta_2\wp_c(c)dc. \tag{7.24}$$

The transformation from residual to kaonness brings the momenta into the probability density through the differences of expected dE/dx values, $\Delta_1(\beta, p_{\rm tot})$ and $\Delta_2(\beta, p_{\rm tot})$. Hence, the correct expression of the joint p.d.f. function of κ becomes a conditional probability density at given momenta: $\wp_{lm}(\kappa_+^{\rm obs}, \kappa_-^{\rm obs}) \longrightarrow \wp_{lm}(\kappa_+^{\rm obs}, \kappa_-^{\rm obs}|\beta, p_{\rm tot})$.

An event in which δ_l and δ_m are the observed dE/dx residuals of the particle pair, contributes to the jth signal mode of the PID p.d.f. with the following term:

$$\begin{aligned} \wp_j^{\rm PID}(\kappa_+^{\rm obs}, \kappa_-^{\rm obs}|\beta, p_{\rm tot}) &= \wp_{l,m}^{\rm PID}(\kappa_+^{\rm obs}, \kappa_-^{\rm obs}|\beta, p_{\rm tot}) \\ &= \frac{1}{K_j}\int_{-\infty}^{+\infty} \wp_l(\delta_l - c)\wp_m(\delta_m - c)\Delta_1\Delta_2\wp_c(c)dc, \end{aligned} \tag{7.25}$$

which includes $K_j = 1/\int_{-\infty}^{+\infty} \wp_j(\kappa_+^{\rm obs}, \kappa_-^{\rm obs}|\beta, p_{\rm tot})d\kappa_+^{\rm obs}d\kappa_-^{\rm obs}$ as a normalization factor. The explicit expression of the p.d.f. was evaluated analytically; we omit here its explicit expression because of its length.

7.6 Probability density function of the background PID term

The PID p.d.f. for combinatorial background uses the same joint two-particle p.d.f. as for the signal. The term corresponding to each possible pair of particle types (l, m) in background, is weighed by a factor $w_l w_m$. Each weight w_l is proportional to the fractional contribution of particles of type l to the background, and it is a free parameter in the fit. We allowed for independent kaon, proton, electron and pion (or muon) contributions, and for positive and negative particles for the combinatorial background, while, for physics background, we allowed for independent kaon and pion contributions, averaging on the particle charge, since in this case we do not expect electrons and protons in the final state and any asymmetry between positive and negative particles. Muons and pions were not differentiated since their contributions are indistinguishable; the ≈ 1.5 ns dE/dx resolution is insufficient to resolve the difference between their ionization rates, which is inappreciable because of the small difference in mass $m_{\pi^\pm} - m_\mu \simeq 34{\rm MeV}/c^2$. This does not affect the signal composition, since muon contamination in the signal peak is negligible, if any, due to the small rates expected for $B^0_{(s)}$ meson decays in muon pairs [114, 115], and muons from semileptonic heavy-flavor decays do not have a peaking distribution in mass. A candidate decaying to particles with $\kappa_+^{\rm obs}$ and $\kappa_-^{\rm obs}$ observed "kaon-nesses", sum of observed scalar momenta $p_{\rm tot}$, and observed momentum imbalance β, contributes to the PID term of the Likelihood of background with the following probability density function:

$$\wp_{\rm A(E)}^{\rm PID} = \sum_{l,m} w_l^{\rm A(E)} w_m^{\rm A(E)} [\wp_{l,m}(\kappa_+^{\rm obs}, \kappa_-^{\rm obs}|\beta, p_{\rm tot}) + \wp_{m,l}(\kappa_+^{\rm obs}, \kappa_-^{\rm obs}|\beta, p_{\rm tot})]. \tag{7.26}$$

The explicit expression of $\wp_{l,m}(\kappa_+^{\rm obs}, \kappa_-^{\rm obs}|\beta, p_{\rm tot})$ is shown in eq. (7.26). While in the signal case the l, m indices run over kaons, pions and protons ($K^\pm$, $\pi^\pm$, p and $\bar{p}$) according to the decay of $B^0_{(s)} \to h^+ h'^-$ and $\Lambda_b^0 \to p h^-$, in the above equation they include also electrons ($e^\pm$) for the combinatorial background (E), while for physics background l, m indexes run over kaons, pions (K, π) only, where $w^{\rm A}_{K^+} = w^{\rm A}_{K^-}$ and $w^{\rm A}_{\pi^+} = w^{\rm A}_{\pi^-}$.

7.7 Sample dependence of correlation

The dE/dx correlation has been parameterized using a sum of two gaussians as described in sec. 7.4. Since we are fitting a data sample different from the calibration sample ($D^0 \to h^+h'^-$), in the central fit we added an additional free parameter $\delta^c_{dE/dx}$ which is a global shift of the correlation template. This has been done to keep into account that the dE/dx parameterization (universal curves and residual templates) has been performed averaging over all data sample. Thus if we use the dE/dx templates on a different sample everything is accurate except for a small global shift of the order 1 nano second or less.

Since the templates of protons were extracted using $\Lambda \to p\pi^-$ decays, which is a third sample, we added an additional free parameter $\delta^p_{dE/dx}$ which is a common global shift of the proton and anti-protons residual templates. This has been done to keep into account, as in the previous case, the fact that the template has been parameterized averaging over all data sample, which is, also in this case, different from $\Lambda^0_b \to ph^-$.

We have now all the ingredients to perform the maximum likelihood fit. The next chap. 8 describes the results obtained and the checks made to test the fitting code.

Chapter 8

Fit results

This chapter reports the results of the fit of composition, not yet corrected for the charge asymmetries and the relative efficiency corrections. The checks produced to ensure the correctness of the fitting code are also reported.

8.1 Introduction

The analysis described in this thesis produced several physics results of branching ratios and $\mathcal{C}P$ violating asymmetries. We first searched for the rare annihilation decays modes $B_s^0 \to \pi^+\pi^-$ and $B^0 \to K^+K^-$ with the data sample available at that time, corresponding to 6.11 fb^{-1} of integrated luminosity. Afterwards, we performed the measurements of $\mathcal{C}P$ violating asymmetries of $B^0 \to K^+\pi^-$, $B_s^0 \to K^-\pi^+$, $\Lambda_b^0 \to p\pi^-$, and $\Lambda_b^0 \to pK^-$ decay modes with the full CDF data sample, corresponding to 9.3 fb^{-1}. The two sets of measurements are performed with the same analysis, except for the addition of new available data and some small refinements. The fit of composition described in the previous chapters is the one performed for the $\mathcal{C}P$ measurements on the full data sample, while the small differences with the search for annihilation modes are described in appendix C.

8.2 Fit results: search for annihilation modes

The analysis of the annihilation decay modes was performed using data collected between February 2002 (run 138809) and February 2010 (run 289197) by the trigger on displaced tracks. After the application of standard CDF data-quality requirements (see sec. 2.5), the sample size corresponds to an integrated luminosity of about 6.11 fb^{-1}. After the selection, a total number of about 24,000 events is found. The results of the fit are shown in tab. 8.1 (top), while tab. 8.1 (middle) shows the signal yields. Table 8.1 (bottom) also summarizes the relevant physics quantities determined by the fit parameters: the relative fraction of $B_s^0 \to \pi^+\pi^-$ and $B^0 \to K^+K^-$ with respect to the $B^0 \to K^+\pi^-$ are used to obtain the $\mathcal{B}$ mea-

surements and the $B^0 \to \pi^+\pi^-$ and $B_s^0 \to K^+K^-$ fractions. The $\mathcal{B}(B^0 \to \pi^+\pi^-)$ and the $\mathcal{B}(B_s^0 \to K^+K^-)$ are known with high experimental precision, being larger with respect to the other charmless $\mathcal{B}$ values, so these two parameters represent a standard "candle" to check the global reliability of the fit. The statistical uncertainties on these quantities have been calculated using the covariance matrix returned from the fit. These results are in agreement with the values obtained in the previous published version of this analysis, performed on a data sample corresponding to 1 fb^{-1} [88].

We observed some hints for the presence of the $B_s^0 \to \pi^+\pi^-$ and $B^0 \to K^+K^-$ modes. A simple estimation of the statistical significance obtained dividing the results of the fit over their statistical uncertainty is of about 3σ for the $B_s^0 \to \pi^+\pi^-$ decay mode, and of about 2σ for the $B^0 \to K^+K^-$ decay mode. However, particular attention has been given to the evaluation of the significance, as will be described in sec. 11.8.2. Since the method will take into account both statistical and systematic uncertainties, we will describe it after the evaluation of the systematics of chap. 11.

Fit parameter	value
$\hat{f}_{B^0\to\pi^+\pi^-}$	0.148 ± 0.006
$\hat{f}_{B^0\to K^+\pi^-}$	0.579 ± 0.008
$\hat{f}_{B_s^0\to\pi^+\pi^-}$	0.005 ± 0.001
$\hat{f}_{B^0\to K^+K^-}$	0.007 ± 0.003
$\hat{f}_{B_s^0\to K^+K^-}$	0.170 ± 0.006
Raw yield	**value**
$\mathcal{N}(B_s^0 \to \pi^+\pi^-) + \mathcal{N}(\overline{B}_s^0 \to \pi^+\pi^-)$	94 ± 28
$\mathcal{N}(B^0 \to K^+K^-) + \mathcal{N}(\overline{B}^0 \to K^+K^-)$	120 ± 49
Physics observable	**value**
$\frac{\hat{f}_{B^0\to\pi^+\pi^-}}{\hat{f}_{B^0\to K^+\pi^-}}$	0.256 ± 0.013
$\frac{\hat{f}_{B^0\to K^+K^-}}{\hat{f}_{B^0\to K^+\pi^-}}$	0.012 ± 0.005
$\frac{\hat{f}_{B_s^0\to\pi^+\pi^-}}{\hat{f}_{B^0\to K^+\pi^-}}$	0.009 ± 0.003
$\frac{\hat{f}_{B_s^0\to K^+K^-}}{\hat{f}_{B^0\to K^+\pi^-}}$	0.295 ± 0.013

Table 8.1: Results of fit of composition performed on 6.11 fb^{-1} and physics observables derived from their values.

8.3 Fit results on the full data sample ($\mathcal{A}_{CP}$)

The fit of composition was applied to the $B \to h^+h'^-$ sample, consisting of a total number of events $N = 28,230$. We minimized the quantity $-2\ln(\mathscr{L})$ using the MINUIT numerical minimization package: the likelihood converges to the minimum $-2\log(\mathscr{L}) = -85,368.98$. The results of the fit are shown in tab. 8.2, and the corresponding correlation matrix is shown in sec. 8.4. Tables 8.4 and 8.3 summarize the most relevant physics quantities and yields determined by the parameters returned from the fit. The statistical uncertainties on these quantities have been calculated using the covariance matrix returned from the fit. We report a brief description of the parameters of the fit; the detailed definitions are in chap. 6 and chap. 7. The numbers refers to those parameters free to float in the fit, and corresponds to the legend of tab. 8.2. The parameters without numbers are fixed in the fit. Using the same notation introduced in sec. 4.2.1, the suffix `A` refers to the `A` sample parameters, while the suffix `C` labels the `C` sample parameters.

- f_i: relative fraction of i-th decay mode with respect to the sum of all $B \to h^+h'^-$ decay modes (par n. 1-11).
- b: relative fraction of background (combinatorial plus physics) events with respect to the sum of background plus signals events (par n. 13,14).
- c_{E}: the slope of the exponential function used to write the p.d.f. of the combinatorial bkg $m^2_{\pi\pi}$ distribution eq. (6.23).
- $w^{\mathrm{E}}_{K^{+(-)}}$: fraction of $K^{+(-)}$ events with respect to combinatorial bkg events (par n. 18,21,24,27).
- $f_{\mathscr{A}}$: relative fraction of physics bkg events with respect to the sum of physics bkg events + comb bkg events (par n. 29, 30).
- $m_{\mathscr{A}}$: Cutoff of the function describing the $m^2_{\pi\pi}$ distribution of the physics bkg events (par n. 33, 35).
- $w^{\mathscr{A}}_{\pi}$: relative fraction of $\pi^{+(-)}$ events with respect to the physics bkg events (par n. 39).
- d^c_1: fraction of the 1^{st} gaussian with respect to the sum of the two gaussians used to write the p.d.f. of the correlation (par n. 43).
- μ^c_1 : the mean of the 1^{st} gaussian used to write the p.d.f. of the correlation (par n. 44).
- σ^c_1: the σ of the 1^{st} gaussian used to write the p.d.f. of the correlation (par n. 45).
- μ^c_2: the mean of the 2^{nd} gaussian used to write the p.d.f. of the correlation (par n. 46).

parameter	value	error	parameter(#)
$\hat{f}_{B^0\to\pi^+\pi^-}$	0.149	0.006	1
$\hat{f}_{B^0\to K^+\pi^-}$	0.5634	0.007	2
$\frac{\hat{f}_{\overline{B}^0\to K^-\pi^+} - \hat{f}_{B^0\to K^+\pi^-}}{\hat{f}_{\overline{B}^0\to K^-\pi^+} + \hat{f}_{B^0\to K^+\pi^-}}$	-0.089	0.013	3
$\hat{f}_{B_s^0\to K^-\pi^+}$	0.044	0.003	4
$\frac{\hat{f}_{\overline{B}_s^0\to K^+\pi^-} - \hat{f}_{B_s^0\to K^-\pi^+}}{\hat{f}_{\overline{B}_s^0\to K^+\pi^-} + \hat{f}_{B_s^0\to K^-\pi^+}}$	0.226	0.074	5
$\hat{f}_{B_s^0\to\pi^+\pi^-}$	0.006	0.001	6
$\hat{f}_{B^0\to K^+K^-}$	0.005	0.002	7
$\hat{f}_{\Lambda_b^0\to pK^-}$	0.029	0.002	8
$\frac{\hat{f}_{\overline{\Lambda}_b^0\to\overline{p}K^+} - \hat{f}_{\Lambda_b^0\to pK^-}}{\hat{f}_{\overline{\Lambda}_b^0\to\overline{p}K^+} + \hat{f}_{\Lambda_b^0\to pK^-}}$	0.089	0.081	9
$\hat{f}_{\Lambda_b^0\to p\pi^-}$	0.022	0.002	10
$\frac{\hat{f}_{\overline{\Lambda}_b^0\to\overline{p}\pi^+} - \hat{f}_{\Lambda_b^0\to p\pi^-}}{\hat{f}_{\overline{\Lambda}_b^0\to\overline{p}\pi^+} + \hat{f}_{\Lambda_b^0\to p\pi^-}}$	-0.080	0.074	11
$\hat{f}_{B_s^0\to K^+K^-}$	0.181	0.006	-
$\hat{b}$ (A)	0.288	0.004	13
$\hat{b}$ (C)	0.230	0.005	14
$\hat{c}_{\mathrm{E}}$ (A)	-0.064	fixed	-
$\hat{c}_{\mathrm{E}}$ (C)	-0.060	fixed	-
$\hat{w}^{\mathrm{E}}_{K+}$ (A)	0.405	0.025	18
$\hat{w}^{\mathrm{E}}_{K-}$ (C)	0.397	0.025	21
$\hat{w}^{\mathrm{E}}_{K+}$ (A)	0.602	0.055	24
$\hat{w}^{\mathrm{E}}_{K-}$ (C)	0.575	0.056	27
$\hat{f}_{\mathscr{A}}$ (A)	0.577	0.010	29
$\hat{f}_{\mathscr{A}}$ (C)	0.778	0.014	30
$\hat{m}_{\mathscr{A}}$ [GeV$^2/c^4$] (A)	26.64	fixed	-
$\hat{m}_{\mathscr{A}}$ [GeV$^2/c^4$] (C)	26.64	fixed	-
$\hat{w}^{\mathscr{A}}_{\pi}$	0.697	0.010	39
$\hat{d}_1^c$	0.013	fixed	-
$\hat{\mu}_1^c$ [ns]	0.905	fixed	-
$\hat{\sigma}_1^c$ [ns]	1.435	fixed	-
$\hat{\mu}_2^c$ [ns]	-0.012	fixed	-
$\hat{\sigma}_2^c$ [ns]	0.398	fixed	-
$\hat{\delta}^c_{dE/dx}$ [ns]	-0.059	0.012	49
$\hat{\delta}^p_{dE/dx}$ [ns]	-0.386	0.066	48
$\hat{\delta}_m$	-0.001	0.001	31
$\hat{N}$	28230	168	52
$\hat{p}$	0.667	0.003	53

Table 8.2: Results of fit of composition. Signal (background) related quantities are reported in the upper (lower) section. The last column reports the legend to convert the parameter number into physics quantity for interpreting the correlation matrix shown at tab. 8.6; the missing codes refer to parameters which are not part of the set of primary fit parameters ($\vec{\theta}$). C-conjugate modes are implied except for the parameter in the third, fifth, ninth and eleventh row.

- σ_2^c: the σ of the 2$^{\text{nd}}$ gaussian used to write the p.d.f. of the correlation (par n. 47).
- $\delta^c_{dE/dx}$: correlation global shift (par n. 49).
- $\delta^p_{dE/dx}$: correlation global shift for the p.d.f. with proton contributions (par n. 48).
- δ_m: shift on the nominal $b-$hadron masses (par n. 31).
- N: total number of events (par n. 52).
- p: fraction of sample `A` events with respect to the total number of events (par n. 53).

mode			
$\mathcal{N}(B^0 \to \pi^+\pi^-)$	+	$\mathcal{N}(\overline{B}^0 \to \pi^+\pi^-)$	3074 ± 121
$\mathcal{N}(B^0 \to K^+\pi^-)$			6348 ± 117
$\mathcal{N}(\overline{B}^0 \to K^-\pi^+)$			5313 ± 109
$\mathcal{N}(B_s^0 \to K^-\pi^+)$			354 ± 46
$\mathcal{N}(\overline{B}_s^0 \to K^+\pi^-)$			560 ± 51
$\mathcal{N}(B_s^0 \to K^+K^-)$	+	$\mathcal{N}(\overline{B}_s^0 \to K^+K^-)$	3738 ± 122
$\mathcal{N}(B_s^0 \to \pi^+\pi^-)$	+	$\mathcal{N}(\overline{B}_s^0 \to \pi^+\pi^-)$	126 ± 30
$\mathcal{N}(B^0 \to K^+K^-)$	+	$\mathcal{N}(\overline{B}^0 \to K^+K^-)$	107 ± 51
$\mathcal{N}(\Lambda_b^0 \to pK^-)$			270 ± 30
$\mathcal{N}(\overline{\Lambda}_b^0 \to \overline{p}K^+)$			324 ± 31
$\mathcal{N}(\Lambda_b^0 \to p\pi^-)$			242 ± 24
$\mathcal{N}(\overline{\Lambda}_b^0 \to \overline{p}\pi^+)$			206 ± 23

Table 8.3: Yields returned from the fit of composition.

observable	raw
$\hat{\mathcal{A}}_{\mathcal{C}P}(B^0 \to K^+\pi^-) = \frac{\hat{f}_{\overline{B}^0 \to K^-\pi^+} - \hat{f}_{B^0 \to K^+\pi^-}}{\hat{f}_{\overline{B}^0 \to K^-\pi^+} + \hat{f}_{B^0 \to K^+\pi^-}}$	$\mathbf{-0.089 \pm 0.013}$
$\hat{\mathcal{A}}_{\mathcal{C}P}(B_s^0 \to K^-\pi^+) = \frac{\hat{f}_{\overline{B}_s^0 \to K^+\pi^-} - \hat{f}_{B_s^0 \to K^-\pi^+}}{\hat{f}_{\overline{B}_s^0 \to K^+\pi^-} + \hat{f}_{B_s^0 \to K^-\pi^+}}$	$\mathbf{0.226 \pm 0.074}$
$\hat{\mathcal{A}}_{\mathcal{C}P}(\Lambda_b^0 \to p\pi^-) = \frac{\hat{f}_{\overline{\Lambda}_b^0 \to \overline{p}\pi^+} - \hat{f}_{\Lambda_b^0 \to p\pi^-}}{\hat{f}_{\overline{\Lambda}_b^0 \to \overline{p}\pi^+} + \hat{f}_{\Lambda_b^0 \to p\pi^-}}$	$\mathbf{-0.080 \pm 0.074}$
$\hat{\mathcal{A}}_{\mathcal{C}P}(\Lambda_b^0 \to pK^-) = \frac{\hat{f}_{\overline{\Lambda}_b^0 \to \overline{p}K^+} - \hat{f}_{\Lambda_b^0 \to pK^-}}{\hat{f}_{\overline{\Lambda}_b^0 \to \overline{p}K^+} + \hat{f}_{\Lambda_b^0 \to pK^-}}$	$\mathbf{0.089 \pm 0.081}$
$\frac{\hat{f}_{B^0 \to \pi^+\pi^-}}{\hat{f}_{B^0 \to K^+\pi^-}}$	0.264 ± 0.012
$\frac{\hat{f}_{B^0 \to K^+K^-}}{\hat{f}_{B^0 \to K^+\pi^-}}$	0.009 ± 0.004
$\frac{\hat{f}_{B_s^0 \to \pi^+\pi^-}}{\hat{f}_{B^0 \to K^+\pi^-}}$	0.011 ± 0.002
$\frac{\hat{f}_{B_s^0 \to \pi^+\pi^-}}{\hat{f}_{B^0 \to \pi^+\pi^-}}$	0.041 ± 0.009
$\frac{\hat{f}_{B_s^0 \to \pi^+\pi^-}}{\hat{f}_{B_s^0 \to K^+K^-}}$	0.034 ± 0.008
$\frac{\hat{f}_{B_s^0 \to K^-\pi^+}}{\hat{f}_{B^0 \to K^+\pi^-}}$	0.079 ± 0.006
$\frac{\hat{f}_{B_s^0 \to K^-\pi^+}}{\hat{f}_{B_s^0 \to K^+K^-}}$	0.245 ± 0.021
$\frac{\hat{f}_{B_s^0 \to K^+K^-}}{\hat{f}_{B^0 \to K^+\pi^-}}$	0.321 ± 0.013
$\frac{\hat{f}_{\Lambda_b^0 \to pK^-}}{\hat{f}_{B^0 \to K^+\pi^-}}$	0.051 ± 0.003
$\frac{\hat{f}_{\Lambda_b^0 \to p\pi^-}}{\hat{f}_{B^0 \to K^+\pi^-}}$	0.038 ± 0.003
$\frac{\hat{f}_{\Lambda_b^0 \to p\pi^-}}{\hat{f}_{\Lambda_b^0 \to pK^-}}$	0.754 ± 0.080

Table 8.4: Physics observables. The quantities reported in boldface are used to evaluate the final measurements. C-conjugate modes are implied in the lower section of the table.

Table 8.4 reports a significant result for the $\mathcal{A}_{\mathcal{C}P}(B^0 \to K^+\pi^-)$, with statistical uncertainty of order 1.3%, that is comparable with the current measurements from the b-factories, but larger than the one recently reported by LHCb [9]. However, a detailed comparison will be presented in chap. 12, after the evaluation of the systematic uncertainties.

We observed from tab. 8.4 some hints for the presence of the $\mathcal{A}_{\mathcal{C}P}(B_s^0 \to K^-\pi^+)$. A simple estimation of the statistical significance obtained dividing the result of the fit over the statistical uncertainty is of about 3σ; in assumption of non relevant systematic uncertainty, this measurement could become an evidence of $\mathcal{C}P$ violation effect in the B_s^0 system, confirming the first observation recently obtained at LHCb [9]. The significance is discussed after the evaluation of the systematic uncertainties.

The results for the $\mathcal{A}_{\mathcal{C}P}(\Lambda_b^0 \to p\pi^-)$ and $\mathcal{A}_{\mathcal{C}P}(\Lambda_b^0 \to pK^-)$ are the most precise up to date. No hints for the presence of $\mathcal{C}P$ violation in these decay modes are indicated by the results of the fit of tab. 8.4.

The results determined by the fit of composition are in agreement with the values obtained in the previous published version of this analysis, performed on a data sample corresponding to 1 fb^{-1} [88]. The agreement is less satisfactory in the $\mathcal{A}_{\mathcal{C}P}(\Lambda_b^0 \to pK^-)$. However, an accurate comparison takes into account also the systematics. Table 8.5 reports the comparison between the fit results. The statistical uncertainty of physics observables is decreased by a factor ≈ 2. This achievement was possible thanks to an increase in statistics of ≈ 3 and to several improvements introduced in the current analysis: more accurate kinematic (mass and momentum) signal templates, a PID analysis especially made for the $B \to h^+h'^-$ analysis, a more accurate treatment of the physics and combinatorial background model.

Observable	Fit result using 1 fb^{-1}	Fit result using 9 fb^{-1}
$\hat{\mathcal{A}}_{\mathcal{C}P}(B^0 \to K^+\pi^-)$	-0.089 ± 0.025	-0.089 ± 0.013
$\hat{\mathcal{A}}_{\mathcal{C}P}(B_s^0 \to K^-\pi^+)$	0.39 ± 0.15	0.23 ± 0.07
$\hat{\mathcal{A}}_{\mathcal{C}P}(\Lambda_b^0 \to p\pi^-)$	-0.03 ± 0.16	-0.08 ± 0.07
$\hat{\mathcal{A}}_{\mathcal{C}P}(\Lambda_b^0 \to pK^-)$	-0.36 ± 0.15	0.09 ± 0.08

Table 8.5: Comparison of the fit results with the previous published results of this analysis.

8.4 Correlation matrix

The correlation matrix corresponding to the fit of composition is shown: it reports the correlation coefficients, defined as $\rho_{ij} = \mathrm{Cov}(\hat{\theta}_i, \hat{\theta}_j)/\hat{\sigma}_{\hat{\theta}_i}\hat{\sigma}_{\hat{\theta}_j}$, where $\mathrm{Cov}(\hat{\theta}_i, \hat{\theta}_j)$ is the off-diagonal element of the estimated covariance matrix of the fit. The legend for the fit parameters is in third column of tab. 8.2. We looked at this matrix to search for possible large correlations that may suggest a better choice of the fit parameters.

Par.	Global	1	2	3	4	5	6	7	8	9	10	11	13	14	18	21	24	27	29	30	31	39	48	49	52	53
1	0.797	1.000																								
2	0.800	-0.448	1.000																							
3	0.116	-0.020	0.030	1.000																						
4	0.590	-0.112	-0.169	-0.002	1.000																					
5	0.199	0.024	0.013	0.050	-0.125	1.000																				
6	0.480	0.033	-0.049	-0.001	-0.315	0.047	1.000																			
7	0.609	-0.216	-0.150	0.005	-0.097	0.012	-0.042	1.000																		
8	0.455	-0.072	-0.072	0.002	-0.092	0.010	-0.085	0.046	1.000																	
9	0.192	0.005	0.002	0.003	0.006	-0.011	-0.003	-0.003	-0.032	1.000																
10	0.455	0.030	-0.141	-0.002	0.024	-0.009	-0.052	-0.043	-0.262	0.028	1.000															
11	0.278	-0.001	-0.001	0.018	0.004	-0.010	-0.013	0.000	-0.015	-0.182	0.041	1.000														
13	0.309	0.014	0.063	-0.001	-0.031	0.008	-0.054	-0.080	-0.049	0.002	-0.116	-0.007	1.000													
14	0.268	0.019	0.034	0.000	-0.018	0.003	-0.017	-0.068	-0.038	0.000	-0.050	-0.007	0.022	1.000												
18	0.321	-0.064	-0.007	0.056	-0.026	-0.080	0.071	0.002	-0.054	-0.000	-0.011	0.124	0.020	0.003	1.000											
21	0.314	-0.063	-0.009	-0.056	-0.014	0.078	0.063	-0.004	-0.062	-0.006	-0.010	-0.120	0.012	0.005	0.059	1.000										
24	0.194	-0.024	0.008	0.031	-0.016	-0.053	0.049	-0.017	-0.047	-0.003	0.014	0.075	-0.004	0.051	0.055	0.023	1.000									
27	0.186	-0.024	0.007	-0.030	-0.011	0.056	0.051	-0.017	-0.051	-0.001	0.010	-0.070	-0.003	0.044	0.023	0.053	0.009	1.000								
29	0.319	-0.010	-0.056	0.002	0.030	-0.007	0.066	0.025	0.060	-0.002	0.138	0.008	-0.265	-0.020	-0.007	0.000	0.003	0.001	1.000							
30	0.306	-0.024	-0.039	0.000	0.025	-0.003	0.029	0.035	0.070	0.000	0.088	0.011	-0.030	-0.250	-0.014	-0.017	-0.081	-0.066	0.036	1.000						
31	0.721	-0.361	0.555	0.026	-0.294	0.042	-0.042	0.337	0.047	-0.002	-0.099	0.002	0.019	0.005	-0.003	-0.010	-0.002	-0.004	0.002	0.012	1.000					
39	0.488	0.235	0.030	0.000	-0.009	0.003	0.046	-0.077	-0.066	0.005	0.020	0.002	0.008	-0.001	0.013	0.014	0.023	0.021	-0.032	-0.065	-0.031	1.000				
48	0.325	0.105	-0.020	0.000	-0.007	-0.002	-0.092	-0.053	0.118	-0.001	0.139	0.025	-0.077	-0.036	-0.018	-0.026	0.004	0.004	0.093	0.062	-0.026	0.090	1.000			
49	0.779	-0.543	-0.065	-0.001	-0.004	-0.006	-0.065	0.286	0.086	-0.011	-0.062	-0.003	-0.027	-0.009	0.205	0.201	0.084	0.083	0.010	-0.002	0.098	-0.447	-0.199	1.000		
52	0.000	0.000	0.000	0.000	0.000	0.000	0.000	0.000	0.000	0.000	0.000	0.000	0.000	0.000	0.000	0.000	0.000	0.000	0.000	0.000	0.000	0.000	0.000	0.000	1.000	
53	0.000	0.000	0.000	0.000	0.000	0.000	0.000	0.000	0.000	0.000	0.000	0.000	0.000	0.000	0.000	0.000	0.000	0.000	0.000	0.000	0.000	0.000	0.000	0.000	0.000	1.000

Table 8.6: Correlation matrix returned by the fit.

8.5 Fit projections

In order to test the goodness of our fit we compare the distributions of data with the joint p.d.f. corresponding to the Likelihood function evaluated with the maximizing set of parameters $\vec{\theta} = \hat{\vec{\theta}}$. If $\vec{x} = x_1, ..., x_n$ is a generic vector of observables and $\wp(\vec{x}|\vec{\theta})$ is the probability density function of the observables $\vec{x}$ we can define the *projection* onto the observable x_i as the following one-dimensional function:

$$\wp_i(x_i; \vec{\theta}) = \int \wp(\vec{x}|\vec{\theta}) dx_1 ... dx_{i-1} dx_{i+1} ... dx_n, \tag{8.1}$$

which is the predicted distribution for x_i under the assumed values for the fit parameters, and can be overlaid to the experimental data. This allows a way of detecting possible discrepancies between the observed distributions and the model. Distributions of the discriminating observables with fit projections overlaid are shown in fig. 8.1, fig. 8.2 and fig. 8.3. The fit reproduces well all the observed distributions. To better visualize the agreement between the PID discriminating observables and the data we complemented the projections of κ_+ and κ_- with the projections of their linear combination $\kappa_+ + \kappa_-$ and $\kappa_+ - \kappa_-$. As a very accurate check on the method, fig. 8.4 shows the distributions of the average value of $\kappa_{sum} = \kappa_+ + \kappa_-$ and $\kappa_{dif} = \kappa_+ - \kappa_-$ as a function of $m^2_{\pi^+\pi^-}$, with fit projections overlaid. While κ_{sum} distribution shows the absolute scale of the dE/dx response, crucial in disentangling the $B^0 \to \pi^+\pi^-$ from the $B^0_s \to K^+K^-$, the three structures present in the κ_{dif} distribution are produced by the observed uncorrected $\mathcal{C}P$ asymmetries of $B^0 \to K^+\pi^-$, $B^0_s \to K^-\pi^+$ and $\Lambda^0_b \to ph^-$, respectively. If no asymmetry was present, the distribution of the difference would be constant at zero. This allows to check if the fit reproduces well the shape of the correlation function between the dE/dx response of the two particles. We find that the fit reproduces accurately the data both in the central part of the distribution, where the signal is present, and in the tails at lower (higher) values of κ, where the contribution is mainly given by the backgrounds. In particular, fig. 8.5 reports the distributions of the discriminating observables for candidates in the signal region only ($5.17 < m_{\pi^+\pi^-} < 5.33$ GeV/c^2) for a further check on whether the fit properly determines the sample composition below the signal peak. The same kind of check was repeated in the $\Lambda^0_b \to ph^-$ mass region only ($5.3 < m_{\pi^+\pi^-} < 5.6$ GeV/c^2) in fig. 8.6.

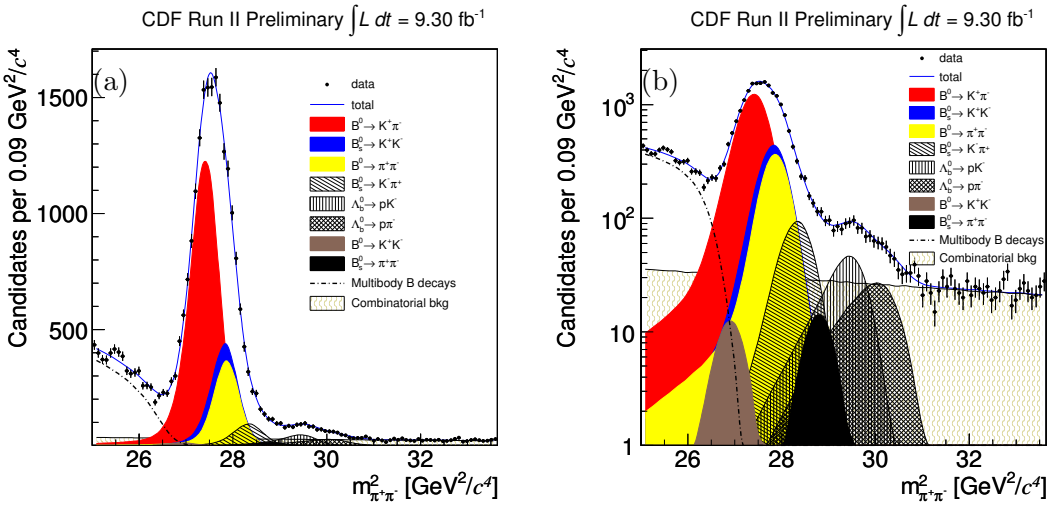

Figure 8.1: Fit projections onto the $m^2_{\pi\pi}$. Linear scale (a) and log scale (b).

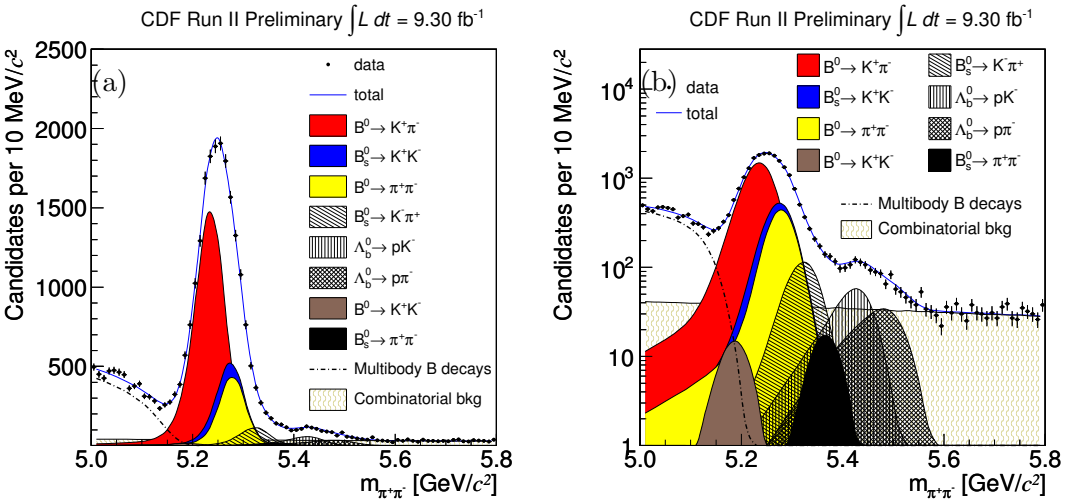

Figure 8.2: Fit projections onto the $m_{\pi^+\pi^-}$. Linear scale (a) and log scale (b).

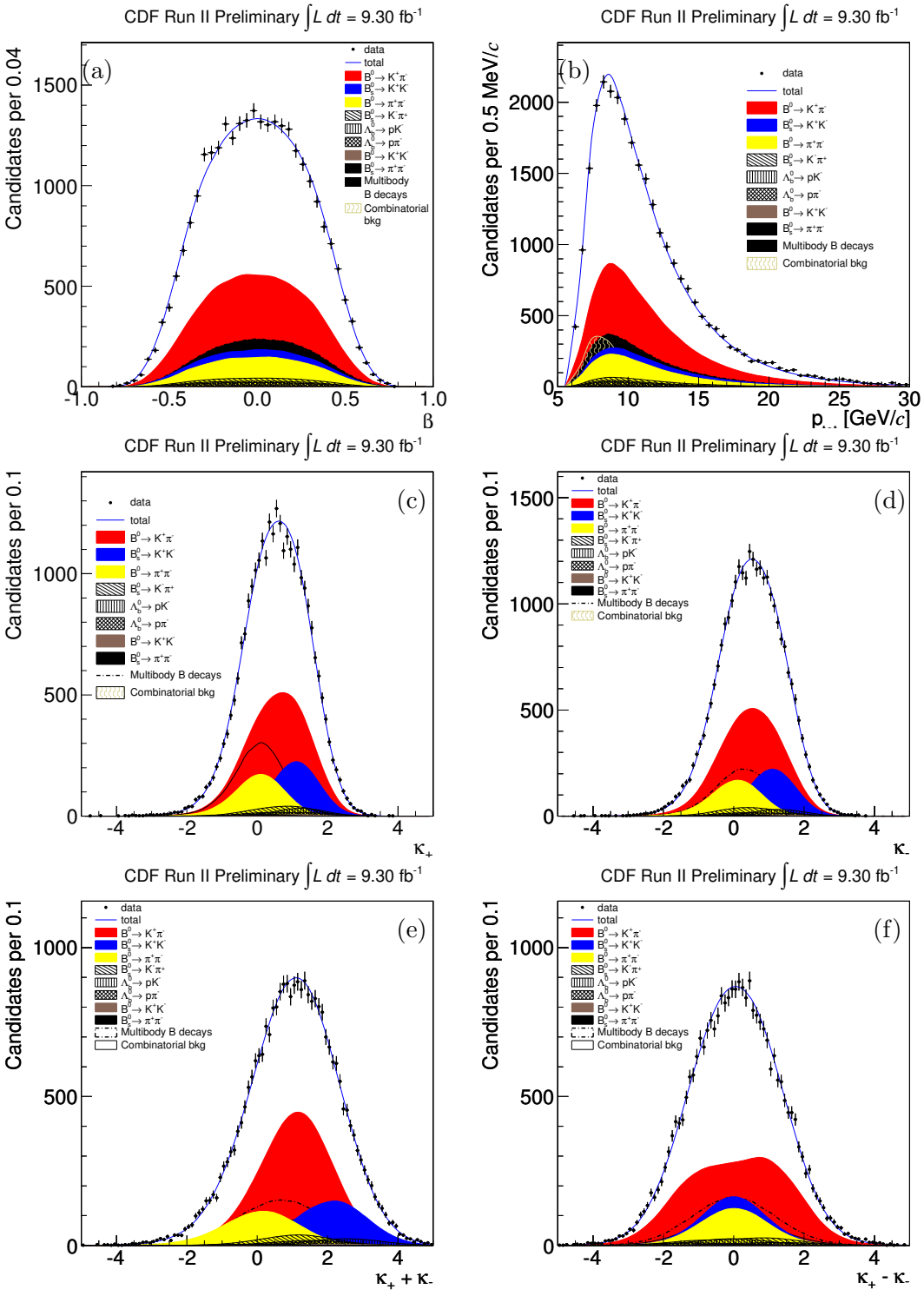

Figure 8.3: Fit projections onto the variables β (a), $p_{\rm tot}$ (b), κ_+ (c), κ_- (d), $\kappa_+ + \kappa_-$ (e), $\kappa_+ - \kappa_-$ (f) in all fit $m_{\pi^+\pi^-}$ range $[5.0, 5.8]$ GeV/c^2.

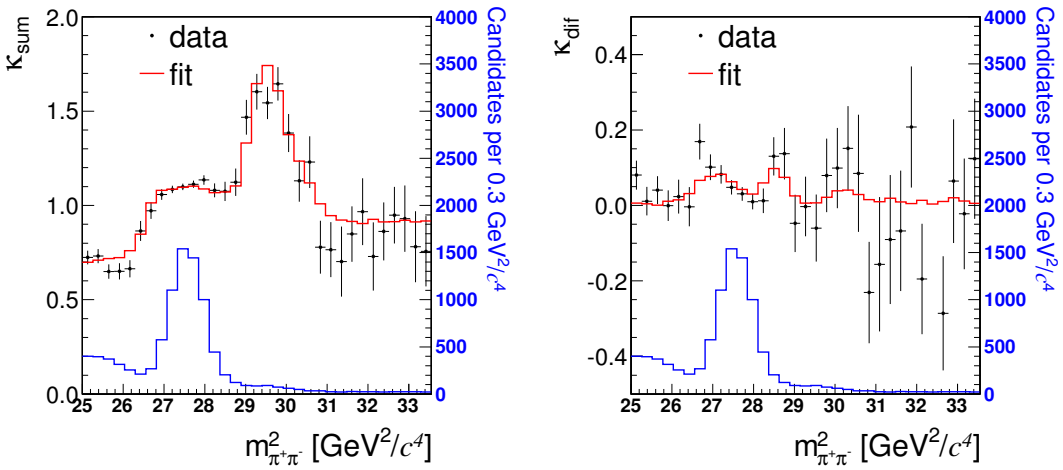

Figure 8.4: Distribution of average value of $\kappa_+ + \kappa_-$ (left) and $\kappa_+ - \kappa_-$ (right) as a function of $m^2_{\pi^+\pi^-}$. The fit function is overlaid. The distribution of $m^2_{\pi^+\pi^-}$ (blue) is superimposed for reference.

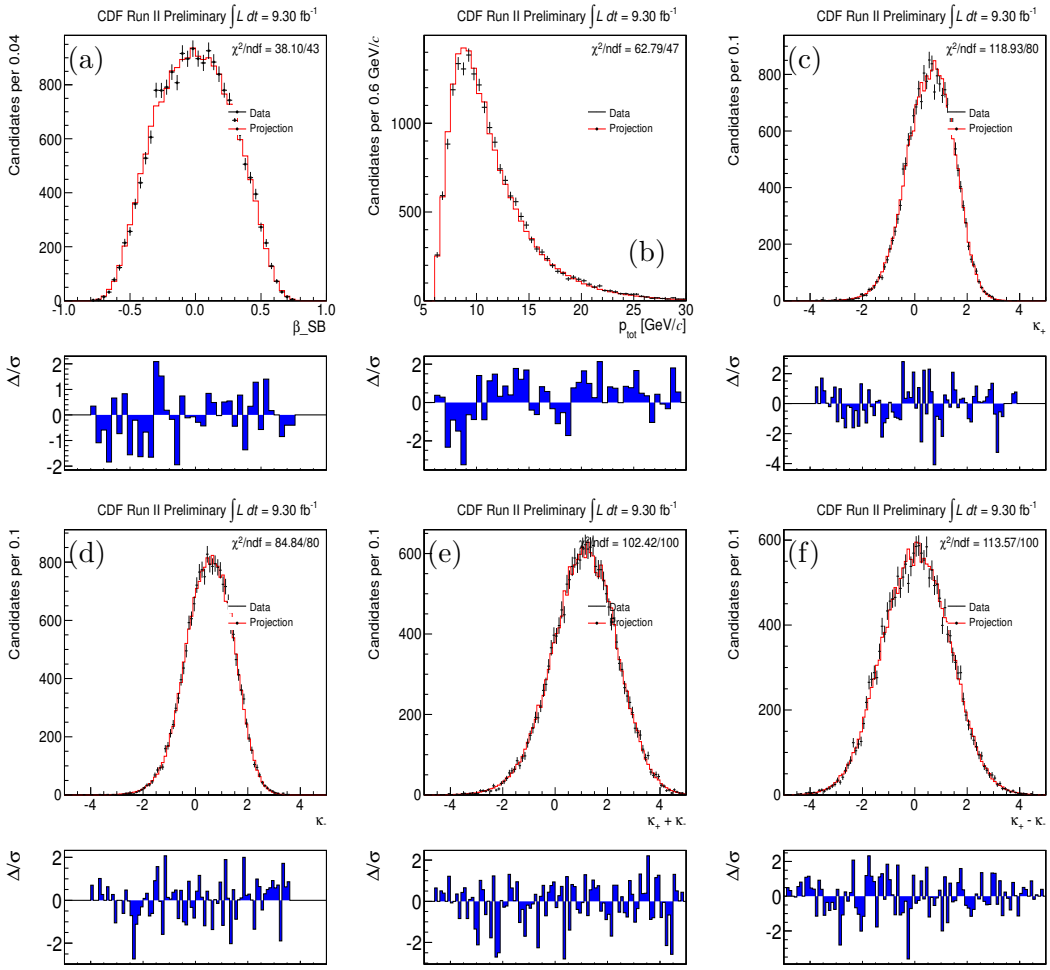

Figure 8.5: Fit projections onto the variables β (a), $p_{\rm tot}$ (b), κ_+ (c), κ_- (d), $\kappa_+ + \kappa_-$ (e), $\kappa_+ - \kappa_-$ (f) in signal mass range $m_{\pi^+\pi^-}$ $[5.17, 5.33]$ GeV/c^2.

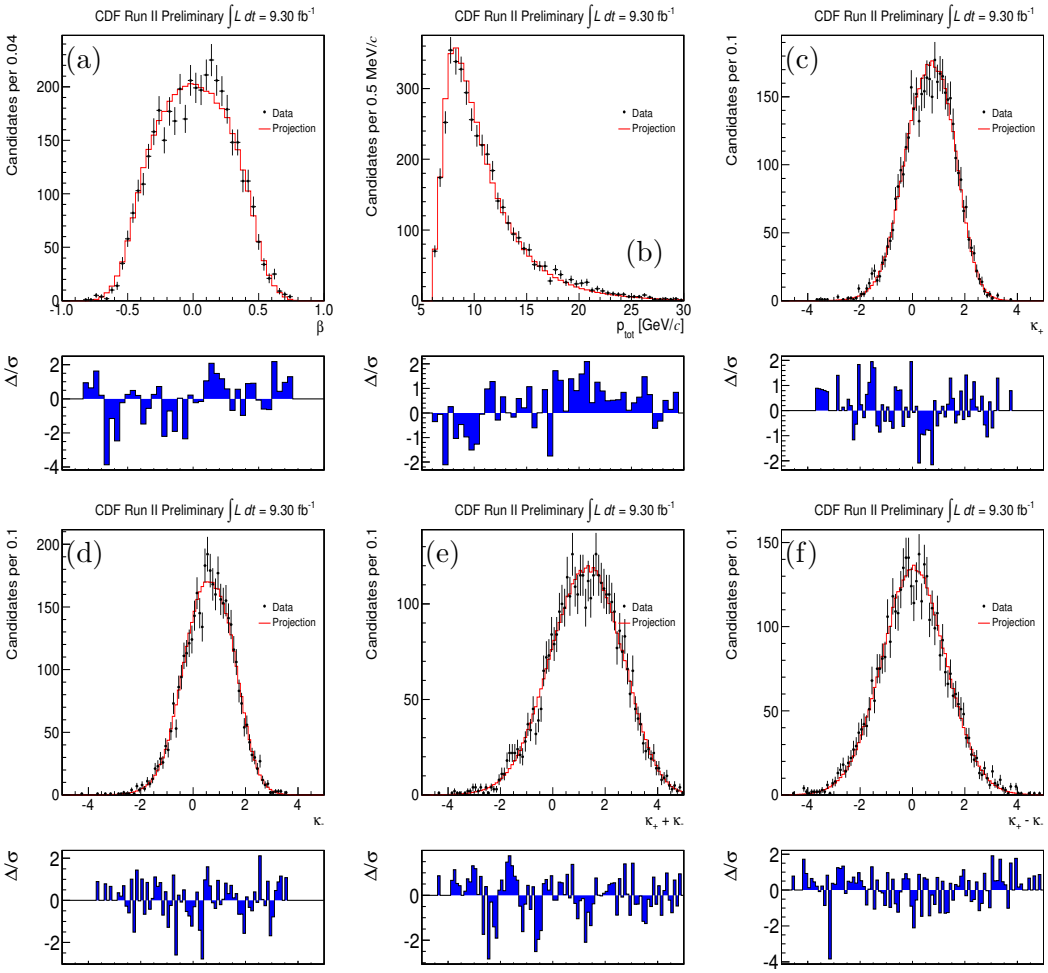

Figure 8.6: Fit projections onto the variables β (a), p_{tot} (b), κ_+ (c), κ_- (d), $\kappa_+ + \kappa_-$ (e), $\kappa_+ - \kappa_-$ (f) in signal mass range $m_{\pi^+\pi^-}$ $[5.3, 5.6]$ GeV/c^2.

8.6 Checks

The fitting code was extensively tested on ensembles of simulated pseudoexperiments of variable size. Additional checks were performed under several configurations of the most critical parameters, such as the contamination of background, absolute scale of the masses, kinematics and PID performance. For the convenience of the reader, when possible we report only the results of the checks made on the full data sample, while we will omit the non relevant checks performed on the sample used for the annihilation decay modes measurements.

8.6.1 Pulls

To investigate the presence of a possible estimation bias, and the stability of the minimization code we studied the the pulls distributions of the fit results. The pull of each fit parameter θ_i is defined as:

$$\mathcal{P}(\theta_i) = \frac{\hat{\theta}_i - \theta_i}{\hat{\sigma}_{\hat{\theta}_i}}, \tag{8.2}$$

where $\hat{\theta}_i$ is the estimate of the parameter, and $\hat{\sigma}_{\hat{\theta}_i}$ is the estimate of its uncertainty. We evaluated the pulls using an ensemble of 500 pseudoexperiments that simulated the experimental circumstance of the fit on $B \to h^+ h'^-$ data. Each pseudoexperiment consisted of the simulated distributions of the five discriminating observables (mass-squared, charge momentum asymmetry, scalar sum of momenta, and dE/dx of both tracks) corresponding to 28,230 total events. The distributions of each signal mode and background component were generated according to the corresponding Likelihood term, using a pseudorandom number generator. The fractions of each signal mode and of background fluctuated from sample to sample according to a poisson distribution with mean the set at true parameters $\vec{\theta}$, while the total number of events fluctuated according to a poisson distribution around the observed number of total events 28,230. We fit the composition of all pseudoexperiments using the same Likelihood function used for the data; we then derived the pull distributions of the relevant physics quantities from the estimated parameters and uncertainties (see fig. 8.7 and fig. 8.8).

The pulls are Gaussian-distributed with approximately unit variance and negligible bias (see tab. 8.7) for each estimated parameter, which is not obvious with finite samples and complicated probability densities. This ensures that the estimated uncertainty of each parameter $\hat{\sigma}_{\hat{\theta}_i}$ to be such that the range $[\hat{\theta}_i - \hat{\sigma}_{\hat{\theta}_i}, \hat{\theta}_i + \hat{\sigma}_{\hat{\theta}_i}]$ contains the true value θ_i with about 68% probability. We observed that the relative fraction and the raw yield of the $B^0 \to K^+K^-$ decays are biased towards positive values. A systematic will be assessed to take into account this effect.

Fit parameter	Pull mean	Pull standard deviation	χ^2/d.o.f.
$\mathcal{A}_{CP}(B^0 \to K^+\pi^-)$	-0.02 ± 0.05	1.04 ± 0.04	14/14
$\mathcal{A}_{CP}(B_s^0 \to K^-\pi^+)$	-0.13 ± 0.05	0.99 ± 0.03	16/14
$\mathcal{A}_{CP}(\Lambda_b^0 \to p\pi^-)$	$+0.00 \pm 0.04$	0.90 ± 0.03	10/11
$\mathcal{A}_{CP}(\Lambda_b^0 \to pK^-)$	$+0.07 \pm 0.05$	0.99 ± 0.03	15/13
$f_{B_s^0\to\pi^+\pi^-}/f_{B^0\to K^+\pi^-}$	-0.07 ± 0.05	1.06 ± 0.04	13/16
$f_{B^0\to K^+K^-}/f_{B^0\to K^+\pi^-}$	$+0.28 \pm 0.05$	0.97 ± 0.03	16/14
$\mathcal{N}_{B_s^0\to\pi^+\pi^-}$	$+0.06 \pm 0.04$	0.93 ± 0.03	13/11
$\mathcal{N}_{B^0\to K^+K^-}$	$+0.23 \pm 0.05$	1.05 ± 0.04	4/10

Table 8.7: Results of the Gaussian fit of the pull distributions for the $\mathcal{A}_{CP}$ (top section) and $B_s^0 \to \pi^+\pi^-$ and $B^0 \to K^+K^-$ measurements (bottom section) results. The pulls for the annihilation modes are obtained with the same methods explained in sec. 8.6.1.

8.6.2 Additional fits

We performed some additional fits of the $B \to h^+h'^-$ data sample, and we compared them with our central results of tab. 8.2.

	central	resol	resol cutoff opt
$\hat{f}_{B^0\to\pi^+\pi^-}$	0.149 ± 0.006	0.149 ± 0.006	0.149 ± 0.006
$\hat{f}_{B^0\to K^+\pi^-}$	0.563 ± 0.007	0.571 ± 0.008	0.571 ± 0.008
$\frac{\hat{f}_{\overline{B}^0\to K^-\pi^+} - \hat{f}_{B^0\to K^+\pi^-}}{\hat{f}_{\overline{B}^0\to K^-\pi^+} + \hat{f}_{B^0\to K^+\pi^-}}$	-0.089 ± 0.013	-0.089 ± 0.013	-0.089 ± 0.013
$\hat{f}_{B^0\to K^+K^-}$	0.005 ± 0.002	0.003 ± 0.003	0.003 ± 0.003
$\hat{f}_{B_s^0\to\pi^+\pi^-}$	0.006 ± 0.001	0.006 ± 0.001	0.006 ± 0.001
$\hat{f}_{B_s^0\to K^-\pi^+}$	0.044 ± 0.003	0.040 ± 0.004	0.040 ± 0.004
$\frac{\hat{f}_{\overline{B}_s^0\to K^+\pi^-} - \hat{f}_{B_s^0\to K^-\pi^+}}{\hat{f}_{\overline{B}_s^0\to K^+\pi^-} + \hat{f}_{B_s^0\to K^-\pi^+}}$	0.226 ± 0.074	0.243 ± 0.082	0.245 ± 0.082
$\hat{f}_{B_s^0\to K^+K^-}$	0.181 ± 0.006	0.181 ± 0.006	0.181 ± 0.006
$\hat{f}_{\Lambda_b^0\to p\pi^-}$	0.022 ± 0.002	0.022 ± 0.002	0.022 ± 0.002
$\frac{\hat{f}_{\overline{\Lambda}_b^0\to\overline{p}\pi^+} - \hat{f}_{\Lambda_b^0\to p\pi^-}}{\hat{f}_{\overline{\Lambda}_b^0\to\overline{p}\pi^+} + \hat{f}_{\Lambda_b^0\to p\pi^-}}$	-0.080 ± 0.074	-0.077 ± 0.074	-0.077 ± 0.074
$\hat{f}_{\Lambda_b^0\to pK^-}$	0.029 ± 0.002	0.029 ± 0.002	0.029 ± 0.002
$\frac{\hat{f}_{\overline{\Lambda}_b^0\to\overline{p}K^+} - \hat{f}_{\Lambda_b^0\to pK^-}}{\hat{f}_{\overline{\Lambda}_b^0\to\overline{p}K^+} + \hat{f}_{\Lambda_b^0\to pK^-}}$	0.089 ± 0.081	0.090 ± 0.083	0.090 ± 0.083
resol	1. (fixed)	1.045 ± 0.014	1.053 ± 0.014
cut-off	26.64 GeV$^2/c^4$	26.64 GeV$^2/c^4$	26.61 GeV$^2/c^4$

Table 8.8: Top table: comparisons between the central fit, the equivalent fit where a global resolution scale factor has been left free to vary in the fit (resol) and the equivalent fit where a global resolution scale factor has been left free to vary in the fit and the cut off value was optimized using the procedure described in sec. 8.3.

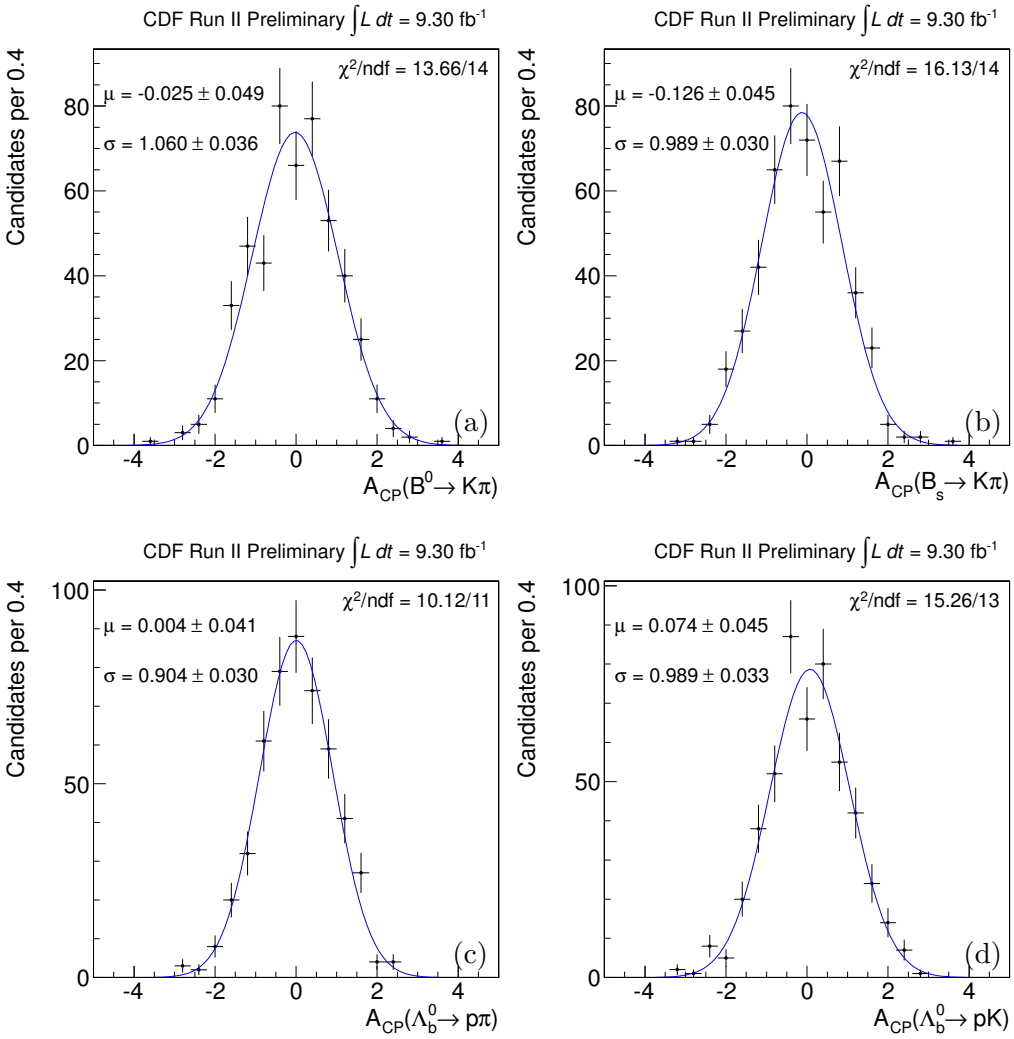

Figure 8.7: Distribution of the pulls of the quoted fit parameters: (a) $\mathcal{A}_{CP}(B^0 \to K^+\pi^-)$, (b) $\mathcal{A}_{CP}(B_s^0 \to K^-\pi^+)$, (c) $\mathcal{A}_{CP}(\Lambda_b^0 \to p\pi^-)$, and (d) $\mathcal{A}_{CP}(\Lambda_b^0 \to pK^-)$. Results of χ^2-fits to Gaussian functions are overlaid in blue.

Mass resolution scale factor (resol)

In the central analysis we scaled the mass resolution extracted from the simulation by a factor obtained from $D^0 \to h^+h'^-$. This has been done to keep into account the observed discrepancy between data and simulation, as described in sec. 4.2.3. To check the correctness of our procedure, we added in the fit an additional free parameter: a global scale factor of the mass resolution which is in common for all signal decays. The value returned from our fit for this parameter is $\sigma = 1.045 \pm 0.014$; while the values for the other parameters are reported on tab. 8.8. The likelihood value at the minimum is $-2\log(\mathscr{L}) = -85382.33$ which is better than 13 units with respect to the central fit having $-2\log(\mathscr{L}) = -85368.98$. This difference has

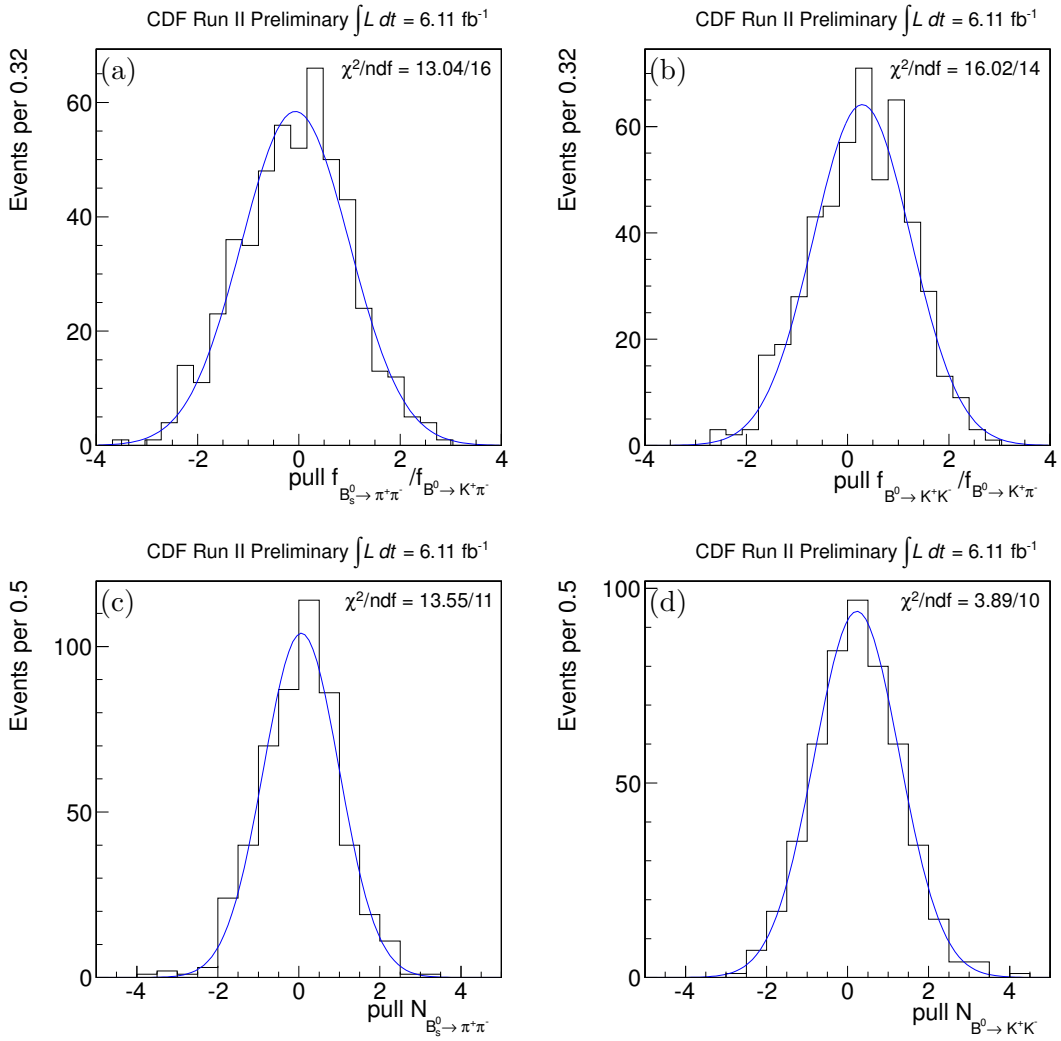

Figure 8.8: Distribution of the pulls of the quoted fit parameters: (a) $f_{B_s^0\to\pi^+\pi^-}/f_{B^0\to K^+\pi^-}$, (b) $f_{B^0\to K^+K^-}/f_{B^0\to K^+\pi^-}$, (c) $\mathcal{N}_{B_s^0\to\pi^+\pi^-}$, and (d) $\mathcal{N}_{B^0\to K^+K^-}$. Results of χ^2-fits to Gaussian functions are overlaid in red.

been ascribed to the sensitivity of the fit to the mass distribution near the regions corresponding to the falling down of the $B^0 \to K^+\pi^-$ decay mode: at lower mass near 5.16 GeV/c^2, corresponding to the cut-off of the distribution describing the physics background, and at higher mass near 5.35 GeV/c^2, in presence of the $B_s^0 \to K^-\pi^+$ signal peak. In these regions, the fitter could be sensitive to small changes of the distributions. To verify this assumption, we performed 400 additional fits where the cut-off was optimized using the procedure described in sec. 8.3. The minimum of the $-2\log(\mathscr{L})$ profile obtained indicates a scaling factor of $\sigma = 1.053 \pm 0.014$ and a cut-off value $m_0^2 = 26.61$ GeV$^2/c^4$, different from the nominal $m_{\rm A}^2 = 26.64$ GeV$^2/c^4$ used in the fit. These results seems to indicate a small sensitivity of the fitter to the mass distributions, and support our choice of evaluating the scaling

	central	A	C
$\hat{f}_{B^0\to\pi^+\pi^-}$	0.149 ± 0.006	0.145 ± 0.007	0.150 ± 0.010
$\hat{f}_{B^0\to K^+\pi^-}$	0.563 ± 0.007	0.564 ± 0.009	0.570 ± 0.012
$\frac{\hat{f}_{\overline{B}^0\to K^-\pi^+} - \hat{f}_{B^0\to K^+\pi^-}}{\hat{f}_{\overline{B}^0\to K^-\pi^+} + \hat{f}_{B^0\to K^+\pi^-}}$	−0.089 ± 0.013	−0.085 ± 0.017	−0.095 ± 0.023
$\hat{f}_{B^0\to K^+K^-}$	0.005 ± 0.002	0.008 ± 0.003	0.001 ± 0.004
$\hat{f}_{B^0_s\to\pi^+\pi^-}$	0.006 ± 0.001	0.006 ± 0.002	0.007 ± 0.002
$\hat{f}_{B^0_s\to K^-\pi^+}$	0.044 ± 0.003	0.042 ± 0.004	0.051 ± 0.006
$\frac{\hat{f}_{\overline{B}^0_s\to K^+\pi^-} - \hat{f}_{B^0_s\to K^-\pi^+}}{\hat{f}_{\overline{B}^0_s\to K^+\pi^-} + \hat{f}_{B^0_s\to K^-\pi^+}}$	0.226 ± 0.074	0.195 ± 0.095	0.242 ± 0.112
$\hat{f}_{B^0_s\to K^+K^-}$	0.181 ± 0.006	0.182 ± 0.007	0.174 ± 0.010
$\hat{f}_{\Lambda^0_b\to p\pi^-}$	0.022 ± 0.002	0.025 ± 0.002	0.016 ± 0.002
$\frac{\hat{f}_{\overline{\Lambda}^0_b\to\overline{p}\pi^+} - \hat{f}_{\Lambda^0_b\to p\pi^-}}{\hat{f}_{\overline{\Lambda}^0_b\to\overline{p}\pi^+} + \hat{f}_{\Lambda^0_b\to p\pi^-}}$	−0.080 ± 0.074	−0.017 ± 0.084	−0.239 ± 0.143
$\hat{f}_{\Lambda^0_b\to pK^-}$	0.029 ± 0.002	0.028 ± 0.002	0.030 ± 0.003
$\frac{\hat{f}_{\overline{\Lambda}^0_b\to\overline{p}K^+} - \hat{f}_{\Lambda^0_b\to pK^-}}{\hat{f}_{\overline{\Lambda}^0_b\to\overline{p}K^+} + \hat{f}_{\Lambda^0_b\to pK^-}}$	0.089 ± 0.081	-0.015 ± 0.107	0.226 ± 0.123

Table 8.9: Top table: comparisons between the central fit, the equivalent fit performed only on `med` events and the equivalent fit performed only on the esclusive `high` events.

factor using an independent $D^0 \to h^+h^{'-}$ sample.

Separate fits on the `A` data sample and the `C` data sample

Table 8.9 reports the comparison between the central fit and a fits performed on the `A` data sample and the `C` sample. The agreement between fits is very good, offering a good cross check that the samples and their different kinematics have been modeled correctly. This ensures that the simultaneous fit correctly combines information from the two scenarios.

Kinematic-only fit (kine)

We performed a fit of composition using only the kinematic information, by turning off the PID information in the Likelihood function: we used only the information from the variables $m_{\pi^+\pi^-}$, β and $p_{\rm tot}$. Since the PID information (contained in κ_+ and κ_- variables) and kinematics are crucial independent ingredients of the analysis, we want to check for possible disagreements between these two informations.

Table 8.10 reports the comparison between the fits with the method explained above, and the agreement obtained is satisfactory. Without the PID information the fit of composition loses much separation power in disentangling among the signal components. In particular, using only the kinematic information it is very difficult to separate the $B^0 \to \pi^+\pi^-$ and $B^0_s \to K^+K^-$ modes, which are very similar kinematically, and to obtain precise $\mathcal{C}P$ measurements. In addition, it is very difficult to disentangle the $B^0_s \to \pi^+\pi^-$ and $B^0 \to K^+K^-$ modes from the

	central	kine
$\hat{f}_{B^0\to\pi^+\pi^-}$	0.149 ± 0.006	0.159 ± 0.021
$\hat{f}_{B^0\to K^+\pi^-}$	0.563 ± 0.007	0.573 ± 0.012
$\frac{\hat{f}_{\overline{B}^0\to K^-\pi^+} - \hat{f}_{B^0\to K^+\pi^-}}{\hat{f}_{\overline{B}^0\to K^-\pi^+} + \hat{f}_{B^0\to K^+\pi^-}}$	−0.089 ± 0.013	−0.150 ± 0.029
$\hat{f}_{B^0\to K^+K^-}$	0.005 ± 0.002	0.027 ± 0.007
$\hat{f}_{B^0_s\to\pi^+\pi^-}$	0.006 ± 0.001	0.001 ± 0.003
$\hat{f}_{B^0_s\to K^-\pi^+}$	0.044 ± 0.003	0.035 ± 0.005
$\frac{\hat{f}_{\overline{B}^0_s\to K^+\pi^-} - \hat{f}_{B^0_s\to K^-\pi^+}}{\hat{f}_{\overline{B}^0_s\to K^+\pi^-} + \hat{f}_{B^0_s\to K^-\pi^+}}$	0.226 ± 0.074	0.559 ± 0.024
$\hat{f}_{B^0_s\to K^+K^-}$	0.181 ± 0.006	0.148 ± 0.017
$\hat{f}_{\Lambda^0_b\to p\pi^-}$	0.022 ± 0.002	0.021 ± 0.002
$\frac{\hat{f}_{\overline{\Lambda}^0_b\to\overline{p}\pi^+} - \hat{f}_{\Lambda^0_b\to p\pi^-}}{\hat{f}_{\overline{\Lambda}^0_b\to\overline{p}\pi^+} + \hat{f}_{\Lambda^0_b\to p\pi^-}}$	−0.080 ± 0.074	−0.011 ± 0.109
$\hat{f}_{\Lambda^0_b\to pK^-}$	0.029 ± 0.002	0.027 ± 0.003
$\frac{\hat{f}_{\overline{\Lambda}^0_b\to\overline{p}K^+} - \hat{f}_{\Lambda^0_b\to pK^-}}{\hat{f}_{\overline{\Lambda}^0_b\to\overline{p}K^+} + \hat{f}_{\Lambda^0_b\to pK^-}}$	0.089 ± 0.081	0.007 ± 0.117

Table 8.10: Comparisons between the central fit, the equivalent fit that uses only the kinematic information (kine).

other signals. The fits are however in good agreement, providing another cross check of the correctness of the procedures.

8.7 Probability ratio plots

The fit of composition disentangles the individual signal components by combining kinematics ($m^2_{\pi\pi}$, β, $p_{\rm tot}$) and PID (κ_+, κ_-) information. It is useful to visualize the effective total separation power of the fit. This can be done by looking at the *probability ratio* variable:

$$\mathcal{PR} = \frac{\wp_{B^0\to K^+\pi^-}}{\wp_{B^0\to K^+\pi^-} + \wp_{\overline{B}^0\to K^-\pi^+}}, \tag{8.3}$$

where $\wp_{B^0\to K^+\pi^-}$ and $\wp_{\overline{B}^0\to K^-\pi^+}$ are the total p.d.f. respectively for the $B^0 \to K^+\pi^-$ and $\overline{B}^0 \to K^-\pi^+$ modes, and they are functions of the complete set of observables $(m^2_{\pi^+\pi^-}, \beta, p_{\rm tot}, \kappa_+, \kappa_-)$. $\mathcal{PR}$ takes values within the interval $[0, 1]$. If we evaluate this variable with an event of $B^0 \to K^+\pi^-$ $\mathcal{PR}$ has a high probability to be close to 1, while if we take an event of $\overline{B}^0 \to K^-\pi^+$ $\mathcal{PR}$ tends to 0. Any other event is distributed between 0 and 1. The probability ratio is a function of the discriminating observables, then we can plot its distribution obtained using the fitted data sample and also the distribution obtained by generating signals and

background events directly from the total p.d.f.s of the fit of composition. Visualization of these plots allows to put into evidence possible discrepancies between the fit model and the distribution of the actual data. Figure 8.9 shows the comparison between the distribution of $\mathcal{PR}$ obtained from the data (point with error bars) ad the distribution of $\mathcal{PR}$ obtained by generating events with the p.d.f.s of the fit of composition. The different colors of the histogram show how the events of $B^0 \to K^+\pi^-$ (red), $\overline{B}^0 \to K^-\pi^+$ (blue), other signals and background (yellow) are distributed in the variable $\mathcal{PR}$. The agreement between data distribution and projection is satisfactory. In addition it is possible to visualize the sizable effective separation power between $B^0 \to K^+\pi^-$ and $\overline{B}^0 \to K^-\pi^+$ which allows to perform a precision measurement of the direct CP asymmetry $\mathcal{A}_{\mathcal{C}P}(B^0 \to K^+\pi^-)$. The same procedure can be repeated for any two signal components S_1 and S_2:

$$\mathcal{PR}_{S_1S_2} = \frac{\wp_{S_1}}{\wp_{S_1} + \wp_{S_2}} \tag{8.4}$$

$$\tag{8.5}$$

$\wp_{S_1}$ and $\wp_{S_2}$ are the total p.d.f.s respectively for the signal component S_1 and S_2.

The probability ratio is also a very instructive variable to visualize the separation power of the fit between a signal S_1 and all the other signals $S_2, S_3, ..., S_N$ plus all backgrounds, that we will indicate with the label "rest". We can define:

$$\mathcal{PR}_{S_1\text{rest}} = \frac{\wp_{S_1}}{\wp_{S_1} + \wp_{\text{rest}}}. \tag{8.6}$$

where $\wp_{S_1}$ is the total p.d.f. for the signal component S_1, while $\wp_{\text{rest}}$ is the sum of the total p.d.f.s of all other signals except S_1 plus the total p.d.f.s of all backgrounds. Each term of the $\wp_{\text{rest}}$ sum is weighted with the relative fraction estimated by the fit of composition without the contribution of the signal S_1. $\mathcal{PR}$ takes values within the interval $[0, 1]$. If we evaluate this variable with an event of the signal component S_1 $\mathcal{PR}$ has a high probability to be close to 1. Any other event is distributed between 0 and 1. Figure 8.10 shows the comparison between the data distribution and the projection of the probability ratio in different cases. The agreement obtained is satisfactory. This fig. 8.10 diplays also the individual contributions of each components (stacked) from other components. Several components are visible in the region close to $\mathcal{PR} = 1$, but they spread all over the $\mathcal{PR}$ interval [0,1], while $B_s^0 \to \pi^+\pi^-$ and $B^0 \to K^+K^-$ are the only component that peaks sharply at the end of the distributions, being mostly confined to the last two bins. It is indeed this segregation that allows us to obtain a clear result: $B_s^0 \to \pi^+\pi^-$ cannot be replaced by an increase of the size of any other component. Figure 8.10 is also a rough pictorial representation of the significance of the $B_s^0 \to \pi^+\pi^-$ and $B^0 \to K^+K^-$ decay modes.

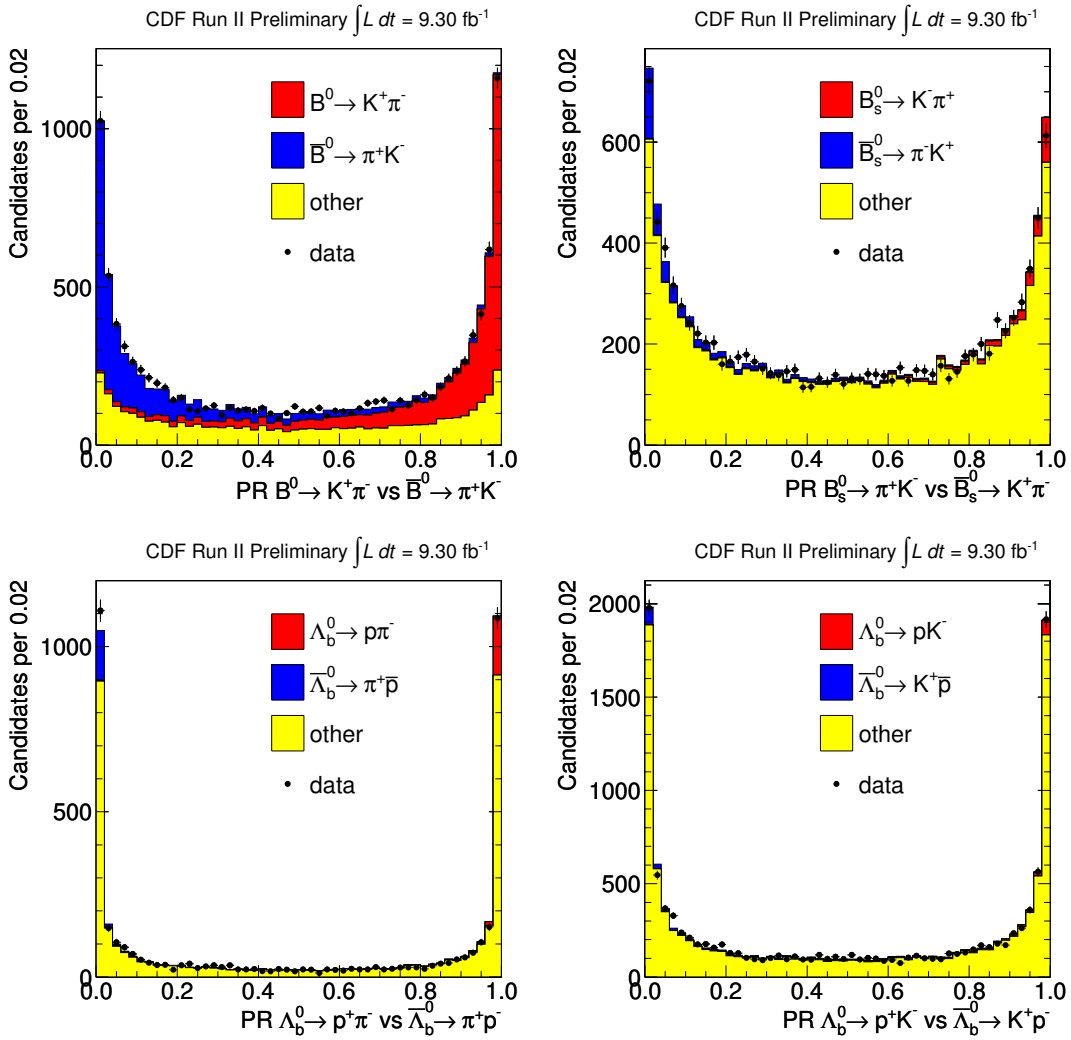

Figure 8.9: Distribution of the probability ratio ($\mathcal{PR}$) in the signal mass region ($5.22 < m_{\pi^+\pi^-} < 5.28$ GeV/c^2 for the $B^0 \to K^+\pi^-$, $5.25 < m_{\pi^+\pi^-} < 5.4$ GeV/c^2 for the $B_s^0 \to K^-\pi^+$, $5.3 < m_{\pi^+\pi^-} < 5.6$ GeV/c^2 for the $\Lambda_b^0 \to p\pi^-$, and $5.25 < m_{\pi^+\pi^-} < 5.55$ GeV/c^2 $\Lambda_b^0 \to pK^-$). The points with the error bars show the distribution obtained on the fitted data sample while the histogram shows the distributions obtained by generating signals and background events directly from the total p.d.f.s of the fit of composition.

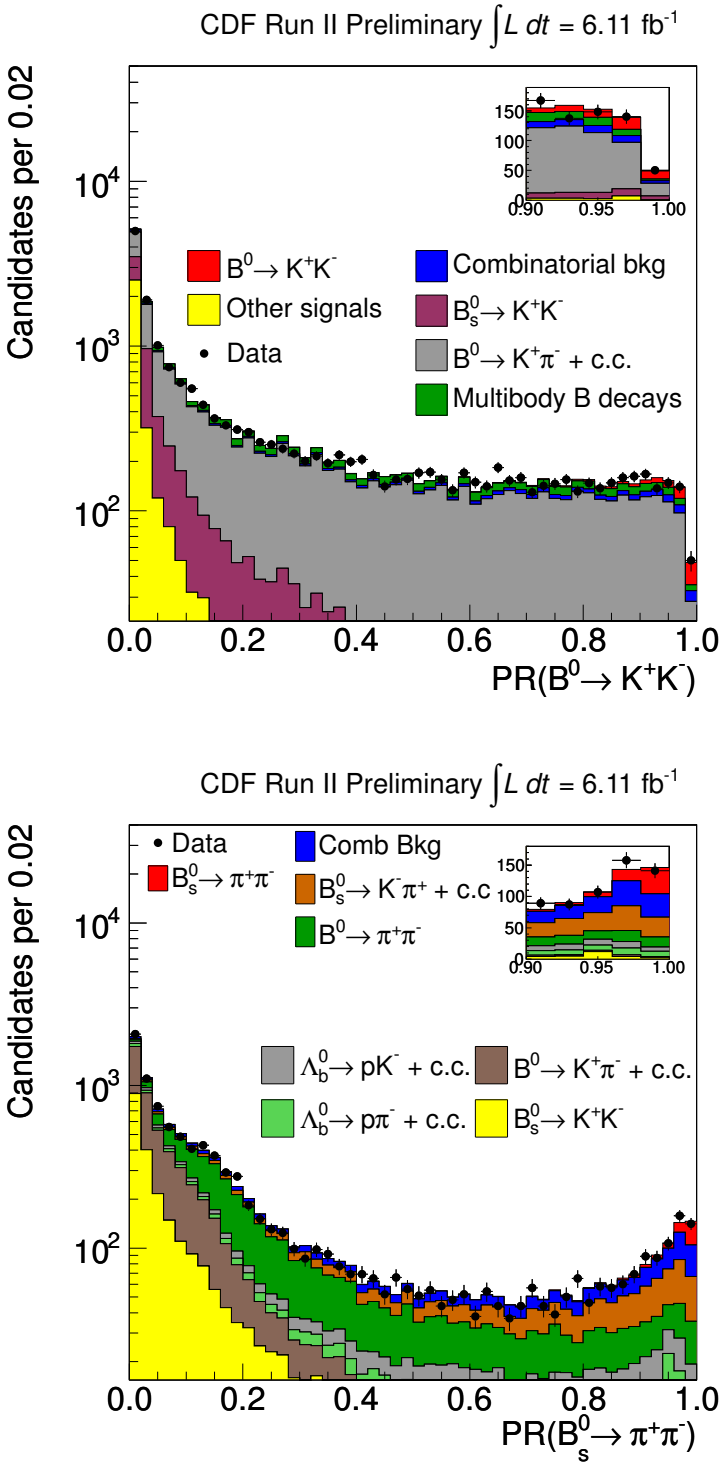

Figure 8.10: Distribution of the probability ratio ($\mathcal{PR}$) where the individual contributions of each components are stacked, for the $B^0 \to K^+K^-$ (top) and the $B_s^0 \to \pi^+\pi^-$ (bottom). The points with the error bars show the distribution obtained on the fitted data sample while the histogram shows the distributions obtained by generating signals and background events directly from the total p.d.f.s of the fit of composition.

Chapter 9

Measurement of relative efficiency corrections

In order to translate the parameters returned from the fit of composition into physics measurements of branching fractions we need to apply the corrections for different efficiency of the selection for the various decay modes. This chapter is devoted to the evaluation of these efficiency corrections extracted from real data.

9.1 Efficiency correction

In order to translate the results returned from the fit of composition into measurements of relative branching fractions we need to apply corrections for the relative efficiencies of the selection between the various decay modes. For each channel, the fraction output by the fit must be corrected by an efficiency factor ε. Below we show how the efficiency corrections are applied to the results determined by the fit.

$$\begin{aligned} \frac{\mathcal{B}(B^0 \to K^+K^-)}{\mathcal{B}(B^0 \to K^+\pi^-)} &= \frac{\hat{f}_{B^0\to K^+K^-}}{\hat{f}_{B^0\to K^+\pi^-}} \cdot \frac{\varepsilon(B^0 \to K\pi)}{\varepsilon(B^0 \to KK)} \\ \frac{f_s}{f_d} \times \frac{\mathcal{B}(B_s^0 \to \pi^+\pi^-)}{\mathcal{B}(B^0 \to K^+\pi^-)} &= \frac{\hat{f}_{B_s^0\to \pi^+\pi^-}}{\hat{f}_{B^0\to K^+\pi^-}} \cdot \frac{\varepsilon(B^0 \to K\pi)}{\varepsilon(B_s^0 \to \pi\pi)} \end{aligned}$$

The notation $\varepsilon(B^0_{(s)} \to hh')$, where the particles in the final state are labeled without the charge, indicates the CP-averaged efficiency for the decay $B^0_{(s)} \to h^+h'^-$. The total reconstruction efficiency ε used in the above relations factorizes as the product of three terms:

$$\varepsilon = \varepsilon_{\rm kin} \cdot c_{\rm XFT} \cdot \varepsilon_{\rm iso}. \tag{9.1}$$

$\boldsymbol{\varepsilon_{\rm kin}}$ — this is the reconstruction efficiency (trigger and offline cuts). This term mostly accounts for the acceptance effects. It includes the trigger efficiency

and the efficiency of the off-line reconstruction and selection. We extract the kinematic efficiency from Monte Carlo simulation. Any geometric acceptance effect is properly taken into account, since the simulation reproduces the kinematic distributions of the decays and it includes an accurate description of the detector geometry. This term does not include the contribution of the isolation requirement and of tracking efficiency which are treated separately.

$c_{\mathbf{XFT}}$ — this correction takes into account detector-induced charge asymmetries between positively and negatively charged particles in the detectors. They are mainly due to the relative efficiency of the XFT on charged kaons and pions, which is not accurately reproduced by the CDF Monte Carlo, and to the COT cell-geometry.

$\varepsilon_{\mathbf{iso}}$ — this is the efficiency that a signal event satisfies the isolation cut. It was determined from real data and it depends only on the initial meson type $\varepsilon_{\rm iso}(B^0_{(s)} \to h^+h'^-) = \varepsilon_{\rm iso}(B^0_{(s)})$. This is due to the fact that our Monte Carlo does not simulate the underlying event, but only the signal, as explained in chap. 4.

9.1.1 Kinematic efficiencies

In order to evaluate the total reconstruction efficiency $\varepsilon_{\rm kin}$ we used the realistic simulation described in chap. 4. The CP-averaged kinematic efficiency, for each signal mode $B^0_{(s)} \to h^+h'^-$, is defined as the ratio between the number of events passing the selection ($N_{\rm passing}$) and the number of events initially generated by the simulation ($N_{\rm generation}$):

$$\varepsilon_{\rm kin} = \frac{N_{\rm passing}}{N_{\rm generation}}. \tag{9.2}$$

Using simulated samples is reliable for this purpose. The effects contributing to the kinematic efficiency are well reproduced by the simulation and are similar among all the signal modes. Any possible small systematic discrepancy between real data and the simulation vanishes in the efficiency ratio between two different modes. The kinematic efficiency corrections extracted from the simulation are :

$$\frac{\varepsilon_{\rm kin}(B^0 \to K\pi)}{\varepsilon_{\rm kin}(B^0 \to KK)} = 1.065 \pm 0.003 \text{ (MC)} \tag{9.3}$$

$$\frac{\varepsilon_{\rm kin}(B^0 \to K\pi)}{\varepsilon_{\rm kin}(B^0_s \to \pi\pi)} = 0.946 \pm 0.003 \text{ (MC)} \tag{9.4}$$

$$\tag{9.5}$$

The uncertainty referred as (MC) is due to the finite statistics of the simulated samples used to estimate the kinematic efficiency $\varepsilon_{\rm kin}$ and it corresponds to the Poisson fluctuation of the number of events passing the selection. This uncertainty will be used to evaluate the relative associated systematics (see chap. 11).

9.1.2 Trigger bias corrections

A separate correction is needed to account for the different XFT efficiency to reconstruct charged kaons and pions. This is due to the different specific ionization of pions and kaons in the COT volume [116, 121]. In the typical momentum range of the $B^0_{(s)} \to h^+h'^-$ decay products, charged pions (with typical Lorentz boost $\beta\gamma \approx 15$) ionize more than charged kaons ($\beta\gamma \approx 4$). The consequence is a larger pulse width of pions than of kaons and, as a consequence a larger hit multiplicity of the pions in the COT. The requirement of the XFT on the minimum number of axial COT hits reflects in a different trigger efficiency for kaons than for pions. This introduces different relative efficiencies between the $B^0_{(s)} \to h^+h'^-$ modes with different number of kaons and pions in the final state. This effect is not reproduced by the CDF II simulation, and was instead measured by a study on pions and kaons from $D^0 \to h^+h'^-$ decays. Using the huge sample of $D^0 \to h^+h'^-$ events from $D^* \to D^0\pi$ decays available at CDF, we measured the efficiency ratio $\varepsilon(D^0 \to \pi^+\pi^-)/\varepsilon(D^0 \to K^-\pi^+)$ from data as follows:

$$\left.\frac{\varepsilon(D^0 \to \pi^+\pi^-)}{\varepsilon(D^0 \to K^-\pi^+)}\right|_{\text{data}} = \left.\frac{N(D^0 \to \pi^+\pi^-)}{N(D^0 \to K^-\pi^+)}\right|_{\text{data}} \cdot \frac{\mathcal{B}(D^0 \to K^-\pi^+)}{\mathcal{B}(D^0 \to \pi^+\pi^-)} \tag{9.6}$$

where $\frac{\mathcal{B}(D^0\to K^-\pi^+)}{\mathcal{B}(D^0\to\pi^+\pi^-)}$ is taken from pdg [51], and the signal yields of $D^0 \to \pi^+\pi^-$ and $D^0 \to K^-\pi^+$ are extracted from a binned χ^2-fit on the invariant $D^0\pi$-mass distributions, as shown in fig. 9.1. For signals and backgrounds we used the templates described in [118].

The reconstruction efficiency extracted in such a way can be compared to the same quantity estimated from the CDF simulation:

$$\left.\frac{\varepsilon(D^0 \to \pi^+\pi^-)}{\varepsilon(D^0 \to K^-\pi^+)}\right|_{\text{MC}} = \left.\frac{N(D^0 \to \pi^+\pi^-)}{N(D^0 \to K^-\pi^+)}\right|_{\text{MC}} \tag{9.7}$$

By this comparison we can define a correction factor $c^{\pi/K}_{\text{XFT}}$ as follows:

$$c^{\pi/K}_{\text{XFT}} = \left.\frac{N(D^0 \to \pi^+\pi^-)}{N(D^0 \to K^-\pi^+)}\right|_{\text{data}} \cdot \frac{\mathcal{B}(D^0 \to K^-\pi^+)}{\mathcal{B}(D^0 \to \pi^+\pi^-)} \cdot \left.\frac{N(D^0 \to K^-\pi^+)}{N(D^0 \to \pi^+\pi^-)}\right|_{\text{MC}} \tag{9.8}$$

We measure:

$$c^{\pi/K}_{\text{XFT}} = 0.943 \pm 0.014, \tag{9.9}$$

where the uncertainty is quoted as the quadrature sum of the uncertainties of the terms involved in the ratio. The main contribution to the uncertainty is due to the finite statistics of the simulated $D^0 \to h^+h'^-$ decays used to estimate the Monte Carlo efficiency of eq. (9.7).

The same method has been used on $D^0 \to K^+K^-$ and $D^0 \to K^-\pi^+$ samples to obtain the $c^{K/\pi}_{\text{XFT}}$ correction:

$$c^{K/\pi}_{\text{XFT}} = 0.969 \pm 0.015. \tag{9.10}$$

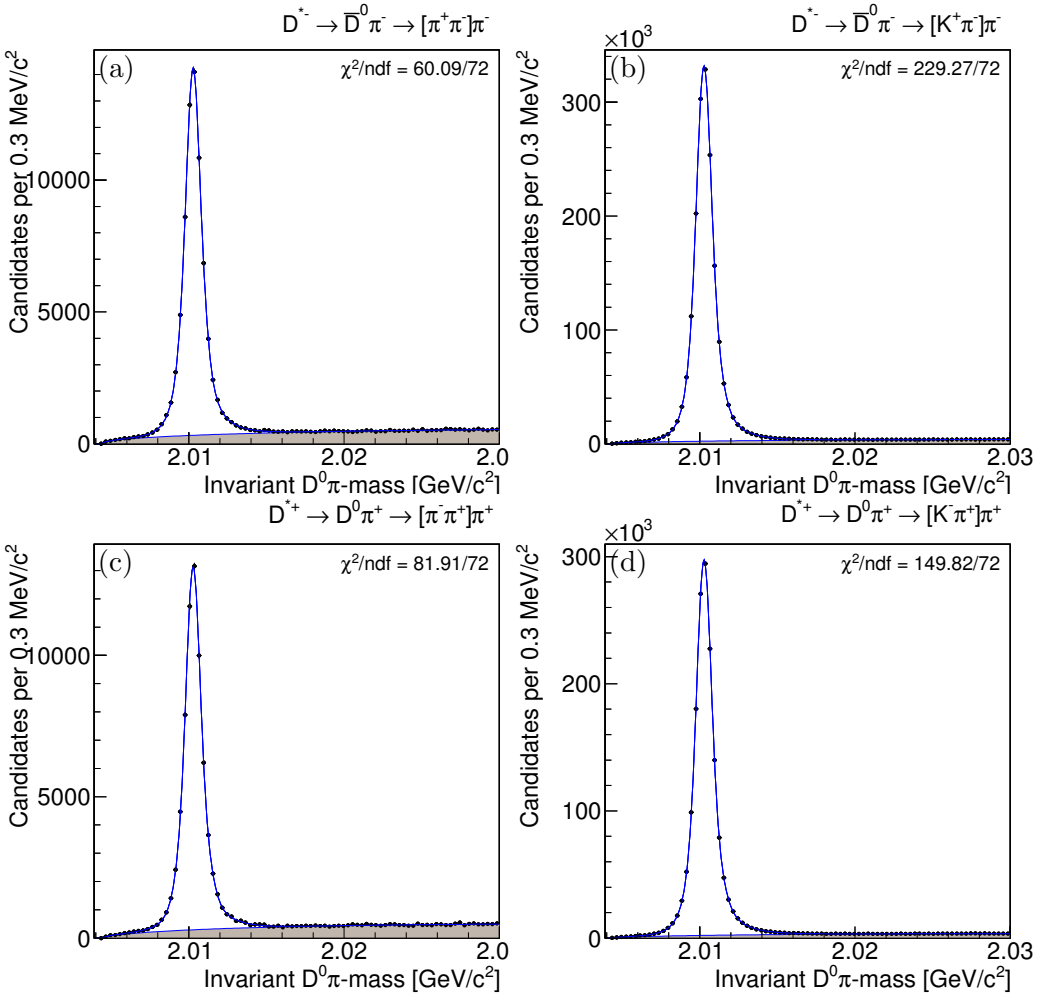

Figure 9.1: Invariant $D^0\pi$-mass for $D^{*-} \to \bar{D}^0\pi^- \to [\pi^+\pi^-]\pi^-$ decays (a) and $D^{*+} \to D^0\pi^+ \to [\pi^+\pi^-]\pi^+$ decays (c). Invariant $D^0\pi$-mass for $D^{*-} \to \bar{D}^0\pi^- \to [K^+\pi^-]\pi^-$ decays (b) and $D^{*+} \to D^0\pi^+ \to [\pi^+K^-]\pi^+$ decays (d). The fit function is overlaid; the random pions component of the fit function is described by a gray curve.

Figure 9.2 reports the binned χ^2-fit on the invariant $D^0\pi$-mass to extract the number of $D^0 \to K^+K^-$ signal events. We naively expected the $c_{\mathrm{XFT}}^{K/\pi}$ to be the inverse of $c_{\mathrm{XFT}}^{\pi/K}$, but our results do not support this assumption. This can be due to the different fit conditions of the $D^0 \to K^+K^-$ decays distributions: as reported in fig. 9.2, for the $D^0 \to K^+K^-$ decays we expect the presence of a sizable multibody D decays component. The correctness of the fit can affect the $c_{\mathrm{XFT}}^{K/\pi}$ evaluation. Thus we evaluated a systematic uncertainty for $c_{\mathrm{XFT}}^{\pi/K}$ and $c_{\mathrm{XFT}}^{K/\pi}$, given by the difference of their values with respect to a different evaluation, based on a different method (details are reported in [88]).

Since this correction has to be applied to the $B \to h^+h'^-$ simulation, exhibiting

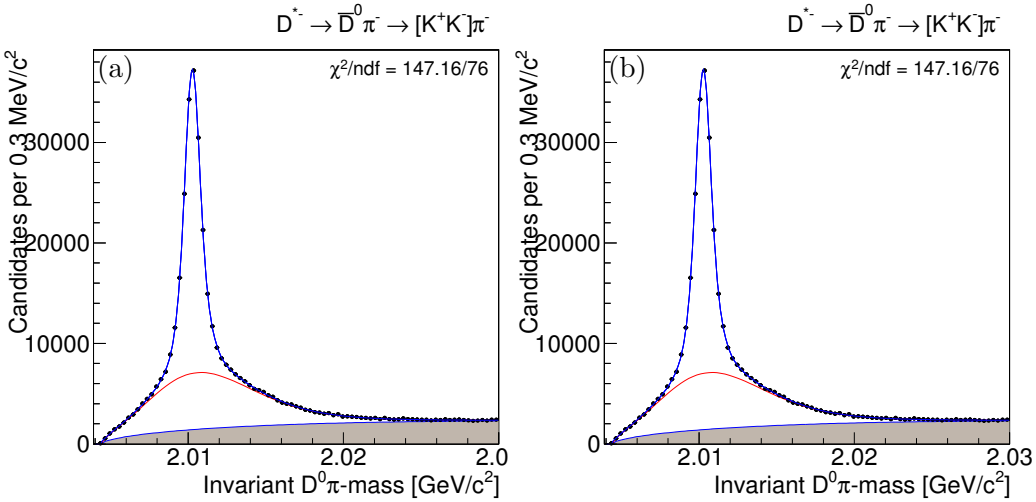

Figure 9.2: Invariant $D^0\pi$-mass for $D^{*-} \to \bar{D}^0\pi^- \to [K^+K^-]\pi^-$ decays (a) and $D^{*+} \to D^0\pi^+ \to [K^+K^-]\pi^+$ decays (b). The fit function is overlaid; a multibody D decays component of the function is drawn as a red line, while the random pions component is described by a gray curve.

a different kinematic, we investigated possible dependence of the correction on some kinematics variables, such as the transverse momentum of the tracks. The correction is found to be almost independent on the transverse momentum, as shown in fig. 9.3, and similar checks have been done for other kinematics variables. Thus we can assume that our correction is valid with good approximation also in the $B \to h^+h'^-$ decay modes. We have now all the ingredients: assuming that track efficiency can

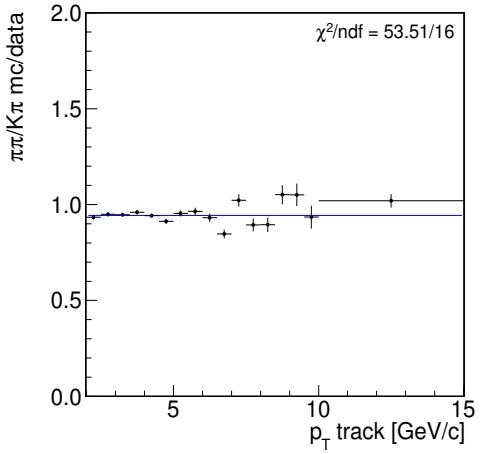

Figure 9.3: $c_{\mathrm{XFT}}^{\pi/K}$ in function of the transverse momentum of the track. The constant function used in the fit is overlaid.

be factorized, the corrected kinematic efficiencies with their uncertainties are:

$$\frac{\varepsilon_{\rm kin}(B^0 \to K\pi)}{\varepsilon_{\rm kin}(B^0 \to KK)} \cdot c_{\rm XFT}^{K/\pi} = 1.032 \pm 0.016 \quad (9.11)$$

$$\frac{\varepsilon_{\rm kin}(B^0 \to K\pi)}{\varepsilon_{\rm kin}(B_s^0 \to \pi\pi)} \cdot c_{\rm XFT}^{\pi/K} = 0.893 \pm 0.014 \quad (9.12)$$

The uncertainty is due to the statistical and systematic uncertainty on the measurement of the parameters $c_{\rm XFT}^{\pi/K}$ and $c_{\rm XFT}^{K/\pi}$ of eq. (9.9) and eq. (9.10). This uncertainty will be used to evaluate the relative associated systematics (chap. 11).

Checks

We observed in the data sample an increasing trend corresponding to different periods of data-taking defined in tab. 9.1. Thus we checked if the simulation shows the same behaviour. The trend observed in data is also well reproduced by the simulation (fig. 9.4). We found that the ratio between data and simulation of the efficiency ratio in reconstructing pion and kaon is approximately constant in time.

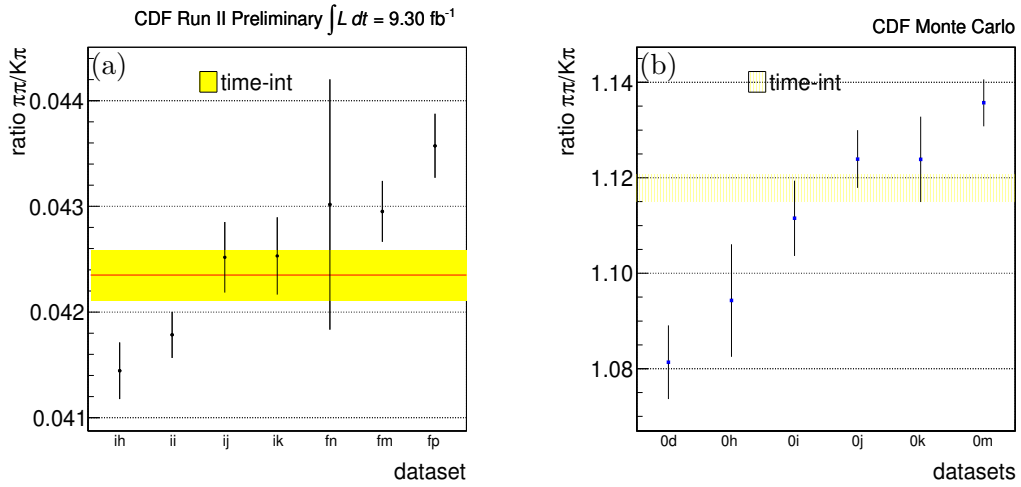

Figure 9.4: $\frac{N(D^0\to\pi^+\pi^-)}{N(D^0\to K^-\pi^+)}$ from data (a) and $\frac{\varepsilon(D^0\to\pi^+\pi^-)}{\varepsilon(D^0\to K^-\pi^+)}$ from simulation (b) for different periods of data taking. The red lines and the yellow bars are the time-integrated value and the uncertainty.

Period name	Run range
xd	138425 - 186598
xh	190697 - 203799
xi	203819 - 233111
xj	233133 - 246231
xk	252836 - 261005
xn	261119 - 264071
xm	264101 - 289197
xp	289273 - 312510

Table 9.1: Definition of the data-taking periods.

9.1.3 Efficiency of the B-isolation cut

The isolation of B meson depends on the multiplicity and momenta of the tracks produced in the b-quark fragmentation, which is not described by the signal-only simulation discussed in chap. 4. We therefore had to use real data to characterize this observable. Ref. [104] describes the measurement of the isolation efficiency for the values of the cut used in the previous analysis [122, 42, 37] using fully reconstructed $B^0_{(s)} \to J/\psi X$ decays. The efficiency ratio value averaged on the transverse momentum distribution of the $B^0_{(s)} \to h^+h'^-$ decays is:

$$\frac{\varepsilon_{\rm iso}(B^0)}{\varepsilon_{\rm iso}(B^0_s)} = 1.000 \pm 0.028, \tag{9.13}$$

This statistical uncertainty will be used to evaluate the relative associated systematics (see sec. 11.4.3).

The isolation efficiency, along with the kinematic, XFT efficiencies completes the set of corrections used to obtain the remaining ratios of branching fractions.

9.2 $B^0 \to K^+K^-$ results

Using the kinematic efficiency, $\frac{\varepsilon(B^0\to K\pi)}{\varepsilon(B^0\to KK)} \simeq 1.032$ (see eq. (9.11)), we corrected the fit results to extract the following measurement of relative branching fraction:

$$\frac{\mathcal{B}(B^0 \to K^+K^-)}{\mathcal{B}(B^0 \to K^+\pi^-)} = 0.012 \pm 0.005\ (stat.). \tag{9.14}$$

9.3 $B^0_s \to \pi^+\pi^-$ results

Following eqs. (9.12) and (9.13), we corrected the fit result for the efficiency ratio $\frac{\varepsilon(B^0\to K\pi)}{\varepsilon(B^0_s\to\pi\pi)} \simeq 0.893$, to extract the following measurement of relative branching fraction:

$$\frac{f_s}{f_d} \times \frac{\mathcal{B}(B^0_s \to \pi^+\pi^-)}{\mathcal{B}(B^0 \to K^+\pi^-)} = 0.008 \pm 0.002\ (stat.). \tag{9.15}$$

Chapter 10

Measurement of charge asymmetries

10.1 Introduction

In the measurement of CP asymmetry the relevant acceptance effects are the detector-induced charge asymmetry between positively and negatively charged particles due to their different probability of strong interaction with the tracker material, and the charge asymmetry induced by the COT cell-geometry. The terms related to the detector-induced charge asymmetry for the b-mesons are the ratios:

$$\frac{\varepsilon(B^0 \to K^+\pi^-)}{\varepsilon(\overline{B}^0 \to K^-\pi^+)} \quad \text{and} \quad \frac{\varepsilon(\overline{B}_s^0 \to K^+\pi^-)}{\varepsilon(B_s^0 \to K^-\pi^+)}. \tag{10.1}$$

Below we show how the efficiency corrections in eq. (10.1) are applied to the results determined by the fit.

$$\begin{aligned}
\mathcal{A}_{\mathcal{C}P}(B^0 \to K^+\pi^-) &= \frac{\mathcal{B}(\overline{B}^0 \to K^-\pi^+) - \mathcal{B}(B^0 \to K^+\pi^-)}{\mathcal{B}(\overline{B}^0 \to K^-\pi^+) + \mathcal{B}(B^0 \to K^+\pi^-)} \\
&= \frac{\hat{f}_{\overline{B}^0 \to K^-\pi^+} \cdot \frac{\varepsilon(B^0 \to K^+\pi^-)}{\varepsilon(\overline{B}^0 \to K^-\pi^+)} - \hat{f}_{B^0 \to K^+\pi^-}}{\hat{f}_{\overline{B}^0 \to K^-\pi^+} \cdot \frac{\varepsilon(B^0 \to K^+\pi^-)}{\varepsilon(\overline{B}^0 \to K^-\pi^+)} + \hat{f}_{B^0 \to K^+\pi^-}}
\end{aligned}$$

$$\begin{aligned}
\mathcal{A}_{\mathcal{C}P}(B_s^0 \to K^-\pi^+) &= \frac{\mathcal{B}(\overline{B}_s^0 \to K^+\pi^-) - \mathcal{B}(B_s^0 \to K^-\pi^+)}{\mathcal{B}(\overline{B}_s^0 \to K^+\pi^-) + \mathcal{B}(B_s^0 \to K^-\pi^+)} \\
&= \frac{\hat{f}_{\overline{B}_s^0 \to K^+\pi^-} \cdot \frac{\varepsilon(B_s^0 \to K^-\pi^+)}{\varepsilon(\overline{B}_s^0 \to K^+\pi^-)} - \hat{f}_{B_s^0 \to K^-\pi^+}}{\hat{f}_{\overline{B}_s^0 \to K^+\pi^-} \cdot \frac{\varepsilon(B_s^0 \to K^-\pi^+)}{\varepsilon(\overline{B}_s^0 \to K^+\pi^-)} + \hat{f}_{B_s^0 \to K^-\pi^+}}
\end{aligned}$$

The terms related to the detector-induced charge asymmetry for the b-baryons are the ratios:

$$\frac{\varepsilon(\Lambda_b^0 \to p\pi^-)}{\varepsilon(\overline{\Lambda}_b^0 \to \overline{p}\pi^+)} \quad \text{and} \quad \frac{\varepsilon(\Lambda_b^0 \to pK^-)}{\varepsilon(\overline{\Lambda}_b^0 \to \overline{p}K^+)}. \tag{10.2}$$

The corrections in eq. (10.2) are applied to the results of the fit to extract the measurements:

$$\mathcal{A}_{CP}(\Lambda_b^0 \to ph^-) = \frac{\mathcal{B}(\Lambda_b^0 \to ph^-) - \mathcal{B}(\bar{\Lambda}_b^0 \to \bar{p}h^+)}{\mathcal{B}(\Lambda_b^0 \to ph^-) + \mathcal{B}(\bar{\Lambda}_b^0 \to \bar{p}h^+)} = \frac{\hat{f}_{\bar{\Lambda}_b^0 \to \bar{p}h^+} \cdot \frac{\varepsilon(\Lambda_b^0 \to ph^-)}{\varepsilon(\bar{\Lambda}_b^0 \to \bar{p}h^+)} - \hat{f}_{\Lambda_b^0 \to ph^-}}{\hat{f}_{\bar{\Lambda}_b^0 \to \bar{p}h^+} \cdot \frac{\varepsilon(\Lambda_b^0 \to ph^-)}{\varepsilon(\bar{\Lambda}_b^0 \to \bar{p}h^+)} + \hat{f}_{\Lambda_b^0 \to ph^-}}$$

Although some CDF measurements confirm that the GEANT package reproduces with good accuracy these effects [116] we preferred to measure it directly from real data, to achieve the best precision and the confidence in the result needed for this delicate measurement.

10.1.1 $K^+\pi^-/K^-\pi^+$ corrections

We measured the efficiency ratios in eq. (10.1) using an unbiased sample of $D^0 \to K^-\pi^+$. By unbiased we mean that the $D^0 \to K^-\pi^+$ decays were reconstructed without requiring they were produced in the decay of a D^{*+}, which is usual in CDF when a clean D^0 sample is desired. The request of an additional charged pion in the final state and of the explicit reconstruction of the $D^{*+} \to D^0\pi^+ \to [K^-\pi^+]\pi^+$ decay chain, would generate an artificial asymmetry, since the CDF II tracking has a different efficiency for reconstructing the tracks associated to π^+ and π^- with low momentum, which would introduce extra uncertainties. For this reason we selected for our purpose about 30×10^6 prompt $D^0 \to K^-\pi^+$ decays and analyzed them with the same methods used for the $B^0_{(s)} \to h^+h'^-$ decays and described here. This is a powerful check of all the analysis since we actually used the same reconstruction and fitting code of the $B^0_{(s)} \to h^+h'^-$ analysis. In this way, we are at same time eliminating possible spurious effects hidden in our procedure. Since the Standard Model predicts a very small $\mathcal{O}(10^{-6})$ [117] direct CP asymmetry in the $D^0 \to K^-\pi^+$ decay, and since the current experimental measurements[1] [51] do not show any indication of a deviation from this prediction, we assume that:

$$\frac{\mathcal{B}(\overline{D}^0 \to K^+\pi^-) - \mathcal{B}(D^0 \to K^-\pi^+)}{\mathcal{B}(\overline{D}^0 \to K^+\pi^-) + \mathcal{B}(D^0 \to K^-\pi^+)} \ll 10^{-3}. \tag{10.3}$$

We will then evaluate a systematic uncertainty on this assumption. If we write relation (10.3) in terms of the measured relative fractions of $D^0 \to K^-\pi^+$ and $\overline{D}^0 \to K^+\pi^-$ and efficiency correction, we obtain:

$$\frac{\mathcal{B}(\overline{D}^0 \to K^+\pi^-) - \mathcal{B}(D^0 \to K^-\pi^+)}{\mathcal{B}(\overline{D}^0 \to K^+\pi^-) + \mathcal{B}(D^0 \to K^-\pi^+)} = \frac{\hat{f}_{\overline{D}^0 \to K^+\pi^-} \cdot \frac{\varepsilon(D^0 \to K^-\pi^+)}{\varepsilon(\overline{D}^0 \to K^+\pi^-)} - \hat{f}_{D^0 \to K^-\pi^+}}{\hat{f}_{\overline{D}^0 \to K^+\pi^-} \cdot \frac{\varepsilon(D^0 \to K^-\pi^+)}{\varepsilon(\overline{D}^0 \to K^+\pi^-)} + \hat{f}_{D^0 \to K^-\pi^+}} \ll 10^{-3} \tag{10.4}$$

from which we can extract the desired ratio $\frac{\varepsilon(\overline{D}^0 \to K^+\pi^-)}{\varepsilon(D^0 \to K^-\pi^+)}$. The work is documented in detail in Ref. [118]. Here we summarize only the relevant aspects.

[1] The current experimental sensitivity is $\mathcal{O}(10^{-2})$.

The detector-induced asymmetry in $D^0 \to K^-\pi^+$ decays is determined through a simultaneous binned χ^2 fit of $D^0 \to K^-\pi^+$ and $\overline{D}^0 \to K^+\pi^-$ samples. For all components, templates are the same for positive and negative sample.

The mass line shape of the $D^0 \to K^-\pi^+(\overline{D}^0 \to K^+\pi^-)$ signal is parameterized using the sum of two Gaussians, and a tail function to parameterize the low mass tail due to the soft photon emission. Similar distributions have been used to parameterize the $D^0 \to \pi^+\pi^-$ component. The mass distributions of the background and of the partially reconstructed decays are parameterized using two different exponential functions. From the results of the fit shown in fig. 10.1 we obtain the following correction:

$$\frac{\varepsilon(D^0 \to K^-\pi^+)}{\varepsilon(\overline{D}^0 \to K^+\pi^-)} = 0.9835 \pm 0.0006\ (stat.) \pm 0.0011\ (syst.) \quad (10.5)$$

$$\frac{\varepsilon(\overline{D}^0 \to K^+\pi^-)}{\varepsilon(D^0 \to K^-\pi^+)} = 1.0168 \pm 0.0007\ (stat.) \pm 0.0012\ (syst.). \quad (10.6)$$

Prompted by recent hints of CP violation in the charm system [119, 120] we added a systematic uncertainty on a possible non-vanishing CP violation, using the available experimental knowledge $\mathcal{A}_{\mathcal{C}P}(D^0 \to K^-\pi^+) = (0.1 \pm 0.7)\%$ [51]. We found:

$$\frac{\varepsilon(D^0 \to K^-\pi^+)}{\varepsilon(\overline{D}^0 \to K^+\pi^-)} = 0.9835 \pm 0.0006\ (stat.) \pm 0.0011\ (syst.) \pm 0.0033(pdg) \quad (10.7)$$

$$\frac{\varepsilon(\overline{D}^0 \to K^+\pi^-)}{\varepsilon(D^0 \to K^-\pi^+)} = 1.0168 \pm 0.0007\ (stat.) \pm 0.0012\ (syst.). \pm 0.0034(pdg) \quad (10.8)$$

By adding in quadrature we obtain:

$$\frac{\varepsilon(D^0 \to K^-\pi^+)}{\varepsilon(\overline{D}^0 \to K^+\pi^-)} = 0.9835 \pm 0.0035 \quad (10.9)$$

$$\frac{\varepsilon(\overline{D}^0 \to K^+\pi^-)}{\varepsilon(D^0 \to K^-\pi^+)} = 1.0168 \pm 0.0037 \quad (10.10)$$

Momentum correction

To keep into account the different momentum distribution of the D^0 and $B^0_{(s)}$ decays we reweighted the joint distribution of $(\beta, p_{\rm tot})$ using the $B^0_{(s)} \to h^+h'^-$ Monte Carlo. We first evaluated the efficiency ratio $\frac{\varepsilon(B^0_s \to K^-\pi^+)}{\varepsilon(\overline{B}^0_s \to K^+\pi^-)}$ without any reweighting, and second reweighting the $(\beta, p_{\rm tot})$ distribution of $B^0_s \to K^-\pi^+$ to that of $D^0 \to K^-\pi^+$. The ratio of these two quantities is equal to 1.0055 and is applied as a multiplicative correction to the values of eq. (10.7) and eq. (10.8), to account for the different D^0 and $B^0_{(s)}$ meson momentum spectrum. The small difference in the momentum $(\beta,p_{\rm tot})$ distribution between $B^0 \to K^+\pi^-$ and $B^0_s \to K^-\pi^+$ has a negligible effect.

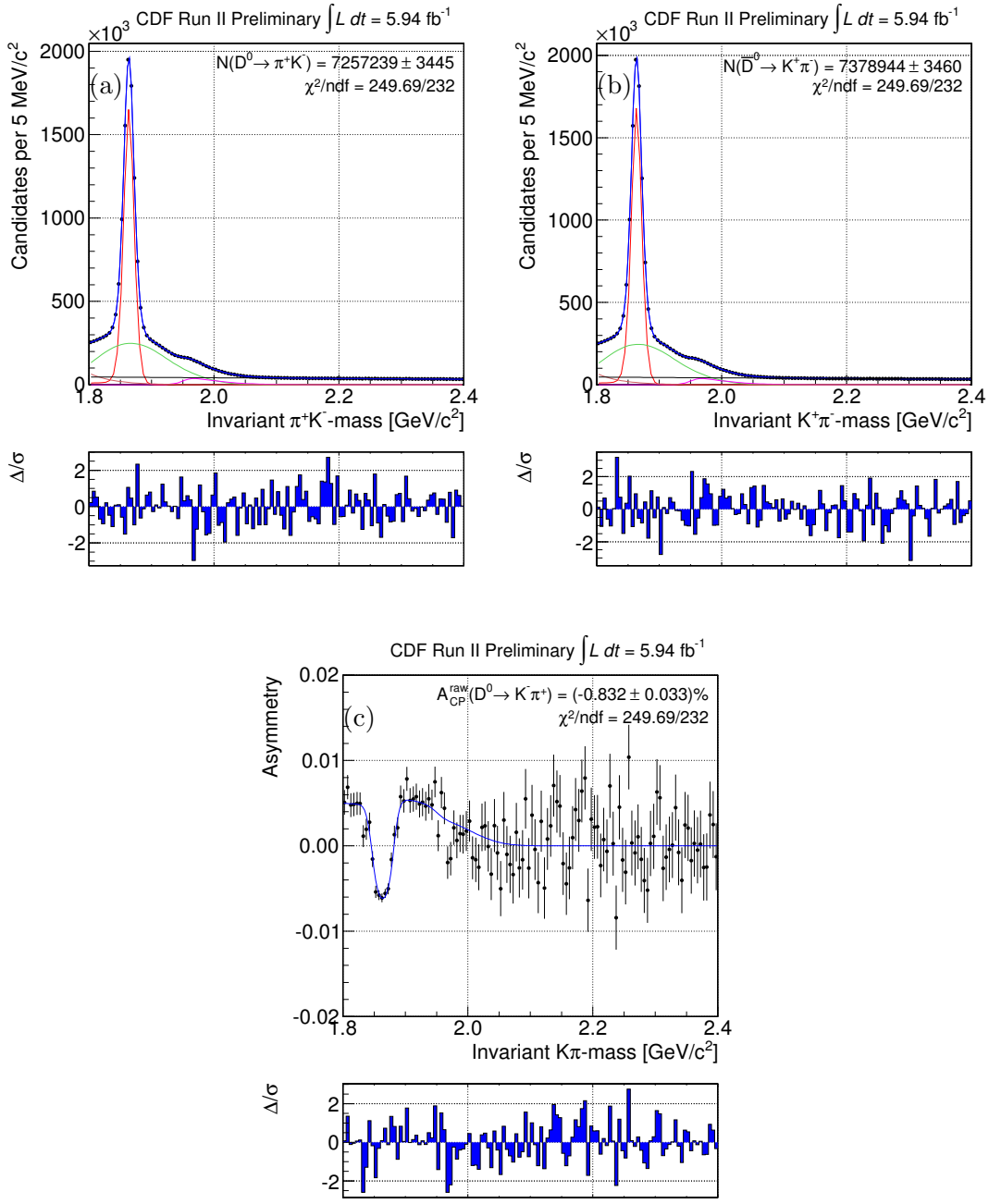

Figure 10.1: Invariant $K^-\pi^+$-mass for $D^0 \to K^-\pi^+$ decays (a), invariant $K^+\pi^-$-mass for $\overline{D}^0 \to K^+\pi^-$ decays (b), and the resulting asymmetry (c). Fit functions overlaid: signal $D^0 \to K^-\pi^+(\overline{D}^0 \to K^+\pi^-)$ peak (red), the CP–conjugated decay contribution (green), the small $D^0 \to \pi^+\pi^-$ contribution at high masses (pink), and a small contribution given the partial reconstructed decays in the low mass region (dark red).

Thus we obtain the final acceptance corrections:

$$\frac{\varepsilon(\overline{B}^0 \to K^-\pi^+)}{\varepsilon(B^0 \to K^+\pi^-)} = \frac{\varepsilon(B_s^0 \to K^-\pi^+)}{\varepsilon(\overline{B}_s^0 \to K^+\pi^-)} = 0.9889 \pm 0.0006\ (stat.) \pm 0.0034\ (syst.) \tag{10.11}$$

$$\frac{\varepsilon(B^0 \to K^+\pi^-)}{\varepsilon(\overline{B}^0 \to K^-\pi^+)} = \frac{\varepsilon(\overline{B}_s^0 \to K^+\pi^-)}{\varepsilon(B_s^0 \to K^-\pi^+)} = 1.0112 \pm 0.0006\ (stat.) \pm 0.0036\ (syst.). \tag{10.12}$$

As a check, we compared these results with the ones obtained using the official CDF Monte Carlo. The agreement obtained is satisfactory.

10.1.2 $ph^-/\bar{p}h^+$ corrections

We used a sample of about 300,000 $\Lambda \to p\pi$ decays to determine the efficiency ratios $\frac{\varepsilon(\Lambda_b^0 \to p\pi^-)}{\varepsilon(\overline{\Lambda}_b^0 \to \bar{p}\pi^+)}$ and $\frac{\varepsilon(\Lambda_b^0 \to pK^-)}{\varepsilon(\overline{\Lambda}_b^0 \to \bar{p}K^+)}$. Assuming no CP asymmetry in the $\Lambda \to p\pi$ decays and assuming the production rate of Λ and a $\bar{\Lambda}$ to be the equal, if any asymmetry is found in the number of Λ with respect to the $\bar{\Lambda}$ this is ascribed to the detection asymmetry. The detector-induced asymmetry in $\Lambda \to p\pi$ decays is determined through a simultaneous binned χ^2 fit of Λ and $\bar{\Lambda}$ samples. The kinematics of this sample allows distinguishing without ambiguity between a Λ and a $\bar{\Lambda}$ decay mode, by evaluating the invariant mass under the hypothesis that the momentum of the proton is always greater than the pion's one. The mass line shape of the signal is parameterized using a double Gaussian function and the mass line shape of the combinatorial background is parameterized using an exponential function, as shown in fig. 10.2. From the results of the fit we obtain the correction:

$$\frac{\varepsilon(\Lambda_b^0 \to p\pi^-)}{\varepsilon(\overline{\Lambda}_b^0 \to \bar{p}\pi^+)} = 1.0235 \pm 0.0054\ (stat.). \tag{10.13}$$

In the fit the charge asymmetry is assumed to be independent of the transverse momentum of the pion and of the proton. While this has been proven in similar conditions [118] to be a very fair assumption for the pions, we checked a possible dependence for the proton case, where no independent studies were available. We repeated the fit to obtain the charge asymmetry in different bins of transverse momentum of the protons, and we evaluated the dependence on the transverse momentum using the results of the linear fit shown in fig. 10.3. A systematic uncertainty was evaluated as the difference between the central value charge asymmetry, with the assumption of no dependence, and the charge asymmetry evaluated considering the dependence.

The charge asymmetry result, including statistical and systematic uncertainties, follows:

$$\frac{\varepsilon(\Lambda_b^0 \to p\pi^-)}{\varepsilon(\overline{\Lambda}_b^0 \to \bar{p}\pi^+)} = 1.0235 \pm 0.0054\ (stat.) \pm 0.0090\ (syst.). \tag{10.14}$$

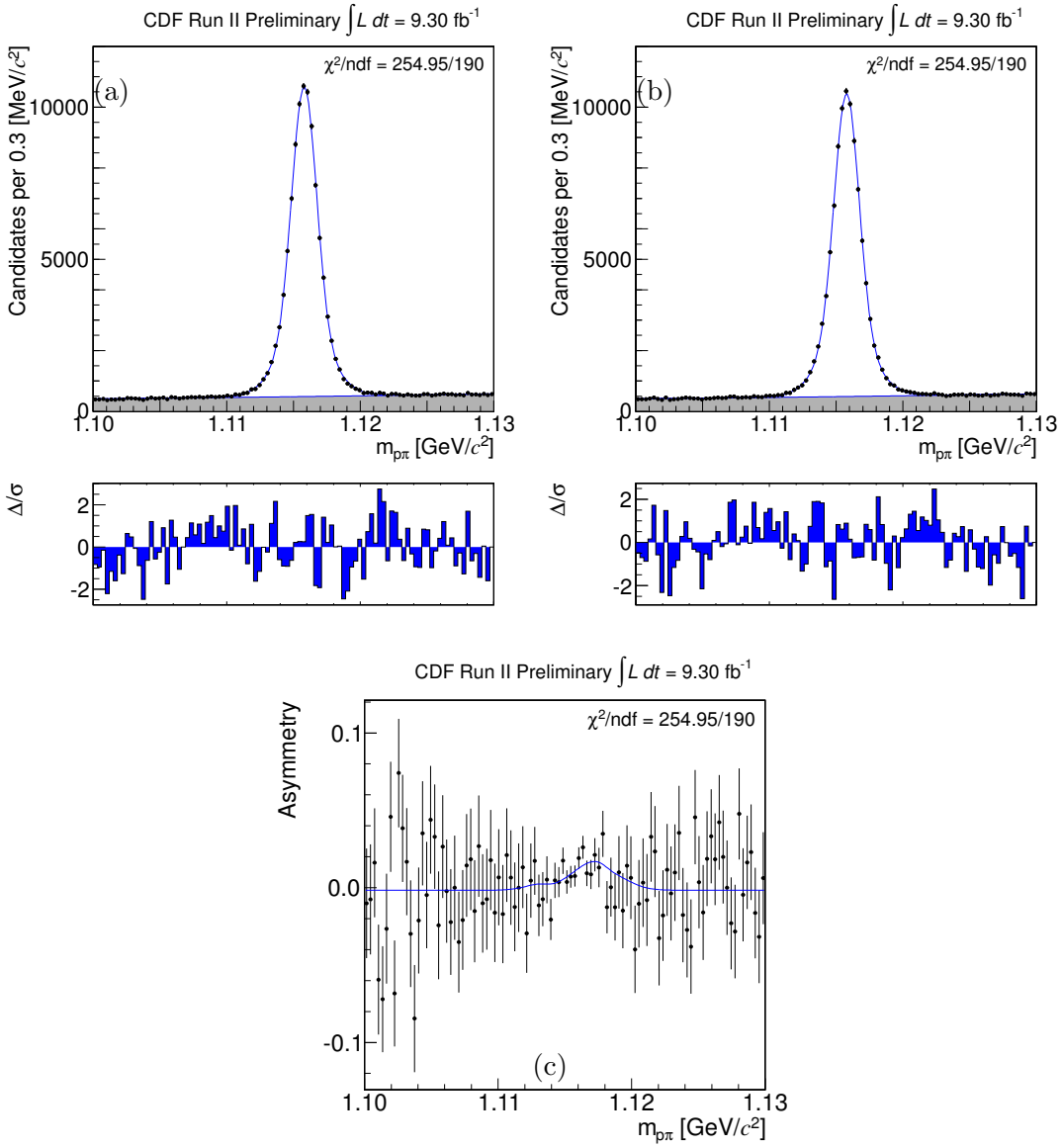

Figure 10.2: Invariant $p\pi^-$-mass for $\Lambda \to p\pi^-$ decays (a), invariant $\bar{p}\pi^+$-mass for $\bar{\Lambda} \to \bar{p}\pi^+$ decays (b), and the resulting asymmetry (c).

Assuming that reconstruction efficiencies factorize as follows:

$$\varepsilon(\Lambda_b^0 \to p\pi^-) = \varepsilon(p) \cdot \varepsilon(\pi^-), \tag{10.15}$$

$$\varepsilon(B_s^0 \to K^-\pi^+) = \varepsilon(K^-) \cdot \varepsilon(\pi^+), \tag{10.16}$$

and combining with the estimate of $\varepsilon(B_s^0 \to K^-\pi^+)/\varepsilon(\overline{B}_s^0 \to K^+\pi^-) = 0.9889 \pm$

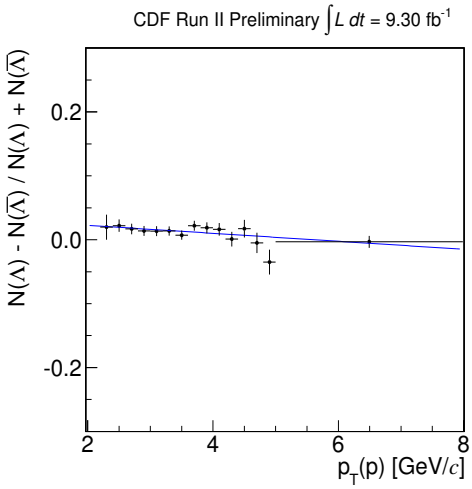

Figure 10.3: Detector-induced charge asymmetry for $\Lambda \to p\pi^-$ decays as a function of transverse momentum of the proton. Fit with a straight line is overlaid.

$0.0006\ (stat.) \pm 0.0034\ (syst.)$ from eq. (10.11) we obtain:

$$\begin{aligned} \frac{\varepsilon(\Lambda_b^0 \to pK^-)}{\varepsilon(\overline{\Lambda}_b^0 \to \overline{p}K^+)} &= 1.0121 \pm 0.0054\ (stat.) \pm 0.0096\ (syst.) \\ \frac{\varepsilon(\overline{\Lambda}_b^0 \to \overline{p}K^+)}{\varepsilon(\Lambda_b^0 \to pK^-)} &= 0.9880 \pm 0.0053\ (stat.). \pm 0.0094\ (syst.). \end{aligned}$$

These results can be compared with the same numbers extracted from the full CDF simulation for $\Lambda_b^0 \to p\pi^-$ and $\Lambda_b^0 \to pK^-$ decays:

$$\begin{aligned} \frac{\varepsilon(\Lambda_b^0 \to p\pi^-)}{\varepsilon(\overline{\Lambda}_b^0 \to \overline{p}\pi^+)}_{\mathrm{CDF-MC}} &= 1.044 \pm 0.005\ (stat.) \\ \frac{\varepsilon(\Lambda_b^0 \to pK^-)}{\varepsilon(\overline{\Lambda}_b^0 \to \overline{p}K^+)}_{\mathrm{CDF-MC}} &= 1.045 \pm 0.005\ (stat.) \end{aligned}$$

where the uncertainty comes from the finite size of the generated samples. The full CDF simulation, that should reproduce the particles interactions with the tracker material (for instance for $\varepsilon(B_s^0 \to K^-\pi^+)/\varepsilon(\overline{B}_s^0 \to K^+\pi^-)$ the agreement between data and simulation is excellent), returns efficiency ratios values higher than ones found in this work. This may be due to lack of accuracy in the way the simulation reproduces protons behavior in the tracker material, being in general less experimentally studied with respect to kaons and pions, or this may due to some "incorrect" assumptions to the strategy adopted to extrapolate the efficiency ratio from $\Lambda \to p\pi^-$ decays to $\Lambda_b^0 \to p\pi^-$ decays. For this reasons we decided to get the average between the result obtained from the real $\Lambda \to p\pi^-$ decays and the result

obtained from CDF simulation. The averaged result is:

$$\begin{aligned}\frac{\varepsilon(\Lambda_b^0 \to p\pi^-)}{\varepsilon(\overline{\Lambda}_b^0 \to \overline{p}\pi^+)} &= 1.033 \pm 0.004\ (stat.) \pm 0.009\ (syst.) \pm 0.010\ (aver.) \\ \frac{\varepsilon(\Lambda_b^0 \to pK^-)}{\varepsilon(\overline{\Lambda}_b^0 \to \overline{p}K^+)} &= 1.028 \pm 0.004\ (stat.) \pm 0.010\ (syst.) \pm 0.016\ (aver.) \end{aligned} \quad (10.17)$$

where we added a systematic uncertainty (*aver.*), given by the semi-difference of the two estimates.

10.2 Corrected results

At this point we have all the corrections for those measurements involving the charge asymmetry correction, and we can extract the corresponding CP asymmetry measurements.

Following eq. (10.12), we corrected the fit results for the charge-asymmetry factor, $\frac{\varepsilon(B^0\to K^+\pi^-)}{\varepsilon(\overline{B}^0\to K^-\pi^+)} = \frac{\varepsilon(\overline{B}_s^0\to K^+\pi^-)}{\varepsilon(B_s^0\to K^-\pi^+)} \simeq 1.0112$, to extract the direct CP asymmetries:

$$\mathcal{A}_{\mathcal{C}P}(B^0 \to K^+\pi^-) = \frac{\mathcal{B}(\overline{B}^0 \to K^-\pi^+) - \mathcal{B}(B^0 \to K^+\pi^-)}{\mathcal{B}(\overline{B}^0 \to K^-\pi^+) + \mathcal{B}(B^0 \to K^+\pi^-)} = -0.083 \pm 0.013 \quad (10.18)$$

$$\mathcal{A}_{\mathcal{C}P}(B_s^0 \to K^-\pi^+) = \frac{\mathcal{B}(\overline{B}_s^0 \to K^+\pi^-) - \mathcal{B}(B_s^0 \to K^-\pi^+)}{\mathcal{B}(\overline{B}_s^0 \to K^+\pi^-) + \mathcal{B}(B_s^0 \to K^-\pi^+)} = +0.216 \pm 0.073, \quad (10.19)$$

where the uncertainties are statistical only.

Following eq. (10.17) we corrected the fit results for the charge-asymmetry factor, $\frac{\varepsilon(\Lambda_b^0\to p\pi^-)}{\varepsilon(\overline{\Lambda}_b^0\to \overline{p}\pi^+)} = 1.033$, and $\frac{\varepsilon(\Lambda_b^0\to pK^-)}{\varepsilon(\overline{\Lambda}_b^0\to \overline{p}K^+)} = 1.028$, to extract the direct $\mathcal{C}P$ asymmetries:

$$\frac{\mathcal{B}(\Lambda_b^0 \to pK^-) - \mathcal{B}(\overline{\Lambda}_b^0 \to \overline{p}K^+)}{\mathcal{B}(\Lambda_b^0 \to pK^-) + \mathcal{B}(\overline{\Lambda}_b^0 \to \overline{p}K^+)} = -0.10 \pm 0.08\ \ (stat.) \quad (10.20)$$

$$\frac{\mathcal{B}(\Lambda_b^0 \to p\pi^-) - \mathcal{B}(\overline{\Lambda}_b^0 \to \overline{p}\pi^+)}{\mathcal{B}(\Lambda_b^0 \to p\pi^-) + \mathcal{B}(\overline{\Lambda}_b^0 \to \overline{p}\pi^+)} = +0.06 \pm 0.07\ \ (stat.). \quad (10.21)$$

Chapter 11

Systematic uncertainties

11.1 General strategy

The measurements object of this thesis are ratios of branching fractions of kinematically similar decay modes and $\mathcal{C}P$-violating asymmetries. Most systematic effects related to the individual modes, e. g., the uncertainty on the integrated luminosity of the sample, cancel out in the ratio, thus resulting in a smaller systematic uncertainty on the measured ratios. Only systematic effects with a different impact on different modes need therefore to be considered. Furthermore, we ignored the systematic effects inducing uncertainties significantly smaller than their largest counterparts, because their contribution to the total systematic uncertainty is negligible. Most of the systematic uncertainties are evaluated by modifying the fit functions to include systematic variations and repeat the fits on data. The differences between results of modified fits and the central one are used as systematic uncertainties.

Some of the systematic uncertainties are relevant only for the annihilation modes, and they are not quoted for the $\mathcal{C}P$-asymmetries measurements. For example the systematics associated to the charge asymmetry correction applied to the raw yields to extract the physical $\mathcal{A}_{\mathcal{C}P}$ asymmetries are not quoted for the $\mathcal{B}(B_s^0 \to \pi^+\pi^-)$ and $\mathcal{B}(B^0 \to K^+K^-)$ measurements. Other systematic uncertainties are common between the annihilation measurements and the $\mathcal{C}P$-violating measurements, like the PID-related asymmetries. In some of these cases, the $\mathcal{C}P$-related systematics were determined with more sophisticated methods, because the $\mathcal{C}P$ measurements are based on a larger sample, and are affected by smaller statistical uncertainties. When necessary, we will describe the difference between the strategies used for the two different analyses.

Sections 11.2–11.6 contain the discussion on the dominant systematic uncertainties, while sec. 11.7 summarizes the effect of each measurement.

11.2 Systematics effects related to kinematics

11.2.1 Nominal b-hadron masses

The B^0, B_s^0 and Λ_b^0 square masses are external inputs to the analytic expression of eq. (5.5). In our main fit they are fixed to the world's averages [51]. To evaluate the systematic uncertainty associated to our limited experimental knowledge of nominal input masses we repeated the fit in which we independently varied the B^0, B_s^0 and Λ_b^0 input masses within $\pm 1\sigma$ uncertainty. We fitted the eight possible combinations of B^0, B_s^0 and Λ_b^0 masses by independently increasing (decreasing) by one statistical standard deviation the masses measured in Ref. [51]. The largest discrepancy between the results of the analysis with alternative masses configurations and the results of the sample with the nominal configuration was taken as the systematic uncertainty.

11.2.2 Charge asymmetries of momentum p.d.f

The momentum probability density functions $\wp_j^p(\beta, p_{\rm tot})$ were extracted from simulated samples for all signal modes. Since the charged-momentum asymmetry (β) and the scalar sum of the momenta ($p_{\rm tot}$) are not independent observables, we used a joint p.d.f. to model their distributions. Chapter 6 describes all the details of the parameterization. The b coefficients of eq. (6.18) characterize the factorized $\beta \frac{p_{\rm tot}}{p_{\rm tot}-4(5)}$ terms. In the parameterization we assumed that $\wp^p(\beta, p_{\rm tot}) = \wp^p(-\beta, p_{\rm tot})$ for decays into $\pi^+\pi^-$ and K^+K^- final states, where the β distributions are symmetric because the two outgoing particles have the same mass. Technically this was done by setting the odd b coefficients to zero in the parameterization of the central analysis. In order to take into account possible hidden asymmetries in the distributions due to any possible detector asymmetries reproduced by the simulation, we repeated the analysis re-parameterizing the momentum probability density functions with asymmetric fit functions for all signal modes (i. e., leaving free to vary also the odd b coefficients). The systematic uncertainty associated is the difference between the results with the asymmetric configuration for $\wp_j^p(\beta, p_{\rm tot})$ and the results with the symmetric nominal configuration.

11.2.3 Combinatorial background momentum p.d.f

The momentum probability density function of combinatorial background $\wp_{\rm E}^p(\beta, p_{\rm tot})$ was extracted from the data using the opposite-χ^2 sample (see sec. 6.3.1). This higher statistics sample allows us to perform an accurate parameterization of the joint probability density function keeping into account all correlations between β and $p_{\rm tot}$.

In order to assess a systematic uncertainty due to our limited knowledge of the real distribution of the combinatorial background momentum term, we parameter-

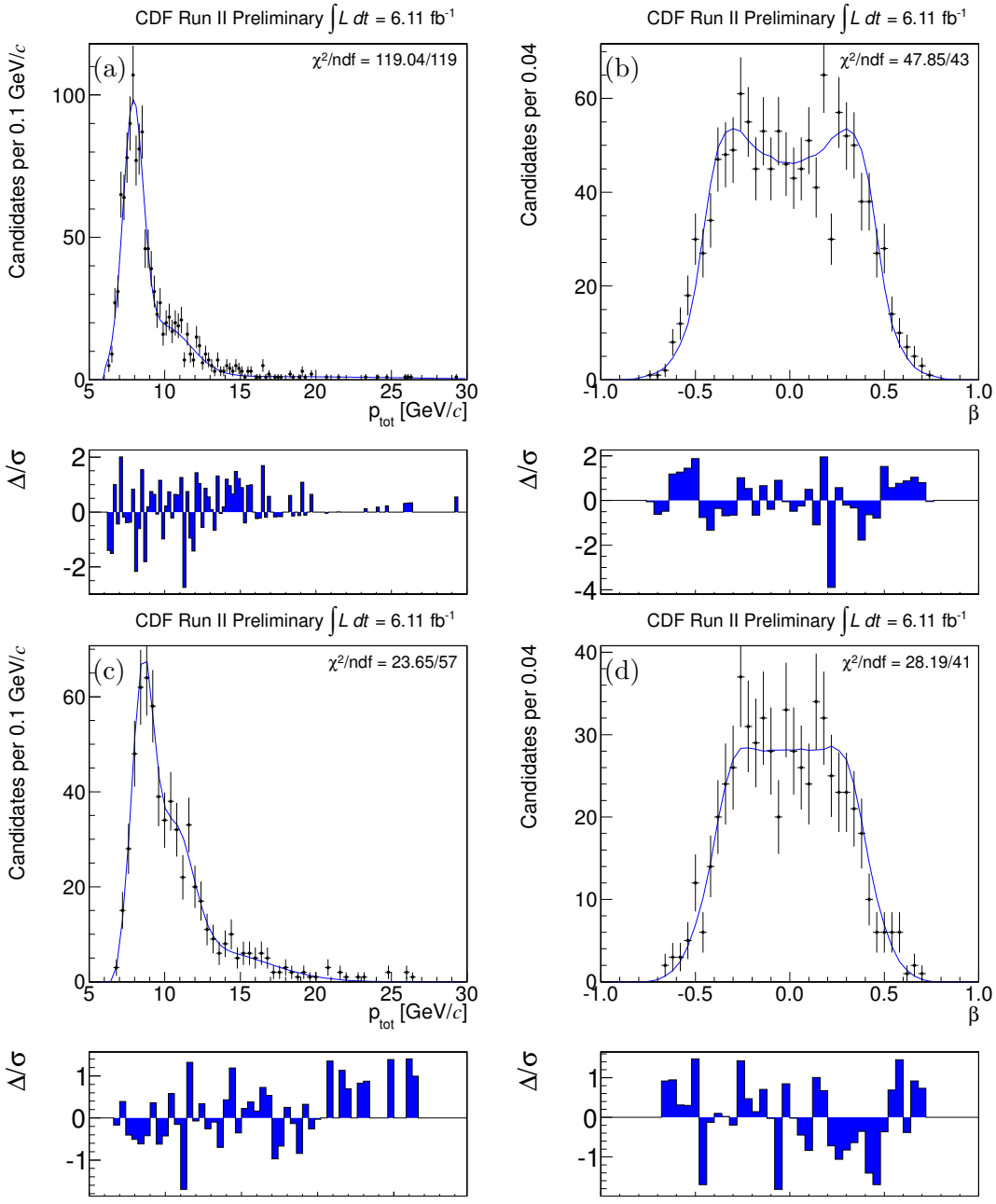

Figure 11.1: Projection of alternative template $\wp^p_{\rm E}(\beta, p_{\rm tot})$ of data at higher mass sideband. (a,b) for `med`, (c,d) for `high`.

ized $\wp^p_{\rm E}(\beta, p_{\rm tot})$ in an alternative way. We used the low statistics sample selected at higher mass values. This is a real combinatorial sample and we can safely assume that the joint (β,$p_{\rm tot}$) distribution is the same in all the mass fit range. Since the statistics is very low, we are not sensitive to all correlations. Then we keep into account kinematics only correlation due to trigger requirements, that are well known

(see sec. 3.1), neglecting the other ones. In other words we used the same functional form of eq. (6.25), where the coefficient b_m^{E} are not anymore function of p_{tot} but numerical constants to be determined in the parameterization. The template overlaid to data is reported in fig. 11.1.

The associated systematic uncertainty is the difference between the results of the analysis performed using this alternative template for $\wp_{\mathrm{E}}^{p}(\beta, p_{\mathrm{tot}})$ and the results obtained with the nominal configuration.

11.2.4 Physics background momentum p.d.f

The template $\wp_{\mathrm{A}}^{p}(\beta, p_{\mathrm{tot}})$ for the momentum term of the physics background has been parameterized using a mixture of partially reconstructed simulated b-hadrons decays. In order to assess a systematic uncertainty due to our limited knowledge of the real distribution we parameterized $\wp_{\mathrm{A}}^{p}(\beta, p_{\mathrm{tot}})$ in an alternative way. We used the low statistics sample selected at lower mass values, in which we subtracted the small contribution from the combinatorial background. This is a real physics background sample.

The associated systematic uncertainty is the difference between the results of the analysis performed using this alternative template for $\wp_{\mathrm{A}}^{p}(\beta, p_{\mathrm{tot}})$ and the results obtained with the nominal configuration.

11.2.5 Combinatorial background mass p.d.f.

In our main fit we extracted the squared invariant $\pi\pi$-mass model of the combinatorial background (E) from the opposite-χ^2 sample which contains events that pass the final selections of tab. 3.3 except for the requirement on the 3-D vertex quality. As demonstrated in sec. 6.3.2 the model accurately reproduces the combinatorial background mass shape. An exponential function has been used to parameterize its distribution.

To evaluate the systematic uncertainty associated to our limited experimental knowledge of real distribution we repeated the analysis in which we independently varied the angular coefficient c_{E}, for the scenarios `med` and `high`, within $\pm 1\sigma$ uncertainty. The four possible combinations were fitted by independently increasing (decreasing) by one statistical standard deviation the angular coefficients: $c_{\mathrm{E}} = -0.064 \pm 0.003$ $(stat.)$ $(\mathrm{GeV}^2/c^4)^{-1}$ for the scenario `med` and $c_{\mathrm{E}} = -0.060 \pm 0.004$ $(stat.)$ $(\mathrm{GeV}^2/c^4)^{-1}$ for the scenario `high`. The largest discrepancy between the results of the analysis of the samples with alternative configurations and the results of the sample with the nominal configuration was taken as the systematic uncertainty.

11.2.6 Physics background mass p.d.f

For the annihilation decay modes, in the central fit the cut-off of the ARGUS function, respectively for the scenarios `med` and `high`, was fixed to the values returned from the one-dimensional fit on simulated partially reconstructed decays. The values are respectively: $m_{\rm A}^2 = 26.49 \pm 0.01$ GeV$^2/c^4$ for `med` and $m_{\rm A}^2 = 26.48 \pm 0.01$ GeV$^2/c^4$ for `high` scenario. The simulation takes into account about 50% of known modes, with an appropriate mixture of B^0, B_s^0 and B^+ multibody decays. We assumed that the inclusive cutoff of the missing modes is the same of simulated ones, since the shape of the misreconstructed multibody decays is dominated by threshold effects plus resolution sculpting. However, a generous systematic uncertainty on the limited knowledge of this parameter has been assessed to cover all the possible shifts caused by the addition of one single background mode with an unlikely relative fraction of 50%, $m_{\rm A}^2 = 26.49 \pm 0.10$ GeV$^2/c^4$. The largest discrepancy between the results of the analysis with alternative configurations and the results of the sample with the nominal configuration was taken as the systematic uncertainty.

For the CP measurements, in the central fit the cut-off of the square invariant mass template of the physics background (A), for both `med` and `high` scenarios, is fixed to $m_{\rm A}^2 = 26.64$ GeV$^2/c^4$. This value is obtained performing 400 fits where the cut-off is fixed to different numbers in the interval [26.4, 26.8] GeV$^2/c^4$, as we described in sec. 6.2.2. To evaluate the systematic uncertainty associated to our limited experimental knowledge of this parameter we estimated a 95% confidence interval, corresponding to likelihood variation of $-2\log(\mathscr{L}) = 4$, using the likelihood profile reported in fig. 11.2. The profile is approximately distributed as a parabolic function. The interval is [26.588, 26.685] GeV$^2/c^4$ @95%CL.

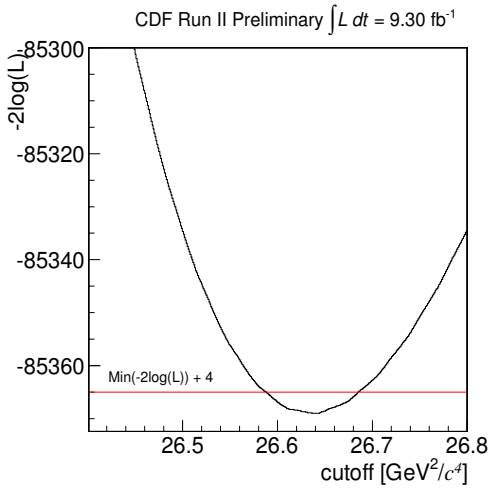

Figure 11.2: $-2\log(\mathscr{L})$ as a function of the cut-off value $m_{\rm A}^2$.

The associated systematic uncertainty is the difference between the results of the analysis performed with the cut-off values fixed to 26.588 GeV^2/c^4 and 26.685 GeV^2/c^4, with respect to the central fit. The largest discrepancy was taken as the systematic uncertainty.

11.2.7 Signal momentum p.d.f

The template $\wp_{\mathrm{i}}^{p}(\beta, p_{\mathrm{tot}})$ for the momentum term of the ith-signal mode has been parameterized using simulation. In order to assess a systematic uncertainty due to our limited knowledge of the real distribution we parameterized $\wp_{\mathrm{i}}^{p}(\beta, p_{\mathrm{tot}})$ in an alternative way. We used the sample selected at $m_{\pi^+\pi^-} \in [5.27,\ 5.33]$ GeV/c^2, corresponding to the signal region, in which we subtracted the contribution from the combinatorial background. Because of the sideband subtraction procedure, we did not take into account the β dependence on p_{tot}. Furthermore, we made the rough assumption that the joint (β,p_{tot}) distribution is similar for all signal modes: this is not the case, for instance we expect the $B^0 \to K^+\pi^-$ and $\overline{B}^0 \to K^-\pi^+$ to be antisymmetric. For these reasons, the systematic uncertainty assessed will be very conservative.

The associated systematic uncertainty is the difference between the results of the analysis performed using this alternative template for $\wp_{\mathrm{i}}^{p}(\beta, p_{\mathrm{tot}})$ and the results obtained with the nominal configuration.

11.2.8 Signal mass p.d.f.

The mass shape was extracted from simulation. Additional studies on independent samples of $D^0 \to h^+h^{'-}$ show that the Monte Carlo is able to accurately reproduce the mass shape of data, except for the mass resolution, that is tighter of about 8%.

In the fit performed for the annihilation measurements we let free to vary a parameter called s_m, which is a global scale factor of the mass template. The fit returns a value $\hat{s}_m = 1.094 \pm 0.015$, in agreement with our estimations (see sec. 4.2.3). The discrepancy between the results of the fit with this free parameter and the results of fit with the nominal configuration was taken as the systematic uncertainty.

For the $\mathcal{C}P$ measurements we improved the mass template description. We performed a detailed study using huge samples of $D^0 \to h^+h^{'-}$ to evaluate accurately the mass resolution of the $B \to h^+h^{'-}$ signal modes (see sec. 4.2.3). Thus the signal templates have been adjusted consequently, and the improved fit does not contain the s_m parameter. The accuracy of the procedure was checked by comparing the observed mass line-shape of 9×10^5 $\Upsilon(1S) \to \mu^+\mu^-$ decays to that predicted by the tuned simulation, obtaining discrepancies below the 2% level as described in sec. 4.2.3. These discrepancies are due to the fact that the $\Upsilon(1S)$ has higher mass with respect to the B^0 mass and there is larger background in the sample. Thus

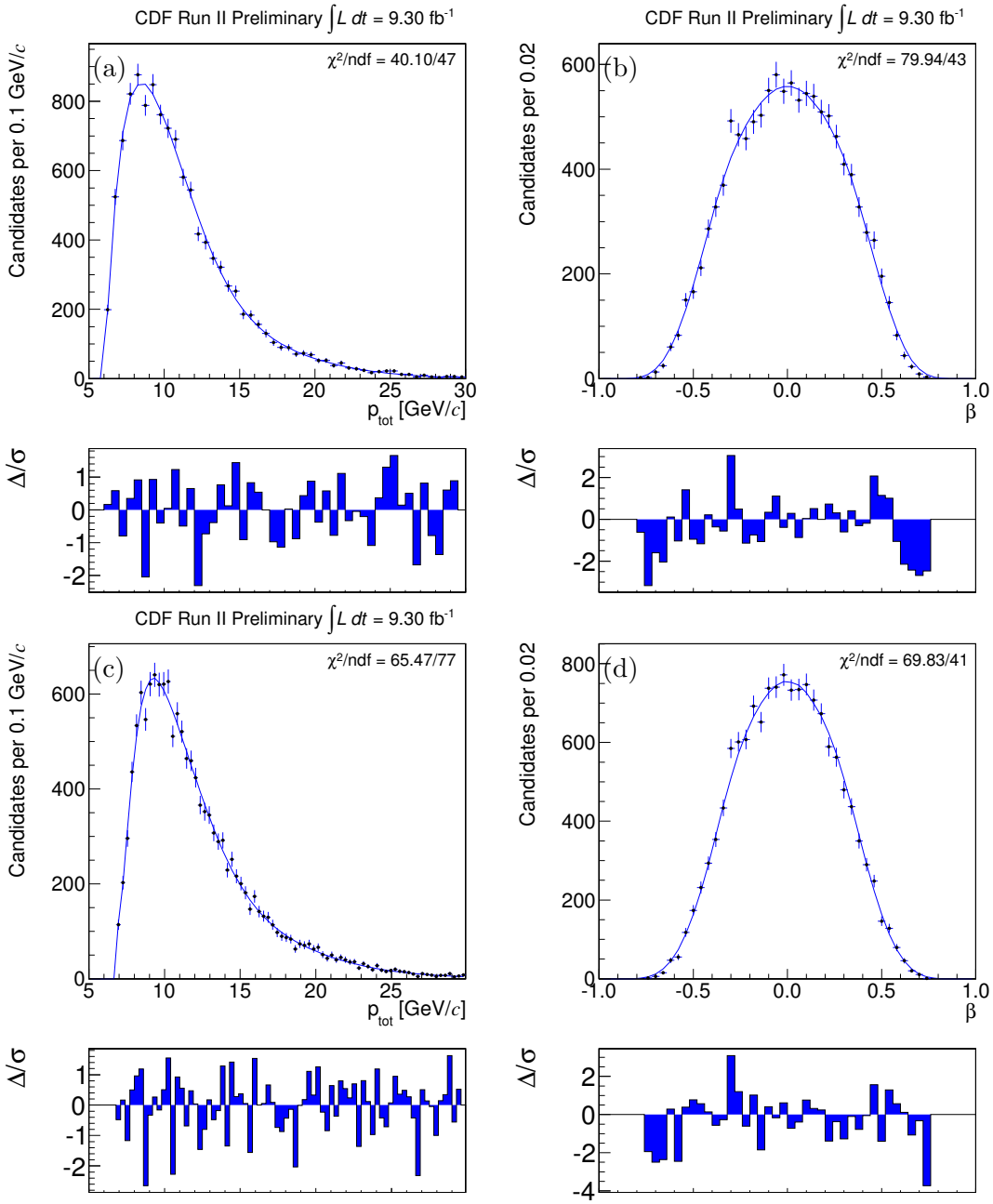

Figure 11.3: Projection of alternative template $\wp_i^p(\beta, p_{\rm tot})$ extracted from data sideband subtracted in the signal region. (a,b) for `med`, (c,d) for `high`.

a conservative systematic uncertainty is assessed repeating the fit using the signal templates adjusted for the resolution extracted from the $\Upsilon(1S)$ sample. The discrepancy between the results of the analysis of the samples with this alternative configuration and the results of the sample with the nominal configuration was taken as the systematic uncertainty.

11.2.9 Λ_b^0 p_{T}-spectrum

The kinematic templates for the Λ_b^0 decay modes has been extracted following exactly the same procedure adopted for B^0 and B_s^0 decays. However, while we know that the differences in momentum between B^0 and B_s^0 are tiny, this is not true for the Λ_b^0. Since $B_s^0 \to \pi^+\pi^-$ decay is located over lower mass tail of $\Lambda_b^0 \to ph^-$ decays it turns out that it is important to evaluate a systematic uncertainty on our limited knowledge of p_{T}-spectrum of the Λ_b^0 baryon. For instance, to extract (β,p_{tot}) templates we reweighted p_{T}-spectrum of Λ_b^0 simulated modes in the same way of $B_{(s)}^0 \to h^+h'^-$ decays, however we also know that the isolation requirement sculpts in different way the p_{T}-spectrum of the candidates if that is a B meson or a Λ_b^0 baryon. We reconstructed samples of $B^0 \to J/\psi K_s$ and $\Lambda_b^0 \to J/\psi\Lambda$. We apply a very simple and similar selection to both data samples to avoid to introduce any artificial kinematic differences and we extracted the transverse momentum distribution of the candidates, as shown in fig. 11.4(a). From the ratio of the two distributions, respectively from Λ_b^0 and B^0 candidates, we extracted the function to reweight our Λ_b^0 simulated decays, as shown in fig. 11.4(b). We re-parameterized (β,p_{tot}) joint probability density for $\Lambda_b^0 \to p\pi^-$ and $\Lambda_b^0 \to pK^-$ decay modes. The difference between the results of the analysis performed using these templates for the $\Lambda_b^0 \to ph^-$ decays and the results of the sample with the nominal configuration was taken as the systematic uncertainty.

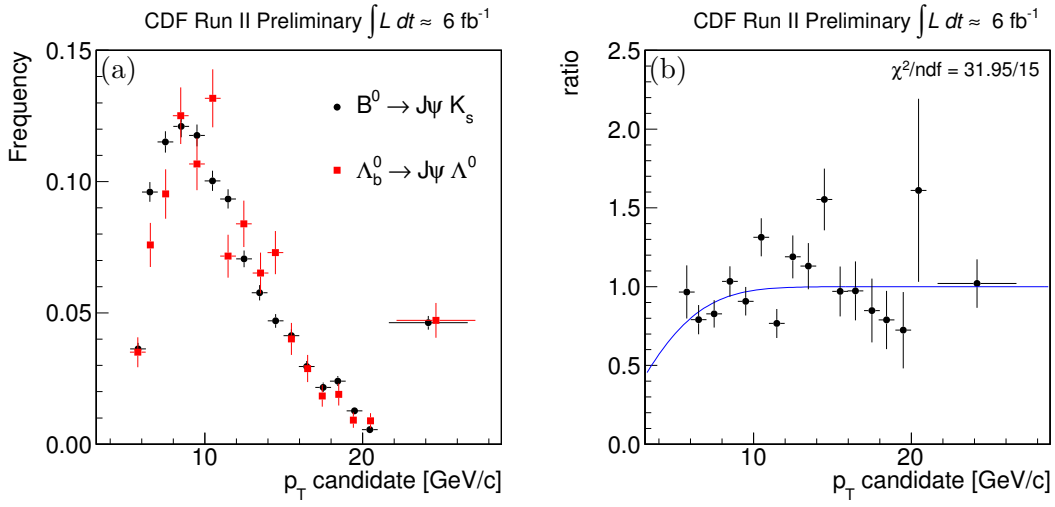

Figure 11.4: Transverse momentum distribution for Λ_b^0 and B^0 hadrons (a), from $B^0 \to J/\psi K_s$ and $\Lambda_b^0 \to J/\psi\Lambda$. Ratio between the two distributions (b), the fit is superimposed.

11.3 Particle Identification-related systematic effects

Chapter 7 summarizes how the fit of composition exploits the PID information in separating the different signal modes and background. The model used to introduce this information in the Likelihood is sophisticated, needing a large number of parameters. For example, the probability density function which describes the $B^0 \to K^+\pi^-$ signal mode results from a convolution integral that combines the intrinsic dE/dx residuals of both particles (δ_{K^+} and δ_{π^-}) through the p.d.f. of correlation, $\wp_c(c)$, yielding the following p.d.f. (see chap. 7):

$$\wp_{B^0\to K^+\pi^-}(\delta^{\rm obs}_{K^+}, \delta^{\rm obs}_{\pi^-}) \quad = \quad [\wp_{K^+}(\delta_{K^+}) \times \wp_{\pi^-}(\delta_{\pi^-})] * \wp_c(c).$$

Just this term of the Likelihood needs eight parameters for the three Gaussians of $\wp_{K^+}$, eight parameters for the three Gaussians of $\wp_{\pi^-}$ and five parameters for the two Gaussians of correlation $\wp_c(c)$, for a total of 21 parameters. If we consider all kind of particles adding the parameters to model the distribution of intrinsic residual of K^-, K^-, π^+, π^-, p and $\bar{p}$ we obtain a total number of 53 parameters. All these parameters have a statistical uncertainty which contributes to the systematic uncertainty on our final measurements. In reality the parameters which model the correlation do not have any statistical uncertainty since they, along with residual parameters, are extracted through an iterative procedure where in the final step the correlation shape is fixed. Therefore the total number is $53 - 5 = 48$.

For the annihilation decay modes analysis, the systematic uncertainty related to the statistical uncertainty on the determination of PID probability density functions was assessed by repeating the fit of composition in which all PID parameters, described above, are randomly varied in a 1σ-radius multidimensional sphere. We varied the parameters of the PID templates in all the possible directions generating randomly shifts in the parameters multi-dimensional space. In order to statistically sample a sufficient number of directions in this large dimensions space, we repeated the analysis for various seed values. For each seed value the PID functions change in a different way and we can obtain a measurement of the effect of systematic uncertainties on the analysis results. Figure 11.5 shows the distribution of the observed residuals for the negatively charged kaons and the positively charged pions (we obtain similar distributions for the other particles). The blue solid line is the template used in the central analysis while the red band, centered around data distribution, is the overlap of 200 templates generating with 200 different x_0 seeds. We repeated the fit of composition using this 200 different PID probability density functions. The systematic uncertainty on the physics observables associated to the statistical uncertainty of the templates parameterization is given by the r.m.s. of the distribution of the observables returned from the fits of composition performed with different seeds. In this procedure we neglected the correlations between the PID parameters: adding the correlations would imply a reduction of the final systematic uncertainty since the correlations tend to compensate the uncertainty of

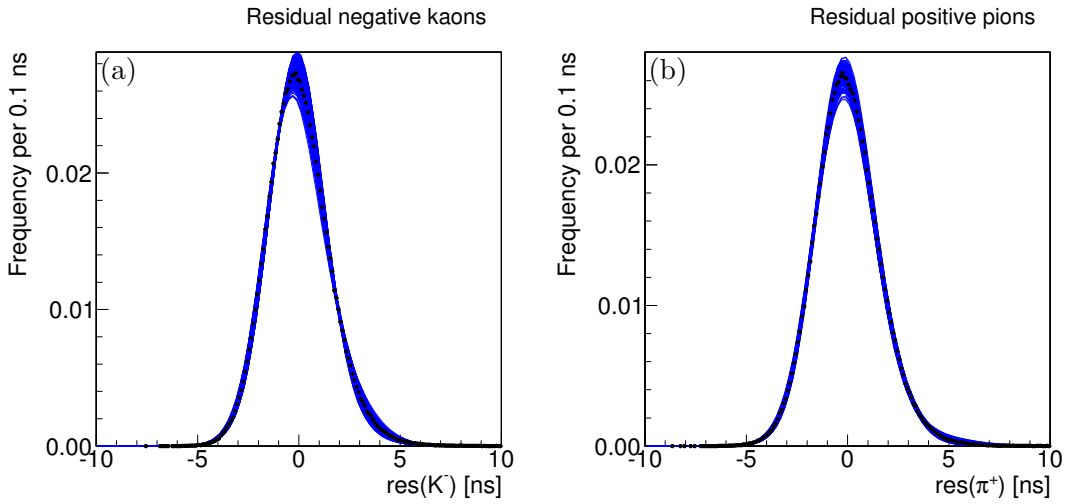

Figure 11.5: Distribution of observed dE/dx residual ($\wp(\delta^{\rm obs}) = \wp(\delta + c) = \wp(\delta) * \wp(c)$), for negatively charged kaons (with kaon mass hypothesis) (a), for positively charged pions (with pion mass hypothesis) (b). The results of the fit to the functions are overlaid (blue, solid line). The red band results from the overlapping of different curves generating with 200 different seed values x_0 from the template used in the standard analysis using the technique described in sec. 11.3.

one parameter with respect to another one. The dE/dx related systematic uncertainty is one of the dominant in our measurements (see tabs. 11.2–11.3) but it is still smaller than the statistical uncertainty, therefore we decide to do not include the correlations in the procedure and to quote a conservative value. As demonstrated in previous analyses the dE/dx systematics evaluated using this procedure is very conservative.

For the $\mathcal{C}P$ measurement analysis, where the needed precision is higher, we added the covariance matrix information in the procedure: we repeated the fit of composition in which all PID parameters are varied as gaussian variables correlated with their correlation matrix obtained from data. We used a numerical algorithm generating multivariate variables (see Cap. 33 of [51]). Figure 11.6 shows the distribution of the observed residuals for the negatively charged kaons and the positively charged pions (we obtain similar distributions for the other particles). The red solid line is the template used in the central analysis while the blue band, centered around data distribution, is the overlap of 500 templates generating with 500 different seeds with the technique described above, in which all PID parameters are varied according to a gaussian distribution correlated with their correlation matrix from data. We repeated the fit of composition using this 500 different PID probability density functions. From the comparison between fig. 11.5 and fig. 11.6 it is possible to appreciate the reduction of the blue band extension due to the additional information contained in the correlation matrix. The systematic uncertainty on the physics observables associated to the statistical uncertainty of

the templates parameterization is given by three times the r.m.s. of the distribution of the observables returned from the fits of composition performed with different seeds. We also add in quadrature to this uncertainty the difference we obtain when

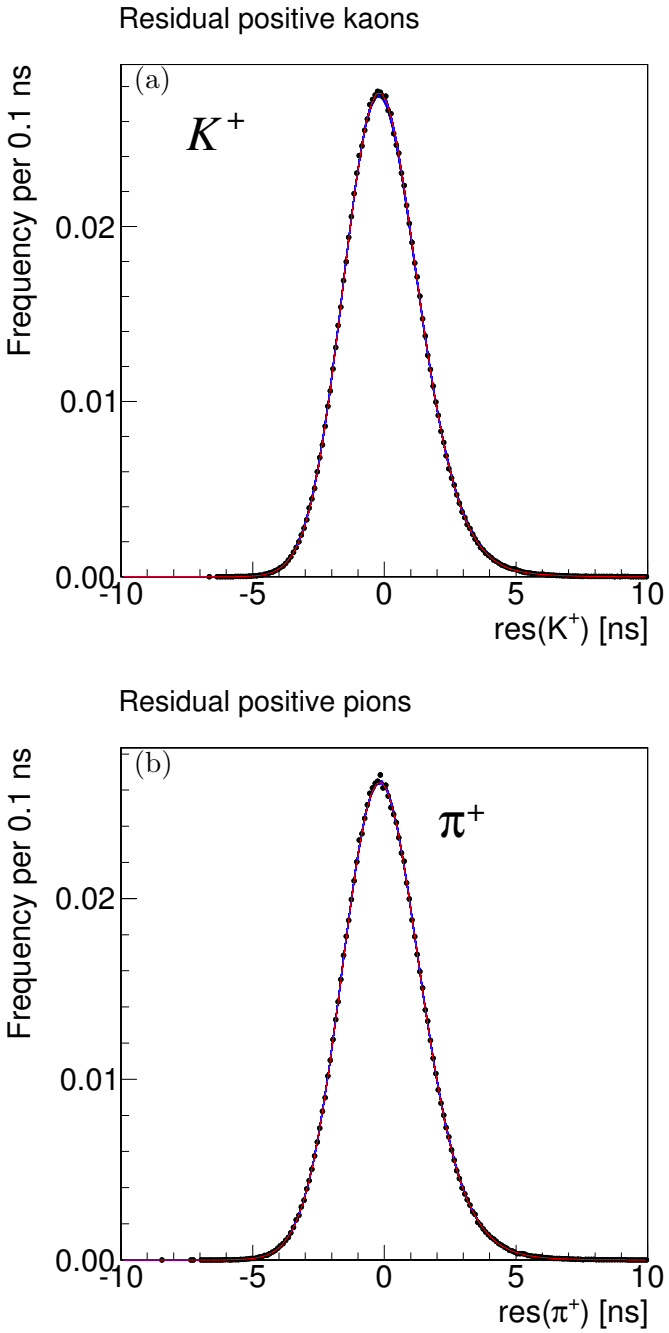

Figure 11.6: Distribution of observed dE/dx residual, for positively charged kaons (a) and pions (b). The results of the fit to the functions are overlaid (red, solid line). The blue band in the results from the overlapping of different curves generating with 500 different seed values x_0 from the template used in the standard analysis.

we repeat the central fit with the correlation shape free to vary. In this case we used a simplified gaussian model, instead of a double gaussian. This has been done to keep into account the fact that in the procedure described above the five parameters of correlation do not contribute.

11.4 Efficiency-related systematic effects

11.4.1 Triggers relative efficiency

In the central fit the relative fractions of signals are common parameters between A and C subsamples (see sec. 5.6). This has been done to avoid to increase too much the number of fit parameters. In such a way we assumed that the relative efficiency in reconstructing signals is the same for subsamples A and C. In principle one may fit them separately for A and C subsamples and combine the final results. To assess a systematic uncertainty we extracted the relative efficiency ratio between C and A subsamples from simulation for all signal modes: $B^0 \to h^+h^{'-}$, $B_s^0 \to h^+h^{'-}$ and $\Lambda_b^0 \to ph^-$. For each jth signal modes we define the factor c_j:

$$f_j^{\mathtt{C}} = c_j \cdot f_j^{\mathtt{A}} \tag{11.1}$$

where $f_j^{\mathtt{A}}$ and $f_j^{\mathtt{C}}$ are the relative signal fractions respectively for A and C subsamples. These factors are extracted from simulation as:

$$c_j = \frac{n_j^{\mathtt{C}}}{n_j^{\mathtt{A}}} \cdot \frac{n_{\mathrm{tot}}^{\mathtt{A}}}{n_{\mathrm{tot}}^{\mathtt{C}}} \tag{11.2}$$

where $n_j^{\mathtt{A(C)}}$ is the number of events reconstructed by the simulation for the jth signal mode for A(C) sample, while $n_{\mathrm{tot}}^{\mathtt{A(C)}}$ is the sum of the number of events of all signal modes reconstructed by the simulation for the A(C) sample weighted using the measured branching ratios $\mathcal{B}_j$ for the observed modes and the theoretical expectations for the not yet observed ones. Table 11.1 reports the coefficients c_j for all signal modes. We repeated the central fit weighting the signal fractions of C subsample using the coefficients in tab. 11.1. The resulting systematic uncertainty is the difference between the results obtained in such a way and the central results.

11.4.2 Efficiency corrections

The relative kinematic efficiency ratios (see sec. 9.1.2) used to convert the ratios of event yields in ratios of branching fractions, were determined within $\mathcal{O}(1.5\%)$ statistical uncertainties. However these results are not perfectly in agreement with the ones obtained in previous works Refs. [122, 88]. While this is crucial for an high precision branching ratio measurement, for the search of the rare modes $B_s^0 \to \pi^+\pi^-$ and $B^0 \to K^+K^-$ these effects are swamped by the statistical uncertainties. Therefore we assign a relative uncertainty on our relative efficiency corrections of

mode	c_j
$B^0 \to \pi^+\pi^-$	1.001
$B^0 \to K^+\pi^-$	0.999
$\overline{B}^0 \to K^-\pi^+$	1.001
$B^0 \to K^+K^-$	1.008
$B^0_s \to \pi^+\pi^-$	0.997
$B^0_s \to K^-\pi^+$	1.003
$\overline{B}^0_s \to K^+\pi^-$	1.000
$B^0_s \to K^+K^-$	1.008
$\Lambda^0_b \to p\pi^-$	0.977
$\overline{\Lambda}^0_b \to \overline{p}\pi^+$	0.982
$\Lambda^0_b \to pK^-$	0.960
$\overline{\Lambda}^0_b \to \overline{p}K^+$	0.967

Table 11.1: Relative factors c_j from simulation. See text.

4.2% which is the difference of the new corrections estimated in sec. 9.1.2 and the old ones as reported in Refs. [122, 88]. We re-evaluated each ratio of branching fractions by using acceptance corrections fluctuated by one standard deviation in either direction. The difference between the resulting branching fraction and the central result was taken as systematic uncertainty. See tabs. 11.2–11.3.

11.4.3 B-isolation efficiency (B-isol.)

The efficiency of the isolation requirement was measured from data (see sec. 9.1.3) with an uncertainty $\approx 2.8\%$ and it contributes to a systematic uncertainty on the measurements of ratios of branching fractions between B^0_s and B^0 decays. We re-evaluated the ratios of branching fractions after fluctuating the relative isolation efficiency by one standard deviation in either directions. The difference between the resulting branching fraction and the central result was used as systematic uncertainty. See tabs. 11.2–11.3.

11.5 Lifetime-related systematic effects

11.5.1 Nominal b-hadrons lifetimes ($B^0_{(s)}$ lifetime)

The selection of the samples used in this analysis relies on cuts on the impact parameter (d_0) of both tracks and on the transverse decay length of the B candidate ($L_{\rm T}$). Therefore we assessed a systematic uncertainty due to the experimental uncertainty of the B^0 and B^0_s lifetime. This affects also the estimate of $c\tau(B^0_s \to K^+K^-)$ and $c\tau(B^0_s \to \pi^+\pi^-)$ since they were extracted from Γ_d and $\Delta\Gamma_s/\Gamma_s$ in the central analysis (see sec. 4.1). The additional systematics due to the uncertainty on

$\Delta\Gamma_s/\Gamma_s$ was evaluated separately in sec. 11.5.2.

To evaluate the systematic uncertainty we generated two simulated samples, one where the B^0 lifetime is increased by a factor 1σ [51] ($c\tau(B^0) = 457.2 + 2.7 = 459.9$ μm) and the B_s^0 lifetime is decreased by a factor 1σ [51] ($c\tau(B_s^0) = 441 - 8 = 433$ μm) and another one where the B^0 lifetime is decreased by a factor 1σ [51] ($c\tau(B^0) = 457.2 - 2.7 = 454.5$ μm) and the B_s^0 lifetime is increased by a factor 1σ [51] ($c\tau(B^0) = 441 + 8 = 449$ μm). We re-evaluated the efficiency correction factors by using these modified simulated samples. The largest difference between the resulting branching fraction obtained and the central result was used as systematic uncertainty. See tabs. 11.2–11.3.

11.5.2 $\Delta\Gamma_s/\Gamma_s$

The measurements involving the $B_s^0 \to K^+K^-$ and $B_s^0 \to \pi^+\pi^-$ decays suffer from the additional systematic uncertainty due to the limited experimental and theoretical knowledge of $\Delta\Gamma_s/\Gamma_s$. To quote the results in the central analysis we used the value $\Delta\Gamma_s/\Gamma_s = 0.092^{+0.051}_{-0.054}$ [51]. Such uncertainty introduces an uncertainty of ± 11 μm in $c\tau(B_s^0 \to K^+K^-)$ and $c\tau(B_s^0 \to \pi^+\pi^-)$. We re-evaluated the efficiency correction factors by using additional simulated samples in which we fluctuated the lifetime of the $B_s^0 \to K^+K^-$ and $B_s^0 \to \pi^+\pi^-$ modes by one standard deviation in either direction ($c\tau(B_s^0 \to K^+K^-) = c\tau(B_s^0 \to \pi^+\pi^-) = 448$ μm and $c\tau(B_s^0 \to K^+K^-) = c\tau(B_s^0 \to \pi^+\pi^-) = 426$ μm). The difference between the resulting branching fraction obtained and the central result was used as systematic uncertainty. See tabs. 11.2–11.3.

11.6 Other systematic uncertainties

11.6.1 Fit Bias

From tab. 8.7 we observed that the relative fraction and the raw yield of $B^0 \to K^+K^-$ decay mode is biased toward positive values. We accounted for this bias assessing an additional systematic uncertainty, which is equal to the size of the bias.

11.6.2 Charge asymmetry correction (charge asymmetry)

The efficiency ratios $\frac{\varepsilon(B^0\to K^+\pi^-)}{\varepsilon(\overline{B}^0\to K^-\pi^+)} = \frac{\varepsilon(\overline{B}_s^0\to K^+\pi^-)}{\varepsilon(B_s^0\to K^-\pi^+)}$, $\frac{\varepsilon(\Lambda_b^0\to p\pi^-)}{\varepsilon(\overline{\Lambda}_b^0\to \overline{p}\pi^+)}$ and $\frac{\varepsilon(\Lambda_b^0\to pK^-)}{\varepsilon(\overline{\Lambda}_b^0\to \overline{p}K^+)}$ were measured with real data (see sec. 10.1) with a total uncertainty $\approx 0.3\%$ for B^0 and B_s^0 and $\approx 2\%$ for Λ_b^0. They contribute to a systematic uncertainty on the related CP-asymmetry measurements.

We re-evaluated the CP related measurements after fluctuating this efficiency ratio by one standard deviation in either direction. The difference between the resulting branching fraction and the central result was used as systematic uncertainty.

See tabs. 11.4–11.2.

11.6.3 Λ_b polarization

In the central fit we assumed no polarization for the Λ_b^0. In case that hadroproduced Λ_b^0 have non–zero polarization, the kinematics of the decay modes would change. This would induce some change in the fit results in consequence of the inaccuracy of parameterizations of the kinematics templates. In the non relativistic worst–case the angular distribution of a final state particle from decays of fully polarized Λ_b^0 is:

$$\frac{dN}{d\cos(\theta^*)} \propto 1 \pm \cos(\theta^*)$$

where θ^* is the polar angle in the center–of–mass reference frame. The $\pm$ choice depends on whether the baryons are positively or negatively polarized. In such case, the global efficiency of reconstructing $\Lambda_b^0 \to p\pi^-$ and $\Lambda_b^0 \to pK^-$ decay modes will be affected of about 1%. However the effect on fit results might be larger since the kinematic variable β is a direct function of θ^* and its distribution strongly depends on θ^* as shown in fig. 11.7. In order to assess a systematic uncertainty due to the possible effects of polarization, we refit the data, allowing for fractions of positively and negatively polarized $\Lambda_b^0 \to p\pi^-$ and $\Lambda_b^0 \to pK^-$. In this fit we used the kinematic distributions obtained reweighting the Monte Carlo distributions for a factor $1 + \cos(\theta^*)$ to parameterize the momentum probability density function of Λ_b^0 $\wp^p_{\mathcal{P}_+}(\beta, p_{\rm tot})$. The same procedure was used for the negative polarization case to obtain $\wp^p_{\mathcal{P}_-}(\beta, p_{\rm tot})$. We introduced in the fit an additional floating parameter $\mathcal{P}$ taking into account the polarization model. The kinematic probability density function $\wp$ of the Λ_b^0 decay modes changes accordingly:

$$\wp^p(\beta, p_{\rm tot}) \to \wp^p(\beta, p_{\rm tot})' = \mathcal{P} \times \wp^p_{\mathcal{P}_+}(\beta, p_{\rm tot}) + (1 - \mathcal{P}) \times \wp^p_{\mathcal{P}_-}(\beta, p_{\rm tot})$$

The fit results show no evidence for polarized Λ_b^0 decay modes, with the current sensitivity: $\mathcal{P} = 0.60 \pm 0.07$ to be compared to $\mathcal{P} = 0.5$ in case of unpolarized baryons, and $\mathcal{P} = 0.55 \pm 0.18$ [37] given by a subsample of the current data corresponding to 1 fb^{-1}. The measured relative branching ratios vary very little with respect to the central fit. The differences between the central fit results and the fit with the polarization parameter were quoted as systematic uncertainties.

11.7 Total systematic uncertainties

A synopsis of all the systematic uncertainties is reported in tabs. 11.2–11.3. The total systematic uncertainty on each measurement has been determined as the sum in quadrature of the single systematic uncertainties. When the systematic uncertainty is asymmetric, the largest value has been used in the squared sum.

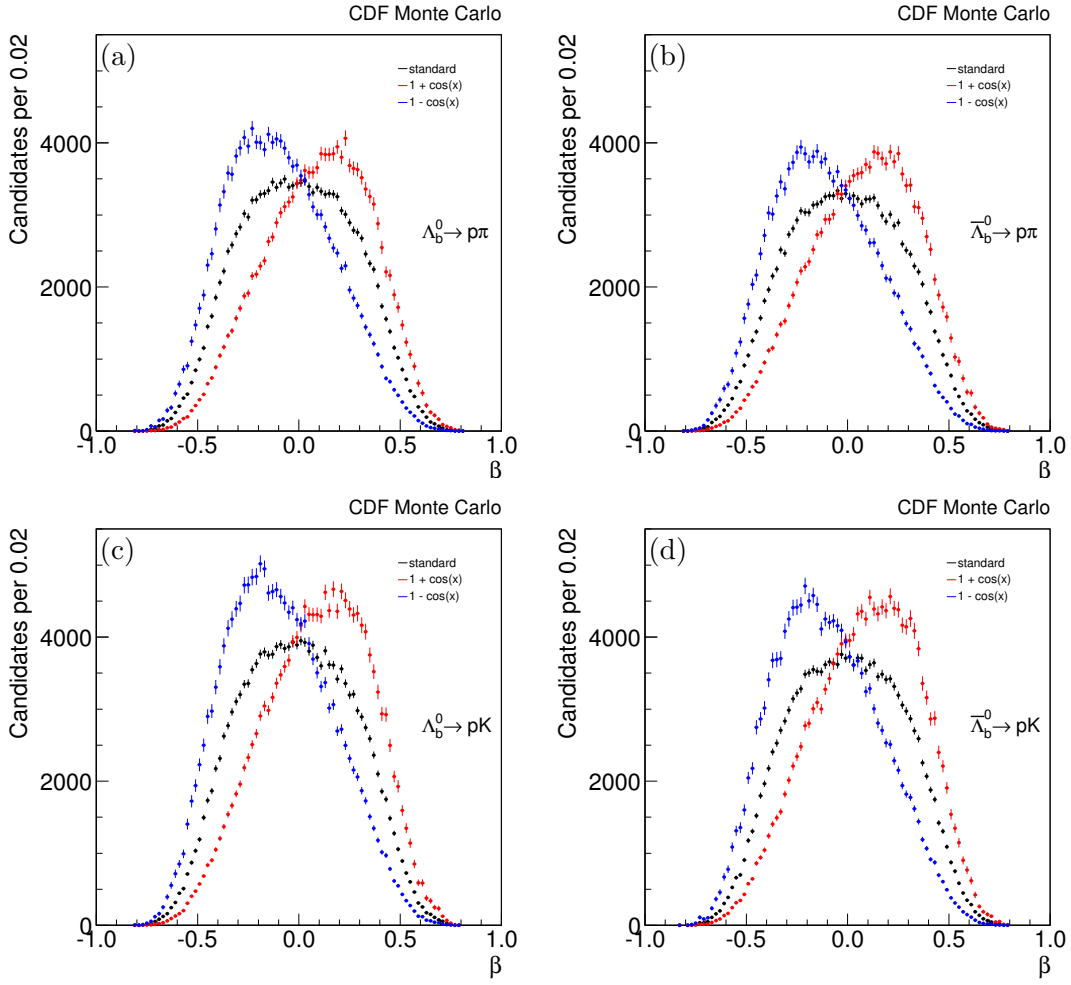

Figure 11.7: β distributions of simulated $\Lambda_b^0 \to p\pi^-$ (a), $\overline{\Lambda}_b^0 \to \overline{p}\pi^+$ (b), $\Lambda_b^0 \to pK^-$ (c) and $\overline{\Lambda}_b^0 \to \overline{p}K^+$ (d) reweighted for $1+\cos\theta^*$ (red line) and $1-\cos\theta^*$ (blue line).

source	$\frac{\mathcal{B}(B^0\to K^+K^-)}{\mathcal{B}(B^0\to K^+\pi^-)}$	$\frac{f_s}{f_d}\times\frac{\mathcal{B}(B_s^0\to\pi^+\pi^-)}{\mathcal{B}(B^0\to K^+\pi^-)}$
Charge asymm. of momentum p.d.f	0.0001	0.0001
Combinatorial back. momentum p.d.f	0.0013	0.0002
Physics back. momentum p.d.f	0.0006	0.
Combinatorial back. mass p.d.f.	0.0001	0.0001
Physics back. mass p.d.f	0.0022	0.0003
Particle Identification model	0.0039	0.0008
$\boldsymbol{p_{\mathrm{T}}(\Lambda_b^0)}$ **spectrum**	0.0006	0.0001
Efficiency corrections	0.0005	0.0004
Triggers relative efficiency	0.0005	0.0001
***B*-isol.**	–	0.0002
$\boldsymbol{\Delta\Gamma_s/\Gamma_s}$	–	0.
Nominal *b*-hadrons lifetimes	–	0.0001
Nominal *b*-hadrons masses	0.0005	0.0002
fit bias	0.0014	–
TOTAL	**0.005**	**0.001**

Table 11.2: Summary of the systematic uncertainties.

source	$\mathcal{N}(B^0 \to K^+K^-)$	$\mathcal{N}(B_s^0 \to \pi^+\pi^-)$
Charge asymm. of momentum p.d.f	1	1
Combinatorial back. momentum p.d.f	13	2
Physics back. momentum p.d.f	7	1
Combinatorial back. mass p.d.f.	1	1
Physics back. mass p.d.f	23	3
Particle Identification model	29	10
$\boldsymbol{p_{\mathrm{T}}(\Lambda_b^0)}$ **spectrum**	6	1
Triggers relative efficiency	5	1
Nominal *b*-hadrons masses	5	3
Fit bias	11	–
TOTAL	**42**	**11**

Table 11.3: Summary of the systematic uncertainties for the yield measurements of rare modes.

source	$\mathcal{A}_{\mathcal{C}P}(B^0 \to K^+\pi^-)$	$\mathcal{A}_{\mathcal{C}P}(B^0_s \to K^-\pi^+)$
Charge asymm. of momentum p.d.f	0.0011	0.0025
Signal momentum p.d.f.	0.0013	0.0043
Combinatorial back. momentum p.d.f	0.0004	0.0072
Physics back. momentum p.d.f	0.0008	0.0002
Signal mass p.d.f.	0.0002	0.0066
Combinatorial back. mass p.d.f.	<0.0001	0.0001
Physics back. mass p.d.f	0.0001	0.0006
Particle Identification model	0.0023	0.0066
Charge asymmetry	0.0018	0.0018
Triggers relative efficiency	0.0003	0.0083
Nominal *b*-hadrons masses	0.0001	0.0049
$\boldsymbol{p_{\mathrm{T}}(\Lambda_b^0)}$ **spectrum**	0.0001	0.0010
Λ_b^0 **polarization**	<0.0001	0.0027
TOTAL	**0.004**	**0.016**
STAT	**0.013**	**0.073**

Table 11.4: Summary of the systematic uncertainties of B–mesons ACPs.

source	$\mathcal{A}_{CP}(\Lambda_b^0 \to p\pi^-)$	$\mathcal{A}_{CP}(\Lambda_b^0 \to pK^-)$
Charge asymm. of momentum p.d.f	0.0009	0.0022
Signal momentum p.d.f.	0.0054	0.0103
Combinatorial back. momentum p.d.f	0.0257	0.0065
Physics back. momentum p.d.f	0.0003	0.0004
Signal mass p.d.f.	0.0018	0.0006
Combinatorial back. mass p.d.f.	<0.0001	<0.0001
Physics back. mass p.d.f	0.0005	0.0001
Particle Identification model	0.0040	0.0046
Charge asymmetry	0.0073	0.0097
Triggers relative efficiency	0.0004	0.0034
Nominal *b*-hadrons masses	0.0007	0.0008
$\boldsymbol{p_{\mathrm{T}}(\Lambda_b^0)}$ **spectrum**	0.0052	0.0021
Λ_b^0 **polarization**	0.0089	0.0364
TOTAL	**0.030**	**0.040**
STAT	**0.074**	**0.080**

Table 11.5: Summary of the systematic uncertainties for $\mathcal{A}_{CP}(\Lambda_b^0 \to p\pi^-)$ and $\mathcal{A}_{CP}(\Lambda_b^0 \to pK^-)$.

11.8 Significance of rare modes signals

In the present work of thesis we searched for the annihilation decay modes $B^0 \to K^+K^-$ and $B_s^0 \to \pi^+\pi^-$still unobserved at the time of the analysis. A correct evaluation of the significance of our results is crucial, because the statistical resolution and the systematics uncertainties is at a level of precision never before achieved for these measurements. We will quote the significance combining statistical and systematic uncertainties.

11.8.1 Test of significance

A test of the current best theory H_0 in favor of an alternative theory H_m, where m indicates the free parameters of the new theory (for example, branching fractions), is specified by defining the set of values of the experimental observables X that will make us decide that H_0 must be rejected ("critical region"); the significance level of the test, indicated by α, is the probability of rejecting H_0 when it is indeed true. α is the probability for X to fall within the critical region, calculated under the assumption that H_0 is true. In the present thesis the significance level α is measured in Gaussian equivalent units ($n\sigma$ where $n = 1, 2, 3, ...$). The notation $\alpha = n\sigma$ correspond to $n\sigma$ single tail of a Gaussian distribution:

$$\alpha = \frac{1}{\sqrt{2\pi}\sigma} \int_{n\sigma}^{+\infty} e^{-\frac{1}{2}\frac{t^2}{\sigma^2}} dt. \tag{11.3}$$

The common practice for claiming new physics discoveries is to require α larger than 5σ, while only a significance of 3σ must be achieved for claiming a signal evidence.

11.8.2 Evaluation of significance

A first estimation of the significance of the $B^0 \to K^+K^-$ and $B_s^0 \to \pi^+\pi^-$ results is done by performing additional fits of composition on real data. For each rare mode ($B^0 \to K^+K^-$, $B_s^0 \to \pi^+\pi^-$) we repeated the fit by fixing its relative fraction to zero. Table 11.6 reports the values of $-2\ln(\mathscr{L})$ of each fit and its difference $-2\Delta\ln(\mathscr{L})$, referred as Likelihood Ratio, with the central fit performed with all relative fractions of rare modes free to vary. Since the distribution of statistical un-

fit	$-2\ln(\mathscr{L})$	$-2\Delta\ln(\mathscr{L})$	α
central fit	-69430.6	0	–
$f_{B^0\to K^+K^-} = 0$	-69423.8	6.8	2.6σ
$f_{B_s^0\to \pi^+\pi^-} = 0$	-69413.3	17.3	4.2σ

Table 11.6: Significance of rare modes computed by performing additional fits of composition on real data. For $B^0 \to K^+K^-$ and $B_s^0 \to \pi^+\pi^-$ decay mode we repeated the fit by fixing its relative fraction to zero.

certainty for each fit parameter is distributed very closely as a Gaussian distribution (see sec. 8.6) the distribution of $-2\Delta\ln(\mathscr{L})$ is distributed with good approximation as a χ^2 distribution with 1 degree of freedom. In fact, for sufficiently regular Likelihoods and in the asymptotic limit, the quantity $-2\Delta\ln(\mathscr{L})$ between two Maximum Likelihood estimators with a difference n in dimensionality, is distributed as a χ^2 with n degrees of freedom. Table 11.6 reports the significance values found for each rare mode and the relative values for $-2\ln(\mathscr{L})$ and the Likelihood Ratio $-2\Delta\ln(\mathscr{L})$. Significance value for $B_s^0 \to \pi^+\pi^-$ is found equal to 4.2σ, larger than 3σ commonly required to claim an evidence of a new signal, while for $B^0 \to K^+K^-$ is equal to 2.6σ. We verified that the distribution of the Likelihood Ratio $-2\Delta\ln(\mathscr{L})$ for each rare mode is regular for values comparable with those reported in the third column of tab. 11.6. We generated about 500 pseudo-experiments for each fit of composition reported in tab. 11.6 and fig. 11.8 shows the distribution of $-2\Delta\ln(\mathscr{L})$. The limited number of pseudo-experiments allows to explore only regions close approximately to significances of 3σ. Higher significance values are hard to explore, since they require a large computing time considering such a sophisticated maximum Likelihood fit.

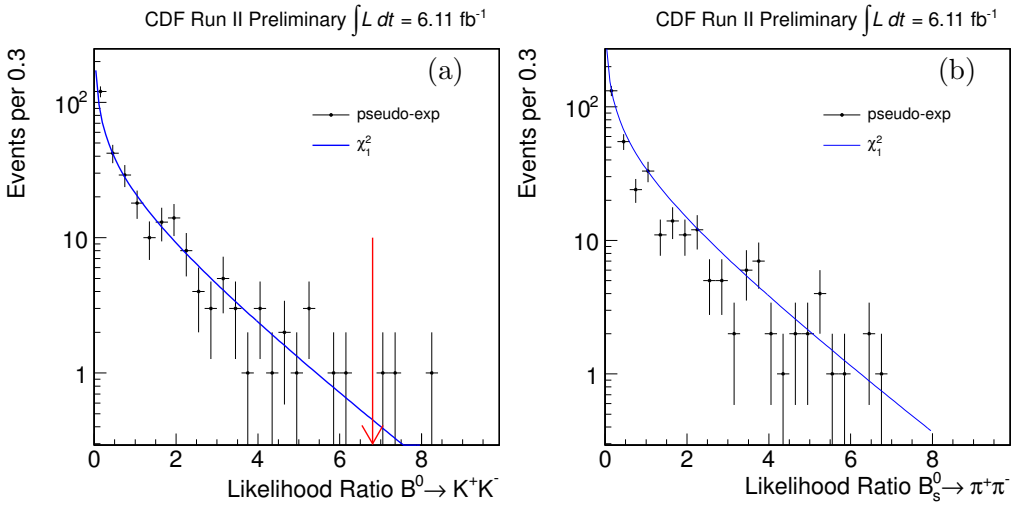

Figure 11.8: Likelihood Ratio distribution for $B^0 \to K^+K^-$ (a) and $B_s^0 \to \pi^+\pi^-$ (b) mode obtained from an ensemble of 500 pseudo-experiments. The red arrow in the $B^0 \to K^+K^-$ (a) plot shows the value of the Likelihood Ratio $-2\Delta\ln(\mathscr{L})$ determined with data (see third column of tab. 11.6).

In fig. 11.9 we report the $\mathcal{PR}$ distribution obtained by the two fits where the $B_s^0 \to \pi^+\pi^-$ and $B^0 \to K^+K^-$ contributions were fixed to zero. The resulting histogram is very similar, but not identical, to the PR histograms of all the other contributions except the $B_s^0 \to \pi^+\pi^-(B^0 \to K^+K^-)$ signal already shown in fig. 8.10. For the $B_s^0 \to \pi^+\pi^-$ plot on the top, it is evident how the large value of $-2\Delta\ln(\mathscr{L})$ is actually driven by the excess in the two last bins, exactly where the $B_s^0 \to \pi^+\pi^-$ signal is expected to show up.

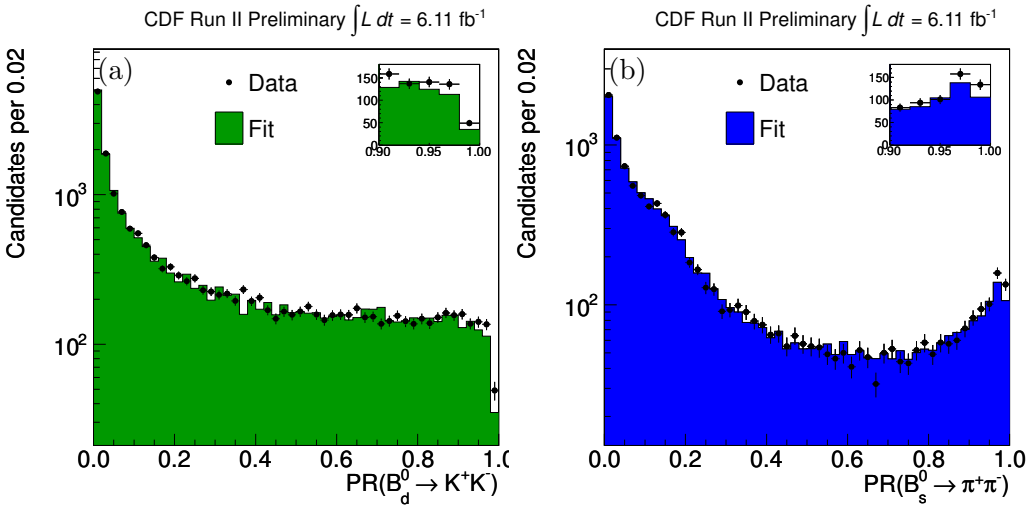

Figure 11.9: Distribution of the probability ratio ($\mathcal{PR}$) of the fits where the $B_s^0 \to \pi^+\pi^-$ (right) and the $B^0 \to K^+K^-$ (left) have been fixed to 0, to give a rough visualization of the significance of the results. The points with the error bars show the distribution obtained on the fitted data sample while the histogram shows the distributions obtained by generating signals and background events directly from the total p.d.f.s of the fit of composition.

The method described above to quote the significance is a standard technique, however it does not keep into account the systematic uncertainty in quoting the significance value. For this reason we used also an other approach, which combines statistical and systematic uncertainty of each measurement, to evaluate the significance. From the statistical point of view this approach is equivalent to the one described above.

The statistical uncertainty to evaluate the significance in this new approach was estimated using an ensemble of 500 pseudo-experiments in which no contribution from the rare signals $B^0 \to K^+K^-$ and $B_s^0 \to \pi^+\pi^-$ was generated, while the relative fraction of all rare modes was left free to vary in each fit of composition. Figure 11.10 shows the distributions of yield determined by the fits of pseudo-experiments. The distributions were fitted with a Gaussian distribution. The mean is centered at zero within the fit resolution while the width is the statistical uncertainty on the yield measurement ($\sigma_0^{stat.}$) with the hypothesis of no rare signal modes in our sample. If N is the yield measured on real data with the complete analysis, $\sigma_N^{stat.}$ is its statistical uncertainty and $\sigma_N^{syst.}$ is its systematic uncertainty (we assume the systematic uncertainty is distributed as a Gaussian) we evaluated the significance, in Gaussian equivalent σ, in the following way:

$$\alpha = \frac{N}{\sqrt{(\sigma_0^{stat.})^2 + (\sigma_N^{syst.})^2}}\sigma. \tag{11.4}$$

Table 11.7 reports (last column) the significance values obtained using this approach that combines statistical and systematic uncertainty. Table 11.7 also reports the values of $\sigma_0^{stat.}$ extracted from the pseudo-experiments with no contributions due to the rare signals and the measurement of yield $N \pm \sigma_N^{stat.} \pm \sigma_N^{syst.}$ for each rare signal modes performed in the present analysis. We obtained a significance for $B^0 \to K^+K^-$ and $B_s^0 \to \pi^+\pi^-$ of 2.0σ and 3.7σ respectively.

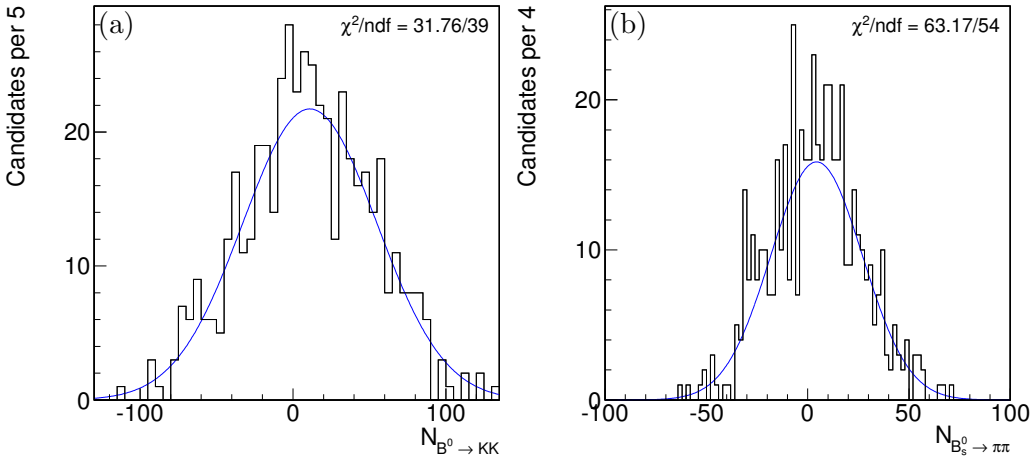

Figure 11.10: Distribution of the number of events for $B^0 \to K^+K^-$ (a) and $B_s^0 \to \pi^+\pi^-$ (b) mode. We used an ensemble of 500 pseudo-experiments in which no contribution from rare signal modes was generated while the relative fraction of all the rare modes was left free to vary in each fit of composition.

mode	$N \pm \sigma_N^{stat.} \pm \sigma_N^{syst.}$	$\sigma_0^{stat.}$	α
$B^0 \to K^+K^-$	$120 \pm 49 \pm 42$	44	2.0σ
$B_s^0 \to \pi^+\pi^-$	$94 \pm 28 \pm 11$	23	3.7σ

Table 11.7: Significance of the rare modes. The significance was estimated by combining the statistical uncertainty on the measurement of each rare mode using an ensemble of pseudo-experiments with no contributions from rare signal modes $\sigma_0^{stat.}$ and the systematic uncertainty $\sigma_N^{syst.}$. See text for details.

After evaluating the significance, we have now all the ingredients to report the measurements and to comment the results in next chap. 12.

Chapter 12

Results and conclusions

This chapter reports the results of this work and contains a brief discussion on their impact on the theoretical framework. It also summarizes the current experimental status.

12.1 Final results

In the present analysis we searched for the pure annihilation decay modes $B^0 \to K^+K^-$ and $B_s^0 \to \pi^+\pi^-$, and we measured the direct $\mathcal{C}P$ violation in the $B^0 \to K^+\pi^-$, $B_s^0 \to K^-\pi^+$, $\Lambda_b^0 \to p\pi^-$, and $\Lambda_b^0 \to pK^-$ decay modes.

Using a sample corresponding to 6.11 fb^{-1} of integrated luminosity, the efficiency-corrected fit results from chap. 9 and the systematics uncertainties from chap. 11 we obtain measurements of the two annihilation decays with a level of precision never achieved before. They correspond to the first evidence for the $B_s^0 \to \pi^+\pi^-$ decay modes, and the most precise measurement of the $\mathcal{B}(B^0 \to K^+K^-)$ at the time of the analysis. The results are summarized in tab. 12.1.

Mode	$\mathcal{N}$	Quantity	Measurement	$\mathcal{B}(10^{-6})$
$B^0 \to K^+K^-$	$120 \pm 49 \pm 42$	$\frac{\mathcal{B}(B^0\to K^+K^-)}{\mathcal{B}(B^0\to K^+\pi^-)}$	$0.012 \pm 0.005 \pm 0.005$	$0.23 \pm 0.10 \pm 0.10$
$B_s^0 \to \pi^+\pi^-$	$94 \pm 28 \pm 11$	$\frac{f_s}{f_d} \times \frac{\mathcal{B}(B_s^0\to \pi^+\pi^-)}{\mathcal{B}(B^0\to K^+\pi^-)}$	$0.008 \pm 0.002 \pm 0.001$	$0.57 \pm 0.15 \pm 0.10$

Table 12.1: Branching fractions. Absolute branching fractions are normalized to the world–average values $\mathcal{B}(B^0 \to K^+\pi^-) = (19.4 \pm 0.6) \times 10^{-6}$ and $f_s = (11.3 \pm 1.3)\%$ and $f_d = (40.1 \pm 1.3)\%$ [51]. $\mathcal{N}$ is the CP–averaged number of fitted events for each mode.

Using a sample corresponding to 9.3 fb^{-1}, the charge-asymmetries corrected fit results from chap. 10 and the systematics uncertainties from chap. 11, we obtain measurements of the $\mathcal{C}P$ violations in $B \to h^+h'^-$ decays summarized in tab. 12.2.

In the next sections we discuss in detail each measurement, and we compare it with the theoretical expectations.

Mode	$\mathcal{N}$	Quantity	Measurement
$B^0 \to K^+\pi^-$	6348 ± 117	$\frac{\mathcal{B}(\overline{B}^0 \to K^-\pi^+) - \mathcal{B}(B^0 \to K^+\pi^-)}{\mathcal{B}(\overline{B}^0 \to K^-\pi^+) + \mathcal{B}(B^0 \to K^+\pi^-)}$	$-0.083 \pm 0.013 \pm 0.004$
$\overline{B}^0 \to K^-\pi^+$	5313 ± 109		
$B_s^0 \to K^-\pi^+$	354 ± 46	$\frac{\mathcal{B}(\overline{B}_s^0 \to K^+\pi^-) - \mathcal{B}(B_s^0 \to K^-\pi^+)}{\mathcal{B}(\overline{B}_s^0 \to K^+\pi^-) + \mathcal{B}(B_s^0 \to K^-\pi^+)}$	$+0.22 \pm 0.07 \pm 0.02$
$\overline{B}_s^0 \to K^+\pi^-$	560 ± 51		
$\Lambda_b^0 \to p\pi^-$	242 ± 24	$\frac{\mathcal{B}(\Lambda_b^0 \to p\pi^-) - \mathcal{B}(\overline{\Lambda}_b^0 \to \overline{p}\pi^+)}{\mathcal{B}(\Lambda_b^0 \to p\pi^-) + \mathcal{B}(\overline{\Lambda}_b^0 \to \overline{p}\pi^+)}$	$+0.06 \pm 0.07 \pm 0.03$
$\overline{\Lambda}_b^0 \to \overline{p}\pi^+$	206 ± 23		
$\Lambda_b^0 \to pK^-$	271 ± 30	$\frac{\mathcal{B}(\Lambda_b^0 \to pK^-) - \mathcal{B}(\overline{\Lambda}_b^0 \to \overline{p}K^+)}{\mathcal{B}(\Lambda_b^0 \to pK^-) + \mathcal{B}(\overline{\Lambda}_b^0 \to \overline{p}K^+)}$	$-0.10 \pm 0.08 \pm 0.04$
$\overline{\Lambda}_b^0 \to \overline{p}K^+$	324 ± 31		

Table 12.2: Direct CP asymmetries. The first quoted uncertainty is statistical, the second is systematic. $\mathcal{N}$ is the number of fitted events for each mode.

12.2 Annihilation modes results

The $B_s^0 \to \pi^+\pi^-$ and the $B^0 \to K^+K^-$ proceed only via annihilation diagrams. Thus a branching ratio at the level of 10^{-7} or less is generally expected. Actually, our $B_s^0 \to \pi^+\pi^-$ result favors a larger annihilation scenario, which is somewhat unexpected, in particular in QCDF calculations. Thus our measurements prompted an intense work of revisiting the calculations. In addition, after our results have been made public in May 2011, LHCb showed the first observation of the $B_s^0 \to \pi^+\pi^-$ decay modes with a value of $\mathcal{B}(B_s^0 \to \pi^+\pi^-) = (0.98^{+0.23}_{-0.19}\ (stat.) \pm 0.11\ (syst.)) \times 10^{-6}$, with a significance of more than 5σ[65], favoring an even larger annihilation scenario. In the following we will discuss our results and we compare them with theoretical predictions.

12.2.1 $B_s^0 \to \pi^+\pi^-$

We report the first evidence of the pure-annihilation $B_s^0 \to \pi^+\pi^-$ decay mode, using a data sample corresponding to 6 fb^{-1}, with a yield of

$$\mathcal{N}(B_s^0 \to \pi^+\pi^-) = 94 \pm 28\ (stat.)\ \pm 11\ (syst.)$$

events, corresponding to a significance of 3.7σ. Using the ratio f_s/f_d of the production fractions between B_s^0 and B^0 from the hadronization of a b-quark in $p\bar{p}$ collision we obtain the measurement of relative branching fraction:

$$\frac{f_s}{f_d} \times \frac{\mathcal{B}(B_s^0 \to \pi^+\pi^-)}{\mathcal{B}(B^0 \to K^+\pi^-)} = 0.008 \pm 0.002\ (stat.)\ \pm 0.001\ (syst.). \tag{12.1}$$

By normalizing the above result to the $B^0 \to K^+\pi^-$ branching fraction by using the world-average value $\mathcal{B}(B^0 \to K^+\pi^-) = (19.4 \pm 0.6) \times 10^{-6}$ [51], and by assuming for f_s/f_d the world-average value from $p\bar{p}$ and e^+e^- collisions, $f_s = (11.3 \pm 1.3)\%$, $f_d = (40.1 \pm 1.3)\%$ [51], we obtain the following results for the absolute branching

fraction:

$$\mathcal{B}(B_s^0 \to \pi^+\pi^-) = (0.57 \pm 0.15\ (stat.) \pm 0.10\ (syst.)) \times 10^{-6}. \tag{12.2}$$

This result corresponds to an improvement in the uncertainty by a factor 2 with respect to of the previous best measurement, coming from the previous version of this analysis $\mathcal{B}(B_s^0 \to \pi^+\pi^-) = (0.52 \pm 0.29\ \ (stat.) \pm 0.38\ \ (syst.)) \times 10^{-6}$[42]. The improved resolution is due to about $\times 3$ statistical increment and to the improvements described during this work of thesis.

Our result favors a large annihilation scenario, which is somewhat unexpected in some QCDF calculations, while our central value is in agreement with the expectations from several calculations available from pQCD or different QCDF approaches.

Within the pQCD approach, Ali et al. predict $\mathcal{B}(B_s^0 \to \pi^+\pi^-) = (0.57^{+0.18}_{-0.16}) \times 10^{-6}$ [57]; in the same approach Li, Lu, Xiao, and Yu calculate $\mathcal{B}(B_s^0 \to \pi^+\pi^-) = (0.42 \pm 0.06) \times 10^{-6}$, but with Sudakov resummation, and including contributions from electroweak and QCD penguin amplitudes [58]. After our results have been published, the pQCD calculations were revisited. Xiao et al. predict $\mathcal{B}(B_s^0 \to \pi^+\pi^-) = (0.51^{+0.20+0.03+0.10+0.03}_{-0.17-0.02-0.08-0.02}) \times 10^{-6}$ [127]. In the same paper it has also been shown that the differences in the predictions from different pQCD approaches are due to slightly different input parameters on the calculations, but all the predictions are consistent with the experimental results. It is also possible to calculate the $B_s^0 \to \pi^+\pi^-$ and the $B^0 \to K^+K^-$ decay modes simultaneously, both in accord with the experimental results. Lastly, Xiao shows also how it is possible to calculate simultaneously the $\mathcal{A}_{\mathcal{C}P}(B_s^0 \to \pi^+\pi^-)$ and $\mathcal{A}_{\mathcal{C}P}(B^0 \to K^+K^-)$. While $\mathcal{A}_{\mathcal{C}P}(B_s^0 \to \pi^+\pi^-)$ is predicted to be too small (about 2%) to be detected at LHCb or CDF, the $\mathcal{A}_{\mathcal{C}P}(B^0 \to K^+K^-)$ should be relatively large (order 19%).

The QCDF approach faces problems in this calculation due to end point singularities, that are parameterized in different ways. Thus the theoretical expressions are complicated and depend on many input parameters including the SM parameters (such as CKM matrix elements, quark masses), Wilson coefficients and the renormalization scales, and some soft and nonperturbative hadronic quantities (such as meson decay constants, form factors, and meson light cone distribution amplitudes). This leads in general to large theoretical uncertainties. Beneke and Neubert, using QCDF, predict values smaller with respect to the pQCD approach, $\mathcal{B}(B_s^0 \to \pi^+\pi^-) = (0.024^{+0.165}_{-0.024}) \times 10^{-6}$ [7], in agreement with Yang et al., that also used QCDF but with a different solution to avoid end-point divergences, obtaining $\mathcal{B}(B_s^0 \to \pi^+\pi^-) = (0.124 \pm 0.028) \times 10^{-6}$ [54].

It can be noted as several approaches based on QCDF, with different parameterization inputs, predict different central values ($\mathcal{B}(B_s^0 \to \pi^+\pi^-) = (0.26^{+0.01}_{-0.09}) \times 10^{-6}$ [55] or $\mathcal{B}(B_s^0 \to \pi^+\pi^-) = 0.022 \times 10^{-6}$ [56]). From the comparison with our results it is possible to observe how in the QCDF approach the predicted branching fractions are systematically below the measurements. Thus our results prompted an intense work, causing a revisit of the QCD factorization calculations. New calcula-

tions by Chang et al. [128] show how it is possible to accommodate the predictions to the experimental results varying the input parameters, but it is then hard to give a consistent QCDF representation for the $\mathcal{B}(B_s^0 \to \pi^+\pi^-)$ and simultaneously other well measured B_d^0 and B_s^0 decays into pseudoscalars (such as $B_s^0 \to K^+K^-$ measurements). Figure 12.1 (courtesy from Prof. Chang Qin, based on [128]) gives a pictorial representations of the constraints given by different measurements on the theoretical input parameters. In particular, fig. 12.1 shows how large annihi-

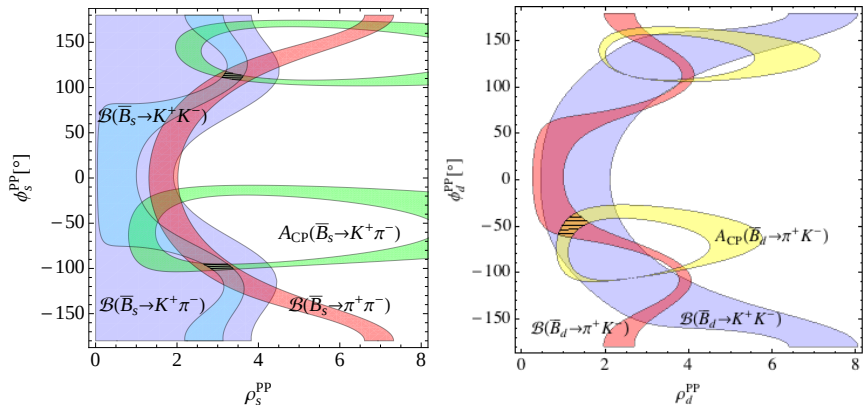

Figure 12.1: The allowed regions for the annihilation parameters $\phi_{s,d}^{PP}$ and $\rho_{s,d}^{PP}$ (from eq. (1.34)) under the constraints from the observables labeled in figures, respectively. The value $\mathcal{B}(B_s^0 \to \pi^+\pi^-) = 0.73 \pm 0.14 \times 10^{-6}$, average between LHCb and CDF measurements, was used. Courtesy from Prof. Chang Qin, based on [128].

lation scenarios can be obtained allowing a value of $\rho_s^{PP} \approx 2$ for the annihilation parameter introduced in eq. (1.34), but this value is strongly disfavored by other well measured $\mathcal{B}$, and it is different from the value $\rho_s^{PP} \approx 1$ adapted in literature. Same conclusions are obtained by Zhu in [129]. Since the more recent LHCb result $\mathcal{B}(B_s^0 \to \pi^+\pi^-) = (0.95^{+0.21}_{-0.17}\ (stat.) \pm 0.13\ (syst.)) \times 10^{-6}$ is even larger, although in agreement with our results, the tension is further increased, which may imply that the parameters (such as ρ_s^{PP}) used in the calculations are non-universal in B_d^0 and B_s^0 decays. If so, the predictive power of the QCD factorization method may be rather limited for many decay channels. Further refined measurements and theoretical studies are so needed to understand the cause of this issue. Finally, fig. 12.2 show the comparison between experimental results and theoretical predictions that have appeared afterwards.

12.2.2 $B^0 \to K^+K^-$

The presence of a large BR$(B_s^0 \to \pi^+\pi^-)$ leads to expect a large BR also for the related channel $B^0 \to K^+K^-$. Although the significance for this channel is limited (2σ), it is meaningful to extract an estimate for the central value of its BR. We

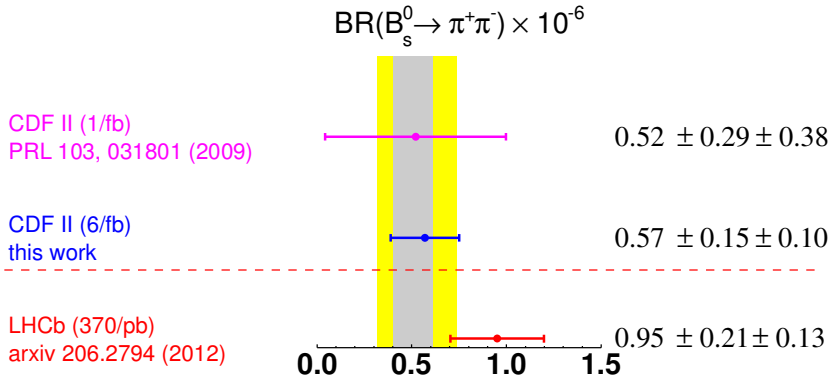

Figure 12.2: Comparison of different experimental results and theoretical calculations for $\mathcal{B}(B_s^0 \to \pi^+\pi^-)$: Xiao calculation $\mathcal{B}(B_s^0 \to \pi^+\pi^-) = (0.51^{+0.23}_{-0.19})\times10^{-6}$ [127] in yellow, one of the possible calculation from Chang $\mathcal{B}(B_s^0 \to \pi^+\pi^-) = (0.50^{+0.11}_{-0.10})\times10^{-6}$ [128] in gray.

report a measurement of the pure-annihilation $B^0 \to K^+K^-$ decay mode, using a sample corresponding to 6 fb^{-1}, with a yield of

$$\mathcal{N}(B^0 \to K^+K^-) = 120 \pm 49\ (stat.)\ \pm 42\ (syst.)$$

events, corresponding to a significance of 2.0σ. We obtain the measurement of relative branching fraction:

$$\frac{\mathcal{B}(B^0 \to K^+K^-)}{\mathcal{B}(B^0 \to K^+\pi^-)} = 0.012 \pm 0.005\ (stat.)\ \pm 0.005\ (syst.). \tag{12.3}$$

By normalizing the above result to the world-average value $\mathcal{B}(B^0 \to K^+\pi^-) = (19.4 \pm 0.6) \times 10^{-6}$ [51], we obtain the following absolute branching fraction:

$$\mathcal{B}(B^0 \to K^+K^-) = (0.23 \pm 0.10\ (stat.) \pm 0.10\ (syst.)) \times 10^{-6}. \tag{12.4}$$

The precision of our result is better than the current measurements.

$$\mathcal{B}(B^0 \to K^+K^-) = \begin{cases} (0.04 \pm 0.15\ (stat.) \pm 0.08\ (syst.)) \times 10^{-6} & \text{BaBar (227M } B\bar{B}\text{) [38]} \\ (0.09^{+0.18}_{-0.13}\ (stat.) \pm 0.01\ (syst.)) \times 10^{-6} & \text{Belle (449M } B\bar{B}\text{) [130]} \end{cases}$$

It supersedes our previous CDF result $\mathcal{B}(B^0 \to K^+K^-) = (0.39 \pm 0.16\ (stat.) \pm 0.12\ (syst.)) \times 10^{-6}$ [42] on 1fb^{-1} of integrated luminosity.

Also, we set a frequentist upper limit (or confidence interval) on the corresponding branching fraction based on Gaussian distributions of the fit pulls (see fig. 8.8) and the Likelihood-Ratio (LR) ordering, following Ref. [131]. Systematic uncertainties were added in quadrature to the statistical uncertainty for a proper inclusion of systematic effects in the extraction of the upper limit. The resulting 90% confidence level (CL) interval on the branching fraction of $B^0 \to K^+K^-$ mode is:

$$[0.05, 0.46] \cdot 10^{-6}\ @\ 90\%\ \text{CL}. \tag{12.5}$$

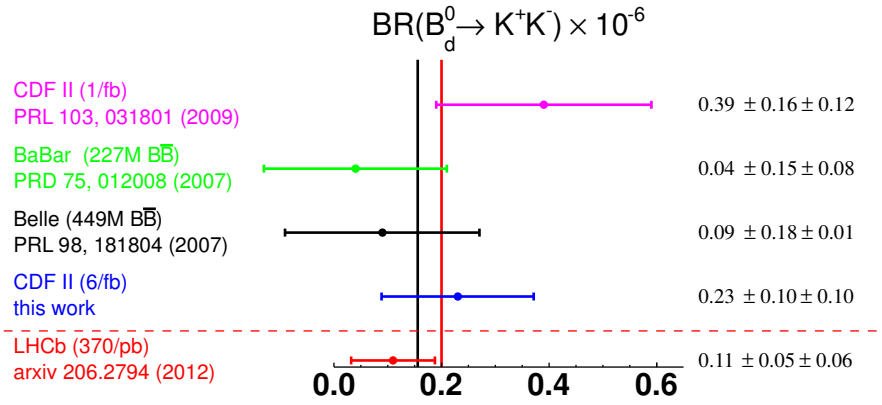

Figure 12.3: Comparison of different experimental results and theoretical calculations for $\mathcal{B}(B^0 \to K^+K^-)$: Xiao calculation $\mathcal{B}(B^0 \to K^+K^-) = (0.156)\times10^{-6}$ [127], black line, and Zhu calculation $\mathcal{B}(B^0 \to K^+K^-) = (0.20)\times10^{-6}$ [129], red line.

The upper bound of this result represents an improvement of approximately 35% with respect to the upper limit, coming from the previous version of this analysis $\mathcal{B}(B^0 \to K^+K^-) < 0.7 \times 10^{-6}$ at 90% CL [42]. It is better than BaBar upper limit, $\mathcal{B}(B^0 \to K^+K^-) < 0.50 \times 10^{-6}$ at 90% CL [38], and very close to the Belle one $\mathcal{B}(B^0 \to K^+K^-) < 0.41 \times 10^{-6}$ at 90%CL [130].

As for the $B^0_s \to \pi^+\pi^-$ decay mode, the QCDF approach has large theoretical uncertainties but the central values predicted are generally below our measurement. Beneke and Neubert, using QCDF, predict $\mathcal{B}(B^0 \to K^+K^-) = (0.013^{+0.087}_{-0.013}) \times 10^{-6}$ [7], while Cheng et al. with different input parameters obtain $\mathcal{B}(B^0 \to K^+K^-) = (0.10 \pm 0.04) \times 10^{-6}$ [55], in agreement with our result.

Following our results, pQCD calculations were revisited, finding $\mathcal{B}(B^0 \to K^+K^-) = 0.156 \times 10^{-6}$ [127]. As for the $B^0_s \to \pi^+\pi^-$ recent calculations from the QCDF approach are able to accomodate the discrepancies between previous predictions and measurements, but using different input parameter from the ones adapted in literature. However, the allowed regions in fig. 12.1 show that the tension between $\rho^{PP}_d = 1$ from eq. (1.34) adopted in literature and the one given by the constraint is stronger in the $B^0_s \to \pi^+\pi^-$ case with respect to the $B^0 \to K^+K^-$ case. This suggests that more precise measurements are needed.

After our results have been made public in May 2011, LHCb reported a measurement of $\mathcal{B}(B^0 \to K^+K^-) = (0.11^{+0.05}_{-0.04} \pm 0.06) \times 10^{-6}$[65], confirming a non negligible annihilation scenario. It should therefore be possible to measure this decay with increased precision with the increased statistics presently available at LHCb.

12.3 $\mathcal{A}_{\mathcal{C}P}$ results

The study of the time-integrated $\mathcal{C}P$ asymmetries in the $B \to h^+h'^-$ decay modes is one of the goal of this thesis. The heavy flavor sector has not yet been fully covered by experiments so far, thus new measurements can reveal the presence of sources of $\mathcal{C}P$ violation beyond the SM. In fact, during the writing of this thesis, first LHCb[119] and then CDF[120] reported hints of unexpectedly large violation in the charm sector, prompting theoretical work to understand the consequence of these results. So today is the appropriate time for a more intensive and more accurate study of the less known B_s^0 and Λ_b^0 sector, where new surprises can be hidden. Using the fit results from sec. 8.3, the efficiency corrections from sec. 9.1 and the systematic uncertainties from sec. 11.7 we obtain the measurements of time-integrated direct $\mathcal{C}P$ asymmetries of two-body b-hadron decays into charmless, charged pseudo-scalar mesons at CDF with 9.3 fb^{-1} of data. Since the size is predicted is small in the $\mathcal{A}_{\mathcal{C}P}$ measurements we neglected the possible contributions of the double Cabibbo suppressed (DCS) decays (such as $B^0 \to K^-\pi^+$ or $\bar{B}^0 \to K^+\pi^-$), asymmetries in the flavor mixing ($B^0 \to \bar{B}^0 \to K^-\pi^+$ and $\bar{B}^0 \to B^0 \to K^+\pi^-$) and possible combined effects.

12.3.1 $\mathcal{A}_{\mathcal{C}P}(B^0 \to K^+\pi^-)$

We report a measurement of

$$\mathcal{A}_{\mathcal{C}P}(B^0 \to K^+\pi^-) = -0.083 \pm 0.013 \pm 0.004, \tag{12.6}$$

with a significance more than 5σ. The uncertainty of the observed asymmetry is consistent and of comparable accuracy with recent results from asymmetric e^+e^- colliders [64], [35], while LHCb recently reported a more precise measurement [9].

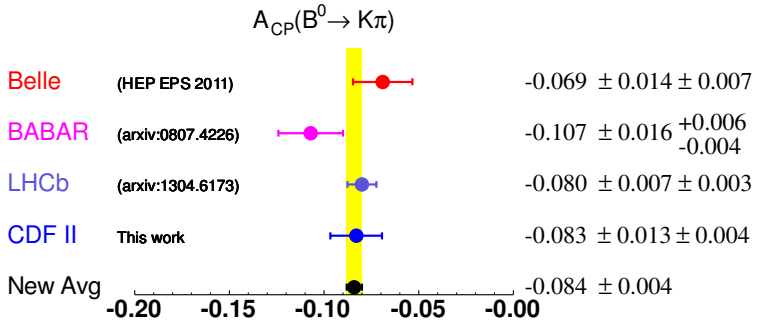

Figure 12.4: Current measurements of $\mathcal{A}_{\mathcal{C}P}(B^0 \to K^+\pi^-)$ as reported on HFAG [47]; the recent LHCb measurement is from Ref. [9]. The yellow band is the resulting average.

As explained in sec. 1.6.1, the comparison between $\mathcal{A}_{\mathcal{C}P}(B^0 \to K^+\pi^-)$ and $\mathcal{A}_{\mathcal{C}P}(B^+ \to K^+\pi^0)$ is a test to confirm theoretical predictions: due to the isospin

asymmetry, several authors [6, 45, 46] predicts equal values for the two measurements in the SM. The new experimental measurements $\mathcal{A}_{\mathcal{C}P}(B^0 \to K^+\pi^-)$ average confirms the deviation of 5σ order with respect to the $\mathcal{C}P$ asymmetry in $\mathcal{A}_{\mathcal{C}P}(B^+ \to K^+\pi^0) = 0.040 \pm 0.021$ [47]. Simple extensions of the standard model could accommodate the discrepancy [48], but uncertainty on the contribution of higher-order SM amplitudes has prevented a firm conclusion [49].

Recently, Lipkin suggested a way [50] to accommodate this discrepancy within the SM, taking into account only constraints imposed by the Pauli principle, but ultimately the question about a possible NP explanation of this discrepancy is still open. High accuracy measurements of the violation of $\mathcal{C}P$ symmetry in charmless modes remains a very interesting subject of study and may provide useful information to our comprehension of this discrepancy. The measurements of direct $\mathcal{C}P$ violation in $B_s^0 \to K^-\pi^+$ decays have been proposed as a test to understand if the $\mathcal{C}P$ violation in the $B^0 \to K^+\pi^-$ origins from NP effects or can be explained just using SM predictions. In the following section we report the $\mathcal{A}_{\mathcal{C}P}(B_s^0 \to K^-\pi^+)$ measurement performed during this work of thesis.

12.3.2 $\mathcal{A}_{\mathcal{C}P}(B_s^0 \to K^-\pi^+)$

Using full CDF II data sample corresponding to 9fb^{-1}, we report a measurement of

$$\mathcal{A}_{\mathcal{C}P}(B_s^0 \to K^-\pi^+) = +0.22 \pm 0.07\ (stat.) \pm 0.02\ (syst.), \tag{12.7}$$

with a significance of 3σ. This result confirms the first observation reported recently at LHCb $\mathcal{A}_{\mathcal{C}P}(B_s^0 \to K^-\pi^+) = 0.27 \pm 0.04\ (stat.) \pm 0.01\ (syst.)$ [9]. The averaged value between this result and LHCb measurement is equal to $\mathcal{A}_{\mathcal{C}P}(B_s^0 \to K^-\pi^+)_{\text{mean}} = +0.26 \pm 0.04$. It is compatible with the pQCD approach prediction $\mathcal{A}_{\mathcal{C}P}(B_s^0 \to K^-\pi^+) = +0.241^{+0.039+0.033+0.023}_{-0.036-0.030-0.012}$ [57] and with recent calculations within the QCD factorization approach [55] $\mathcal{A}_{\mathcal{C}P}(B_s^0 \to K^-\pi^+) = 0.207^{+0.050+0.039}_{-0.030-0.088}$. In the SCET framework a value of $\mathcal{A}_{\mathcal{C}P}(B_s^0 \to K^-\pi^+) = 0.20 \pm 0.17 \pm 0.19 \pm 0.05$ is obtained, with large theoretical uncertainties. The LHCb and CDF measurements are the first $\mathcal{A}_{\mathcal{C}P}$ measurements in charmless B_s^0 decays, and represent a large step forward in our knowledge of these decay modes. The $\mathcal{A}_{\mathcal{C}P}(B_s^0 \to K^-\pi^+)$ measurement can be used to perform test of the Standard Model, such as the comparison between $\mathcal{A}_{\mathcal{C}P}(B_s^0 \to K^-\pi^+)$ and $\mathcal{A}_{\mathcal{C}P}^{\text{dir}}(B^0 \to \pi^+\pi^-)$, the direct $\mathcal{C}P$ asymmetry in $B^0 \to \pi^+\pi^-$ decay. Under the assumption of neglecting W-exchange and penguins annihilations contributing to $B_{(s)}^0 \to h^+h'^-$ decays the decay rates and $\mathcal{C}P$-asymmetries in the $B_s^0 \to K^-\pi^+$ and $B^0 \to \pi^+\pi^-$ are related by the SU(3) symmetry. In this limit the SM predict:

$$\mathcal{A}_{\mathcal{C}P}(B_s^0 \to K^-\pi^+) = \mathcal{A}_{\mathcal{C}P}^{\text{dir}}(B^0 \to \pi^+\pi^-). \tag{12.8}$$

In these assumptions, deviations from this relation are expected to be due to U-spin symmetry breaking. The current experimental results are:

$$\mathcal{A}_{\rm CP}^{\rm dir}(B^0 \to \pi^+\pi^-) = \begin{cases} +0.33 \pm 0.06\ (stat.) \pm 0.03\ (syst.) & \text{Belle [124]} \\ +0.21 \pm 0.09\ (stat.) \pm 0.02\ (syst.) & \text{BaBar [125]} \\ +0.11 \pm 0.21\ (stat.) \pm 0.03\ (syst.) & \text{LHCb [126].} \end{cases} \quad (12.9)$$

The three measurements are in agreement at about 1σ level, and are also in agreement with the averaged value of $\mathcal{A}_{\mathcal{C}P}(B_s^0 \to K^-\pi^+) = 0.24 \pm 0.05$. Actually, in view of the results obtained in this thesis for $\mathcal{B}(B_s^0 \to \pi^+\pi^-)$ and $\mathcal{B}(B^0 \to K^+K^-)$, one may need to reconsider the assumption of neglecting W-exchange and penguins annihilations contributions. Still, more precise measurements are possible, and welcome, at LHCb, where the statistical resolution is still the dominant source of uncertainty.

In conclusion, we performed the $\mathcal{A}_{\mathcal{C}P}(B_s^0 \to K^-\pi^+)$ measurement using the full CDF II data sample of about 9 fb^{-1}. As far as today, the limiting factor in the $\mathcal{A}_{\mathcal{C}P}(B_s^0 \to K^-\pi^+)$ measurements for CDF and LHCb is the statistical uncertainty. While this result is the last for CDF, at LHCb the statistical resolution is expected to further decrease with the increasing in data taking. While the statistical resolution decreases, the improvements in the systematic uncertainties will become fundamental to perform updated measurements.

Lipkin-Gronau test

As explained in sec. 1.6.2, under simple assumptions the standard model predicts a simple relationship between $\mathcal{A}_{\mathcal{C}P}(B_s^0 \to K^-\pi^+)$ and $\mathcal{A}_{\mathcal{C}P}(B^0 \to K^+\pi^-)$:

$$\Gamma(B_s^0 \to K^-\pi^+) - \Gamma(\overline{B}_s^0 \to K^+\pi^-) = \Gamma(\overline{B}^0 \to K^-\pi^+) - \Gamma(B^0 \to K^+\pi^-), \quad (12.10)$$

$$\mathcal{A}_{\mathcal{C}P}(B_s^0 \to K^-\pi^+) = -\mathcal{A}_{\mathcal{C}P}(B^0 \to K^+\pi^-) \times \frac{\mathcal{B}(B^0 \to K^+\pi^-)}{\mathcal{B}(B_s^0 \to K^-\pi^+)} \times \frac{\tau(B_s^0)}{\tau(B^0)}. \quad (12.11)$$

Using the $\mathcal{A}_{\mathcal{C}P}(B^0 \to K^+\pi^-) = -0.086 \pm 0.007$ average from the experimental measurements [47], $\mathcal{B}(B_s^0 \to K^-\pi^+) = (5.4 \pm 0.6) \times 10^{-6}$ and $\mathcal{B}(B^0 \to K^+\pi^-) = (19.55^{+0.54}_{-0.53}) \times 10^{-6}$ from [47], $\tau(B^0) = (1.519 \pm 0.007) \times 10^{-12}$ and $\tau(B_s^0) = (1.497 \pm 0.015) \times 10^{-12}$ from [51], eq. (12.11) predicts:

$$\mathcal{A}_{\mathcal{C}P}(B_s^0 \to K^-\pi^+)|^{SM} = 0.31 \pm 0.04. \quad (12.12)$$

which is compatible at about 1σ level with our result. Assuming this relationship valid only within the SM, a different configuration would be due to the presence of a different source of $\mathcal{C}P$ from NP.

12.3.3 $\mathcal{A}_{\mathcal{C}P}(\Lambda_b^0 \to ph^-)$

Using the full CDF II data sample, we measured

$$\mathcal{A}_{\mathcal{C}P}(\Lambda_b^0 \to p\pi^-) = \frac{\mathcal{B}(\Lambda_b^0 \to p\pi^-) - \mathcal{B}(\overline{\Lambda}_b^0 \to \overline{p}\pi^+)}{\mathcal{B}(\Lambda_b^0 \to p\pi^-) + \mathcal{B}(\overline{\Lambda}_b^0 \to \overline{p}\pi^+)} = +0.06 \pm 0.07 \pm 0.03$$

$$\mathcal{A}_{\mathcal{C}P}(\Lambda_b^0 \to pK^-) = \frac{\mathcal{B}(\Lambda_b^0 \to pK^-) - \mathcal{B}(\overline{\Lambda}_b^0 \to \overline{p}K^+)}{\mathcal{B}(\Lambda_b^0 \to pK^-) + \mathcal{B}(\overline{\Lambda}_b^0 \to \overline{p}K^+)} = -0.10 \pm 0.08 \pm 0.04$$

These measurements were performed using the final CDF data sample; being unique to CDF, they are the world's best up to date. The observed asymmetry are consistent with zero. The experimental precision achieved allows for the first time to investigate the $\mathcal{A}_{\mathcal{C}P}$ values with uncertainties below the 10% level. Still, the precision does not allow a conclusive discrimination between the standard model prediction (8%) and much suppressed values ($\approx 0.3\%$) expected in R–parity violating supersymmetric scenarios [52]. Recent pQCD calculations [53], with large theoretical uncertainties, predict a central value of $\mathcal{A}_{\mathcal{C}P}(\Lambda_b^0 \to pK^-) \approx +5\%$, while the expected central value for the $\mathcal{A}_{\mathcal{C}P}(\Lambda_b^0 \to p\pi^-)$ is larger, about +30%. The observed asymmetries are consistent with the previous results from CDF in Ref. [37] and supersedes them.

As for the other $B \to h^+h'^-$ decay modes, only at LHCb it is possible to perform high precision direct $\mathcal{C}P$ violation measurements in these decay modes. As far as the statistical resolution will increase, the understanding of all the systematic uncertainties will be playing a fundamental role in performing the analyses.

12.4 Conclusions

In this thesis I report on several results obtained from an accurate analysis of the $B \to h^+h'^-$ data sample:

Annihilation decay modes: using 6 fb^{-1} of data collected by the CDF experiment, I obtained the **first evidence of the** $B_s^0 \to \pi^+\pi^-$ decay mode, with a significance of about 3.7σ, and I performed the most precise measurement of the Branching Ratio of the $B_d^0 \to K^+K^-$ decay mode at the time, corresponding to an excess of 2σ level. These measurements have important consequences as discussed in the previous sections: the comparison between these branching fractions and the theoretical predictions provides unique information for tuning the phenomenological models. Our results prompted intense theoretical work both using pQCD and QCDF approaches to accommodate the discrepancies between predictions and experimental results.

$\mathcal{C}P$ **violation:** using the full CDF 10 fb^{-1} of data collected by the CDF experiment, I found evidence of the **CP violation** of $B_s^0 \to K\pi$ decay mode,

with a significance of 3σ, confirming the result recently obtained at LHCb. I also measured the $\mathcal{C}P$ asymmetries of the $B^0_d \to K\pi$ decay modes, in agreement and of comparable resolution with the b-factories experiments, while the most precise measurement up to date is from LHCb. The precision reached in the $\mathcal{A}_{\mathcal{C}P}(B^0_s \to K^-\pi^+)$ measurement gives the possibility to perform interesting checks of the Standard Model predictions, explained in the previous sections. I also obtained the world's best measurements of the $\mathcal{C}P$ asymmetries in $\Lambda^0_b \to p\pi$ and $\Lambda^0_b \to pK$ decay modes. These measurements are unique and represent a step forward in the understanding of the $\mathcal{C}P$ violation phenomena in the relatively unexplored Λ^0_b sector.

All the results of this thesis have been approved by the CDF collaboration; the BR measurements have been published in Phys. Rev. Lett. 108, 211803 (2012) [132], while the $\mathcal{A}_{\mathcal{C}P}$ measurements are under internal review for publication.

Appendices

Appendix A

Parameterization of $\wp(\beta,p_{\rm tot})$

This appendix reports the parameterization of $\wp(\beta,p_{\rm tot})$ for the simulated $B^0 \to K^+\pi^-$ and $\overline{B}^0 \to K^-\pi^+$ decay modes, as an example. The other $B \to h^+h'^-$ decay modes have similar parameterizations and were not reported here, not to weight down the text.

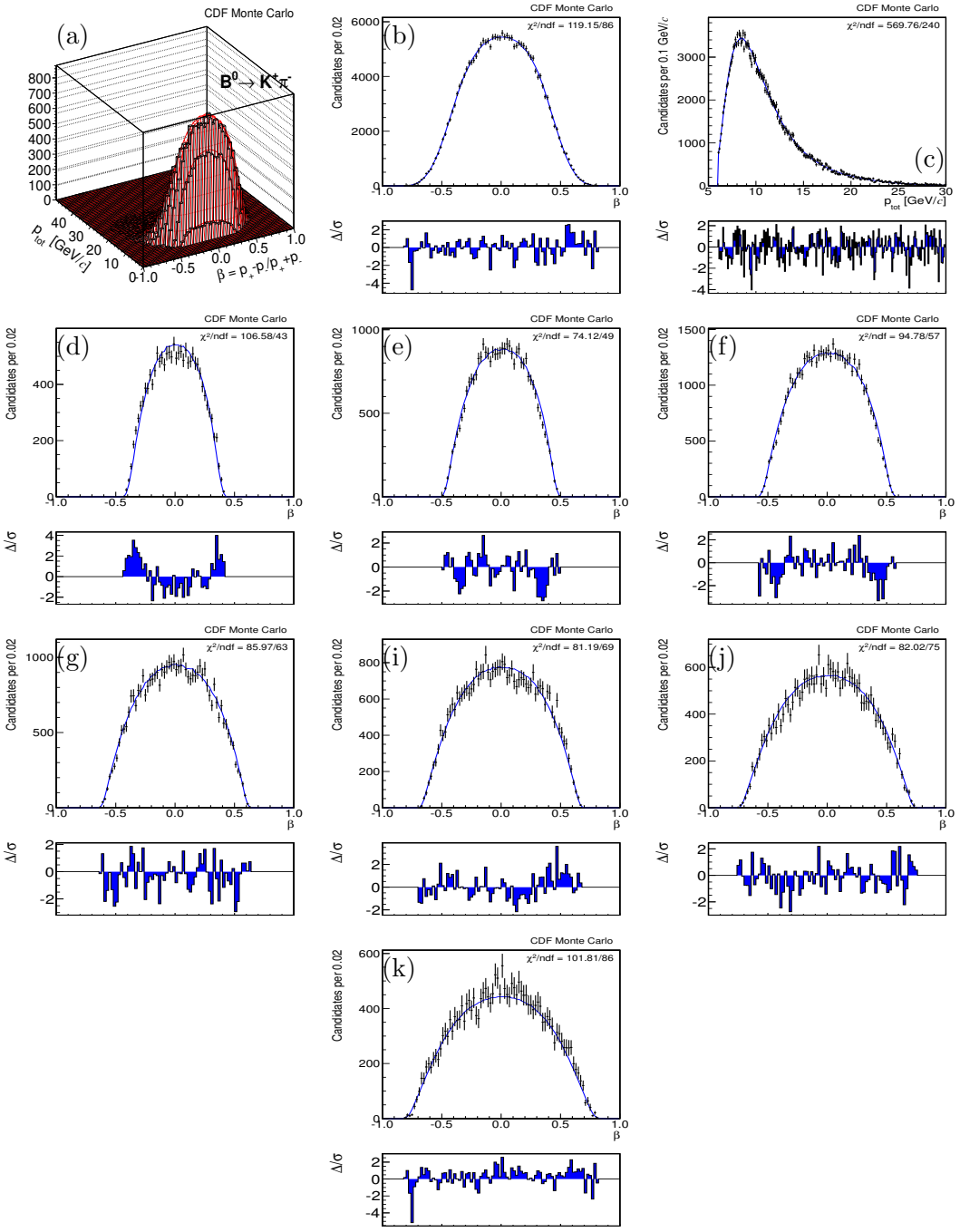

Figure A.1: Templates of the two-dimensianal joint distribution for the $B^0 \to K^+\pi^-$ decay mode (`med`). (a) 2-dimensional projection, (b) β projection, (c) $p_{\rm tot}$ projection, (d)−(k) projections of β in $p_{\rm tot}$ slices.

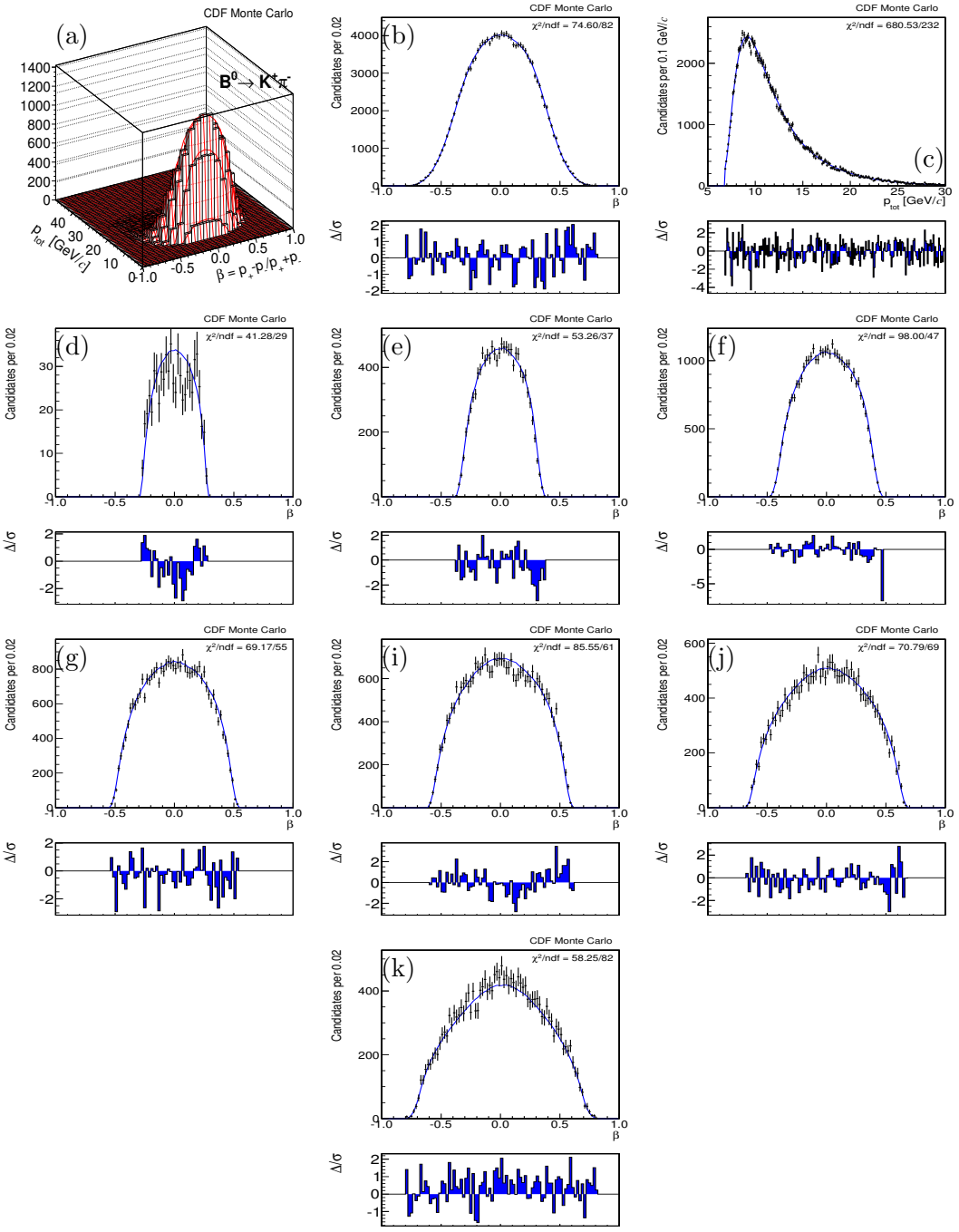

Figure A.2: Templates of the two-dimensianal joint distribution for the $B^0 \to K^+\pi^-$ decay mode (`high`). (a) 2-dimensional projection, (b) β projection, (c) $p_{\rm tot}$ projection, (d)−(k) projections of β in $p_{\rm tot}$ slices.

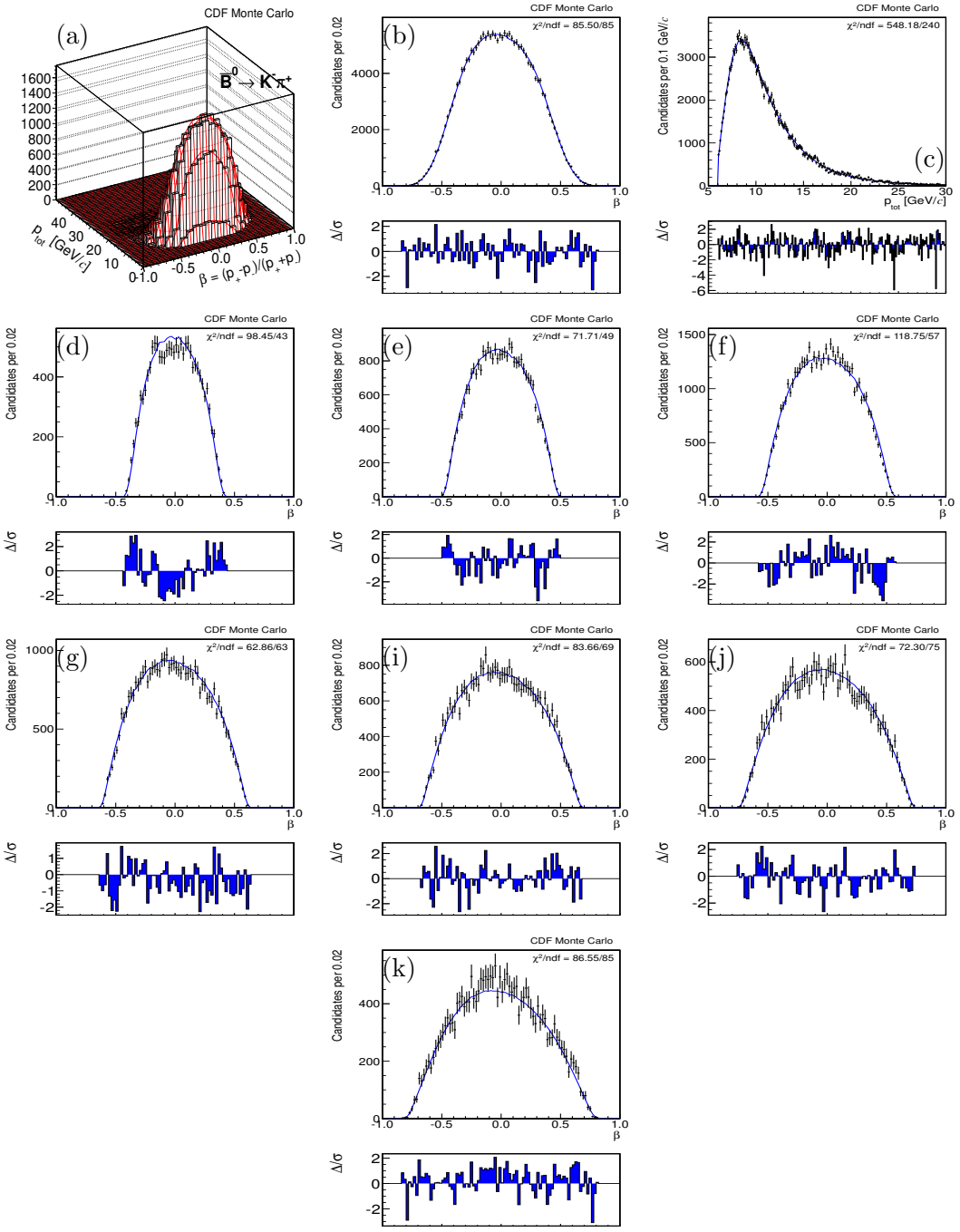

Figure A.3: Templates of the two-dimensianal joint distribution for the $\overline{B}^0 \to K^-\pi^+$ decay mode (`med`). (a) 2-dimensional projection, (b) β projection, (c) $p_{\rm tot}$ projection, (d)−(k) projections of β in $p_{\rm tot}$ slices.

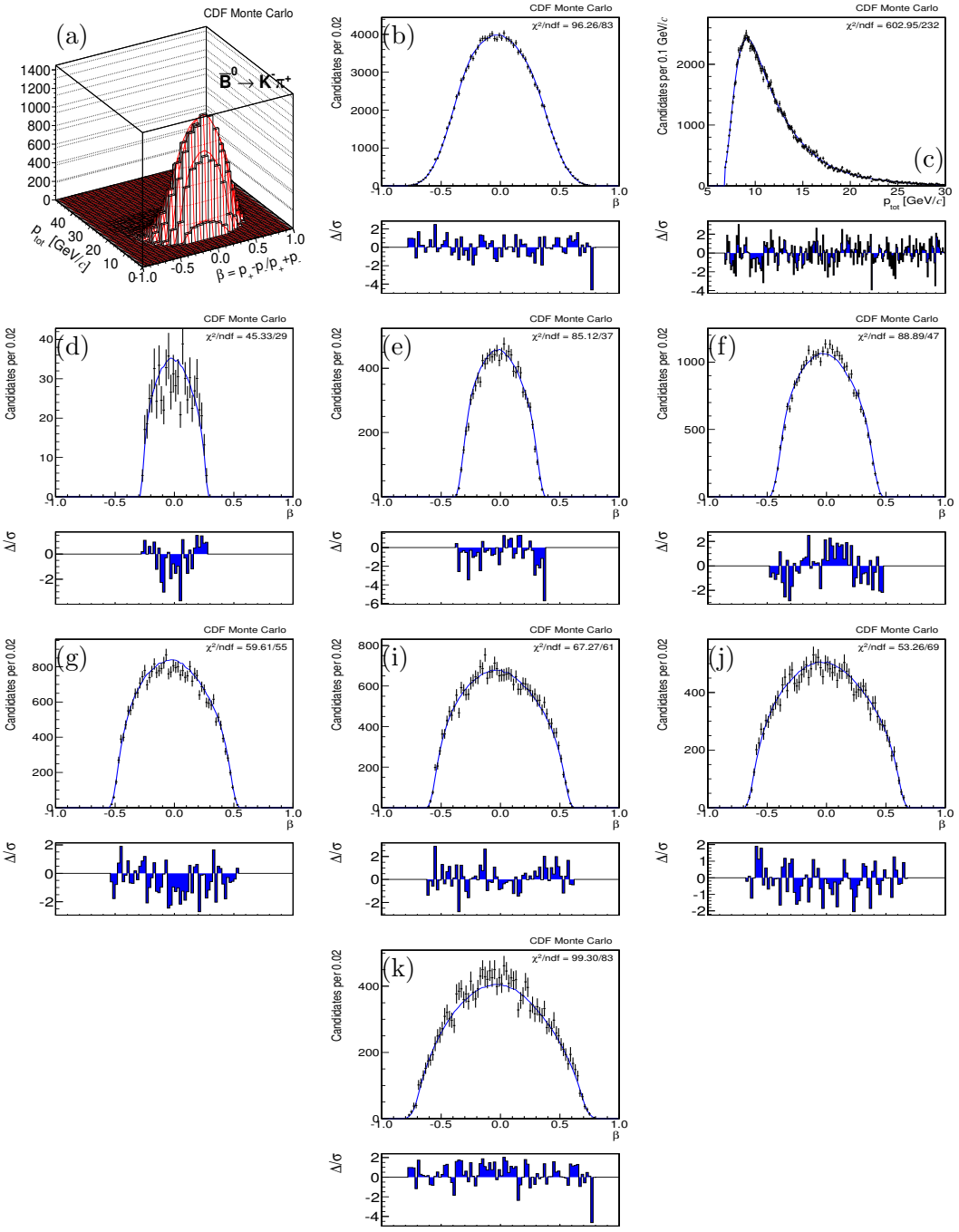

Figure A.4: Templates of the two-dimensianal joint distribution for the $\overline{B}^0 \to K^- \pi^+$ decay mode (`high`). (a) 2-dimensional projection, (b) β projection, (c) $p_{\rm tot}$ projection, (d)−(k) projections of β in $p_{\rm tot}$ slices.

Appendix B

Check of the dE/dx calibration

We checked that the official CDF dE/dx calibration [133], performed up to about 3 fb^{-1}, can be extended up to 9 fb^{-1} without compromising the performances in separating different classes of particles. Thus we applied the calibration following the standard prescriptions as described in Ref. [133]. We plotted the corrected dE/dx for pions, kaons and protons as a function of the following macroscopic observables: run number, number of dE/dx hits, instantaneous luminosity, pseudorapidity, azimuthal angle and secance. The distributions for charged pions and kaons coming from $D^0 \to K^-\pi^+$ decays are shown in fig. B.1, while those for protons and pions coming from $\Lambda \to p\pi^-$ decays are shown in fig. B.2.

The distributions for XFT-triggered pions, kaons and protons do not show any relevant issues and are compatible with the same distributions shown in Ref. [133]. We observed some issues only in the calibration of the dE/dx in function of the run number, in the first periods of data taking, corresponding to the first 400 pb^{-1} of data. In this period of time, the performance of the COT was compromised and the resultant effects are difficult to calibrate, as shown in fig. B.3 and reported in [133]. In principle, this problem in the calibration can affect the results of the $\mathcal{A}_{CP}$ analysis. Thus we decided to exclude these events form this work of thesis, losing 400 pb^{-1} of data but gaining in accuracy. After excluding this data, the calibration is found to be satisfactory. Just some small issues can be however observed for non-triggered soft pions. The calibration has been done only for triggered tracks, and some difficulties can raise when it is applied to very low momentum tracks, below 2 GeV/c. For instance we expect that the correction as a function of the secance does not accurately work for low momentum tracks since it has been done only for triggered tracks. However this is not a main stopper for the aim of this work, since we are interested in modeling the dE/dx response only for triggered tracks. The low momentum pions are a different chapter and are beyond our current scope. We just expect to get a larger correlation between protons and pions from $\Lambda \to p\pi^-$ with respect to that one between pions and kaons from $D^0 \to K^-\pi^+$ decays.

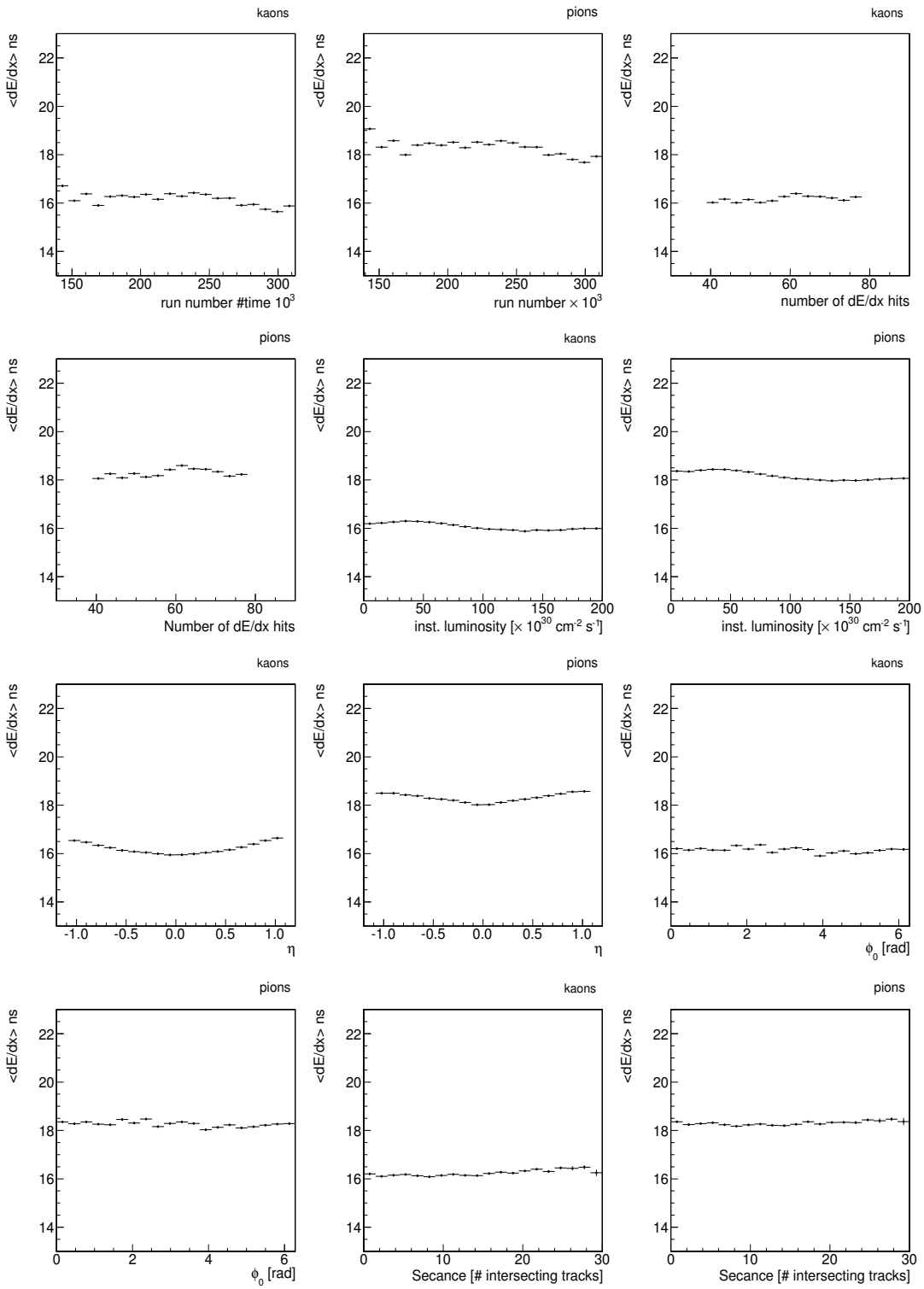

Figure B.1: Corrected dE/dx for pions and kaons from $D^0 \to K^-\pi^+$ decays up to 9 fb^{-1}.

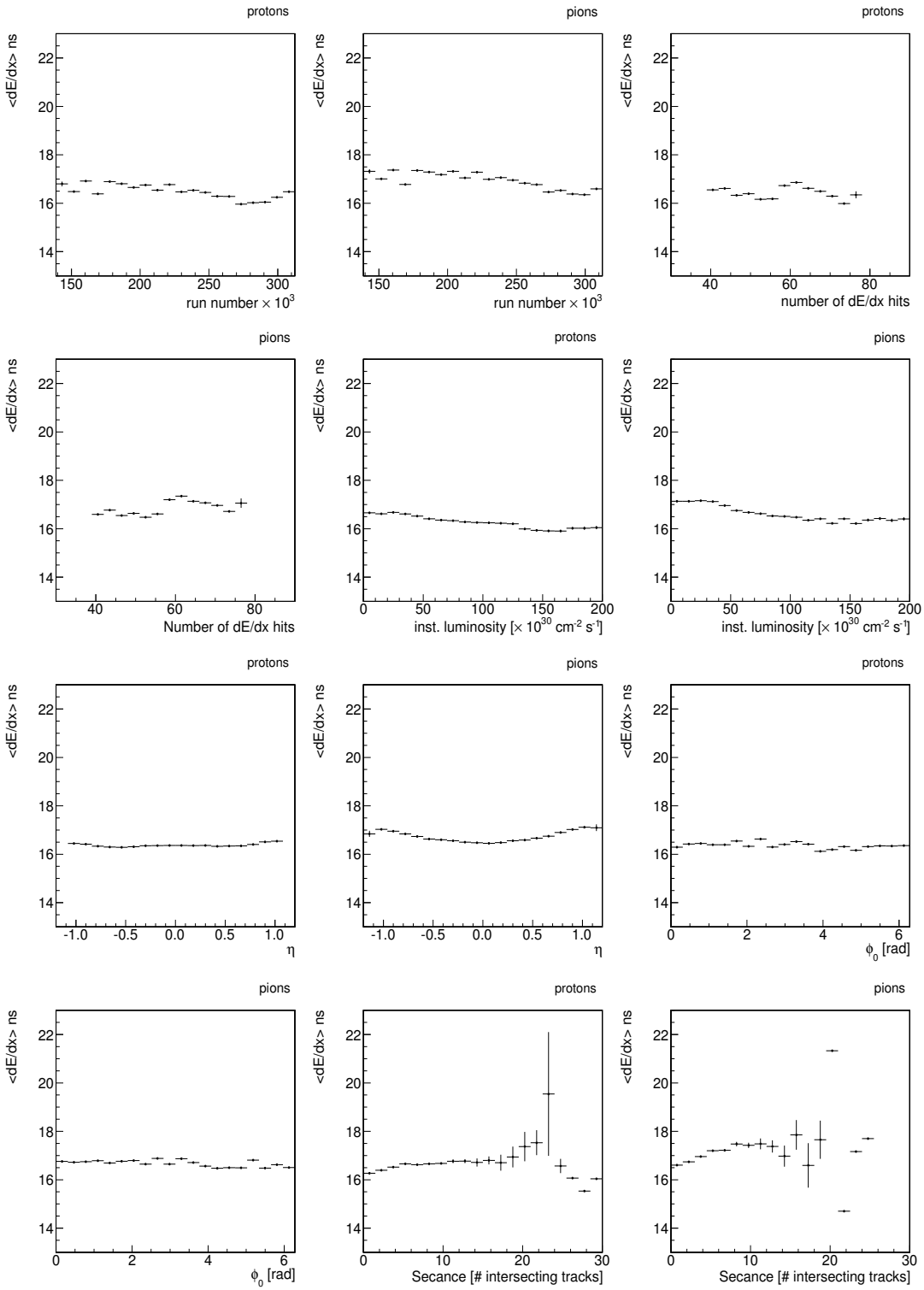

Figure B.2: Corrected dE/dx for pions and protons from $\Lambda \to p\pi^-$ decays up to 9 fb^{-1}.

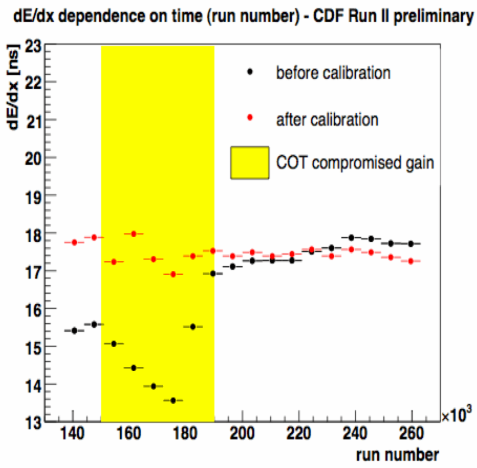

Figure B.3: dEdx dependence on run number. The yellow box enlighten the COT compromised runs, where the calibration is not trivial. Fig. from [133]

Appendix C

Search for annihilation modes

C.1 Introduction

We described in detail the analysis of the measurement of the $\mathcal{C}P$ asymmetries on 9 fb^{-1}. In this appendix we focus our attention on the analysis of the annihilation modes, which provided very important results: the first evidence for charmless annihilation $B_s^0 \to \pi^+\pi^-$ decays, and the first two-sided limit of $\mathcal{B}(B^0 \to K^+K^-)$.

Even if these measurements have been performed using 6 fb^{-1}, and therefore can be considered as an intermediate step of the $\mathcal{C}P$ analysis, there are some substantial differences that are worth describing. The annihilation modes analysis is a search for rare not yet observed decay modes, thus the significance of the results is the key point of the analysis. Therefore particular attention has been given to the evaluation of the systematics uncertainties, to the checks of the fit results, and to the evaluation of the significance itself. In addition, the knowledge gained during the annihilation mode analysis has been used to increase the accuracy of the $\mathcal{C}P$ violation analysis. Thus some the technical points, explained in the following, are different in the two analyses.

C.2 Data sample and selection

The analysis of the annihilation decay modes was performed using data collected between February 2002 (run 138809) and February 2010 (run 289197) by the trigger on displaced tracks. After the application of standard CDF data-quality requirements (see sec. 2.5), the sample size corresponds to an integrated luminosity of about 6.11 fb^{-1}. The reconstruction of $B \to h^+h'^-$ candidates is the same as the one already introduced in sec. 3.3 exploiting the full CDF data sample, and we used the same cuts selection (as reported in tab. 3.3). This cuts selection was specifically made to optimize the probability of discovery of the $B_s^0 \to K^-\pi^+$ mode, and have been proven to be optimal also for the detection of $B_s^0 \to \pi^+\pi^-$. After the selection, a total number of about 24,000 events is found, to be compared with about 28,200

events of the full CDF data sample. This corresponds to a difference in statistics of a factor about 0.85. The comparison between the $m_{\pi^+\pi^-}$ distributions of the candidates for the two samples is shown in fig. C.1.

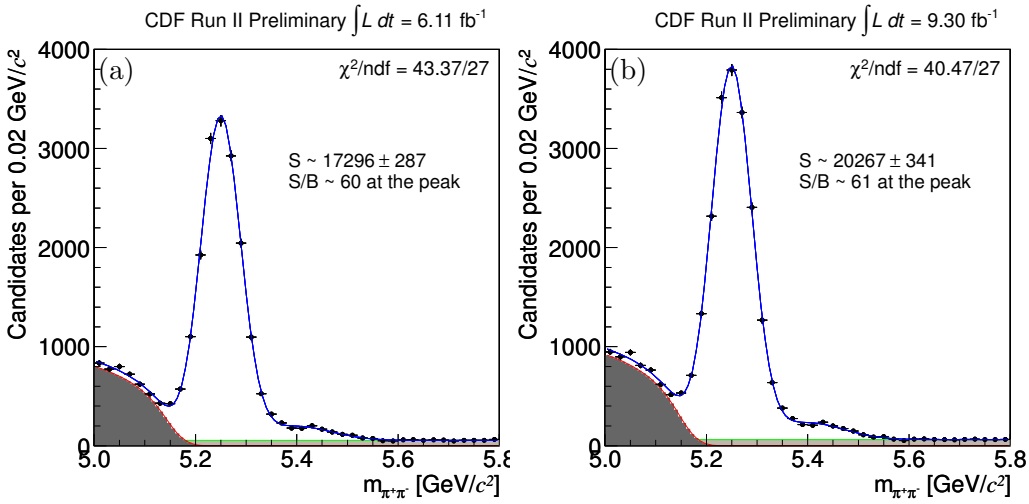

Figure C.1: Invariant $\pi\pi$-mass distribution of the events passing the final selection. for 6.11 fb^{-1} sample (a) and 9.3 fb^{-1} sample (b). Two Gaussians (signal) plus exponential (combinatoric background, light grey) plus a smeared Argus (physics background, dark grey) fit function is overlaid.

C.3 Analysis overview

The analysis strategy and the key points of the serch for the rare modes are essentially the same of the analysis described so far: the problem is to disentangle the different $B \to h^+h'^-$ decay modes between themselves and between the backgrounds; this is possible, at statistical level, combining kinematics and PID information in a multidimensional likelihood fit. We used simulations and independent data to obtain the kinematics and PID templates exploited in the Likelihood function. For the convenience of the reader, we briefly review the strategy flow, and the few differences between the two analysis.

C.3.1 Simulation

A sample of simulated $B \to h^+h'^-$ decays is needed to study the kinematics information of the different signal components and of the physics background sample, as explained in detail in chap. 4. We used the official CDF II simulation to produce these distributions, and we tuned the Monte Carlo distributions to take into account the known discrepancies with respect to the data. The tunings and the checks are the same described in sec. 4.2, with the exception of the treatment of the squared

mass resolution of simulated samples. We recall, as described in sec. 4.2.3, that the comparison of the invariant mass peaks of the $D^0 \to \pi^+\pi^-$ and $D^0 \to K^-\pi^+$ decays with their relative simulated peaks shows that the simulated square mass width is a little bit narrower of that observed in data. For the annihilation measurements we did not inflate the Monte Carlo mass distributions as we did in the $\mathcal{C}P$ analysis: in the fit of composition we simply added a free parameter s_m which is a global scale factor of mass templates described in sec. 6.1.1. We refined the technique in the analysis of the $\mathcal{C}P$ asymmetries because we needed a higher level of accuracy. Actually, the main difference is that the free parameter s_m takes into account only the bulk of the $m^2_{\pi\pi}$ signal distributions and not the tails due to the FSR, while the global enlargement $m^2_{\pi\pi} \to (m^2_{\pi\pi} - m^2)/s$ is able to modify the whole distribution. The two techniques are found to be in very good agreement.

To check the correctness of the method using a free parameter in the fit, a posteriori we verified that the value returned by the fit, $\hat{s}_m = 1.094 \pm 0.015$, was in agreement with the ratio of the mass widths between the invariant mass peaks of the $D^0 \to h^+h^{'-}$ decays for data and for simulation. Table C.1 reports the values of the widths we estimated performing a simple binned Gaussian fit in a small mass range, while fig. C.2 shows distributions for data and simulation (the fit is superimposed).

mode	Data [MeV$^2/c^4$]	Simulation [MeV$^2/c^4$]	ratio
$D^0 \to \pi^+\pi^-$	34975 ± 173	32649 ± 106	≈ 1.071
$D^0 \to K^-\pi^+$	30878 ± 26	29016 ± 81	≈ 1.064

Table C.1: Square mass widths for data and simulation for the $D^0 \to \pi^+\pi^-$ and $D^0 \to K^-\pi^+$ decays.

C.3.2 Fit of composition

The kinematics and PID information (obtained with the same methods described for the analysis using 9 fb^{-1}) are then combined in a maximum likelihood fit to disentangle the different decay modes. The kinematics templates for $m^2_{\pi\pi}$, β, $p_{\rm tot}$ were obtained using the simulation for the signal components and the physics background, and using data for the combinatorial background. The PID templates were obtained from $D^0 \to h^+h^{'-}$ and $\Lambda \to p\pi^-$ independent data samples, with the same strategy described in chap. 7 for the analysis using 9 fb^{-1}, but with the statistics available at the time of the work, that is about 6 fb^{-1}. The likelihood structure is the same described in sec. 5.6, with only a difference on how we treated the p.d.f. of the physics background mass term.

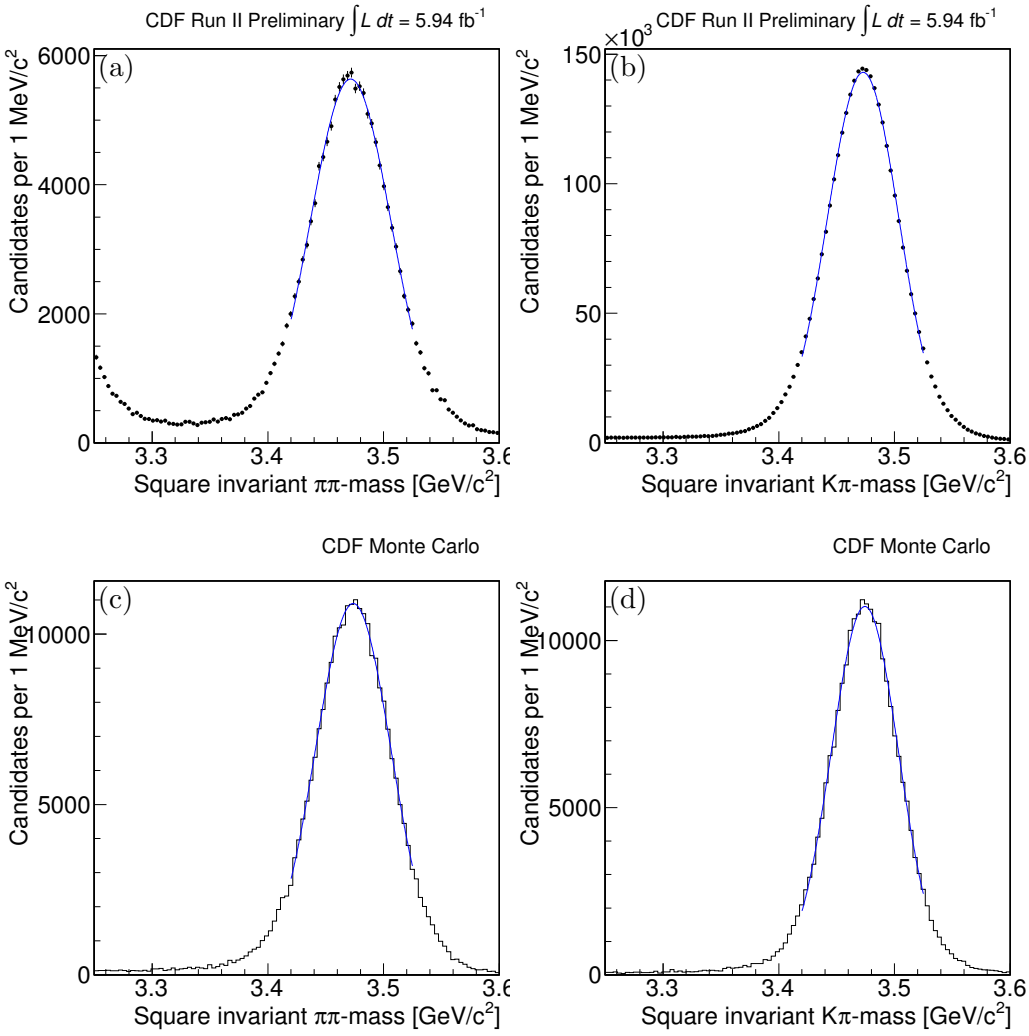

Figure C.2: Comparison of square mass resolution between data and simulation using $D^0 \to \pi^+\pi^-$ (a,c) and $D^0 \to K^-\pi^+$ (b,d) decays.

Probability density function of the physics background mass term

For the analysis of the annihilation decay modes in the p.d.f. of the physics background mass term we let free to float the parameter $c_{\rm A}$, while we fixed the cut-off $m^2_{\rm A}$ to the value returned by the one-dimensional fit of the mass shape from the simulation. Since this is an important point for the extraction of the $B^0 \to K^+K^-$ decay mode, we assessed a very conservative systematic uncertainty on our limited knowledge of this parameter (see sec. 11.2.6).

Acknowledgements

I would like to thank Prof. Giovanni Punzi, for giving me the opportunity to work in this analysis, and to teaching me how the plots can be read: looking at the other dimensions, and letting the plots themselves tell where you failed and where you did just fine.

I would like to thank Dr. Michael J. Morello, for teaching me the work style: not to be satisfied until everything was done with the most rigorous way possible, documented in the more accurate way, with the more make-sure-of checks possible performed.

I would like to thank Prof. Chang Qin for providing fig. 12.1.

I would like to thank my family for supporting me during this Ph.D. period and for letting me free do live the way I decide to. I always felt how they were looking after me, not overlooking me. For this, I thank them.

Bibliography

[1] G. Aad *et al.* [ATLAS Collaboration], "Observation of a new particle in the search for the Standard Model Higgs boson with the ATLAS detector at the LHC," Phys. Lett. B **716** (2012) 1 [arXiv:1207.7214 [hep-ex]].

[2] S. Chatrchyan *et al.* [CMS Collaboration], "Observation of a new boson at a mass of 125 GeV with the CMS experiment at the LHC," Phys. Lett. B **716** (2012) 30 [arXiv:1207.7235 [hep-ex]].

[3] RAaij *et al.* [LHCb Collaboration], "First evidence for the decay $B_s \to \mu^+\mu^-$," Phys. Rev. Lett. **110** (2013) 021801 [arXiv:1211.2674 [Unknown]].

[4] M. Gronau and J. L. Rosner, "The Role of $B_s \to K\pi$ in determining the weak phase γ," Phys. Lett. B **482** (2000) 71 [hep-ph/0003119].

[5] H. J. Lipkin, "Is observed direct CP violation in $B(d) \to K^+pi^-$ due to new physics? Check standard model prediction of equal violation in $B(s) \to K^-pi^+$," Phys. Lett. B **621** (2005) 126 [hep-ph/0503022].

[6] Y. Y. Keum and A. I. Sanda, "Possible large direct CP violations in charmless B decays: Summary report on the pQCD method," Phys. Rev. D **67** (2003) 054009 [hep-ph/0209014].

[7] M. Beneke and M. Neubert, "QCD factorization for B→PP and B→PV decays," Nucl. Phys. B **675** (2003) 333 [hep-ph/0308039].

[8] R. Aaij *et al.* [LHCb Collaboration], "First evidence of direct CP violation in charmless two-body decays of Bs mesons," Phys. Rev. Lett. **108** (2012) 201601 [arXiv:1202.6251 [hep-ex]].

[9] R. Aaij *et al.* [LHCb Collaboration], "First observation of CP violation in the decays of Bs mesons," Submitted to: Phys.Rev.Lett. [arXiv:1304.6173 [hep-ex]].

[10] R. Fleischer, "Flavour Physics and CP Violation," hep-ph/0608010.

[11] S. L. Glashow, "Partial Symmetries of Weak Interactions," Nucl. Phys. **22** (1961) 579.

S. Weinberg, "A Model of Leptons," Phys. Rev. Lett. **19** (1967) 1264.
A. Salam, in *Elementary Particle Theory*, ed. N. Svartholm (Almqvist and Wiksell, Stockholm, 1968).

[12] N. Cabibbo, "Unitary Symmetry and Leptonic Decays," Phys. Rev. Lett. **10** (1963) 531.

[13] M. Kobayashi and T. Maskawa, "CP Violation in the Renormalizable Theory of Weak Interaction," Prog. Theor. Phys. **49** (1973) 652.

[14] S. L. Glashow, J. Iliopoulos and L. Maiani, "Weak Interactions with Lepton-Hadron Symmetry," Phys. Rev. D **2**, 1285 (1970).

[15] L. Wolfenstein, "Symmetrical Parametrization Of The K-m Matrix," Phys. Rev. D **31** (1985) 2381.

[16] C. Jarlskog, "Commutator of the Quark Mass Matrices in the Standard Electroweak Model and a Measure of Maximal CP Violation," Phys. Rev. Lett. **55** (1985) 1039.
"A Basis Independent Formulation of the Connection Between Quark Mass Matrices, CP Violation and Experiment," Z. Phys. C **29** (1985) 491.

[17] J. Bernabeu, G. C. Branco and M. Gronau, "Cp Restrictions On Quark Mass Matrices," Phys. Lett. B **169** (1986) 243.

[18] K. G. Wilson, "Nonlagrangian models of current algebra," Phys. Rev. **179** (1969) 1499.

[19] A. J. Buras, "Weak Hamiltonian, CP violation and rare decays," [hep-ph/9806471].

[20] G. Buchalla, A. J. Buras and M. E. Lautenbacher, "Weak decays beyond leading logarithms," Rev. Mod. Phys. **68** (1996) 1125 [hep-ph/9512380].

[21] M. Bander, D. Silverman and A. Soni, "CP Noninvariance in the Decays of Heavy Charged Quark Systems," Phys. Rev. Lett. **43** (1979) 242.

[22] R. Fleischer, "CP violating asymmetries in penguin induced B meson decays beyond the leading logarithmic approximation," Z. Phys. **C58** (1993) 483.

[23] A. J. Buras and R. Fleischer, "Limitations in measuring the angle Beta by using SU(3) relations for B meson decay amplitudes," Phys. Lett. **B341** (1995) 379.

[24] M. Ciuchini, E. Franco, G. Martinelli, M. Pierini and L. Silvestrini, "Charming penguins strike back," Phys. Lett. **B515** (2001) 33; [arXiv:hep-ph/0104126].
C. Isola, M. Ladisa, G. Nardulli, T.N. Pham and P. Santorelli, "Charming penguin contributions to charmless B decays into two pseudoscalar mesons,"

Phys. Rev. **D65** (2002) 094005;[arXiv:hep-ph/0110411].
C.W. Bauer, D. Pirjol, I.Z. Rothstein and I.W. Stewart, "B $\to$ M(1) M(2): Factorization, charming penguins, strong phases, and polarization," Phys. Rev. **D70** (2004) 054015.

[25] R. Fleischer, "Electroweak Penguin effects beyond leading logarithms in the B meson decays $B^- \to K^-\Phi$ and $B^- \to \pi^-\bar{K}^0$," Z. Phys. **C62** (1994) 81; "Analysis of penguin induced B decays of the type b $\to$ M phi (M epsilon (pi, rho, ...)) beyond leading logarithms," Phys. Lett. **B321** (1994) 259 and "Search for the angle gamma in the electroweak penguin dominated decay $B(s) \to \pi^0\phi$," **B332** (1994) 419.

[26] R. Fleischer, "CP violation and the role of electroweak penguins in non-leptonic B decays," Int. J. Mod. Phys. **A12** (1997) 2459.

[27] N. G. Deshpande and X.-G. He, "Isospin structure of penguins and their consequences in B physics," Phys. Rev. Lett. **74** (1995) 26 [E: ibid., p. 4099];
M. Gronau, O. F. Hernandez, D. London and J. L. Rosner, "Electroweak penguins and two-body B decays," Phys. Rev. **D52** (1995) 6374. [hep-ph/9504327].

[28] M. Neubert, B. Stech, "Non-leptonic weak decays of B mesons," Adv. Ser. Direct. High Energy Phys. **15** (1998) 294, and references therein.

[29] M. Beneke, G. Buchalla, M. Neubert and C. Sachrajda, "QCD factorization for B $\to$ pi pi decays: Strong phases and CP violation in the heavy quark limit," Phys. Rev. Lett. **83** (1999) 1914; Nucl. Phys. **B591** (2000) 313; "QCD factorization in $B \to \pi K, \pi\pi$ decays and extraction of Wolfenstein parameters," Nucl. Phys. **B606** (2001) 245.

[30] J. D. Bjorken, "Topics in B Physics," Nucl. Phys. Proc. Suppl. **11** (1989) 325;
M. J. Dugan and B. Grinstein, "QCD basis for factorization in decays of heavy mesons," Phys. Lett. B **255** (1991) 583;
H. D. Politzer and M. B. Wise, "Perturbative corrections to factorization in anti-B decay," Phys. Lett. B **257** (1991) 399.

[31] M. A. Shifman, A. I. Vainshtein and V. I. Zakharov, "QCD and Resonance Physics. Sum Rules," Nucl. Phys. B **147** (1979) 385.

[32] H. -n. Li and H. -L. Yu, Phys. Rev. D **53** (1996) 2480 [hep-ph/9411308];
Y. -Y. Keum, H. -n. Li and A. I. Sanda, "Fat penguins and imaginary penguins in perturbative QCD," Phys. Lett. B **504** (2001) 6 [hep-ph/0004004];
Y. -Y. Keum and H. -n. Li, "Nonleptonic charmless B decays: Factorization versus perturbative QCD," Phys. Rev. D **63** (2001) 074006 [hep-ph/0006001];
Y. -Y. Keum and A. I. Sanda, eConf C **0304052** (2003) WG420 [hep-ph/0306004].

[33] C. W. Bauer, D. Pirjol and I. W. Stewart, "A proof of factorization for $B \to D\pi$," Phys. Rev. Lett. **87** (2001) 201806;
C. W. Bauer, D. Pirjol and I. W. Stewart, "Soft-collinear factorization in effective field theory," Phys. Rev. **D65** (2002) 054022 [arXiv:hep-ph/0109045];
C. W. Bauer, S. Fleming, D. Pirjol, I. Z. Rothstein and I. W. Stewart, "Hard scattering factorization from effective field theory," Phys. Rev. **D66** (2002) 014017 [arXiv:hep-ph/0202088];
C. W. Bauer, B. Grinstein, D. Pirjol and I. W. Stewart, "Testing factorization in B → D(*) X decays," Phys. Rev. **D67** (2003) 014010 [arXiv:hep-ph/0208034].

[34] A. Khodjamirian, "$B \to \pi\pi$ decay in QCD," Nucl. Phys. **B605** (2001) 558;
A. Khodjamirian, T. Mannel and B. Melic, "QCD light-cone sum rule estimate of charming penguin contributions in $B \to \pi\pi$," Phys. Lett. **B571** (2003) 75 [arXiv:hep-ph/0304179].

[35] B. Aubert *et al.* [BABAR Collaboration], "Measurement of CP Asymmetries and Branching Fractions in $B^0 \to\to \pi^+\pi^-$, $B^0 \to K^+\pi^-$, $B^0 \to \pi^0\pi^0$, $B^0 \to K^0\pi^0$ and Isospin Analysis of $B \to \pi\pi$ Decays," arXiv:0807.4226 [hep-ex].

[36] S. W. Lin *et al.* [Belle Collaboration], "Difference in direct charge-parity violation between charged and neutral B meson decays," Nature **452** (2008) 332.

[37] T. Aaltonen *et al.* [CDF Collaboration], "Measurements of Direct CP Violating Asymmetries in Charmless Decays of Strange Bottom Mesons and Bottom Baryons," Phys. Rev. Lett. **106** (2011) 181802 [arXiv:1103.5762 [hep-ex]].

[38] B. Aubert *et al.* [BABAR Collaboration], "Improved Measurements of the Branching Fractions for $B^0 \to \pi^+\pi^-$ and $B^0 \to K^+\pi^-$, and a Search for $B^0 \to K^+K^-$," Phys. Rev. D **75** (2007) 012008 [hep-ex/0608003].

[39] R. Louvot [Belle Collaboration], "B0(S) Decays at Belle," PoS EPS - **HEP2009** (2009) 170 [arXiv:0909.2160 [hep-ex]].

[40] K. Abe *et al.* [Belle Collaboration], "Observation of B decays to two kaons," Phys. Rev. Lett. **98** (2007) 181804 [hep-ex/0608049].

[41] K. Abe *et al.* [Belle Collaboration], "Measurements of Branching Fractions for B → K pi and B → pi pi Decays with 449 million B anti-B Pairs," Phys. Rev. Lett. **99** (2007) 121601 [hep-ex/0609015].

[42] T. Aaltonen *et al.* [CDF Collaboration], "Observation of New Charmless Decays of Bottom Hadrons," Phys. Rev. Lett. **103**, 031801 (2009) [arXiv:0812.4271 [hep-ex]].

[43] M. Morello [CDF Collaboration], "Branching fractions and direct CP asymmetries of charmless decay modes at the Tevatron," Nucl. Phys. Proc. Suppl. **170** (2007) 39 [hep-ex/0612018].

[44] S. W. Lin *et al.* [Belle Collaboration], "Difference in direct charge-parity violation between charged and neutral B meson decays," Nature **452** (2008) 332.
B. Aubert *et al.* [BABAR Collaboration], "Observation of CP violation in $B^0 \to K^+\pi^-$ and $B^0 \to \pi^+\pi^-$," Phys. Rev. Lett. **99** (2007) 021603 [hep-ex/0703016 [hep-ex]].
B. Aubert *et al.* [BABAR Collaboration], "Study of $B^0 \to \pi^0\pi^0$, $B^\pm \to \pi^\pm\pi^0$, and $B^\pm \to K^\pm\pi^0$ Decays, and Isospin Analysis of $B \to \pi\pi$ Decays," Phys. Rev. D **76** (2007) 091102 [arXiv:0707.2798 [hep-ex]].

[45] M. Beneke, G. Buchalla, M. Neubert and C. T. Sachrajda, "QCD factorization in $B \to \pi K, \pi\pi$ decays and extraction of Wolfenstein parameters," Nucl. Phys. B **606** (2001) 245 [hep-ph/0104110].

[46] M. Gronau and J. L. Rosner, "The $b \to s$ penguin amplitude in charmless $B \to PP$ decays," Phys. Rev. D **71** (2005) 074019 [hep-ph/0503131].

[47] Y. Amhis *et al.* [Heavy Flavor Averaging Group Collaboration], "Averages of b-hadron, c-hadron, and tau-lepton properties as of early 2012," arXiv:1207.1158 [hep-ex].

[48] W. -S. Hou, M. Nagashima and A. Soddu, "Difference in B^+ and B^0 direct CP asymmetry as effect of a fourth generation," Phys. Rev. Lett. **95** (2005) 141601 [hep-ph/0503072].
S. Baek, P. Hamel, D. London, A. Datta and D. A. Suprun, "The $B \to \pi K$ puzzle and new physics," Phys. Rev. D **71** (2005) 057502 [hep-ph/0412086].

[49] H. -n. Li, S. Mishima and A. I. Sanda, "Resolution to the $B \to \pi K$ puzzle," Phys. Rev. D **72** (2005) 114005 [hep-ph/0508041].

[50] H. J. Lipkin, "Pauli Blocking and Entanglement Solve $K\pi$ Puzzle. CP Violation in $B^o \to K\pi$: not in $B^\pm \to K\pi$ decays," arXiv:1105.3443 [hep-ph].

[51] K. Nakamura *et al.* [Particle Data Group Collaboration], J. Phys. G **37** (2010) 075021.

[52] R. Mohanta, "Effects of R-parity violation on CP asymmetries in $\Lambda_b \to p\pi$ decay," Phys. Rev. D **63** (2001) 056006 [hep-ph/0005240].

[53] C. -D. Lu, Y. -M. Wang, H. Zou, A. Ali and G. Kramer, "Anatomy of the pQCD Approach to the Baryonic Decays $\Lambda_b \to p\pi, pK$" Phys. Rev. D **80** (2009) 034011 [arXiv:0906.1479 [hep-ph]].

[54] Y. -D. Yang, F. Su, G. -R. Lu and H. -J. Hao, "Revisiting the annihilation decay $\bar{B}_s \to \pi^+\pi^-$," Eur. Phys. J. C **44** (2005) 243 [hep-ph/0507326].

[55] H. -Y. Cheng and C. -K. Chua, "QCD Factorization for Charmless Hadronic B_s Decays Revisited," Phys. Rev. D **80** (2009) 114026 [arXiv:0910.5237 [hep-ph]];
H. -Y. Cheng and C. -K. Chua, "Revisiting Charmless Hadronic B(u,d) Decays in QCD Factorization," Phys. Rev. D **80** (2009) 114008 [arXiv:0909.5229 [hep-ph]].

[56] J. -f. Sun, G. -h. Zhu and D. -s. Du, "Phenomenological analysis of charmless decays $B(s) \to PP, PV$, with QCD factorization," Phys. Rev. D **68** (2003) 054003 [hep-ph/0211154].

[57] A. Ali, G. Kramer, Y. Li, C. -D. Lu, Y. -L. Shen, W. Wang and Y. -M. Wang, "Charmless non-leptonic B_s decays to PP, PV and VV final states in the pQCD approach," Phys. Rev. D **76** (2007) 074018 [hep-ph/0703162 [HEP-PH]].

[58] Y. Li, C. -D. Lu, Z. -J. Xiao and X. -Q. Yu, "Branching ratio and CP asymmetry of $B(s) \to \pi^+\pi^-$ decays in the perturbative QCD approach," Phys. Rev. D **70** (2004) 034009 [hep-ph/0404028].

[59] C. W. Bauer, S. Fleming and M. E. Luke, "Summing Sudakov logarithms in $B \to X(s\gamma)$ in effective field theory," Phys. Rev. D **63** (2000) 014006 [hep-ph/0005275].

[60] A. Soni and D. A. Suprun, "Determination of gamma from Charmless $B \to$M(1) M(2) Decays Using U-Spin," Phys. Rev. D **75** (2007) 054006 [hep-ph/0609089].

[61] A. J. Buras, R. Fleischer, S. Recksiegel and F. Schwab, "Anatomy of prominent B and K decays and signatures of CP violating new physics in the electroweak penguin sector," Nucl. Phys. B **697** (2004) 133 [hep-ph/0402112].

[62] D. London and J. Matias, "Testing the standard model with $B^0_{(s)} \to$K+ K- decays," Phys. Rev. D **70** (2004) 031502 [hep-ph/0404009].

[63] R. Fleischer, "$B_{s,d} \to \pi\pi, \pi K, KK$: Status and Prospects," Eur. Phys. J. C **52** (2007) 267 [arXiv:0705.1121 [hep-ph]].

[64] P. Chang, "Direct CP violation and charmless B decays at Belle", PoS EPS -HEP2011 (2011) 140.

[65] R. Aaij *et al.* [LHCb Collaboration], "Measurement of b-hadron branching fractions for two-body decays into charmless charged hadrons," JHEP **1210** (2012) 037, [arXiv:1206.2794 [hep-ex]].

[66] R. Blair *et al.* [CDF Collaboration], "The CDF II Detector, Technical Design Report", FERMILAB-Pub-96/390-E CDF (1996).

[67] D. P. McGinnis, "Fermilab Tevatron operational status", in C. Horak (ed.), proceedings of the Particle Accelerator Conference (PAC 05), (2005); in addition, detailed and updated information on the Tevatron is available in the following web-pages:
`http://www-bd.fnal.gov/runII/index.html`
`http://www-bdnew.fnal.gov/operations/rookie_books/rbooks.html`.

[68] J. Marriner, "Secondary vertex fit with mass and pointing constraints (CTVMFT)", CDF Internal Note 1996 (1993), unpublished.

[69] C. S. Hill, "Initial experience with the CDF layer 00 silicon detector" Nucl. Instrum. Methods **A511**, 118 (2003).

[70] A. Sill, "CDF Run II silicon tracking projects" Nucl. Instrum. Methods **A447**, 1 (2000).

[71] M. Bishai *et al.*, "An SVX3D chip user's companion", CDF Internal Note 5062 (1999), unpublished.

[72] A. Affolder *et al.*, "Status report of the intermediate silicon layers detector at CDF II", Nucl. Instrum. Methods **A485**, 6 (2002).

[73] T. Affolder *et al.*, "CDF Central Outer Tracker", Nucl. Instrum. Methods **A526**, 249 (2004).

[74] L. Balka *et al.* [CDF II Collaboration], "The CDF Central Electromagnetic Calorimeter", Nucl. Instrum. Meth. A267, 272 (1988).

[75] P. Gatti, "Performance of the new tracking system at CDF II", Tesi di Dottorato (Ph. D. thesis), University of Padova, FERMILAB-THESIS-2001-23 (2001);
S. Menzemer, "TrackingCal - A tracking and alignment software package for the CDF II silicon detector", Ph. D. thesis, University of Karlsruhe and CDF Internal Note 5968 (2002), unpublished.

[76] D. Acosta *et al.*, "A Time-of-Flight detector in CDF-II", Nucl. Instrum. Methods **A518**, 605 (2004).

[77] L. Balka *et al.*, "The CDF central electromagnetic calorimeter", Nucl. Instrum. Methods **A267**, 272 (1988);
S. R. Hahn *et al.*, "Calibration systems for the CDF central electromagnetic calorimeter", Nucl. Instrum. Methods **A267**, 351 (1988).

[78] M. Gallinaro, "A New Scintillator Tile/Fiber Preshower Detector for the CDF Central Calorimeter", IEEE Trans. Nucl. Sci. **52**, 879 (2005), [physics/0411056].

[79] S. Bertolucci *et al.*, "The CDF central and endwall hadron calorimeter", Nucl. Instrum. Methods **A267**, 301 (1988).

[80] M. Albrow *et al.*, "The CDF plug upgrade electromagnetic calorimeter: test beam results", Nucl. Instrum. Methods **A480**, 524 (2002);
M. Albrow *et al.*, "A preshower detector for the CDF Plug Upgrade: test beam results", Nucl. Instrum. Methods **A431**, 104 (1999);
G. Apollinari *et al.*, "Shower maximum detector for the CDF plug upgrade calorimeter", Nucl. Instrum. Methods **A412**, 515 (1998).

[81] G. Ascoli *et al.*, "CDF central muon detector", Nucl. Instrum. Methods **A268**, 33 (1988);
C. M. Ginsburg, "CDF Run 2 Muon System", Eur. Phys. J. **33**, S1002 (2004).

[82] C. Avila *et al.* [E811 Collaboration], "A measurement of the proton-antiproton total cross-section at $\sqrt{s}$=1.8 TeV", Phys. Lett. **B445**, 419 (1999);
F. Abe *et al.* [CDF Collaboration], "Measurement of the anti-proton proton total cross-section at $\sqrt{s}$=546 GeV and 1800 GeV", Phys. Rev. D **50**, 5550 (1994).

[83] D. Acosta *et al.*, "The performance of the CDF luminosity monitor", Nucl. Instrum. Methods **A494**, 57 (2002).

[84] E. J. Thomson *et al.*, "Online Track Processor for the CDF Upgrade", IEEE Trans. Nucl. Sci. **49**, 1063 (2002).

[85] A. Abulencia *et al.* [CDF II Collaboration], "The CDF II eXtremely fast tracker upgrade", Nucl. Instrum. Meth. A572, 358 (2007).

[86] For more details on the SVT, see the following conference proceedings (and references therein):
B. Ashmanskas *et al.*, "The CDF Silicon Vertex Trigger", Nucl. Instrum. Methods **A518**, 532 (2004), [physics/0306169];
M. Dell'Orso, "The CDF Silicon Vertex Trigger", Nucl. Phys. **B** (Proc. Suppl.) **156**, 139 (2006).

[87] J. Antos *et al.*, "Data processing model for the CDF experiment", submitted to IEEE Trans. Nucl. Sci., [physics/0606042] (2006).

[88] M. J. Morello,, Ph.D. thesis, Scuola Normale Superiore, Pisa, Fermilab Report No. FERMILAB-THESIS-2007-57.

[89] For a simple introduction to the concepts of Kalman filtering, see
P. Maybeck, "Stochastic Models, Estimation, and Control", Vol. 1, New York: Academic Press, 1979, and references therein.

[90] D. Acosta *et al.* [CDF Collaboration], "Measurement of Bottom-Quark Hadron Masses in Exclusive J/ψ Decays with the CDF Detector", Phys. Rev. Lett. **96**, 202001 (2006), [hep-ex/0508022].

[91] J. D. Bjorken, "Properties of hadron distributions in reactions containing very heavy quarks",

[92] H. Albrecht *et al.* [ARGUS Collaboration], "Search for hadronic $b \to u$ decays", Phys. Lett. **B241**, 278 (1990).

[93] CDF Detector Simulation, http://www-cdf.fnal.gov/cdfsim/

[94] P. Sphicas, "A $b\bar{b}$ Monte Carlo Generator", CDF Internal Note 2655 (1994), unpublished;
K. Anikeev, P. Murat, and Ch. Paus, "Description of Bgenerator II", CDF Internal Note 5092 (1999), unpublished.

[95] T. Sjostrand, S. Mrenna, and P. Skands, "High-Energy-Physics Event Generation with PYTHIA 8.1", JHEP05 (2006) 026, Comput. Phys. Comm. 178 (2008) 852. Pythia home page: http://www.thep.lu.se/ torbjorn/Pythia.html.

[96] P. Nason, S. Dawson, and R. Ellis, "The Total Cross-Section for the Production of Heavy Quarks in Hadronic Collisions", Nucl. Phys. B303, 607 (1988).

[97] P. Nason, S. Dawson, and R. Ellis, "The One Particle Inclusive Differential Cross-Section for Heavy Quark Production in Hadronic Collisions", Nucl. Phys. B327, 49 (1989).

[98] M. L. Mangano, P. Nason, and G. Ridolfi, "Heavy quark correlations in hadron collisions at next-to-leading order", Nucl. Phys. B373, 295 (1992).

[99] G. Nanava and Z. Was, "Scalar QED, NLO and PHOTOS Monte Carlo", The European Physical Journal C - Particles and Fields, vol. 51, pp. 569583. http://dx.doi.org/10.1140/ep jc/s10052-007-0316-5

[100] P. Golonka and Z. Was, "PHOTOS Monte Carlo: A Precision tool for QED corrections in Z and W decays", Eur. Phys. J., 2006, vol. C45, pp. 97107, arXiv:hep-ph/0506026.

[101] Philippe Roy, "Relative Transverse Momentum Distributions of Bottom Hadrons in 1.96 TeV ppbar Collisions", CDF Internal Note 9338 (2008), unpublished.

[102] R. Fleischer and J. Matias, "Searching for New Physics in Non-Leptonic B Decays", Phys. Rev. D **61**, 074004 (2000), [hep-ph/9906274];
R. Fleischer and J. Matias, "Exploring CP Violation through Correlations in $B \to \pi K$, $B_d \to \pi^+\pi^-$, $B_s \to K^+K^-$ Observable Space", Phys. Rev. D **66**, 054009 (2002), [hep-ph/0204101].

[103] R. Brun et al., Geant: Simulation Program For Particle Physics Experiments. User Guide and Reference Manual, CERN-DD-78-2-REV (1978).

[104] M. Casarsa and M. J. Morello, "Isolation of B^0 and B_s^0 mesons", CDF Internal Note 9193 (2008), unpublished.

[105] M. J. Morello, G. Punzi, and G. Volpi, "A Fast Monte Carlo for generation of accurate kinematic templates of non-leptonic B and D decay", CDF Internal Note 8800 (2007), unpublished.

[106] G. Punzi, "Useful formulas on statistical separation of classes of events", [physics/0611219].

[107] Although the inequality was first (implicitly) derived by Aitken and Silverstone, it is generally referred to as Cramér-Rao (or Fréchet) inequality, following the papers below:
C. R. Rao, "Information and accuracy attainable in the estimation of statistical parameters", Bull. Calcutta Math. Soc., **37**, 81 (1945);
H. Cramér, "Mathematical Methods of Statistics", Princeton University Press (1946).

[108] D. Ayres *et al.*, "Design Report Of the Fermilab Collider Detector Facility (Cdf), August 1981", Batavia, USA, Fermilab (1981);
F. Abe *et al.* [CDF Collaboration], "The CDF Detector: An Overview", Nucl. Instrum. Methods **A271**, 387 (1988).

[109] For a discussion on the bias related to the use of multiple variables in multi-component fits see
G. Punzi, "Comments on Likelihood fits with variable resolution", eConf. **C030908** WELT002 (2003), [physics/0401045].

[110] M. J. Morello and F. Ruffini, "dE/dx for pions, kaons and protons for 6 fb^{-1} analyses.", CDF Internal Note 10442 (2011), unpublished.

[111] H. A. Bethe, "Theory of passage of fast corpuscular rays through matter", Annalen Phys. **5**, 325 (1930), in German;
H. A. Bethe, "Scattering of electrons", Z. Phys. **76**, 293 (1932);
F. Bloch, "Stopping power of atoms with several electrons", Z. Phys. **81**, 363 (1933).

[112] D. Tonelli, "First observation of the $B_s^0 \to K^+K^-$ decay mode, and measurement of the B^0 and B_s^0 mesons decay-rates into two-body charmless final states at CDF.", Ph. D. thesis, Scuola Normale Superiore, Pisa, FERMILAB-THESIS-2006-23 (2006).

[113] S.-S. 'Eiko' Yu *et al.*, "COT dE/dx Measurement and Corrections", CDF Internal Note 6361 (2004), unpublished.

[114] T. Aaltonen *et al.* [CDF Collaboration], Phys. Rev. Lett. **107** (2011) 239903 [Phys. Rev. Lett. **107** (2011) 191801] [arXiv:1107.2304 [hep-ex]].

[115] R. Aaij *et al.* [LHCb Collaboration], Phys. Rev. Lett. **108** (2012) 231801 [arXiv:1203.4493 [hep-ex]].

[116] D. Acosta *et al.* [CDF Collaboration], "Measurement of Partial Widths and Search for Direct CP Violation in D^0 Meson Decays to K^-K^+ and $\pi^-\pi^+$", Phys. Rev. Lett. **94**, 122001 (2005), [hep-ex/0504006].

[117] S. Bianco, F. L. Fabbri, D. Benson, and I. Bigi, "Riv. Nuovo Cimento, **26N7**, 1 (2003).",

[118] T. Aaltonen *et al.* [CDF Collaboration], "Measurement of CP–violating asymmetries in $D^0 \to \pi^+\pi^-$ and $D^0 \to K^+K^-$ decays at CDF," Phys. Rev. D **85** (2012) 012009 [arXiv:1111.5023 [hep-ex]].

[119] R. Aaij *et al.* [LHCb Collaboration], Phys. Rev. Lett. **108** (2012) 111602 [arXiv:1112.0938 [hep-ex]].

[120] T. Aaltonen *et al.* [CDF Collaboration], "Measurement of the difference of CP–violating asymmetries in $D^0 \to K^+K^-$ and $D^0 \to \pi^+\pi^-$ decays at CDF," Phys. Rev. Lett. **109** (2012) 111801 [arXiv:1207.2158 [hep-ex]].

[121] R. Carosi *et al.*, "Relative branching fractions and CP-violating decay rate asymmeteries in Cabibbo supressed decays of the D^0 meson", CDF Internal Note 6391 (2004), unpublished.

[122] S. Donati *et al.*, "Branching Ratios and CP asymmetries in $B^0_{(s)} \to h^+h'^-$ decays from 1 fb^{-1}", CDF Internal Note 8464 (2006), unpublished.

[123] See, for istance,
D. Brunner and A. Uhl, "Optimal Multipliers for Linear Congruential Pseudo Random Number Generators with Prime Moduli: Parallel Computation and Properties", BIT. Numer. Math. **39**, 193-209, (1999);
E.W. Weisstein, "Linear Congruence Method", From MathWorld–A Wolfram Web Resource.
`http://mathworld.wolfram.com/LinearCongruenceMethod.html`

[124] I. Adachi *et al.* [Belle Collaboration], "Measurement of the CP Violation Parameters in $B^0 \to \pi^+\pi^-$ Decays," arXiv:1302.0551 [hep-ex].

[125] B. Aubert *et al.* [BaBar Collaboration], "Observation of CP violation in $B^0 \to K^+\pi^-$ and $B^0 \to \pi^+\pi^-$", Phys. Rev. Lett. **99**, 021603 (2007). [hep-ex/0703016].

[126] S. Perazzini, "Measurement of time dependent CP violation in two-body decays", Talk given at 7th International Workshop on the CKM Unitarity Triangle (CKM 2012), Cincinnati, Ohio, 28 Sep -02 Oct 2012.

[127] Z. -J. Xiao, W. -F. Wang and Y. -y. Fan, "Revisiting the pure annihilation decays $B_s \to \pi^+\pi^-$ and $B^0 \to K^+K^-$: the data and the pQCD predictions," Phys. Rev. D **85** (2012) 094003 [arXiv:1111.6264 [hep-ph]].

[128] Q. Chang, X. -W. Cui, L. Han and Y. -D. Yang, "Revisiting the Annihilation Corrections in Non-leptonic $\bar{B}_s^0$ Decays within QCD Factorization," Phys. Rev. D **86** (2012) 054016 [arXiv:1205.4325 [hep-ph]].

[129] G. Zhu, "Implications of the recent measurement of pure annihilation decays in QCD factorization", Phys. Lett. **B702**, 408 (2011) doi: 10.1016/j.physletb.2011.07.045

[130] K. Abe *et al.* [Belle Collaboration], "Observation of B decays to two kaons", Phys. Rev. Lett. **98**, 181804 (2007), [hep-ex/0608049].

[131] G. J. Feldman and R. D. Cousins, "Unified approach to the classical statistical analysis of small signals", Phys. Rev. D **57**, 3873 (1998), [hep-physics/9711021].

[132] T. Aaltonen *et al.* [CDF Collaboration], "Evidence for the charmless annihilation decay mode $B_s^0 \to \pi^+\pi^-$," Phys. Rev. Lett. **108** (2012) 211803 [arXiv:1111.0485 [hep-ex]].

[133] F. Azfar, L. Oakes, and D. Tonelli, "Extended and improved dE/dx calibration for $3fb^{-1}$ analyses", CDF Internal Note 6361 (2008), unpublished.